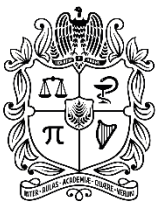

UNIVERSIDAD
NACIONAL
DE COLOMBIA

Influence of the Micro-Geometry of a Scaffold for Bone Regeneration on the Stresses of the Newly Formed Tissue

Óscar Libardo Rodríguez Montaño

Universidad Nacional de Colombia
School of Engineering, Mechanics and Mechatronics Department
Biomechanics Research Group GIBM-UN
Bogotá, Colombia

2021

Influence of the Micro-Geometry of a Scaffold for Bone Regeneration on the Stresses of the Newly Formed Tissue

Óscar Libardo Rodríguez Montaño

A Dissertation Presented in Partial Fulfillment of the Requirements for the Degree:

Doctor in Engineering – Mechanics and Mechatronics Engineering

Advisor:

Dr. -Ing. Carlos Julio Cortés Rodríguez, Universidad Nacional de Colombia, Colombia

Co-Advisor:

Ph.D. Antonio Boccaccio, Politecnico di Bari, Italy

Line of research:

Biomechanics

Research Group:

Biomechanics Research Group GIBM-UN

Universidad Nacional de Colombia

School of Engineering, Mechanics and Mechatronics Department

Bogotá, Colombia

2021

Influencia de la Micro-Geometría de un Scaffold para regeneración ósea en los esfuerzos en el tejido en formación

Óscar Libardo Rodríguez Montaño

Tesis presentada como requisito parcial para optar al título de:

Doctor en Ingeniería – Ingeniería Mecánica y Mecatrónica

Director:

Dr. -Ing. Carlos Julio Cortés Rodríguez, Universidad Nacional de Colombia, Colombia

Co-Director:

Ph.D. Antonio Boccaccio, Politecnico di Bari, Italia

Línea de investigación:

Biomecánica

Grupo de investigación:

Grupo de investigación en biomecánica GIBM-UN

Universidad Nacional de Colombia

Facultad de Ingeniería, Departamento de Ingeniería Mecánica y Mecatrónica

Bogotá, Colombia

2021

A papá y mamá, por su infinito amor…

…y entonces vi el título… “Cómo funcionan las cosas” …ahí …ahí empezó este camino.

Acknowledgments

First and foremost, I thank God for my life and the lives of all people that I love, for his grace and all blessings that He gives me every day.

I also express my special gratitude to Professor Antonio Boccaccio for the wonderful opportunity to work with him and all his teachings and guidance. To the crew of Politecnico di Bari: Professors Antonio Uva and Michele Fiorentino, Michele Gatullo, Vito Manghisi and all the kind people there. It is always a pleasure to work with them.

I thank Professor Carlos Julio Cortés Rodríguez for his guidance, support and assistance every time that I need it, and Universidad Nacional de Colombia for the opportunity to participate in the different challenges raised in this project.

I am very grateful with my friends Hector, Javier, Kalenia, Alejandro, Jennifer, Marcela, Santiago, Diana, Nikolay, Christian, Juan and the rest of my colleagues and friends in the University for the good moments that we lived there.

I thank the Colombian Ministry of Science, Technology and Innovation (MINCIENCIAS) for granting me the forgivable loan under Call 647 from 2015, which allow me to make this project possible.

Last but not least, I thank my beloved parents, Libardo and Betty, for all the love and support that they have given me throughout my whole life, and all rest of my family, Yira, my friends and the people that have always supported me.

Resumen

Influencia de la Micro-Geometría de un Scaffold para regeneración ósea en los esfuerzos en el tejido en formación

Los scaffolds para ingeniería de tejidos son dispositivos que han ganado una enorme atención en múltiples disciplinas durante las últimas décadas, como apoyo para los procesos de reparación que no ocurren de forma espontánea por medio de mecanismos naturales. Dado que los procedimientos *in vitro* e *in vivo* permiten evaluar los diferentes factores claves en el diseño de scaffolds y sus resultados, la investigación *in silico* brinda una herramienta excepcional para entender los procesos que ocurren dentro de estos dispositivos y cómo las diferentes variables de diseño influencian sus resultados finales.

Es bien sabido que las señales biomecánicas son relevantes en los procesos de reparación ósea y éstas están relacionadas con los estímulos transmitidos al ambiente de reparación como el callo en procesos normales o a las estructuras de soporte como dispositivos ortopédicos de fijación y/o scaffolds que favorecen el proceso de regeneración. En las últimas décadas los investigadores han hecho esfuerzos por caracterizar los estímulos biofísicos favorables para la formación de hueso y otros tipos de tejidos. Diferentes configuraciones geométricas de un scaffold pueden transmitir las cargas al tejido en formación en diferentes maneras dependiendo de la topología de su microestructura, pero no es claro como es este proceso durante la regeneración, y más aún, se desconoce como el ambiente biofísico dentro del scaffold está cambiando como consecuencia de su degradación. Pese a lo anterior, ha sido demostrado que hay micro-geometrías de scaffolds más favorables que otras para la regeneración ósea.

El objetivo general es investigar computacionalmente como la micro-geometría de un scaffold para regeneración ósea influencia los esfuerzos en el tejido en formación. Para lograr este objetivo, un marco computacional basado en el método de los elementos finitos es usado para representar la evolución del tejido dentro del scaffold, en conjunto con análisis estadísticos para determinar la evolución de los esfuerzos en el tejido. Dicho marco tambien es usado para encontrar parámetros favorables que definen la micro-geometría de diferentes diseños de scaffolds. Los resultados obtenidos en esta tesis enriquecen la comprensión y discusión sobre los fenómenos biofísicos que suceden dentro del scaffold, permitiendo identificar mejores diseños desde una perspectiva biomecánica.

Palabras clave: Scaffold, Hueso, Modelamiento, Computacional, Degradación, Diferenciación, Tejido en formación.

Abstract

Influence of the Micro-Geometry of a Scaffold for Bone Regeneration on the Stresses of the Newly Formed Tissue

Scaffolds for tissue engineering are porous devices that have gain an enormous attention in the last decades for multiple disciplines, as solution to help the repair process that cannot heal spontaneously by natural mechanisms. Since the *in vitro* and *in vivo* procedures test the different key factors in the design and its outcomes, *in silico* research brings an unbeatable tool for understanding the processes that occur within these devices and how different design variables will influence the final result of the treatment.

It is well known that the biomechanical cues are relevant in the bone repair processes and those are related to the stimuli transmitted to the repair environment, as the callus in a normal healing process, or to the support structure, such as orthopedic fixation devices and/or the scaffold to help the regeneration process. Researchers in the last decades have made efforts to characterize the favorable biophysical stimuli to the formation of bone and other types of tissue. Different geometric configurations of the scaffold microstructure can transmit the loads to the newly formed tissue in different ways, depending on the topology of the microstructure, but it is not clear how this process takes place during the regeneration, and moreover, how it changes if the biophysical environment is changing, as a consequence of the scaffold degradation. However, it has been demonstrated that there are more favorable scaffold micro-geometries to the bone healing process than others.

The general aim of this research was to investigate computationally, how the micro-geometry of scaffolds for bone regeneration influences the stresses on the newly formed tissue. To achieve this objective, an *in silico* framework based on the finite element method is used to represent the tissue evolution inside the scaffold and statistical analysis is used to determine the evolution of the stresses within the neo-formed tissue. The *in silico* framework is also used to find favorable parameters that define the micro-geometry of different bone tissue scaffold designs. The results obtained in this thesis enrich the understanding and discussion regarding the biophysical phenomena that occur inside the scaffold, thus allowing to identify better designs from a biomechanical perspective.

Keywords: Scaffold, Bone, Healing, Computational, Modeling, Degradation, Differentiation, Newly formed tissue.

Contents

List of figures

Page.

List of tables

Pág.

List of symbols and abbreviations

Abbreviation	Definition
ABS	Absolute
$BO_{\%MAX}$	Maximum amount of mature bone
c	Water content
$\dot{c}$	Rate of water content
C_{ij}	Effective stiffness tensor
C_{22}	Effective normal stiffness
BTE	Bone tissue engineering
D	Cross section parameter
Dc	Diameter of cylindric feature
Ds	Diameter of spheric pore
E	Young's modulus
ECM	Extra cellular matrix
$\boldsymbol{F}$	Ramp load function
FEM	Finite element method
LT	Large topology
MSC	Mesenchymal stem cells
p	Apparent compression load
Q	Side of cubic unit cell
REL	Relative amount of bone
RV	Representative volume
S	Mechanical stimulus
SFF	Solid free form
ST	Small topology
t	Time
TB	Total bone
TET	Tissue engineering triad
$V_{available}$	Volume available inside the unit cell
V_{RV}	Total volume of RV
v_{ib}	Immature bone volume
v_{mb}	Mature bone volume
VMMean	Von Mises mean
VMMedian	Von Mises median
W	Molecular weight
$\dot{W}$	Decrease rate in molecular weight
α	Diffusion coefficient
β	Material constant
γ	Octahedral shear strain
$\varepsilon_I, \varepsilon_{II}, \varepsilon_{III}$	Principal strains
ε_{ij}	Strain tensor
$\bar{\varepsilon}_{ij}$	Average strain tensor
σ_{ij}	Stress tensor
$\bar{\sigma}_{ij}$	Average stress tensor
v	Interstitial fluid velocity

Associated publications

The research work produced in this dissertation was carried out by means of a collaboration between the biomechanics research group GIBM-UN from Universidad Nacional de Colombia, Colombia and the Virtual Reality and Reality Reconstruction Lab VR3Lab from Politecnico di Bari, Italy. This collaboration was sponsored by the Colombian Ministry of Science, Technology and Innovation (MINCIENCIAS) under Call 647 from 2015. The research resulted in the following associated publications:

I) Rodríguez-Montaño, Ó. L., Cortés-Rodríguez, C. J., Uva, A. E., Fiorentino, M., Gattullo, M., Monno, G., & Boccaccio, A. (2018). **"Comparison of the mechanobiological performance of bone tissue scaffolds based on different unit cell geometries".** *Journal of the Mechanical Behavior of Biomedical Materials*, *83*, 28-45.

II) Rodríguez-Montaño, Ó. L., Cortés-Rodríguez, C. J., Naddeo, F., Uva, A. E., Fiorentino, M., Naddeo, A., ... & Boccaccio, A. (2019). **"Irregular load adapted scaffold optimization: a computational framework based on mechanobiological criteria".** *ACS Biomaterials Science & Engineering*, *5*(10), 5392-5411.

III) Rodríguez-Montaño, Ó. L., Cortés-Rodríguez, C. J., Uva, A. E., Fiorentino, M., Gattullo, M., Manghisi, V. M., & Boccaccio, A. (2020). **"An Algorithm to Optimize the Micro-Geometrical Dimensions of Scaffolds with Spherical Pores".** *Materials*, *13*(18), 4062.

IV) Rodríguez-Montaño, Ó. L., Cortés-Rodríguez, C. J., Uva, A. E., Fiorentino, M., Evangelista, A., Gattullo, M., ... & Boccaccio, A. (2021). **Geometry optimization of scaffolds for bone tissue engineering.** In *Computational Modelling of Biomechanics and Biotribology in the Musculoskeletal System* (pp. 277-301). Woodhead Publishing.

1. Introduction

A scaffold for regenerative medicine is defined as a 3D porous structure for physically supporting cells and tissues that provides a suitable environment for cellular processes in tissue regrowth and development. These processes are influenced by various factors of biological, chemical and physical nature and they occur at different temporal and size scales. At macro-scale, the scaffold becomes a temporary structure that supplies functions such as guaranteeing a biomechanical integrity to the target tissue [1], load bearing among others. At micro-scale, cells infiltrate and colonize the available volume inside the porous scaffold, where they can undergo many processes, e.g. proliferation, migration differentiation and synthesize extracellular matrix (ECM). At the same time, the scaffold material and micro-geometrical features will determine the mechanical properties of the whole scaffold at macroscopic level.

Commonly, the tissues are composed of cells and ECM, which is synthesized and maintained by specialized cells. When a scaffold is used, it behaves like a temporary substitute for the ECM. The cells are either seeded or migrate from the surrounding tissue into the scaffold. Then, they produce new matrix inside the void spaces, thus filling the pores and other spaces produced by scaffold degradation, as long as the scaffold material is biodegradable.

Bone is one of the most studied tissues in regenerative medicine and tissue engineering, since it is one of the most implanted and transplanted tissues worldwide [2], [3]. Bone loss by trauma or disease remains one of the main challenges of the clinical practice and the regenerative medicine. Its healing process inside scaffolds is a very complex phenomenon, whose exact mechanisms remain unclear. Many studies have been conducted to enhance understanding and performance of bone regeneration within scaffolds. This process is regulated by a set of different signals that influences cell behavior. A classic approach used to focus mainly on biochemical signals but, in recent years, physical signals have gained attention from researchers [4]. One of the most important physical signals is the mechanical stimulus, which is a signal related to loads, deformations and thus stresses on cells and tissues. The importance of a mechanical stimulus is that this signal plays a key role in the fate of cell: this theory is known as mechano-regulation [5]. This stimulus depends on both

the macroscopic biomechanical environment and scaffold micro-geometrical features, such as pore shape and size. However, the relation between these features and mechanical stimulus on cells and tissues is not clear yet [1].

The critical size bone defects represents a challenge for clinical context, as they are healing orthopedic defects that do not heal spontaneously and where no union or mal union could be occur [6], [7]. One of the main reasons of the no union case is the wrong differentiation of the MSC [8]. A delayed union is another problem in the clinical practice, since the injury could take more time to heal than expected [7]. These issues are studied in the regenerative medicine field and can be managed with cell and gene therapies, using MSC and bone grafts, where the latter still show issues related to rejection and availability. Among bone grafts, scaffolds are a promising solution to repair critical-sized bone defects that would normally require bone substitutes [9]. They can be composed of biomaterials that support the newly formed tissue and cells, and promote its appropriate differentiation [10].

Mechanical stimuli are difficult to determine on cells and tissues within scaffold, because of the complexity of the micro-geometrical features of the device and due to the structural changes produced by scaffold degradation. Oftentimes, the complexity of the scaffold topology is produced by its fabrication method. These porous structures can be obtained by physical and chemical methods where most of them produce irregular porosities and hinder a precise control over the micro-geometrical features [11]. A strategy that has been gaining attention in last years is to obtain scaffolds by advanced manufacturing technologies, e.g. additive manufacturing processes. A great advantage of additive technologies is their capability of obtaining a better geometric control than other methods, which opens up the possibility to make regular structures to achieve a regularity in the physical conditions throughout the scaffold domain, and thus in the newly formed tissue.

As discussed previously, mechanical stimuli have a key role in bone healing and are related to the scaffold features. Consequently, the lack of knowledge about mechanical effects on newly formed tissue produced by the scaffold can lead to the use of scaffold designs that produce unexpected tissues or start bone resorption processes in some regions.

There is a need to enhance scaffold design from a biomechanical perspective and taking into account its interactions with biological processes. Additionally, the assessment of the

new designs and their evolution in time is required. It is a common practice that the criteria used to design scaffolds are based on trial and error approaches. To assess scaffold designs (*in vitro* or *in vivo*), costly and time-consuming experiments are required. Therefore, assessment through computer simulation is a good option to complement and evaluate the scaffold designs, hence reducing the number of expensive trials.

Reviewing the main points above and considering its importance, it can be stated that the temporal evolution of the state of stresses on the newly formed tissue, inside a biodegradable scaffold, is unknown with respect to its micro-geometrical characteristics. In this context, this research addressed the question “How does the micro-geometry of scaffolds for bone regeneration influence the stresses on the newly formed tissue?” Our initial hypothesis is that the scaffold micro-geometrical characteristics, such as shape, size and pore interconnection, have a significant relation to stress patterns and magnitudes on the newly formed tissue.

The aim of this research is to determine how the micro-geometrical features of a scaffold for bone healing influence the newly formed tissue from a biomechanical perspective, that is, how are the stresses within these evolving tissues and if there are any relationships between these stresses and the predicted behavior regarding its mechanobiological performance. This aim is divided into three specific objectives. The first one is to find possible relationships between the scaffold micro-geometrical features and the stress distributions on the newly formed tissue. The second one is to determine how geometrical and physical changes produced by scaffold degradation influence the stresses on the newly formed tissue and the mechanical behavior of the scaffold-tissue system. Finally, the third objective is to suggest trial scaffold micro-geometrical features that produce favorable stress distributions for typical loading conditions of bone tissue, that is, provide an adequate mechanobiological stimulation. By means of these objectives, it was possible to respond the research question and demonstrate our initial hypothesis. This hypothesis was confirmed initially for regular geometries. Also, as result of the analysis of the different scaffold designs, it was possible to compare the predicted performance of each of them and establish which design and which parameters are suitable for a set of loads, from a biomechanical perspective.

In order to achieve the proposed objectives, a combination of *in silico* approaches based on the finite element method (FEM) were used to determine and predict the behavior of scaffolds under several conditions. We proposed and simulated a considerable number of scenarios to determine stress distributions. Finally, by means of statistical analyses, we determined relationships between the scaffold micro-geometrical features, the stress distributions on the newly formed tissue and their changes over time. As part of the research process developed, a stage of qualitative and quantitative verification of the results obtained through simulation using scenarios from scientific literature was performed to corroborate the consistency of those results.

For simplicity purposes, the research was limited to a biomechanical perspective, and conditions such as vascularization, oxygen and nutrients supply and removing of waste were supposed as ideal. Also, the temperature influence and the metabolic effects caused by the scaffold degradation were neglected.

The knowledge of the relation between micro-geometrical features and the stresses within the scaffold and the newly formed tissue will allow a better understanding of what is happening biomechanically inside the scaffold. Additionally, the possibility of identifying favorable scaffold micro-geometrical features for bone regeneration can become a tool to enhance the scaffold design and performance in the bone tissue engineering field.

The thesis is articulated in six chapters. Chapter two presents a review of the theoretical background with the relevant concepts used along this dissertation and the state of the art in the field of scaffolds for bone tissue engineering. Chapter three describes the methodology to model scaffolds, compute the stress distributions and predict the tissue phenotypes that will be developed inside the scaffold considering the geometry and loads applied on the scaffold-tissue system at a very early stage of the healing, that is, without taking into account the evolution in time. Afterward, in this chapter a statistical analysis is performed to verify if there are relations between the geometrical scaffold features and the stress state acting on the neo-formed tissue. Chapter four is focused on the optimization of different scaffold unit cells to maximize the formation of bone. Chapter five describes a methodology to simulate the evolution in time of the scaffold-tissue system. Finally, in chapter six, all the results obtained will be discussed together and possible conclusions will be drawn.

As contributions, we present a description of the relationships between scaffold micro-geometrical features and the stresses on the newly formed tissue. Based on these relationships, it will be possible to enhance scaffold performance and obtain possible strategies to control it.

The enhancement of design and performance of scaffolds will have a direct consequence in the application of these devices in the clinical practice, where the control and predictability of the biological responses on the patient is a key requirement to apply these technologies.

Finally, this work will be useful in future research as a computational framework to include and assess other stimuli such as biochemical gradients in the field of bone tissue engineering.

2. Theoretical background

The major goals of tissue engineering are to apply engineering principles and methods to restore organs, tissues or their functionality, and enhancing wound healing. This field is highly multidisciplinary and requires interactions from professionals of clinical medicine, several fields of engineering and basic sciences like math, physics, chemistry and life sciences [12]. Three components have been identified as key factors in tissue engineering: Cells, Regulatory Signals and Scaffolds [13], known as Tissue Engineering Triad (TET). Based on the TET and with particular emphasis on the Bone Tissue Engineering (BTE) context, we introduce and describe the generalities needed to contextualize this research.

2.1 Cells

The cell, as a basic biological unit, is the first element of the triad. From a structural perspective, these units are composed of a membrane that separates them from their external environment. Cytoskeleton, cytoplasm, nucleus and other sub-cellular components are surrounded and enclosed by this cell membrane. Intra and extra cellular events occur due to cascades of biochemical signals triggered by cell-environment or cell-to-cell interactions. Specialized cells work together to synthesize and maintain an ECM to perform their processes and form a tissue. This occurs *in vivo,* as well as in cell cultures for study purposes. Regardless of the cell environment, there is a need to maintain an adequate and continuous supply of nutrients and oxygen, as well as to remove metabolic waste products to maintain the necessary cell functions to keep the cell alive. In the tissue engineering field, the cells can be autologous, allogenic or xenogeneic. Autologous cells are derived from the own cells of the individual, allogenic cells are derived from a donor of the same species and xenogeneic cells are derived from other species [13].

In BTE, it is important to delve into the concepts of the target tissue, i.e. the bone, which is one of the most influenced tissues by physical signaling, due to its natural physiological function: body support and protection of organs. Therefore, bone cells are notably influenced by physical cues which produce several responses by mechano-transduction mechanisms. These responses may belong to the processes of bone development and bone healing, which have been extensively studied and well documented in the literature

[5], [14]–[17]. BTE uses the knowledge about bone biology, healing, structure and mechanics to repair and regenerate bone tissue successfully.

Bone is a connective tissue with a high degree of complexity from different scale levels and it has unique capabilities, such as renewing and healing itself, and adaptation to its biomechanical environment [14]. It carries out important functions at different levels. For example, at macroscale, it has the functions to be the main structural framework of the muscle-skeletal system, to protect vital organs and store bone marrow, and at lower scales, to serve as reserve of mineral salts and also endocrine functions [15].

From a material perspective, bone is a porous biocomposite comprised by organic and inorganic phases with structural features from nano to macro-scale levels. The former phase is composed of cells, collagen fibers oriented and other proteins, and the latter by hydroxyapatite crystals and calcium carbonates [14]. Mineral components from the inorganic phase provide compression resistance, whilst organic phase components confer tensile resistance. It is possible to distinguish between two types of bone: immature or woven bone and mature bone. The immature bone has an unorganized structure that exhibits isotropic properties and is present at early stages of development and repairing of bone and in pathological conditions [16].

The mature bone is a hierarchical structure that can be either cortical or compact, or spongy, cancellous or trabecular, which approximately encompass the 80% and 20% of total bone in humans, respectively [17]. The porosities of these types can vary between 5 to 95 percent [18]. Histologically the mature bone types are composed of the same elements but in different organization, hence, different function. Some common elements are the lamellae, which are thin layers of calcified bone matrix that envelop small spaces called lacunae, where the cells responsible of the bone tissue maintenance reside. Connections between lacunae and bone surface are achieved by small channels, called canaliculae.

Spongy bone is made of irregular trabeculae composed of lamellae covered by a thin layer of connective tissue known as endosteum. This bone type has high porosities that range from 50 to 95% and it is filled by bone marrow [18]. On the other hand, compact bone is composed of concentric layers of lamellae forming dense structures known as haversian

system or osteon, with central connectivity called haversian canal, and transverse connectivity by canaliculae to supply the inner cells by means of blood vessels. Different osteons are interconnected by means of transverse branches known as Volkmann channels. As trabecular bone, the compact bone is enveloped externally by a membrane of connective tissue called periosteum and also have endosteum covering the bony interconnectivity channels.

Bone exhibits principally five types of cells that work in synergistic way to develop and maintain its processes: osteoprogenitor cells, osteoblasts, osteocytes, bone lining cells and osteoclasts [16], [19]. The first four have a common lineage from Mesenchymal Stem Cells (MSC) and they are a result of its subsequent differentiation process. MSC are multipotent cells which can differentiate into osteoprogenitor cells (among others such as adipocytes) that will further become pre-osteoblasts, and mature osteoblasts that synthesize bone matrix proteins, known as osteoid, which in turn will be mineralized to model the bone tissue [20]. Finally, several osteoblasts are enveloped by the locally produced osteoid and become osteocytes to carry out activities of monitoring and upkeep of a balanced environment for the bone, such as the calcium phosphorus balance and the adaptation in response to mechanical stimulation [21]. The rest of osteoblast transforms into bone lining cells, which have flat morphology and lie inactive on the bone surface, and their functions are not completely understood. Osteoblasts can also undergo programmed cell death known as apoptosis [19].

Unlike bone lining cells, osteoblasts and osteocytes, osteoclasts come from the hematopoietic stem cells lineage and have a considerable bigger size than the cells of mesenchymal lineage [19]. Osteoclast is responsible of resorption of bone matrix by means of enzymatic degradation, essential activity in bone remodeling. Additionally to the aforementioned cells, fibroblasts and chondrocytes are other types of cells of mesenchymal lineage involved in bone formation and healing processes. Fibroblasts are the characteristic cells of fibrous tissue and chondrocytes are the characteristic cells of cartilage tissue. All these cells belong to the family of connective tissue cells [22].

Physiologically, the processes of bone synthesis and resorption are always active throughout life since the embryonic development. These processes occur simultaneously through the coordinated actuation of osteoblast and osteoclast groups that together form

bone remodeling units (BMUs), which perform the remodeling process regulated by a variety of biophysical and biochemical stimuli [23].

Ossification or osteogenesis is the process in which the bone formation occurs. It could be of two types: endochondral and intramembranous. The former consists in the straight bone formation by the osteoblast differentiated from MSC cells, while the latter implies the presence of cartilage cells to form a cartilaginous matrix as temporal template that will finally be replaced later by the bone tissue. The osteogenesis of most bones is endochondral, a low proportion is intramembranous, and some bones require both mechanisms.

The process of bone development, remodeling and healing occurs in a different way. When the bone tissue is damaged, healing is involved [24]. There are several varieties of bone along the skeletal system of vertebrae species, depending on the anatomic site, which leads to different healing processes depending on the bone function and ubication [16], [25]. The bone repairs in primary/direct healing or indirect/secondary healing depending on the severity of the injury and other factors such as gap size, amount of fragments, interfragmentary strains, lack of vascularization and the presence of pathological conditions such as infections.

The direct healing mechanism will be present in small bone injuries, such as little cracks and gaps, where there is alignment of cortical fragments and stability (no displacement) in the damaged tissue and neighboring zones. If those conditions are fulfilled, BMUs create channels over the wound and refill it with new bone, process known as Haversian remodeling. If the intensity of the injury is higher, e.g. the gap is large, the disruption of the tissues will lead to a hemorrhagic response. This response will produce a clot in the tissue debris that will be invaded by fibroblast and neo vascular network forming the granulation tissue and then a structure known as soft callus composed of remnant clot and debris, fibrous tissue and blood vessels [24]. This early phase is known as inflammatory phase and it is part of the secondary healing process, also called spontaneous or direct healing, that is, the most common pathway of bone healing [26], [27].

As the time passes, the soft callus evolves to a hard callus by the action of MSC that invade the hematoma, and then differentiate into fibroblasts and chondrocytes to form a fibrocartilage matrix. When this matrix obtains enough blood supply, it will be calcified to

serve as a highly vascularized scaffold for the woven bone formation by osteoblasts. All these events comprise the reparative phase. From the newly formed tissue in the early state of healing until the ossification of hard callus and its transformation to woven bone, it is worth noting that these tissues have an unorganized structure, unlike the mature bone [28].

At the end of the reparative phase and after recovering the gap and enough stiffness to support the physiological functions, the remodeling phase will start recovering the original shape and adapting the structure to the physiological biomechanical environment. Oftentimes, intramembranous and endochondral ossification are combined during bone healing [29]. Trabecular bone fractures heal through intramembranous ossification while diaphyseal fractures heal through endochondral ossification [30]. In humans, the average healing time from the injury formation until a significant degree of healing is between 6-12 weeks, depending on the specific bone. The gap bridging occurs in the first days, while the remodeling phase takes the remainder of the time, even months or years. In summary, Figure 2.1(a) shows the main cellular evolution that takes place in the secondary healing process after the cloth formation, and Figure 2.1(b) shows the three phases of this process globally.

2.2 Regulatory signals

Cell activities can be understood as sensing, transduction and responding activities. The last group is well identified by biology as recruitment, migration, proliferation, differentiation, apoptosis, synthesizing of ECM and other proteins and biomolecules. Behind all these activities there are many very complex mechanisms regulated by multiple signaling pathways that influence its behavior. Three fundamental pathways of the cell to communicate with other cells or the environment are mechanical, electrical and biochemical [31], [32]. Some additional pathways from the physical environment are thermal, magnetic, ultrasound and photostimulation, which have been recognized and researched in the last years [33].

Biochemical signaling is a pathway that has attracted the interest of researchers in the last three decades. Chemical reactions series between biomolecules and substances of proteic

nature, such as grow factors, cytokines and hormones occur intracellularly and extracellularly. The signaling agents pass messages using molecular mechanisms to trigger or shutdown cellular activities, that is, acting as positive or negative regulators following a complex sequence of well-orchestrated events [34]. The nature of signaling may come from endogenous expression, interaction with stimulator or inhibitor substances secreted by other cells, by chemical reactions or by ECM interactions. Even cell activities such as apoptosis trigger other activities using biochemical signaling, thus releasing agonist or antagonist messengers. To name a rough example, there are numerous molecular mechanisms involved in secondary healing of bone tissue, where recruitment of cells, osteoblastogenesis, chondroblastogenesis, synthesis of cartilage, apoptosis of chondrocytes, synthesis of osteoid and its subsequent mineralization occur by the action of several time-coupled biochemical cascades.

Figure 2-1: (a) Cellular evolution and (b) phases of secondary bone healing.

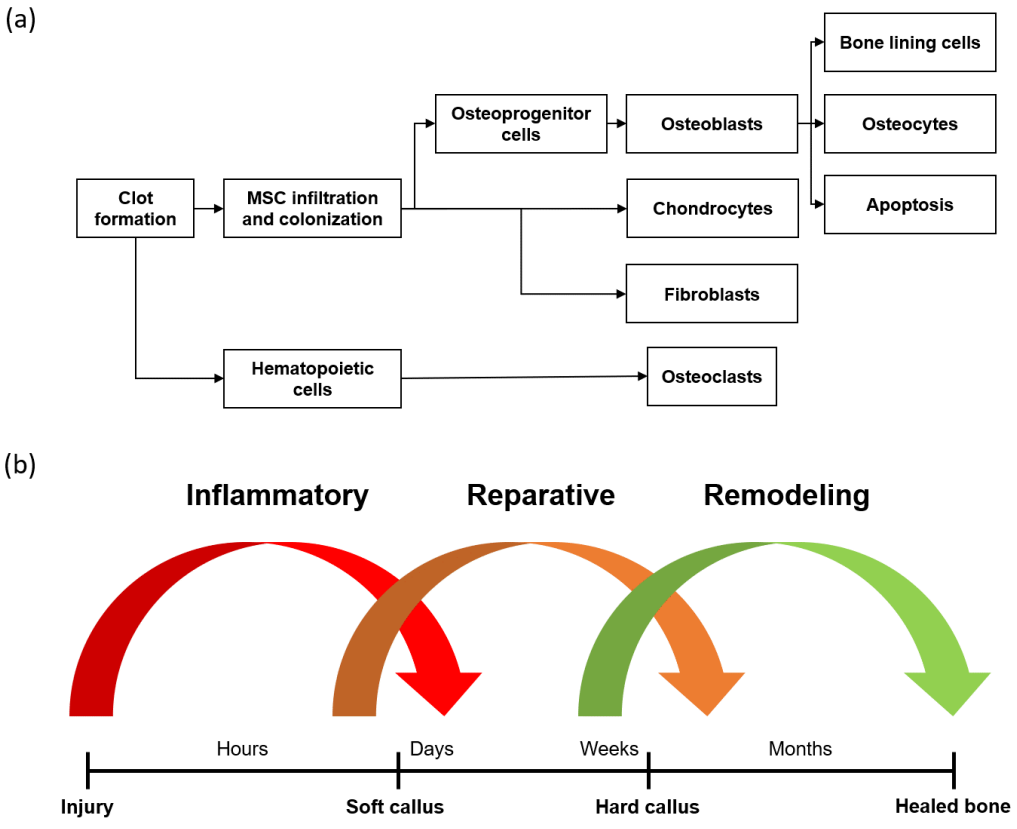

In the BTE context, Bone Morphogenetic Proteins (BMPs), Insulin-like Growth Factors (IGFs), Fibroblast Growth Factors (FGF), Vascular Endothelial Growth Factors (VEGF),

Platelet Derived Growth Factors (PDGF) and Transforming Growth Factor-β (TGF-β) proteins have a paramount influence on bone development and healing [35]. Both Intramembranous and endochondral ossification mechanisms have similar biochemical signaling in its development. Some biochemical signaling pathways are exclusive for development, others are exclusive for healing, and some have place in both, such as the Wnt pathway [36].

Although the biochemical and mechanical pathways are usually recognized as the most important in bone biology, electromagnetic signaling has been investigated due to molecular mechanisms, such as pumps, transporters and ion channels (molecular machines), and their close relationship with physiological, cellular and tissue electrical dynamics and other phenomena as galvanotaxis [37]. Transmembrane voltage gradients and bioelectrical cues have an instructive role. Regarding BTE, significant attention has been gained by the piezoelectric nature of bone and the presence of electric fields in cyclic loading that could benefit bone healing. Electro stimulation has demonstrated positive osteogenic effects at molecular and cellular levels [31]. It is proven that different cellular mechanisms and functions in bone biology are influenced by electrical stimulation, such as migration, proliferation, attachment, adhesion, organization, differentiation and apoptosis, among others [38]. Despite the poor understanding of the mechanism underlying this phenomenon [39], several signals have been identified, such as electrical currents and potentials, and electric and electromagnetic pulsed fields. These fields can be exogenous or endogenous [40] and have shown positive influence on the skeleton system in morphogenesis and regenerative processes.

Other physical signals less investigated are ultrasound and photostimulation. Ultrasound consists in mechanical sound waves at high frequencies, which are supposed to affect (accelerates and enhance) bone ossification processes and angiogenesis by means of the generation of mechanical forces, e.g. acoustic gradient pressures, that produce micro fluid flows and influence the diffusion processes of biochemical factors [41], [42]. On the other hand, photostimulation employs a source of light to produce stimuli that modulate biochemical events in cells and tissues [33].

The role of physical signals and their influence has been debated for years and most researches have been focused on biochemical signaling. The general process by which

cells sense external loading transmitted through the ECM is known as mechano-sensing and the cellular response (biophysical and biochemical) derived from this process is known as mechano-transduction [43].

The underlying mechanism for this research is the mechanical pathway. There are different mechanical cues acting on tissues and influencing its behavior. Particularly, several musculoskeletal tissues seem to be more sensible to mechanical signaling than other tissues in biological systems, because their physiological functions are related to mechanical functions and its lineage comes from mesenchymal tissue. Several categories have been identified and can be grouped, on the one hand, into substrate features such as topography and stiffness that cells are capable to sense to adapt its shape and respond to it. On the other hand, extrinsic cues such as forces and strains come from macroscopic or organ tissue levels and are transferred to the cell level by means of axial and shear stress and strains, and/or by its tensorial components, strain energy density, residual stresses, wall shear stresses, hydrostatic pressures and shear stresses induced by fluid flow, among others [31], [44]. The fluid flow may act electrostatically showing the interrelation between different pathways [45]. In this sense, it is worth noting that the fundamental pathways can be coupled, for instance, physical pathways (mechanical or electrical) trigger the biochemical response. Additionally, redundant signaling assures the successful accomplishment of programed biological events. In general, physical signaling will be transduced to biochemical signaling [13].

Cytoskeleton plays a fundamental role in cell sensing activities. It is believed that cells sense strain by means of its attachment mechanism, while fluid flow is sensed by cell membrane. Both of them produce cell deformations that lead to trigger cascade signaling [46]. However, the precise mechanisms are not understood completely.

The mechanical cues have the potential to trigger bone tissue and cell activities if they are applied continuously. Different theories and models were proposed by different researchers in last thirty years to explain the behavior of cells under the different mechanical stimuli. Therefore, the next section reviews the main models available in the literature to explain this phenomenon regarding osteogenic pathway.

2.3 Mechano-regulation theories and models

Mechanobiology is the field that bridges cellular biology, biochemistry and mechanics to expand the understanding of how the different biomechanical stimuli and sensing and transductions mechanisms of cells interact and respond, i.e., how is the mechano-regulation process of diverse cell functions. Both soft and hard tissues are thought to be modulated in activities like growth and remodeling by the action of mechanical cues, such as stress. In this context, non-specific tissue mathematical models has been proposed to enhance the understanding of this phenomenon [47], [48].

Diving deep into hard tissues, many researchers recognized that bone modeling and remodeling respond to stress trajectories. Specifically, one of these researchers was Julius Wolff, who suggested that the shape and architecture of bone are related to mechanical stress by a mathematical law, known as Wolff's law. Although, Wolff did not prove his assertions, the law was proved years later through the work of Wilhelm Roux. Roux's work was related to tissue differentiation and inspired one of the first research works on the physical signals that was carried out by Friedrich Pauwels, who suggested several hypotheses regarding the relationship between biophysical stimuli and tissue phenotypes in bone healing.

Pauwels assumed that the mechanical stimuli on tissues (such as forces, deformations and thus stresses) are transferred in similar form from the macroscopic to cell level [49]. Prendergast et al. describe Pauwels hypotheses as follows [49]:

1. "Deformation causes mesenchymal stem cells to differentiate to form fibrous connecting tissue whereas hydrostatic compression causes them to differentiate to form cartilage; combined stress states tend to cause tissue differentiation of fibrocartilage." [52, p. 360].

2. "Bone formation only occurs after soft tissue formation has stabilised the mechanical environment." [52, p. 360].

These hypotheses have some limitations, such as the difficulty of the author to measure strains and stresses within the bone and the absence of a specific stimulus for bone

formation [50]. However, other authors worked on these hypotheses using animal and numerical models, which were useful for developing later theories and researches focused on determining the mechanical signals that control cell differentiation and other cellular processes.

One of the first attempts of a quantitative theory of bone repair was the interfragmentary strain (IFS) theory proposed by Perren et al. [51]. Based on the tolerance of tissues to rupture, they hypothesize strain levels in which tissue differentiation fate is driven by the ratio between the relative displacement of the fracture ends versus the original gap width. In this sense, bone formation is expected for IFS<2%, cartilage tissue is expected for 2%<IFS<10%, and IFS>10% represents granulation tissue and thus no-union. Albeit this approach has a one-dimensional character and is not completely related to *in vivo* observations, it describes a basis of knowledge about how the mechanical environment influences the tissue differentiation and evolution in fracture healing. Since IFS theory does not consider the multiaxial state of stress and strain, later models include this feature using different invariants of stress and strain tensors to address this issue.

Formally, the first and classic mathematical description of bone remodeling and adaptation was introduced by Frost with the mechanostat theory, in which activation thresholds were proposed for processes such as modeling, remodeling, damage and maintenance of the existing conditions for load bearing bones [52]. The concept of bone as a material composed of a solid porous matrix and fluid constituents and the adaptative elasticity theory based on this concept were introduced and discussed by Cowin [53], [54]. Based on Cowin, Huiskes and Weinans presented an alternative theory of adaptative elasticity with the strain energy density as control variable and its applications using FEM [55], [56].

Some of the modern highlighted researches in this topic were carried out by Carter [57], who correlated new tissue formation with the local stress history. Claes and Heigele used principal strain and hydrostatic pressure to predict the differentiation of the callus tissue close to calcified surfaces in fracture healing [58]; and Prendergast proposed octahedral shear strain and interstitial fluid velocity as variables of stimulus function [59], [60].

Mathematical formulations have also been proposed in an attempt to translate these theories into functional models capable of predicting and being comparable to experimental

findings. To tackle the qualitative limitation of Carter's theory, the osteogenic index (OI) was introduced in order to obtain consistent physiological patterns [61]:

$$OI = \sum_{i=1}^{c} n_i(S_i + kD_i)$$

where c is the number of load cases, n_i the number of their repetitions, S_i the octahedral shear stress, D_i the hydrostatic compressive stress and k is an experimental constant.

Figure 2-2: Mechano-regulation diagram proposed by Lacroix and Prendergast.

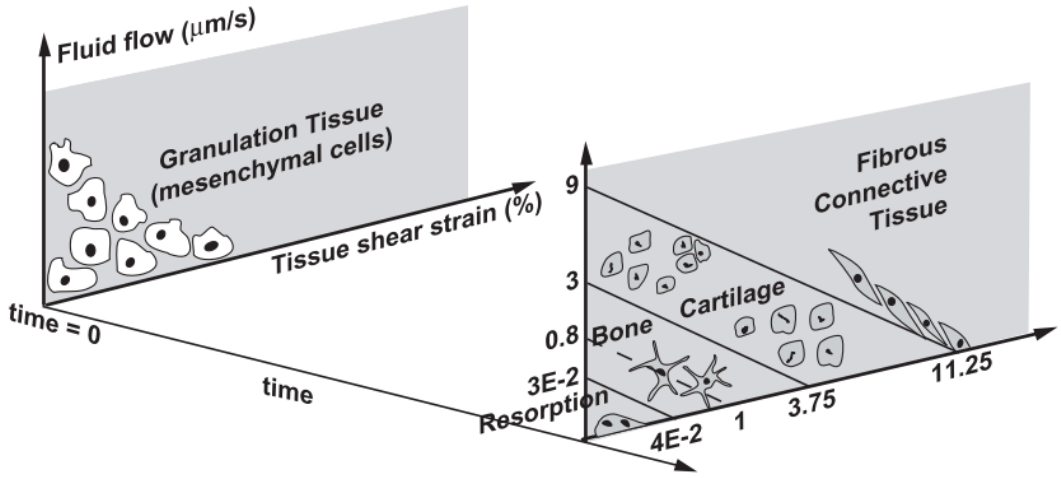

Image taken from Lacroix et al., 2002 [60].

The model proposed by Prendergast and later models developed by his co-workers contained also biological relevant processes in bone healing such as cell movement, proliferation and synthesis of matrix by differentiated cells [62]. These features make it a suitable model to describe and predict biomechanical behaviors in bone healing processes [63].

The models previously discussed, are related to the mechanical stimuli that influence bone healing. However, another process that influences the mechanical stimuli is bone remodeling. This process consists in bone adaptation of its structure and properties to the mechanical loading.

From the previous mathematical models, several computational models have been proposed to study the effects of different physical and biochemical factors involved, that are thought as key factors in modeling, remodeling, healing and even in tissue engineering scenarios. In general, the models describe the biological process of bone healing from differentiation and from remodeling perspectives. Representative researches in computational mechanobiology models such as [64]–[67] use remodeling theories for different topics of bone development and healing, while other authors such as [68]–[71] employ differentiation theories. Interesting features such as callus tissue growth have been incorporated in this kind of models to assess the volumetric evolution of tissue, unlike other models that use a fixed geometry of the problem [72].

The purpose of previous theories is to represent the events in bone development and healing, and predict outcomes of different scenarios close to those observed experimentally. Alternatively, strategies to achieve this objective have been developed, such as cellular automata using local rules to model bone healing [73]. More sophisticated models have been published as the developed by Shefelbine et al. [30] and Wang et al. [74] that uses fuzzy logic and classic theories to model bone fracture healing. Interesting alternatives to model processes such as volumetric tissue growth and tissue deposition inside scaffolds have been also documented in the literature [75]–[77].

Previous studies promise to be powerful tools to predict bone tissue behavior, but also have certain limitations. As models, they have simplifications that include partially or totally neglect many aspects on the physical, biological and chemical standpoints.

Most of the aforementioned models are phenomenological models. The internal relationships in the model seek to describe the data observed in a phenomenon of interest in the best possible way through statistical or empirical facts. On the other hand, mechanistic models stablish explicit and independent relationships for the key factors involved in the phenomenon of interest in order to explain it widely in the range of the different variables through deterministic laws. However, both of them have advantages and disadvantages related to the amount of available data to feed the model and the difficulty to implement it.

2.4 Scaffolds

Another key factor in the TET is the scaffold. This structure has some requirements such as being able to provide a suitable environment for cellular processes, guarantee the mechanical stiffness of the neotissue-scaffold system, allow its vascularization and prevent the invasion of fibrous tissue [78]. Many scaffold properties play a role in order to bring an appropriate micro-environment to the structure and surround host tissues. There are many complex interactions between cells and the scaffold contact surface interface that produce biochemical responses that will affect the newly formed tissue. These interactions are, firstly, due to intrinsic properties of the base material or material properties, which are directly related to the cell response from a molecular level to a cellular level and modulate processes such as cell attachment (binding sites), biochemical interactions, protein-surface interactions, degradation kinetics and adsorption phenomena, among others [79].

Regarding material properties, two key design requirements for scaffold materials are described in the literature: biocompatibility and bioresorbability. The former is ability of the material to interact with a biological environment without producing adverse effects or responses, whereas the latter is its ability to degrade in an *in vivo* environment in non-toxic components that can be eliminated from the body [80].

Besides the aforementioned roles of the scaffold, some studies have suggested that the scaffold micro-geometrical features influence the mechanical stimuli on the newly formed tissue within the scaffold [81]. However, this influence is not clear yet due to the scale level and the different particularities of the scaffold micro-geometrical features. These features are considered of great importance in the mechanical environment, since the microstructure governs the bone mechanical function [29]. Furthermore, the scaffold microstructure may determine the spatial and directional distribution of newly formed tissue [82]. Additionally, the scaffold geometry becomes more complex when the scaffold degradation occurs, which makes the micro-geometrical features and physical properties time dependent. However, there are constructs that are designed as permanent for different situations such as implants that do not change its geometry notably as time passes [83]. It is worth noting that in the context of the scaffold micro-geometrical features discussed in this work, the micro-

scale is referred to sizes in the range of 50-500 μm, according to the definition and scales presented in [82], [84].

Design parameters of scaffolds are mostly related to material properties and micro-geometrical features. The global mechanical stiffness depends on the elastic modulus properties of the base material that composed the scaffold and on the micro-geometrical features such as pore size, pore shape and pore interconnections. These properties influence cell morphology, cell migration, vascularization and permeability, where the last one has effects on transport of mass, nutrients, oxygen, regulatory factors and removal of metabolic wastes [80]. Properties such as curvature and tortuosity of pores and interconnections between them determine design parameters, such as specific surface area, which are related to the available area for cell attachment.

The mechanical stiffness of the tissue-scaffold system determines the strain over the regenerated tissue hence the mechanical stimuli over it, even if it is supported by orthopedical hardware or employed on an immediate loading bearing application. Another consequence of the mechanical strain will be the displacement of pore fluid, thus creating a fluid flow inside the pores and the tissue. Elastic stiffness, fracture toughness and compressive strength are typical measures of the mechanical reliability of the scaffold for weight bearing applications [85], [86].

Frequently, the specific pore features cannot be described due to the poor control over geometry, given by the classic fabrication methods that will be further discussed below. In this sense, porosity is a simpler physical property and easier to measure. It is defined as the ratio between the available void space for neo-tissue growth and the volume occupied by the scaffold material.

Ideal specific features of bone scaffolds that may depend on the combined effect of material properties and micro-geometrical features are also described in the literature [87][88]. Osteoconductivity is the ability to support bone cell processes such as adhesion, proliferation and synthesis of ECM. Osteoinductivity refers to the ability to induce new bone formation by stimuli. In fact, the greatest part of the bone fracture healing process is dependent on osteoinduction [87]. Osteogenicity is the capability of containing cells that are able to differentiate into bone cells and synthesize ECM. Osteointegrity denotes the

capability of forming an adequate union with native bone. Finally, biofunctionality is the ability to perform its functions in an *in vivo* environment.

The fabrication techniques to obtain scaffolds are one of the main constraints to tweak the different key parameters in the design of these constructs. The different manufacture techniques limit the type of materials that can be used, thus affecting the material properties of the construct and the controllability of its different physical features.

Principally, there are four global methods of scaffold manufacturing. On the one hand, the first two methods lead to the production of porous structures [89]. The classic and one of the most employed approach is the obtention of pre-made porous scaffolds from different materials and technologies, which will be discussed in more detail below. Another strategy is based on the postulate that histoarquitecture of same native tissues is optimal to conduit healing processes [31], therefore, scaffolds for tissue engineering are obtained from the decellularization of similar tissues derived from the same species (allogenic) or from different species (xenogeneic), to provide a naturally derived structure that serves as support [90]. These decellularized structures exhibit numerous biological properties that facilitate the tissue growth inside them, but also can potentially provoke immune responses and subsequent rejection.

On the other hand, the last two global methods are oriented to produce engineered constructs containing cells without a cell seeding step to finally implant or inject them in the injured region [89]; The self-assembly process uses natural or synthetic polymeric networks known as hydrogels to produce small blocks with encapsulated cells to build the desired structure. Similarly, the assembling of two-dimensional cell sheets containing cells and ECM synthesized by them aims to conform a tridimensional construct that is used as scaffolding technique in tissue engineering. The main weakness of these methods is the poor mechanical properties of the achieved constructs.

Considering the pre-made scaffolding group, the first and most experimentally used scaffolds generations were obtained by conventional physical and chemical processes such as foaming methods, casting methods, fiber-based methods, sintering, solvent casting in combination with space holders, particulate leaching, porogen leaching, phase separation, cryogelation and freeze drying, among others [11], [91]. These methods use

ceramic-based materials such as hydroxyapatite (HA), tricalcium phosphate (TCP), bioactive glasses and natural or synthetic polymers, e.g. collagen, silk, cellulose, alginate, gelatin, chitosan, poly-glycolic acid (PGA), poly-lactic-co-glycolic acid (PLGA) and poly-L-lactic acid (PLLA) [92], [93]. A limitation of these methods is that they lack a precise control over pore morphology, whilst allowing some tunability of features in a statistical base, such as average porosity and pore size, but not in critical factors like pore shape and interconnectivity. As a result, all these methods produce irregular micro-geometries that do not guarantee a regular physical environment throughout the scaffold.

From a stiffness perspective, the discussed manufacturing techniques produce soft-polymers based scaffolds and stiff mineralized scaffolds, but a limitation of most of the materials employed in these processes is its inapplicability in weight bearing locations due to the low stiffness, low elasticity and brittleness. This means that these materials do not have suitable mechanical properties [31]. Metals and their alloys are more appropriate for load bearing applications, but they outperform its elastic properties regarding native tissues. In consequence, these materials produce negative effects that reduce the mechanical stimulation on surrounding tissues and lead to their resorption, phenomenon known as stress shielding [86]. Also, the poor degradation capabilities of metals and their alloys prohibit its use in non-permanent applications. Engineered composites attempt to overcome the different drawbacks of the materials, thus taking advantage of the great potential of tunability properties of the different materials that formed it.

From the pre-made scaffolds type, there is a special interest in fabrication approaches that make possible to obtain regular geometries through advanced manufacturing technologies such as additive layer processes (e.g. 3D printing, fused deposition, stereolithography and selective laser sintering). Some advantages of regular geometries are their ability to offer a physically, and biologically homogeneous environment, which is traduced into predictable and reproducible features. A homogeneous environment also avoids common effects of random irregular porosity such as dead porosity and incomplete interconnectivity, which leads to poor cell seeding (mainly in the core region), insufficient vascular networking and low cell viability [94]. However, materials with suitable biological and physical properties that can be used in these processes are still limited. Biofunctionalization strategies, such as surface modification, surface and bulk treatments and coatings to enhance the interactions between cells, tissue and scaffold, have been used to address the lack of

appropriate biological properties of the synthetic materials [31]. Through of some of those advanced manufacturing techniques, it is possible to achieve the concept of bioprinting, in which cells, biomaterials and biochemical factors are integrated to print living structures [95], [96].

Regular scaffolds are also an ideal platform to study cell behavior *in vitro* under controlled environments and to verify these results through computer simulation. The regular structure allows isolating a representative unit cell or a volume of interest to analyze and make conclusions about the whole structure behavior, thus reducing the computational cost of analysis [97].

Some common pore shapes used in regular-structured scaffolds are prismatical [76], spherical [66], lattice-like [66], tetrakaidecahedral [80], [98], truncated cuboctahedron [99], and those produced by orthogonal perforations of simple forms, such as ellipses and rectangles on a solid domain [81], [100].

Porous scaffolds can show a foam-like or a regular structure that could be mechanically analyzed by models for open-cell foams from cellular solids to describe their mechanical behavior [80], including relative Young's modulus, stress-strain curves and failure mechanisms.

As previously mentioned, a simple requirement derived from the scaffold pore geometry is the specific surface-area volume ratio (*SA/V*). There is a strong correlation between cell attachment and the *SA/V*, which can be calculated by assuming the scaffold as an open-cell foam and depends on the pore size and the relative density. For instance, for the tetrakaidecahedral model of an open-cell foam, this area is inversely proportional to the mean pore size [101].

Scaffold typical loads can be the same loads that bone could be experiment at the macroscale: tension, compression, shear, torsion, bending and combinations between these loading types [102]. At the microscale, representative unit cells are generally loaded by axial (tensile or compressive), transverse (shear) load conditions and combinations of them, besides shear loading caused by interstitial fluid flow. There is a relation between

macro-scale loads and interstitial fluid flow, because the deformation experimented by axial and shear deformation induces a flow through the porous media.

The scaffold biodegradation is an important requirement to allow growth tissue within the structure, thus successfully healing the defect of interest. This is a complex phenomenon that must occur in a controlled and balanced manner as the tissue grows and becomes capable to support its natural functions. Additionally, it is possible to include biochemical factors, drugs and nutrients in the biomaterial to be released in a controlled way in order to benefit the healing process.

Degradation mechanisms of biomaterials are highly environment dependent [103]. Some environmental factors that influence the behavior of the material are pH, temperature, mechanical strains and subsequent disintegration, light, radiation and chemical interactions with oxygen, water or other fluids [104]. The types of materials used to build tissue engineering conduits determine the mechanism of degradation. Architectural features such as micro/nano porosities and high *SA/V* accelerate the degradation by increasing the contact with body fluids, water intake and cell contact.

Metals and its alloys such as those based on magnesium and iron [105] degrade by electrochemical corrosion processes, while ceramics degrade principally by means of two mechanisms: chemical dissolution in body fluids and cellular mediated action [106]. Polymers can be degraded in two pathways. The first is by the action of water, process known as hydrolysis. It is caused by the water diffusion in the material, in which hydrophilicity and hydrophobicity properties of materials and enzymatic interactions with the biological environment affect the process. The second pathway is the oxidative one caused by reactive molecules derived from host cellular activities [107].

Degradation in polymers results in erosion processes of two types that can occur simultaneously: surface erosion and bulk erosion. In the former, the polymer erodes from the external surface towards the inside, which represent a volume reduction in the exterior surfaces in contact with the degradative agents. In contrast, the latter loses mass by the penetration of the degradative agents through the entire volume (Figure 2-3).

Figure 2-3: Schematic of the surface and bulk erosion mechanisms of polymers degradation.

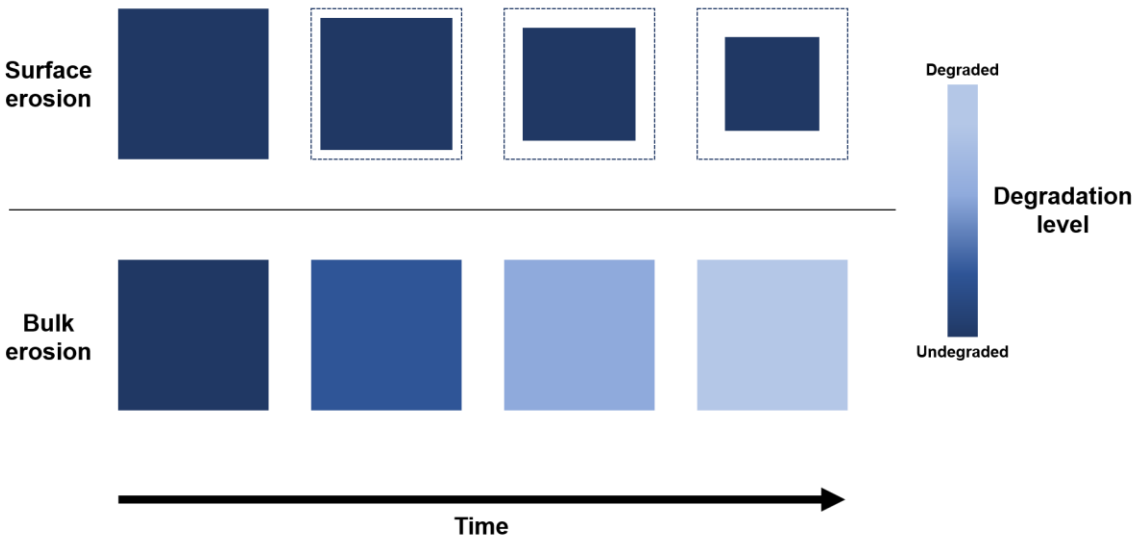

Depending on the material type, degradation leads to a change of properties. Indicators of this process are commonly molecular weight (in biopolymers), mass loss, porosity change, changes of mechanical properties, such as stiffness, and morphological variations due to erosion such as pore size change, among others [103]. An interesting concern in biomaterials is the active control of the degradation rate to address the open loop approach, in which once the biomaterial is implanted, any control is exerted on the degradation process [104].

A highlighted simulation work on scaffold degradation and its relation with the newly formed tissue was carried out by Adachi et al. [66]. They develop a framework for the optimal design of a porous scaffold microstructure by computational simulation of bone regeneration to study the relationships between pore shape, growth tissue and mechanical function, taking into account the material degradation. In this study, they developed a simple model in which the domain is discretized using voxel elements to describe the degradation of scaffold material based on bulk erosion due to hydrolysis, which is represented by a system of coupled equations. The details of this model and its implementation are described in chapter 5 of this thesis.

Nowadays, It is possible to find more complex models that describe scaffold degradation [108]–[115]. Also, simpler phenomenological models have been reported in the literature to represent the geometrical changes produced in the scaffold due to the surface erosion degradation mechanism [116]. However, Adachi's model is still enough for several applications that require to consider polymer scaffold degradation in a simple way [82], [117].

2.5 State of the art: Scaffolds design and assessment

Scaffolds for tissue engineering have had a rapid development in last two decades, evidenced by the exponential increase of publications on this subject [118]. There are several fronts of research in different disciplines in the concerns of design, fabrication, application and assessment of these devices.

The development of assessment techniques for scaffolds has become strong in order to obtain better predictive capabilities and reduce the trial and error and open loop approaches in which the only data available refer to the performance of the device during its use (*in situ*). Evaluation procedures *in vitro*, *in vivo* and *in silico* have been developed in the literature to determine the relevance of the different scaffold design factors identified.

Currently, there are several experimental studies that evaluate the mechanical, biochemical and biological responses of scaffolds in *in vitro* and *in vivo* environments, where the latter are assessed principally using animal models. Cell viability is one of the most important factors in *in vitro* approaches, and there is an incessant evaluation of the scaffold fabrication methods and enhancements to increase cell survival.

Regular and irregular geometries have been employed to evaluate the influence of micro-geometrical features in experimental researches. For instance, some authors have studied the effect of pore size on cell attachment [101], the effect of the scaffold geometric features on global rate of tissue formed [119], the effects of different pore sizes and materials *in vivo* [120], cartilage-bone transitional scaffold structures [121], internal architecture assessment and characterization [122] and assessment of *in vitro* and *in vivo* responses of a regular and cell seeded scaffold [123]. A comparison with other grafting techniques such as

autografts, xenografts, and allografts was carried out in [124]. Permanent scaffolds that are not designed to disappear in the body for loading bearing applications are proposed in order to treat critical defects [83], [125]. Also, scaffolds have been used as platforms to study new signaling and stimulation techniques such as those based on ultrasound [126], [127].

Regarding scaffold fabrication, new manufacturing methodologies and engineered materials have gained major interest, especially in materials such as hydrogels, composites and bioactive glasses [128]. Evaluation of mechanical properties designed vs. those obtained after the fabrication process has been carried out [129]. Current topics of interest are the development of bioprinters and bioinks for different scenarios, modification of surface features of the materials, and coatings and treatments in materials to enhance the healing process that can include drugs, genetic material, growth factors and even cells [96], [130]–[136].

3D printing and bioprinting techniques are valuable due to their potential in tissue repair and artificial organ development. Each day various materials are studied to be employed in these techniques. Interestingly, it is possible to find experimental results illustrating that the scaffold microarchitecture is capable of guiding the tissue formation at early stages of implantation and enhance noticeably bone volume and functionality, thus showing the importance of the micro-geometry control in bioprinted structures [137], [138].

Unfortunately, consequences of experimental research in this field are the high costs associated with the methods and techniques required, especially if *in vivo* approaches are involved. These studies require advanced techniques to perform the analyses, such as micro Computed Tomography (micro-CT), Magnetic Resonance Imaging (MRI), Atomic Force Microscopy (AFM), Scanning Electronic Microscopy (SEM) and Confocal Imaging (CI), among others. Also, cell cultures and biological tests require specialized equipment, supplies and personal to ensure the reliability and validity of the studies. Usually together with the biological assessment of scaffolds, there is a mechanical properties assessment, which requires additional custom test machines or adaptations for this purpose [138], [139].

In response to the aforementioned shortcomings, analytical and computational techniques allow avoiding to some extent the issues of experimental studies. On the one hand, analytical works have been performed regarding structural analyses of scaffolds [99], [140],

and regarding the modeling of the contractile forces applied to scaffold struts [141]. On the other hand, *in silico* analyses are considerably more frequent, since they have the potential to provide tools to simulate nature events without falling into costly experimental techniques, and to allow computer design strategies based upon the real nature of biological and biophysical phenomena. In this way, the design and understanding of scaffold behavior and its interactions with the biological environment are the main goals to study these devices.

The research in this topic requires integrative approaches that combine mathematical and computational modeling with experimental research. For example, Afshar et al. carried out experimental and numerical procedures to assess the mechanical behavior of graded porosity scaffolds [142]. Another example of these approaches was presented by Carlier et al., who developed a bioregulatory model to predict the effect of calcium phosphate scaffolds on the behavior of osteogenic cells. Their model was based on the framework by Geris et al. [70] and the authors dedicated experimental work to fed the model [143]. Extending the integration procedures, concepts such as Computer Assisted Tissue Engineering (CATE) combine the tissue engineering field with advanced modeling, fabrication and simulation techniques [144]. Since the phenomena that occur inside the scaffolds have different scale levels, multiscale approaches have been developed in order to integrate the events that occur in the different scales [145], [146].

Currently, it is supposed that the same biological principles of the fracture healing phenomena occur inside the bone scaffolds, for this reason, numerous studies around this topic are constantly reported. The integration of these phenomena is commonly studied with processes such as angiogenesis [147], release of biochemical cues [148], different key factors of biological and biophysical nature and interactions with fluid and its dynamics. Also, scaffolds oriented to bioreactors and other *in vitro* scenarios and the modeling of specific culture conditions have been computationally studied. Pham et al. determined the flow-induced stresses over the surface of regular structured scaffolds used typically in bioreactors and found statistical distributions to describe them [149]. Zhao et al. studied the mechanical stimulation of bone cells in a scaffold caused by fluid flow and mechanical loading [150]. Nevertheless, their study uses discrete cells and does not take into account the changes in geometry and mechanical properties caused by the newly formed tissue and by the scaffold degradation. Finally, Campos and Lacroix conducted simulations to

characterize and analyze commercial scaffolds to demonstrate that structural variability of scaffolds affects the micromechanical cell environment on structural and fluid dynamics concerns [151].

Regarding geometrical features, tissue evolution has been discussed in the literature for different complex architectures of scaffolds such as triply periodic minimal surfaces (TPMS), geometries obtained by mean of reversed engineered techniques, and features such as gradients, multiporosity and multilayer [100], [152]–[157]. Other works pointed out the matching of biophysical properties regarding the host tissue environment at different scale levels, which is thought as criteria of goodness in those constructs [158]–[160]. For this purpose, homogenization theories are applied to describe the global properties of the entire structures through the properties of an enough representative volume, or the contrary process known as localization [64].

Due to the geometrical complexity of the microstructure of scaffolds, it is impossible to couple and solve simultaneously the different equations required to predict the scaffold behavior without computational methods. FEM allows solving the equations that predict the scaffold behavior in coupled form. This method is the most common computational technique in mechanical analyses of scaffolds for tissue engineering [161], while for analyses that involve permeability and fluid interactions, computational fluid dynamics (CFD) predominates.

Representative approaches to *in silico* scaffold analyses were carried out by Adachi et al. [66] and Byrne et al. [62]. These approaches were highlighted to consider the evolution of tissue inside the scaffold and the changes regarding physical properties of the scaffold-tissue system, both under frameworks based on FEM. As previously discussed, Adachi et al. integrated and simulated phenomena such as degradation with tissue growth driven by mechanical stimuli on two different pore shapes, lattice-like and spherical. Their results showed that pore shapes are related to the bone growth pattern. Another representative work related to scaffold simulation was performed by Sanz-Herrera et al. who explore the bone growth inside a regular scaffold composed of cells with a Face Centered Cubic (FCC) structure [64].

Using Prendergast's theory of mechano-regulation, Byrne et al. developed a simulation of bone regeneration in a regular scaffold to assess design parameters such as porosity, Young's modulus and dissolution rate. The simulation model was based on discrete elements for both the scaffold and the newly formed tissue inside the scaffold. This work was limited to square pore shape, but it gives a platform to assess and predict the behavior of scaffolds with specific geometries considering the changes of properties of the tissue synthesized by different cells, main cell activities, and the scaffold dissolution in a linear form.

Several studies have used concepts from Byrne's model to design scaffolds for specific purposes such as reconstruction of tendon attachment [162], prediction of bone ingrowth into a coated porous implant [163] and optimization purposes [164]. A highlighted research influenced by Byrne’s work was performed by Boccaccio and coworkers [81] to optimize the microstructure geometry of bone tissue scaffolds. Their study was based on regular structured open porous scaffolds and graded scaffolds [100], generated by orthogonal "perforations" on a solid cube of basic geometric 2D forms such as ellipses and rectangles, and by 3D beams to form regular unit cells, irregular structures and geometries similar to those obtained in extrusion based methods [165]–[167]. This model modifies the geometric parameters of the pore and evaluates the tissue growth produced by repeating this process until the stopping criteria are satisfied, i.e., when the amount of bone predicted is maximized.

Limitations of these studies are the restricted number of pore shape geometries and that they consider neither the behavior of cells in time nor the environmental changes caused by the scaffold degradation. Some approaches to analyze periodic structures typical from solid free form fabrication (SFF), taking into account the degradation process, were performed by Gorriz et al. [168] and Chen et al. [164]. The last group of authors presents a multiobjective optimization of the scaffold structure regarding criteria, such as permeability and stiffness.

Even though there are a huge number of key factors identified in the design of scaffolds and the optimization approaches have been developed for isolated or a limited number of these key factors. However, this situation leads to obtain improved structures optimized

only in relation to one or few parameters. It is worth noting that eventually some parameters can be opposed, as in the case of porosity and stiffness.

Another perspective to scaffold design is presented by Velasco and his co-workers [169], who used reaction-diffusion equations to generate the scaffold micro-geometry. Also, It is possible to find work related to the design of the scaffold microstructure based on biomimetic approaches [144], [170], [171], which are supposed to provide a better environment for the biological processes.

Despite the significant progress in research of scaffolds for bone tissue engineering, there is no successful clinical translation of the strategies proposed into a clinical and commercial context [172], [173]. Although the many efforts for optimizing the performance of scaffolds in practice, the *in vivo* experimental research still results in a wide range of outcomes, sometimes showing inefficacy. This issue is related to some limitations in the tissue engineering field such as the lack of biomaterials with suitable properties and difficulties in the management of cells [10].

2.6 Brief numerical overview

2.6.1 Finite Element basics

Many phenomena in the contexts of physics, biology, chemistry, and even economics problems are described mathematically by Partial Differential Equations (PDE) that usually could be difficult to solve in complex domains. To overcome this issue, the finite element method is presented as a computational alternative to solve these complex systems of PDE. This method is a numerical approximation technique based on governing equations including the constitutive terms that describe the particular phenomenon analyzed with boundary conditions. The constitutive equations have the following form, since they were developed for problems of elasticity based on Hooke's law:

$$\{\mathbf{F}\} = [\mathbf{K}]\{\mathbf{u}\} \tag{2.1}$$

where **K** is an inherent set of properties of the domain, **u** is a set of behaviors and **F** is a set of external actions or conditions [174].

Roughly, the concept behind this technique is the division of the domain of interest into several discrete elements called finite elements. These elements are geometrically defined through a mesh that discretizes all the domain and the resultant elements are linked by entities known as nodes. A set of simultaneous algebraic equations that will be solved locally in each node is established. After solving it, equations are assembled in a global system, then, an interpolation process is applied over the entire domain, thus obtaining the solution of the problem. For this reason, the method is unaffordable without a computational implementation. For further details of the method, please refer to Chandrupatla et al. [175].

2.6.2 Elasticity

It describes the mechanical behavior of deformable solids, with respect to how they deform by the action of external loadings. This behavior is typically characterized by the following constitutive equation:

$$\boldsymbol{\sigma}_{ij} = \boldsymbol{C}_{ijkl}\boldsymbol{\varepsilon}_{kl} \tag{2.2}$$

where $\boldsymbol{\sigma}_{ij}$ is the *Cauchy* tensor, $\boldsymbol{C}_{ijkl}$ is the constitutive elastic tensor and $\boldsymbol{\varepsilon}_{kl}$ is the strain tensor [176].

2.6.3 Poroelasticity

The poroelasticity theory comes from soils mechanics and additionally to the classic theory of the elastic media, it involves concepts regarding the pore pressures and strains. Assuming the tissue as a biphasic poroelastic medium, its behavior can be described using the following equations [176]:

Continuity Equation for biphasic media:

$$\boldsymbol{\nabla} \cdot \left(\emptyset^s \boldsymbol{v}^s + \emptyset^f \boldsymbol{v}^s\right) = 0 \tag{2.3}$$

where $\emptyset^s$, $\emptyset^f$ are the volume fractions and $\boldsymbol{v}^s$, $\boldsymbol{v}^f$ are the velocities of the solid and liquid phases, respectively.

Effective stress:

$$\overline{\boldsymbol{\sigma}}^* = \overline{\boldsymbol{\sigma}} + \chi \boldsymbol{u_w} \boldsymbol{I} \tag{2.4}$$

where $\overline{\boldsymbol{\sigma}}^*$ is the effective stress of the porous medium, $\overline{\boldsymbol{\sigma}}$ is the effective stress in the solid matrix, χ is the saturation and $\boldsymbol{u_w}$ is the wetting liquid pressure.

Darcy's Law:

$$\boldsymbol{Q} = -\boldsymbol{K} \cdot \boldsymbol{\nabla}(\boldsymbol{h}) \tag{2.5}$$

where ***Q*** is the volumetric flow rate, ***K*** is the permeability of the medium and ***h*** is the piezometric head.

2.7 Conclusions

After a comprehensive analysis of the scientific literature on scaffolds for bone tissue engineering, this chapter shows the generalities involved in the processes that occur within a scaffold for bone regeneration and its principal concepts. These processes are complex and influenced by phenomena of different nature. The scope of this dissertation will be limited to understand and describe the events occurring during the scaffold use until its dissolution, from a biomechanical perspective and with special emphasis on the influence of the scaffold micro-geometrical features, such as pore shape, size and interconnection between the scaffold pores, on these events.

The state-of-the-art shows that there are many efforts to understand, characterize, and assess the influence of design parameters of the scaffold and their responses (Biological and mechanical), but experimentally these studies require costly and time-consuming experiments and there is still a discussion about some key factors in the design and the control of the *in vivo* outcomes. Regarding *in silico* methods, they have been applied to the

design, assessment and verification of the influence of different scaffold design parameters. However, several processes inside the scaffold are understood and modeled as black-box systems. Particularly, there is no theoretical or computational description of stress patterns and distributions related to the micro-geometrical features and their changes during the tissue growth and/or scaffold degradation. This knowledge is important since the stresses are related to the mechanical stimuli, thus they regulate the tissue development within the scaffold, together with biochemical and other biophysical stimuli.

Combination of computational analysis and design methods, additive manufacturing, optimization, and simulation techniques will allow making predictions and comparisons between different designs in computational environments. This will in turn allow designers to select the suitable features from a theoretical standpoint and then fabricate this kind of devices, thus helping to reduce extensive experimental tests.

In the future, it is necessary to search for strategies to monitor and control the properties of scaffolds in *in vivo* scenarios. The tracking and control in the scaffold properties, such as the degradation and loss of mechanical stiffness will allow better control over the biological outcomes, for instance, reducing the early failure of the scaffolds for fast degradation or controlling the releasing of growth factors [104].

The concepts reviewed here indicate the complex phenomena that occur regarding the scaffolds for bone tissue engineering. Many disciplines are involved and an interdisciplinary research is necessary in order to achieve better techniques and solutions with the potential to be translated into clinical scenarios. All these efforts should try to lead this discipline to the application of concepts of patient-specific and precision medicine.

The searching for better scaffolds that successfully help to heal bone fractures is still a relevant concern for researchers in biomaterial and tissue engineering field. The understanding of the phenomena occurring inside the scaffold and the interactions between them could lead to obtain more repeatable and efficient outcomes and increase its functionality and scalability in order to enhance the available treatments for fracture healing.

3. Stresses on newly formed tissue

The aim of this chapter is to introduce a methodology for modelling the mechanobiological behavior of scaffolds and analyzing the stresses acting within the newly formed tissue. These strategies allow exploring the biophysical phenomena that occur within the tissue that fills regular scaffold geometries in early stages of healing and finding possible relationships between the scaffold micro-geometrical features and the stress distributions developing inside the newly formed tissue.

3.1 Representative volume modeling

To determine the stresses of the newly formed tissue inside a bone tissue scaffold when micro-geometrical features of pores changes, finite element models for representative volumes (RV) of different microgeometries of scaffolds were modeled. The RVs are consistent with the scaffold geometries studied experimentally by Entezari et al. [138] and similar in the size with those used in computational studies from other authors [66], [117]. RVs of different families and sizes of pores were represented in a cube with side of h=2.34 mm (Figure 3-1) including different arrangements of the studied unit cells, which are expected to produce different biophysical responses. Following the shape, size and porosity of the conventional square architecture presented in [138], square pores with a side 0.39 mm were modeled thus obtaining a reference porosity of 50%.

A script to model the different geometries was implemented in the Python interface of the FEM software package Abaqus® (version 6.12, Dassault Systèmes, Vélizy-Villacoublay, France) to provide automated parametric analysis and post-processing operations. The different pore geometries were modeled through unit cells, in which pores are made using perforations of rectangular or elliptic cross sections along the faces of unit cells and geometric primitives, such as spheres and cylinders, which will be discussed in detail in next section. Once the pore is created inside the raw unit cell, the resultant geometry is replicated using an orthogonal pattern to form the entire RV including 3x3x3 unit cells.

Figure 3-1: Model of scaffold representative volume (RV).

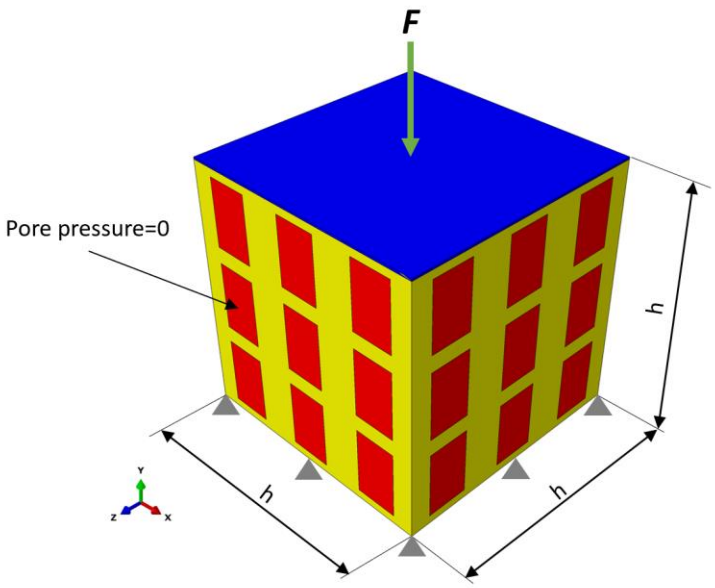

After defining the geometry of the scaffold, an identical solid cube of RV size is created and, by means of subtraction Boolean operations, the negative of the scaffold is obtained, which represents the geometry of the newly formed tissue inside the scaffold. The biomaterial that composes the scaffold and the granulation tissue were defined with the isotropic materials properties consigned in Table 3-1 to configure a poroelastic analysis of the scaffold-tissue system, according to those used in [62], [81]. The entire domain was meshed with tetrahedral pore fluid/stress elements C3D4P of average element size of 35 μm and maximum deviation factor for the curvature control of 0.01.

Table 3-1: Material properties used in the model.

Material properties	Granulation Tissue	Scaffold
Young's Modulus [MPa]	0.2	1000
Poisson's ratio	0.167	0.3
Porosity	0.8	0.5
Permeability [m^4/N/s]	1E-14	1E-17
Bulk of grain [MPa]	2300	13920
Bulk of fluid [MPa]	2300	2300

Once the geometry of scaffold-tissue system is defined, a tie constraint between the shared surfaces of granulation tissue and the scaffold material is settled. A clamp boundary condition was set in the bottom of the RV, while a ramp load function ***F*** is applied during one second through a rigid plate also tied on the upper surface of the RV and constrained to move only in vertical direction, to produce an apparent uniform compression loading through the structure (Figure 3-1). To simulate the free exudation of the fluid, pore pressure in the outside surfaces was set to zero according to Byrne et al. [62].

3.2 Geometry setup

As stated above, the reference geometry was a scaffold with square pores and 50% porosity. Additionally, a set of three different geometries was investigated: square pores with porosities of 25%, 75% and 90% were obtained using the equation 3.1 developed for these rectangular architectures.

$$Porosity = \frac{(L_{UC} \cdot X \cdot Y) + (X \cdot Y \cdot (L_{UC} \cdot X)) + (X^2 \cdot (L_{UC} - Y))}{{L_{UC}}^3} \cdot 100\% \qquad (3.1)$$

where L_{UC} is the length of the unit cell, which according to the studied RV size, is $L_{UC} = \frac{h}{3} = 0.78\, mm.$ *X* and *Y* are the horizontal and vertical dimension of the square section of the pore, respectively.

The resultant cross sections from the parameters *X* and *Y* will be cut through faces in planes **XY** and **ZY**, while the cut extrusion perpendicular to the **XZ** plane will be hypothesized to have a square shape with a *X* side (Figure 3-2), according to Boccaccio et al. [81]. The parameters *X* and *Y* that define the four initial porosities are combined into a new set of 16 geometries (Table 3-2) in order to explore the influence on the change of these parameters in the stresses of the newly formed tissue (Figure 3-3). The diagonal of the set in Figure 3-3 (left) shows the square geometries **A**, **F**, **K** and **P** with porosities of 25%, 50%, 75% and 90% respectively. The pore dimension *Y* will be increased in each geometry from left to right, while the *X* dimension increases from top to down in the array. Rows will have same *X* parameter, and columns will have the same *Y* parameter.

Table 3-2: Micro-geometrical parameters and resultant porosities for rectangular pore array.

Geometry ID	X (mm)	Y (mm)	Porosity (%)
A	0.2545	0.2545	25.00
B	0.2545	0.3900	32.63
C	0.2545	0.5254	40.27
D	0.2545	0.6272	46.01
E	0.3900	0.2545	41.31
F	0.3900	0.3900	50.00
G	0.3900	0.5254	58.68
H	0.3900	0.6272	65.20
I	0.5254	0.2545	59.72
J	0.5254	0.3900	67.36
K	0.5254	0.5254	75.00
L	0.5254	0.6272	80.74
M	0.6272	0.2545	74.95
N	0.6272	0.3900	80.42
O	0.6272	0.5254	85.88
P	0.6272	0.6272	90.00

Figure 3-2: Cubic Unit Cell Geometry.

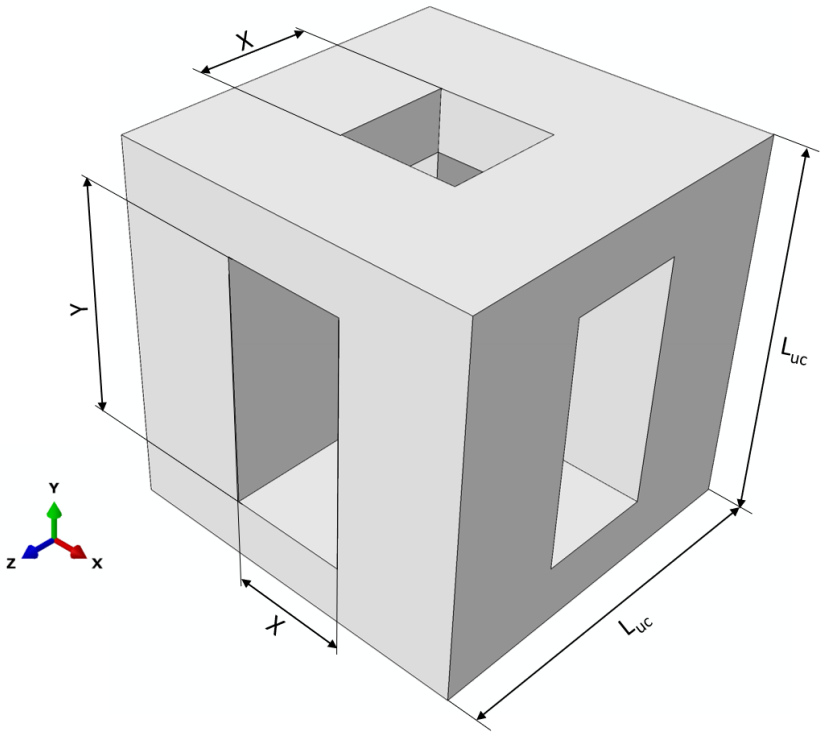

Figure 3-3: Profile view of the array of rectangular (Left) and elliptic (Right) unit cells.

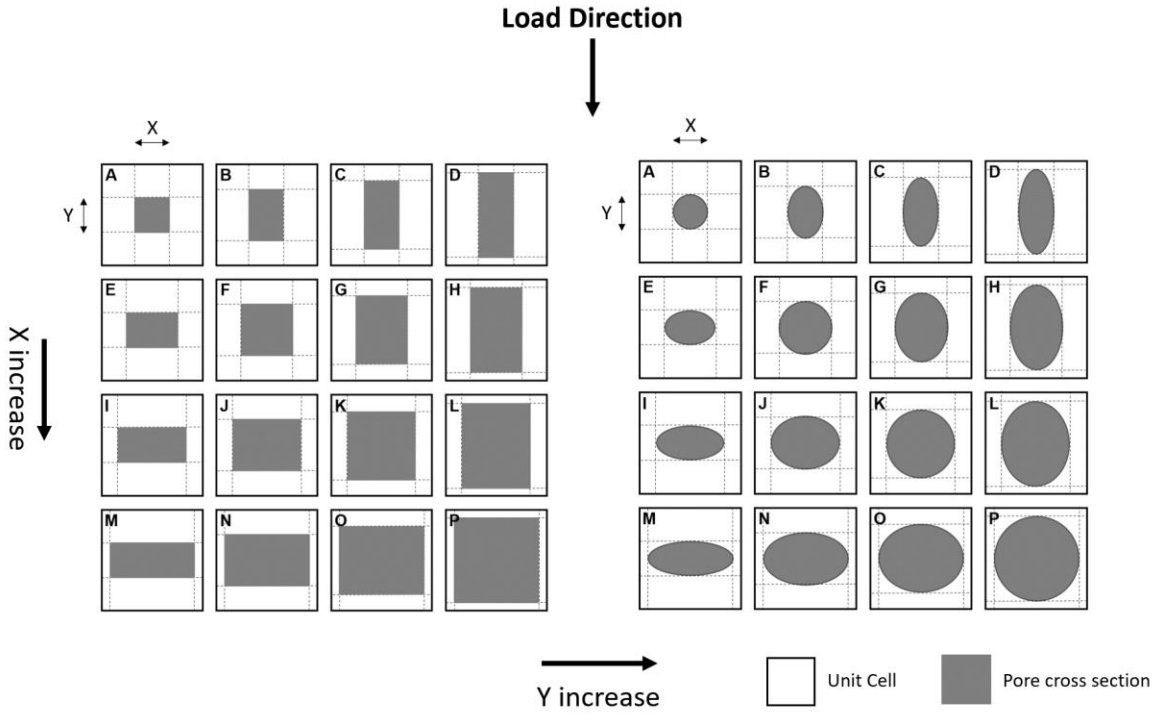

Similar to the creation of the set of rectangular pore family, an elliptic pore set was proposed to complete the hexahedron families studied by Boccaccio et al. in [81] and defined by micro-geometrical parameters in orthogonal directions. In the array of elliptic pore family, the *Y* dimension defines the ellipse axis oriented in load direction and the *X* dimension defines the ellipse axis perpendicular to load direction. In the diagonal of the array, *X* and *Y* dimensions have equal values producing circular pore profiles (Figure 3-3, right).

Scaffold geometries with spherical pores are interesting for analysis due to their curvature properties that can favor the cellular processes [119]. In the case of spherical pores modeling, it is possible to obtain two different topologies due to the geometric constraints reported in a previous study by the author [177]. In the arrangement of this pore family, the parameter in the vertical direction is the spherical pore diameter *Ds*, which increases from top to bottom, and the parameter in the horizontal direction is the cylindrical interconnection diameter *Dc*, which increases from left to right, as disposed in Figure 3-4a.

Figure 3-4: Spherical pores: (a) Arrangement of pore set (b) Small (ST) and (c) large (LT) topologies (Adapted from [177]).

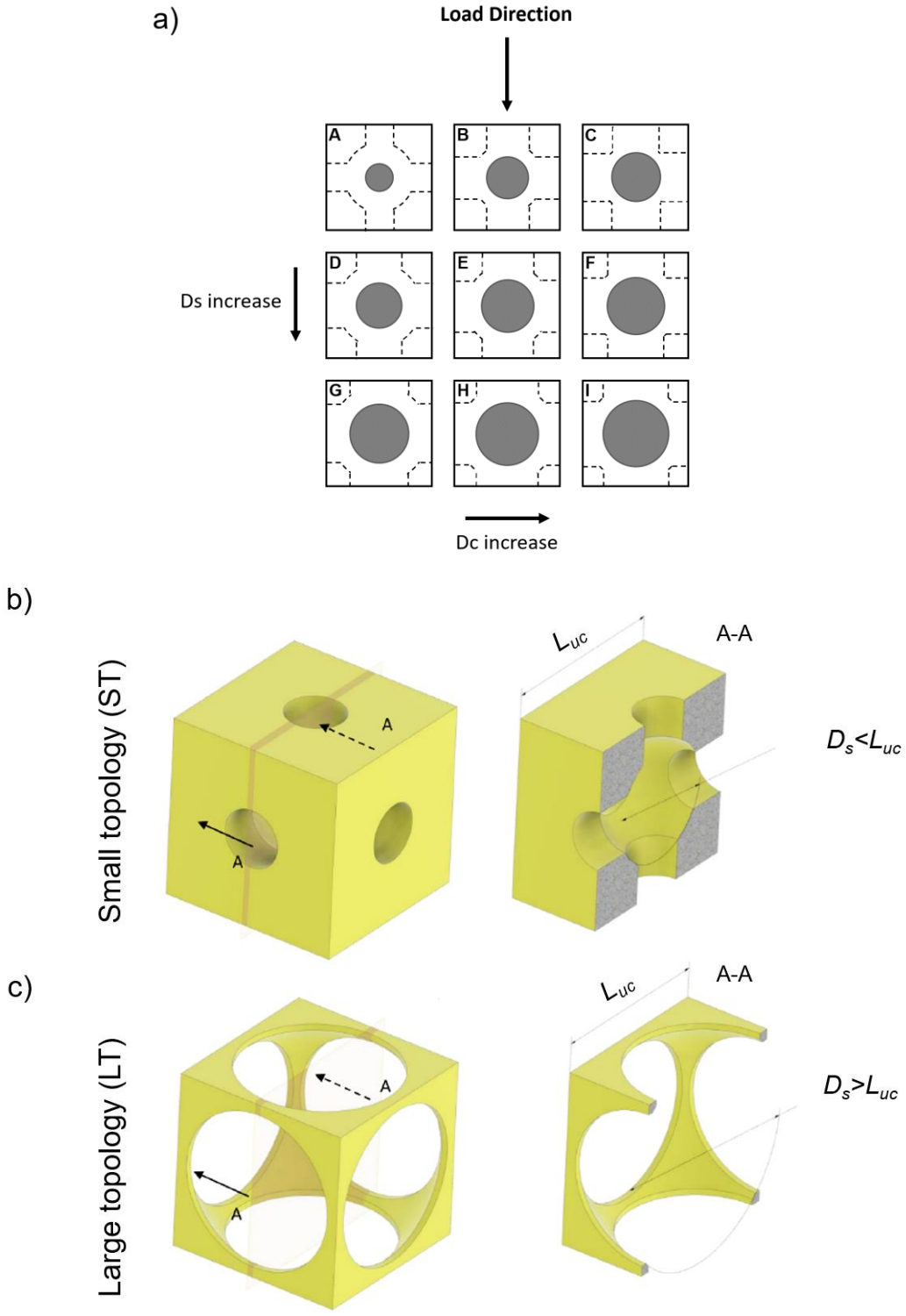

Depending on the size of cylindrical interconnection, the topologies could become very similar to hexahedron with circular pores, that is, the diagonal geometries in the elliptic pore family set (Figure 3-3, right). As the diameter of cylindrical interconnection gets close to the diameter of sphere, the sphere pore will disappear, and the geometry will only have the cylindrical perforation. Since we are not interested in the spherical geometry getting close to those obtained by circular perforations, we will try to move away from this geometry family and make strong the spherical component rather than the cylindrical component. In this way, to make the spherical component in the cell topology predominant, the maximum value that the cylindrical parameter must have is set at 90% of the value provided by the constraint *Ds*/1.4142, as reported in our previous study [177].

Taking as reference the diagonal porosities from rectangular pore families, the minimum porosity of the spherical arrangement was set to 25%. To avoid that the unit cell become circular pores topology, the maximum *Dc* for porosity of 25% was set in 65% from the maximum possible value. This *Dc* is increased to values of 80% and 95% of the maximum possible value to analyze the influence of the *Dc* parameter on the stresses within the granulation tissue. In the same way, geometries with 37.5% and 50% of porosity were obtained and the same previous percentages for *Dc* were explored to complete a set of nine geometries. In the proposed set, rows will have fixed *Ds* values and columns will have fixed percentages of the *Ds* values in the row (65%-80%-95%). This set is composed of the "small" topology (ST) characterized by the spherical pore and completely inside the unit cell (*Ds<Luc*) [177], which allows a maximum value of porosity close to 68%. To obtain porosities of 75% and 90%, it is necessary to use the "large" topology (LT), in which the spherical pore exceeds the unit cell dimensions (*Ds>Luc*) (Figure 3-4c).

In the large topology, the constraints between *Dc* and *Ds* interfere with the use of fixed percentages of *Dc* as those used in ST topologies. Considering this, three values of *Dc* between the minimum and maximum obtainable from the constraints were selected to analyze the influence of the changes of this parameter on the stresses of the granulation tissue. Target porosities of 60%, 75% and 90% were achieved using the minimum *Dc* parameter. A total of nine geometries were studied in the LT topology family.

3.3 Stress analysis

A poroelastic analysis is performed for each family and geometry in the proposed arrangement in order to determine how the changes in the parameters influence the stresses in the granulation tissue, which is supposed to fill the scaffold pores in an early stage of the bone healing process.

Due to the complexity of the general state of stress in the tissue, we used reduced stress measures such as von Mises stress, which incorporates the components of the Cauchy tensor into a single scalar value, and the maximum principal stress absolute. These measures of stress are inherently isotropic and common in finite element models of tissue mechanics [178]. The material models employed for scaffold and biological tissue were of isotropic nature.

The von Mises stress for all elements in the granulation tissue domain for each geometry was plotted using frequency distribution histograms to determine the predominance of stresses on the tissue. Maximum principal stress absolute shows the predominant principal stress over each element, hence its histograms in all tissue domain allows establishing the proportion of elements of the tissue that are in compression and tension for each scaffold geometry.

After the model execution, stress components of each element in the model and its invariants were obtained. Von Mises stress distributions were extracted using a custom Python script and statistical measures such as mean (VMMean) and median (VMMedian) were calculated in the newly formed tissue.

Distributions of von Mises stress and maximum principal absolute stress were depicted to observe the changes of stresses produced by the change of micro-geometrical features in the topology families. All those stress histograms related to each geometry were normalized regarding the counts, thus producing that the integral under the histogram be equal to one. Finally, these histograms were compared to identify features and patterns in the distributions.

3.4 Mechanobiological approach

To measure the mechanobiological performance of each geometry in the proposed arrays, the mechanobiological approach of Prendergast et al. [59] in equation 3.2 was used:

$$\boldsymbol{S} = \frac{\gamma}{a} + \frac{\nu}{b} \tag{3.2}$$

where $\boldsymbol{S}$ is the mechano-regulatory stimulus, γ is the octahedral shear strain, $\boldsymbol{\nu}$ is the interstitial fluid flow velocity, and, *a* and *b* are experimental constants, with values of 3.75 (dimensionless) and 3 μm/s, respectively [179].

From equation (3.2), the octahedral shear strain γ is defined using the principal strains ε_I, ε_{II}, ε_{III} obtained from FEM analysis:

$$\gamma = \frac{2}{3}\sqrt{(\varepsilon_I - \varepsilon_{II})^2 + (\varepsilon_{II} - \varepsilon_{III})^2 + (\varepsilon_I - \varepsilon_{III})^2} \tag{3.3}$$

Solving equation (3.2) with values provided by the boundaries of mechano-regulation diagram (Figure 2-2), it is possible to determine the changes of cell phenotype in each element [81]. The following inequalities were utilized:

$\boldsymbol{S} > 3$	Fibroblasts (Produce Fibrous tissue)
$1 < \boldsymbol{S} \leq 3$	Chondrocytes (Produce Cartilage tissue)
$0.53 < \boldsymbol{S} \leq 1$	Osteoblasts (Produce Immature bone tissue)
$0.01 < \boldsymbol{S} \leq 0.53$	Osteoblasts (Produce Mature bone tissue)
$0 < \boldsymbol{S} \leq 0.01$	Bone resorption

The predicted scaffold performance and statistical measures were related to the geometrical parameters using the MATLAB curve fitting toolbox in order to find expressions that show the existing relations (Version R2016b, MathWorks, Natick, MA, USA). We

determined the performance of scaffold in terms of the amount of bone predicted in relation to the cell volume and the available space for tissue growth.

Total bone (TB) is defined as the volume occupied by elements in which the differentiation of MSC to immature (v_{ib}) and mature bone (v_{mb}) is predicted, divided by the total volume of the RV (V_{RV}), that is, h^3.

$$TB = \frac{\sum v_{mb} + \sum v_{ib}}{V_{RV}} \cdot 100\% \tag{3.4}$$

Bone relative tissue (REL) is calculated dividing the total bone predicted by the volume available for tissue growth in the RV, i.e. the porosity.

$$REL = \frac{TB}{V_{available}} = \frac{TB}{Porosity} \tag{3.5}$$

3.5 Results and discussion

In this section, the results regarding the stresses on newly formed tissue for the studied sets will be discussed, which are presented through tables, response surfaces and histograms.

3.5.1 Rectangular pores

Each geometry of the rectangular set and its respective geometrical parameters of pores, resultant porosities, VMMean, VMMedian and TB and REL percentages are presented in Table 3-3. Third order polynomial surfaces were generated to illustrate the influence on the micro-geometrical parameters that define the pores in the von Mises mean and median of rectangular pores family set (Figure 3-5). The detailed statistics of coefficients and goodness of fit can be found in Annex A. Von Mises mean statistics show a slightly better goodness of fit than von Mises median statistics in response surfaces, all with values of R^2>0.99.

Table 3-3: Micro-geometrical parameters, stress statistics on the newly formed tissue domain, and TB and REL for rectangular pore array for 1 MPa.

Geometry ID	X (mm)	Y (mm)	Porosity (%)	VMMean (MPa)	VMMedian (MPa)	TB (%)	REL (%)
A	0.2545	0.2545	25.00	0.00280	0.00233	22.45	89.80
B	0.2545	0.3900	32.63	0.00252	0.00209	31.04	95.12
C	0.2545	0.5254	40.27	0.00232	0.00189	39.03	96.92
D	0.2545	0.6272	46.01	0.00219	0.00175	44.90	97.58
E	0.3900	0.2545	41.31	0.00353	0.00299	35.21	85.23
F	0.3900	0.3900	50.00	0.00316	0.00270	45.84	91.68
G	0.3900	0.5254	58.68	0.00289	0.00243	56.18	95.73
H	0.3900	0.6272	65.20	0.00270	0.00224	63.29	97.07
I	0.5254	0.2545	59.72	0.00566	0.00475	39.78	66.61
J	0.5254	0.3900	67.36	0.00537	0.00472	48.14	71.46
K	0.5254	0.5254	75.00	0.00506	0.00442	57.57	76.76
L	0.5254	0.6272	80.74	0.00480	0.00419	65.50	81.12
M	0.6272	0.2545	74.95	0.01067	0.00868	26.19	34.94
N	0.6272	0.3900	80.42	0.01097	0.00981	18.75	23.31
O	0.6272	0.5254	85.88	0.01101	0.01002	11.98	13.94
P	0.6272	0.6272	90.00	0.01086	0.00987	8.19	9.10

Figure 3-5: Response surfaces of pore parameters vs. von Mises mean (Left) and von Mises median (right) of rectangular pore family for 0.5 MPa, 1 MPa and 1.5 MPa.

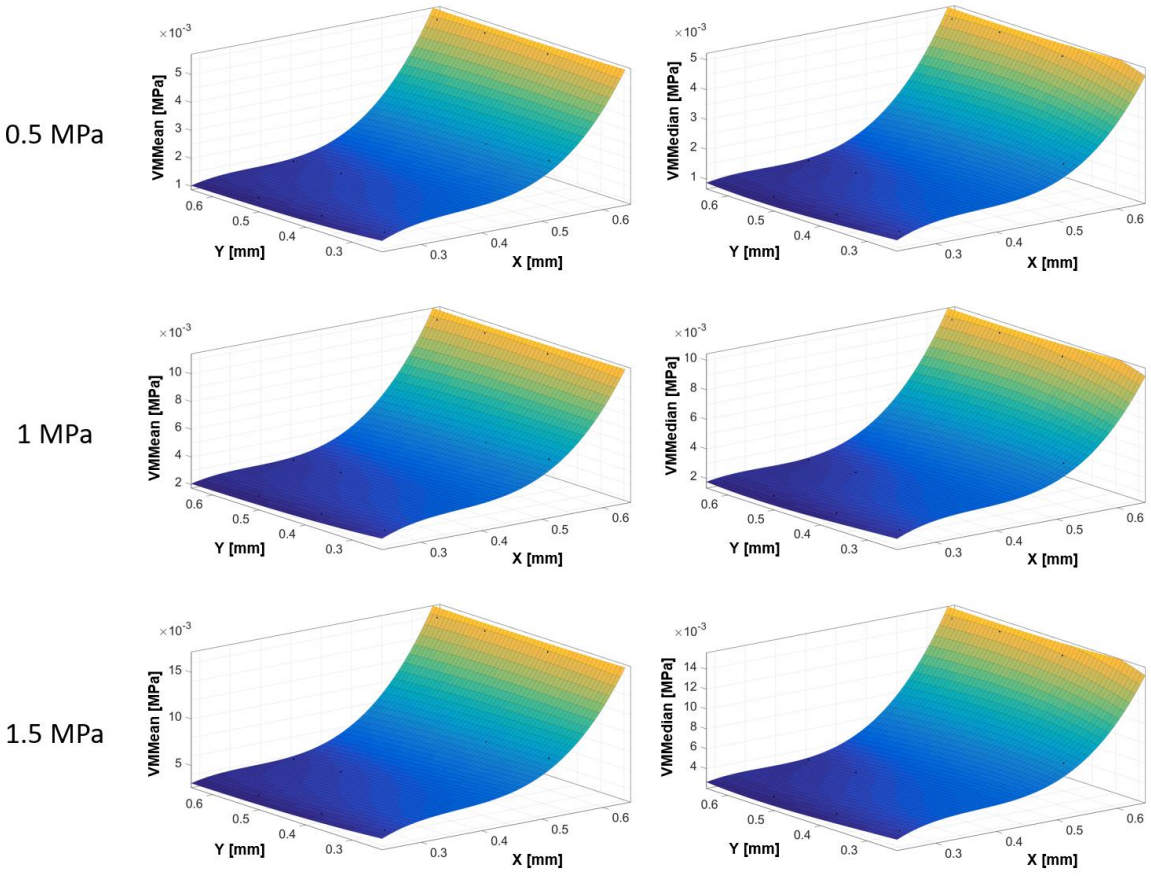

In the range of the pore dimensions, the response surface shows that the increase of size of pore in the load direction *Y* slightly affects the von Mises stress mean and median, while the increase in the size of pore perpendicular to load direction *X* increases notably those statistics, as the parameter value gets close to L_{UC}. Three magnitudes of load ***F*** equal to 0.5 MPa, 1 MPa and 1.5 MPa were simulated to validate whether the load influences the response surface. The response surfaces do not change in shape with the different applied loads but von Mises statistics magnitudes do change. This behavior suggests a linear relation between the von Mises stress in the granulation tissue elements and the load in the scaffold-tissue system. Histogram graphs were developed and plotted for each pore type in the same scheme of the pore array to study the von Mises stress distributions in the newly formed tissue. All distributions are not symmetric as expected since there is no uniformity in the stresses inside the pores (Figure 3-6).

Figure 3-6: Normalized von Mises distributions of rectangular sets for 1 MPa.

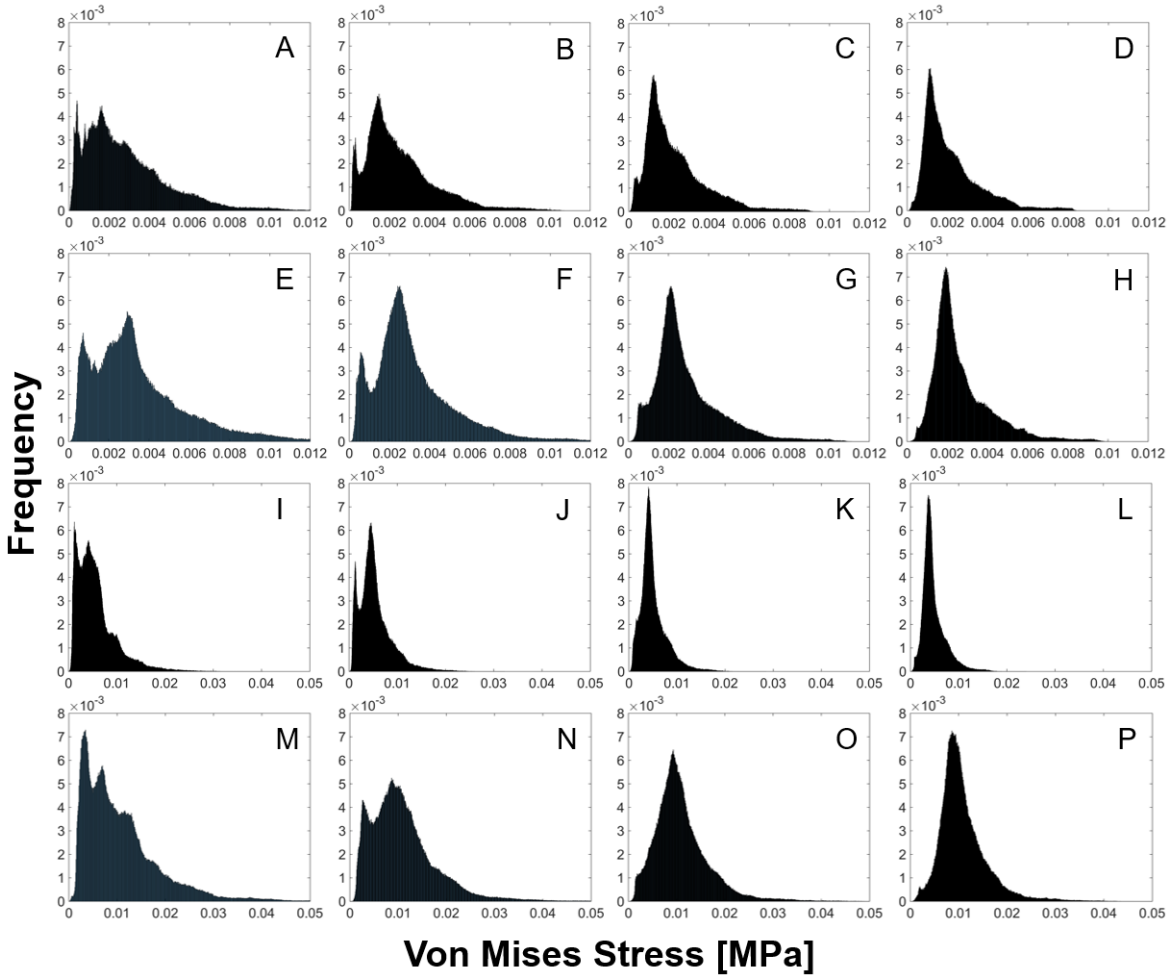

In general, the von Mises stress distributions show right skewed shapes, with the presence of two peaks (bimodal): one close to the lowest von Mises stress values and one close to the mode region (Figure 3-7).

Figure 3-7: Normalized von Mises distribution of rectangular **F** geometry for 1 MPa.

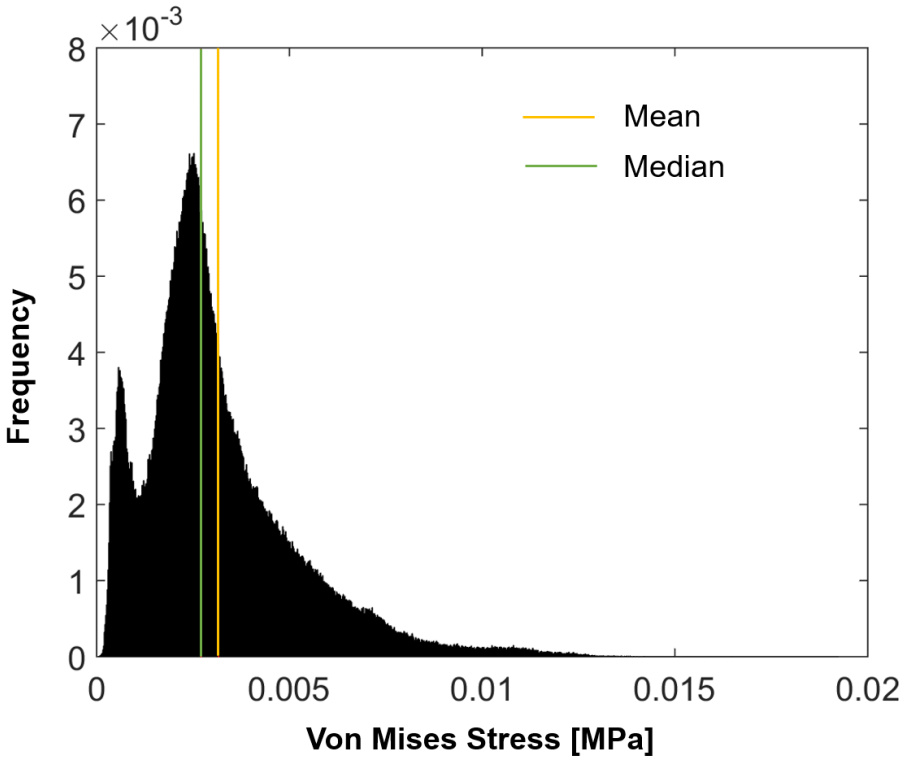

Geometry **A** shows multimodal distribution with an edge peak close to zero, which is the highest peak, or in other words the mode. When *Y* increases and pore geometry turns into **B**, the distribution becomes bimodal with an edge peak close to zero von Mises values. Finally, this peak is redistributed in the transition from **B** to **D**, and the histogram shape becomes a pure right skewed unimodal distribution with the highest peak in the row. Physically this implies that stresses in tissue elements are crowded towards the central tendency and the outliers values decrease. This fact is reflected on the reduction of VMMean and VMMedian as *Y* increases in the **ABCD, EFGH** and **IJKL** rows. In the case of the **MNOP** row, von Mises statistics increases, and bone amounts decreases as *Y* increases, thus suggesting the presence of an inflection line when the *X* dimension gets close to L_{UC}.

Increasing pore dimension *X* leads to a spread/widening of the stress in elements towards greater magnitude values in all columns of the array and promotes the increase of peaks towards multimodal shapes for low *Y* values columns.

Histogram representations for **F** geometry were plotted for the three load regimes studied (Figure 3-8). The shape of distribution is the same for the different loads and the difference is the values of stress of the elements in the horizontal axis, thus demonstrating that the stress distribution shape depends essentially on the geometry of the pores and not on load magnitude.

Figure 3-8: Stress distributions for 0.5 MPa, 1MPa and 1.5 MPa in rectangular **F** geometry.

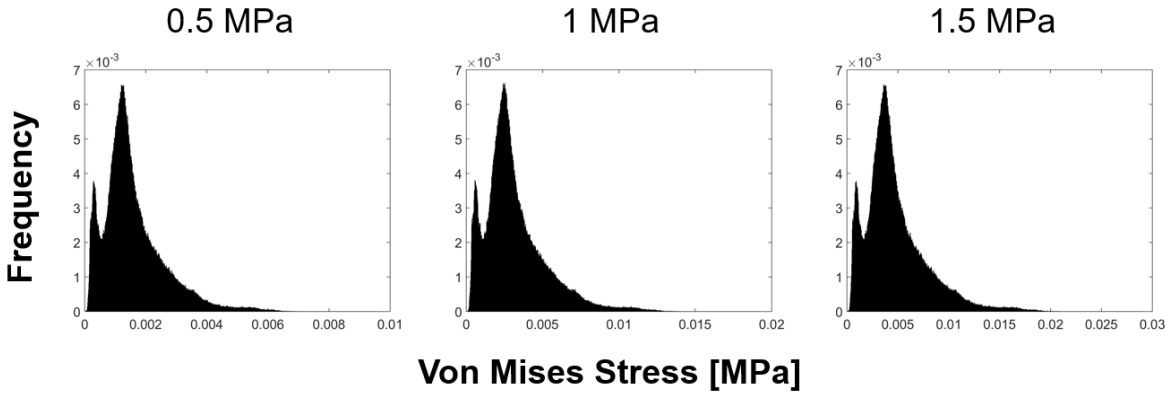

Square and cubic polynomial fits between mean and median values and relative amount of bone predicted were obtained for 0.5 MPa, 1 MPa and 1.5 MPa to depict the relation between von Mises statistics and relative amount of bone predicted (Figure 3-9). Non-linear negative correlation between von Mises stress and REL was found. Contrary to the case of pore parameters and von Mises statistics relations, VMMedian shows a slightly better goodness of fit than VMMean in the curves from cubic fittings, all with values of R^2>0.95. Coefficients and goodness of fit statistics of these curves can be found in detail in Annex A.

Figure 3-9: Curve fitting between the relative amount of bone predicted (REL) and the VMMean (Left) and VMMedian (right) for rectangular pore set for 0.5 MPa, 1 MPa and 1.5 MPa.

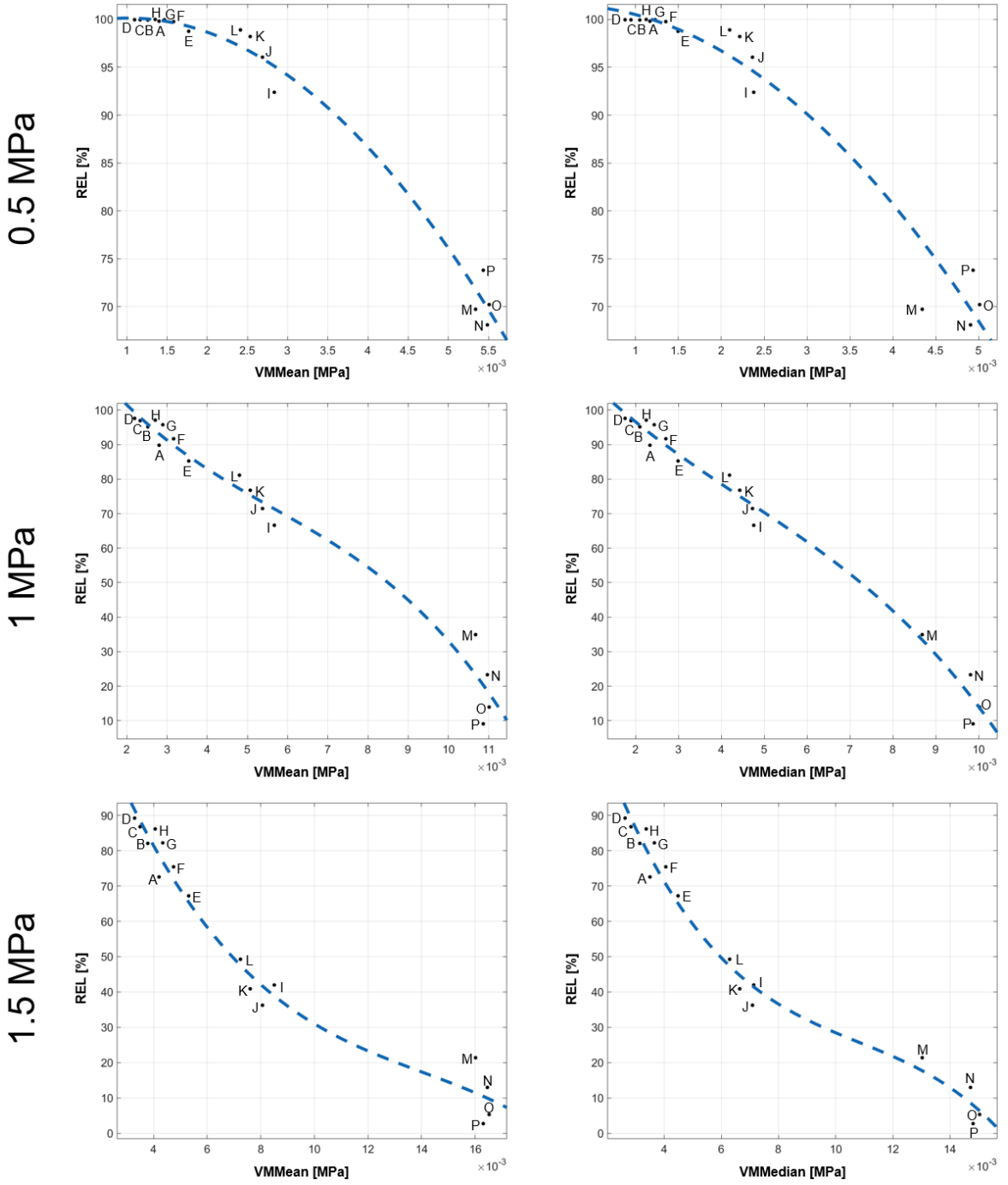

For each geometry in the array, maximum principal stress absolute histograms were plotted in Figure 3-10 and in general, these graphs exhibit two groups around the zero point: one with the frequency of elements with positive values of maximum principal stress and one with negative values. The positive group shows right skewed distribution, while the negative group shows left skewed shape. Some features observed in von Mises stress histograms are present in these distributions, such as multimodality in the lowest values of *Y* dimension, the smoothing of the shape as the *Y* dimension increases and the increase of absolute values when *X* increases.

Figure 3-10: Normalized histogram of the maximum principal stress absolute of rectangular geometry for 1 MPa.

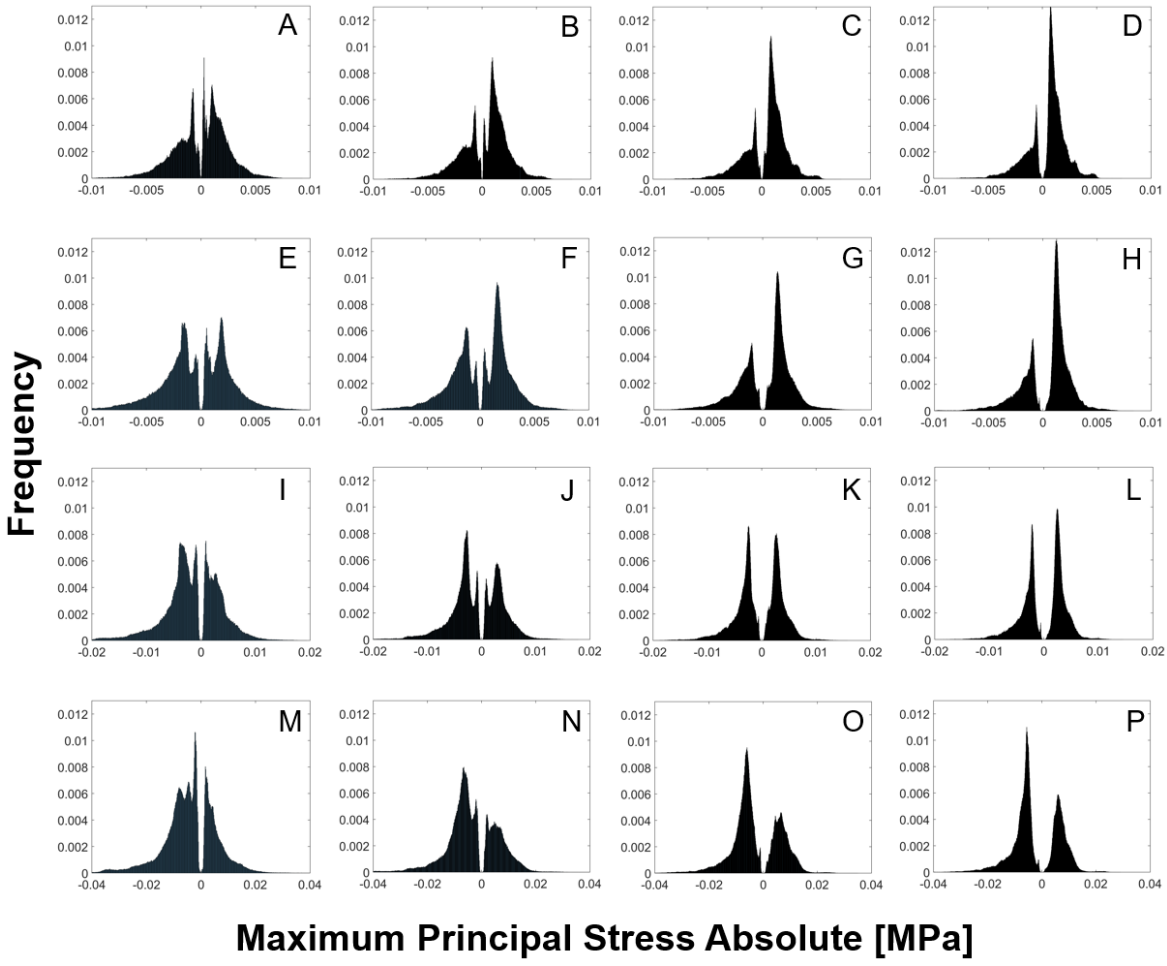

Examining **ABCD** and **EFGH** rows in the array of maximum principal stress absolute, the predominance and frequency seem to be related to performance, since less elements under compression are present in better performance geometries of scaffold to induce bone and the highest frequency of elements under positive maximum principal stress coincides with better performance topologies. Increasing pore dimension along the load axis reduces elements in compression, while increasing the dimension perpendicular to the load direction increases the amount and frequency of elements under compression. There is a change of tendency in the rows **IJKL** and **MNOP**. In **I, J** and **K** geometries, the predominance and maximum frequency is in negative values of maximum principal stress, while in **L** geometry the maximum frequency is in positive values. Finally, in **MNOP** row, the predominance of the maximum principal stress negative values is shown in the four geometries and same that in the previous rows, as the *Y* dimension increases in the row, the distribution is smoothed.

As in von Mises distributions, the change of scaffold loading does not affect the shape regarding the frequency, and just scale the axis in which stresses values are represented (Figure 3-11).

Figure 3-11: Distributions of the normalized maximum principal stress absolute for 0.5, 1 and 1.5 MPa for rectangular **J** geometry.

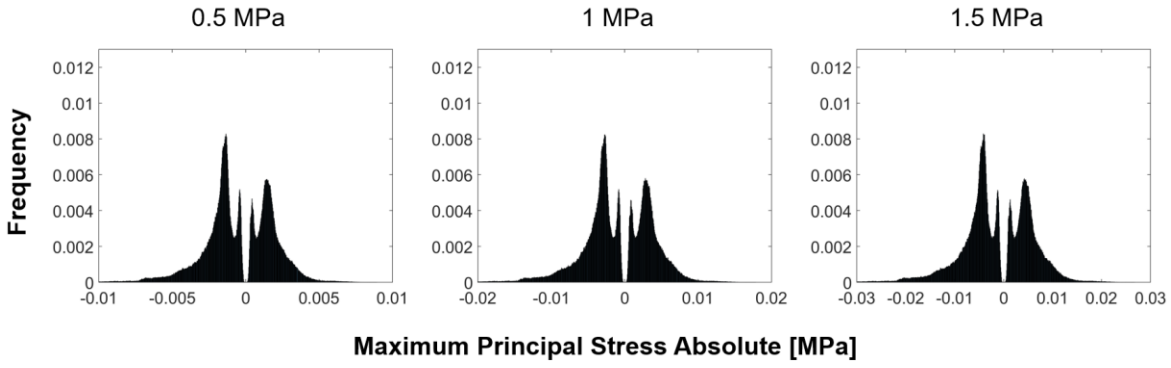

3.5.2 Elliptic pores

The diagonal of rectangular scaffold array is composed of square pores, which is a particular case of rectangular shape when the dimension of its sides is equal. The equivalent situation in the elliptic pore family is that the diagonal includes circles. Adjusting the axis dimension of circles to obtain the same porosities in the diagonal of rectangular scaffolds set leads obtaining similar porosities in the remainder of the sixteen geometry array.

Comparing the von Mises statistics of rectangular and elliptic pores (Tables 3-3 and 3-4) in the first two rows of the array, there is a tendency of stresses to be higher in rectangular pores than in elliptic pores. On the contrary, in the last two rows stresses are higher in elliptic pores than in rectangular pore geometries. As the von Mises statistics are considerably higher in the last rows, particularly in the last row whose values of stresses in elliptic pores reach more than the double of the value obtained by the rectangular pores, the curvature of the surface seems to be slightly greater in elliptic pores response surfaces (Figure 3-12).

Table 3-4: Micro-geometrical parameters, stress statistics on the newly formed tissue domain, and TB and REL for elliptic pore array for 1 MPa.

Geometry ID	X (mm)	Y (mm)	Porosity (%)	VMmean (MPa)	VMMedian (MPa)	TB (%)	REL (%)
A	0.28797	0.28797	25.00	0.00258	0.00224	23.27	93.08
B	0.28797	0.44243	32.51	0.00221	0.00190	31.67	97.44
C	0.28797	0.59965	40.33	0.00199	0.00167	39.71	98.47
D	0.28797	0.72503	46.57	0.00187	0.00153	46.02	98.83
E	0.44243	0.28797	41.22	0.00360	0.00304	35.46	86.03
F	0.44243	0.44243	50.00	0.00298	0.00261	47.09	94.18
G	0.44243	0.59965	58.67	0.00268	0.00233	57.06	97.26
H	0.44243	0.72503	65.69	0.00249	0.00215	64.63	98.39
I	0.59965	0.28797	60.02	0.00703	0.00613	34.15	56.89
J	0.59965	0.44243	67.40	0.00622	0.00554	41.82	62.04
K	0.59965	0.59965	75.00	0.00575	0.00517	50.56	67.42
L	0.59965	0.72503	80.90	0.00543	0.00492	59.51	73.56
M	0.72503	0.28797	76.56	0.02420	0.02003	7.77	10.15
N	0.72503	0.44243	81.29	0.02521	0.02198	4.16	5.12
O	0.72503	0.59965	86.11	0.02647	0.02372	1.49	1.73
P	0.72503	0.72503	90.00	0.02701	0.02458	0.46	0.51

Figure 3-12: Response surfaces of pore parameters vs. von Mises mean (Left) and von Mises median (right) of elliptic pore family for 0.5 MPa, 1 MPa and 1.5 MPa.

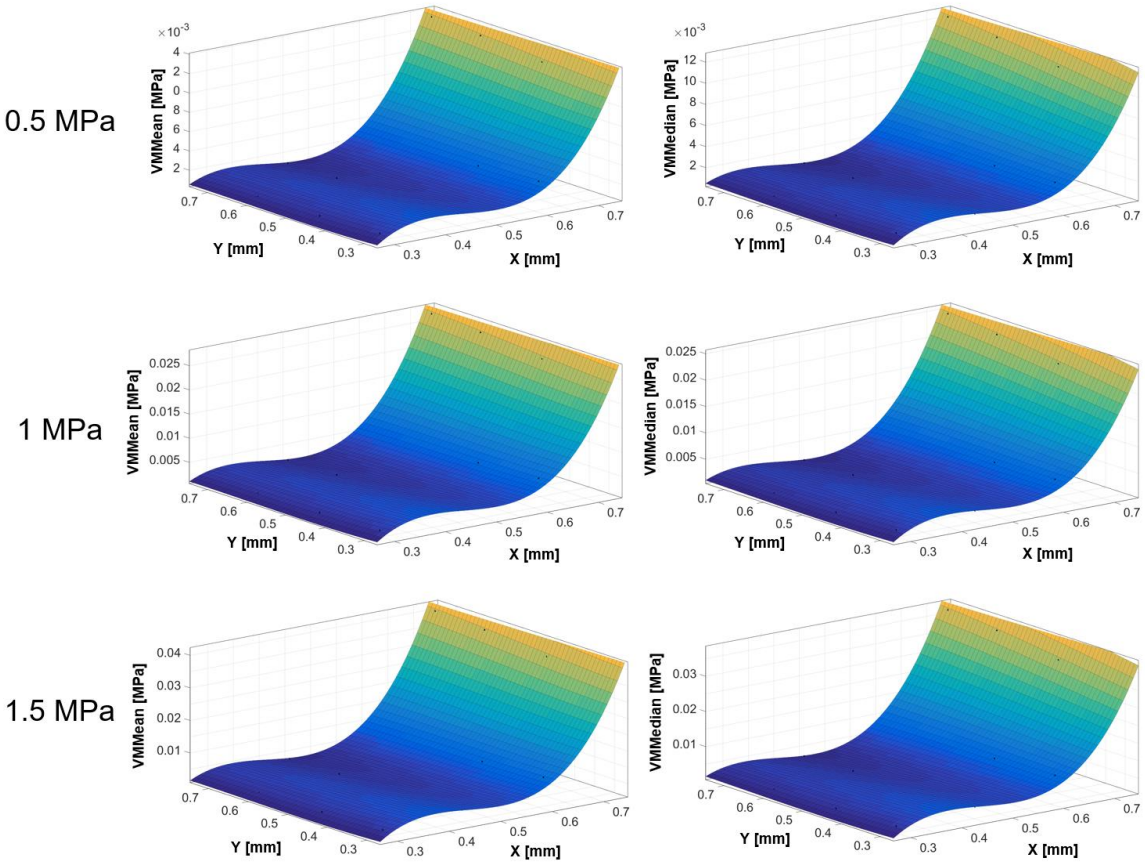

Von Mises stress distributions for elliptic pores (Figure 3-13) did not show substantial differences with respect to those shown in rectangular pores. Additional peaks in lower stress values were found in the first column of the array and less pronounced secondary peaks in the **BFJN** column.

Figure 3-13: Normalized von Mises distributions of elliptic sets for 1 MPa.

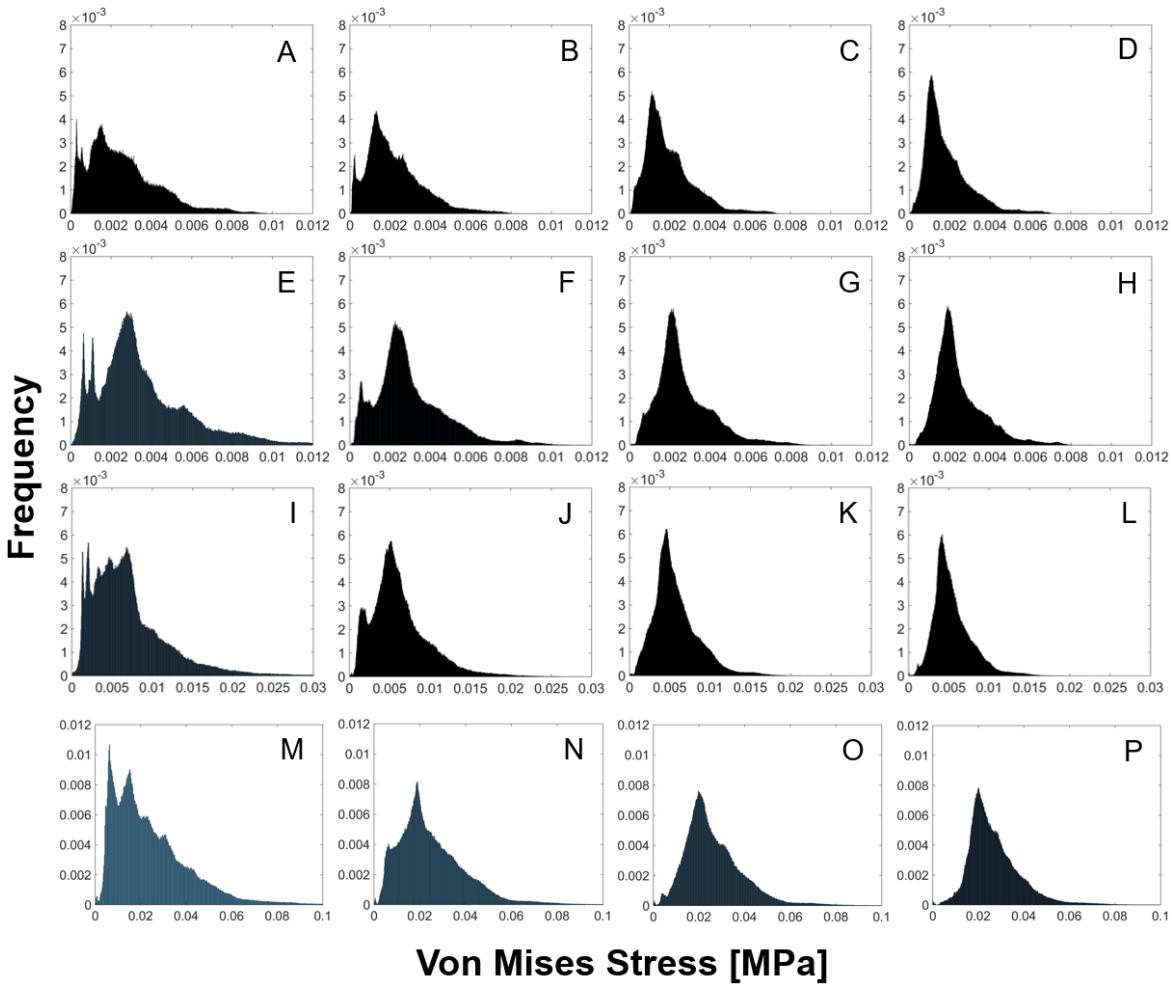

The comparison of the histograms of maximum principal stress absolute of rectangular and elliptic pores presented in Figures 3-10 and 3-14 respectively, shows that in the first row of the array, the peaks of counts in the stresses close to zero are lower in elliptic pores. As *Y* increases, the peaks are less pronounced in elliptic geometries than in rectangular ones, suggesting a wide uniformity of the stresses around the central tendency. This effect can be related to the curved surfaces generated by the rounded profile of pores that reduces the stress concentrations compared with those the produced by right angles. In contrast, peaks are more pronounced in the last two rows in elliptic set compared with rectangular set.

In general, the difference between positive and negative maximum principal stresses is upheld for both geometries, but in **L** geometry rectangular pores have the majority of elements in tension, while in the elliptic case the majority is in compression.

Figure 3-14: Normalized histograms of maximum principal stress absolute of elliptic geometries for 1 MPa.

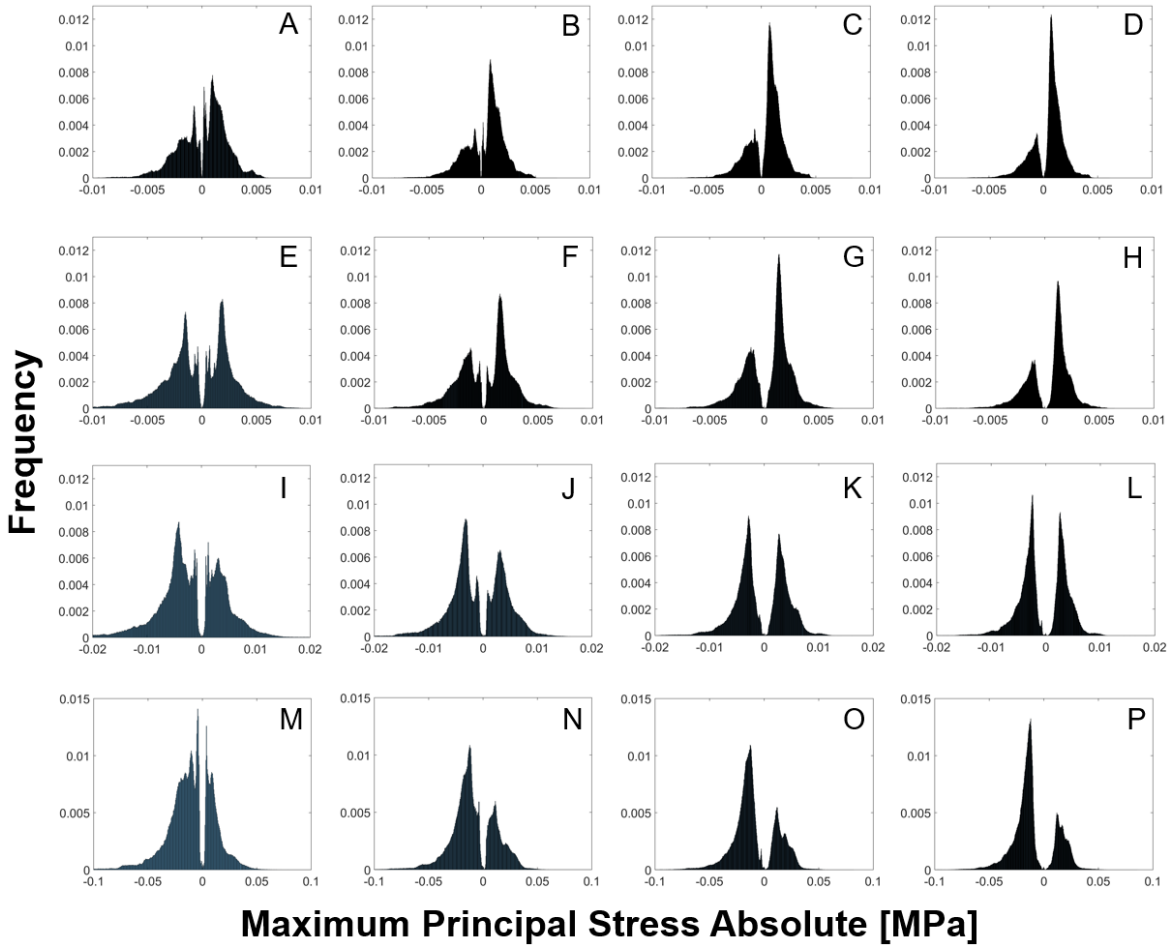

As in the rectangular pore set, the shape of both von Mises and maximum principal stress absolute distributions (Figure 3-15) are not influenced by the magnitude of load acting on the scaffold tissue system.

Figure 3-15: Distributions of the normalized maximum principal stress absolute for 0.5, 1 MPa and 1.5 MPa in elliptic **E** geometry.

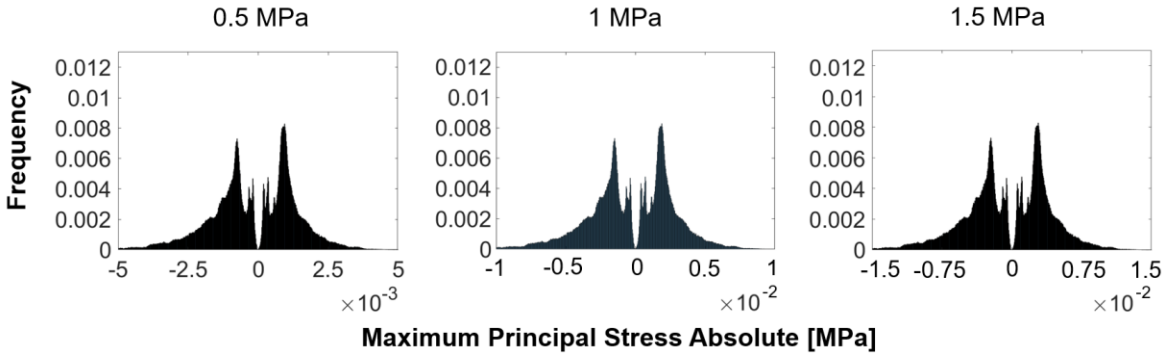

Again, a nonlinear negative correlation is found between the relative amount of bone predicted and von Mises statistics (Figure 3-16). Performance regarding the amount of bone predicted is remarkably affected as the *X* parameter increases in elliptic pore scaffolds compared with rectangular pore scaffolds. This behavior is consistent with the fact observed in von Mises statistics in which the stresses are considerably higher in elliptic pores than in rectangular pores in the last rows of the array. Data of von Mises statistics and REL fit well with cubic polynomial curves for 0.5 MPa and 1 MPa loads. In the case of 1.5 MPa, the behavior is better described by exponential or polynomial fourth degree curves.

3.5.3 Spherical pores results

The nature of spherical pores family presented here is different from the previous studied geometries, since the parameters control symmetrically the geometrical features. This implies that any change in these parameters is not distinguished between parallel and perpendicular directions of the load.

Nine sets of small topologies (ST) and large topologies (LT) were analyzed. According to our findings in previous works [177], small topologies have one constraint that defines an upper bound of *Dc* related to *Ds*, while large topologies have two constraints, upper and lower values of *Dc* related to *Ds*. The solution space is very complex due to these constraints and for this reason the two topologies are analyzed separately.

Figure 3-16: Curve fitting between the relative amount of bone predicted and the VMMean (Left) and VMMedian (right) in elliptic pore set for 0.5 MPa, 1 MPa and 1.5 MPa.

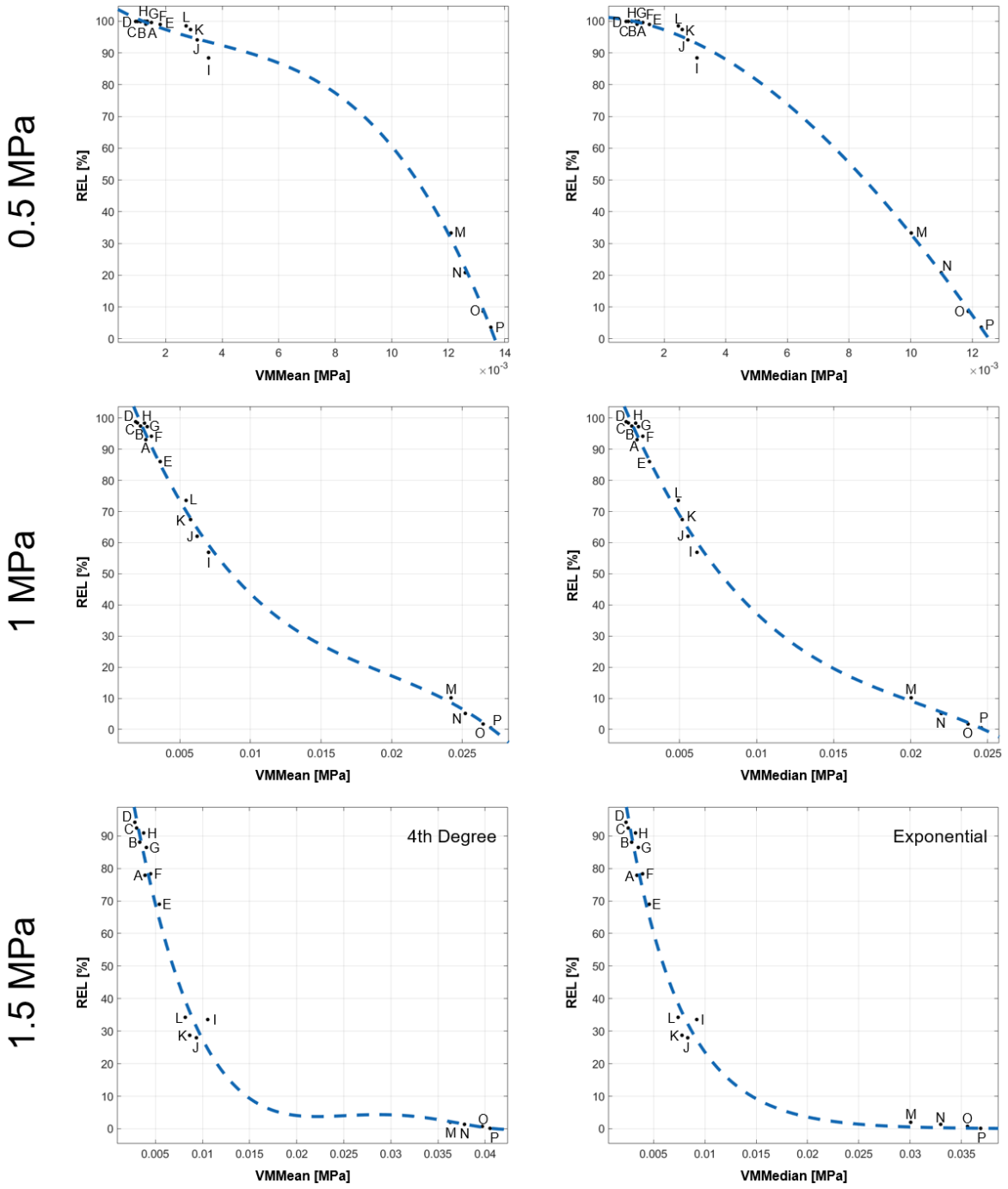

Small topology

Table 3-5 presents the parameters obtained to reach the desired reference porosities by using the constraint equation between *Dc* and *Ds* from [177]. This equation defines the maximum value of *Dc* to avoid the spherical topology become the same of circular pores.

Table 3-5: Mean and median stresses on the newly formed tissue domain for small spheric pore array for 1 MPa.

Geometry ID	*Ds* (mm)	*Dc* (mm)	Porosity (%)	VMMean (MPa)	VMMedian (MPa)	REL (%)
A	0.53363	0.24527	**25.00%**	0.00262	0.00187	90.52
B	0.53363	0.30187	29.76%	0.00260	0.00210	93.78
C	0.53363	0.33960	36.50%	0.00271	0.00232	95.53
D	0.64882	0.29821	**37.50%**	0.00263	0.00198	92.40
E	0.64882	0.36702	42.42%	0.00274	0.00225	94.34
F	0.64882	0.41290	49.89%	0.00297	0.00256	94.86
G	0.74531	0.34256	**50.00%**	0.00290	0.00225	91.76
H	0.74531	0.42161	54.17%	0.00309	0.00258	93.37
I	0.74531	0.47431	61.29%	0.00346	0.00306	91.05

High degree surfaces of response will hardly give relevant data about the behavior of the geometric design parameters and the VMMean, due to the narrow range of von Mises statistics and constraints between *Dc* and *Ds*. To avoid badly conditioned fitting, polynomial first degree surfaces were plotted to analyze the relation between these parameters and the stresses (Figure 3-17), obtaining values of R^2>0.85. Additional goodness of fit measurements can be found in detail in Annex A. However, the generated surface does not take into account the constraints in the solution space.

Figure 3-17: Response surfaces of pore parameters vs. von Mises mean (Left) and von Mises median (right) of spheric small topology for 1 MPa.

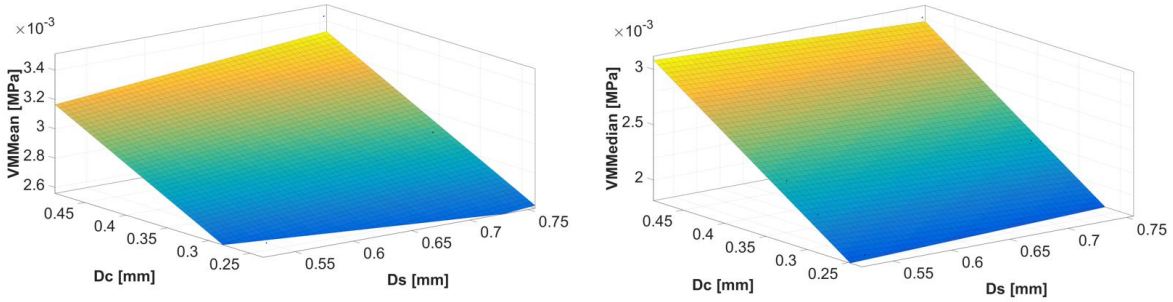

Response surfaces in Figure 3-17 suggest that the sphere component in the topology has lower influence in the von Mises statistics, while the cylindrical component affects more the stresses of the granulation tissue inside the pores. Due to the narrow range of von Mises statistics in the set of small topology and the high relative amounts of bone predicted for each one of its geometries, curve fitting could not be done successfully.

Regarding the von Mises stress histograms presented in Figure 3-18, geometries **A**, **B** and **C** show three peaks, **D, E** and **F** exhibit double peaked distributions, and **H** and **I** geometries exhibit a plateau shape. As *Dc* increases, VMMean and VMMedian increase and redistribute the principal peak or mode towards the tail, thus leading to multimodal stress distributions and plateau formations. As von Mises statistics increases, there is a stress redistribution along the tail of the histogram and a decrease in standard deviation. An increase in *Ds* exhibits a smoothing of the peaks suggesting an increase in the uniformity of the stresses in the granulation tissue.

Figure 3-18: Normalized von Mises distributions of small spheric set under 1 MPa.

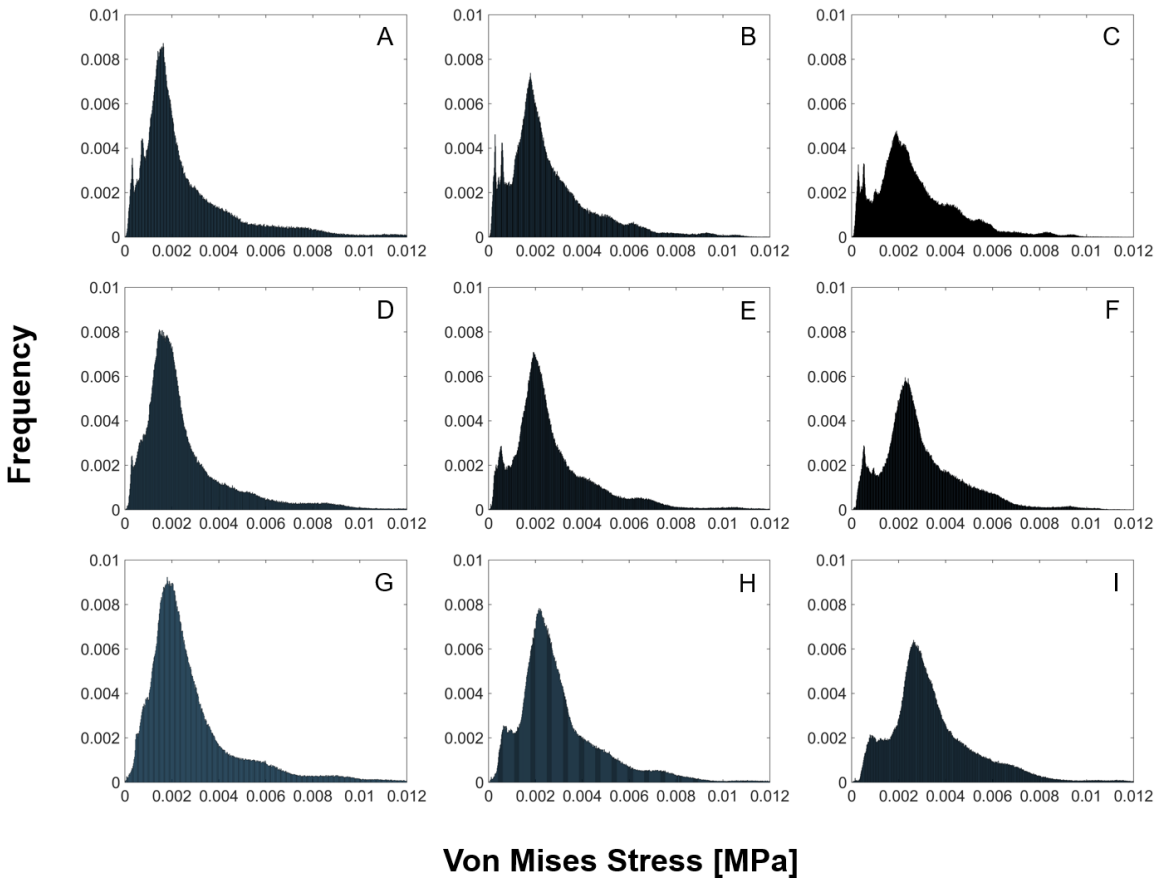

The change of parameters allowed in spherical ST topologies lead to no substantial stress variations, which means that the mechanical environment is relatively stable. This fact is consistent with the tight values in von Mises statistics and predicted relative amounts of bone. This hypothesis is also supported by the maximum principal stress absolute plots shown in Figure 3-19, in which it is evidenced that stresses do not change their maximum values in stress axis and the main changes are in small smoothing of peaks in the frequency axis and increase of density around the central region. The plots show that in spherical pores with small topology, most elements are subjected to a positive maximum principal stress and maximum frequencies correspond to these regions, but **G** and **H** have similar maximum frequencies for elements under both tensile and compression stress.

Figure 3-19: Normalized histograms of maximum principal stress absolute for small spheric set under 1 MPa.

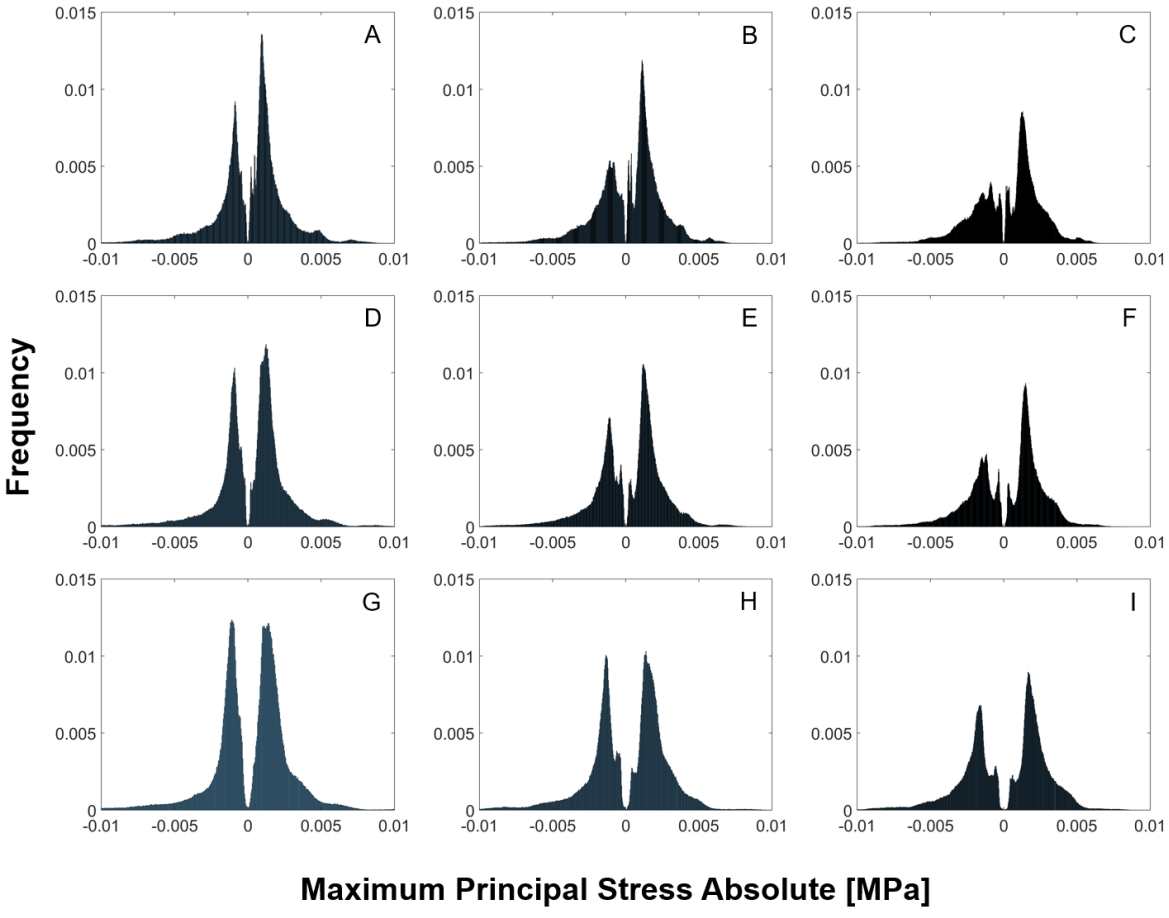

Large topology

Spherical large topologies allow reaching high porosity values that are not achievable with small topology. These porosity values produce more notable changes in von Mises statistics and the relative amount of bone predicted for each geometry as shown in Table 3-6. However, it is important to remember that the space of solution in the large topology has upper and lower constraints for *Dc* related to *Ds*, which introduces an additional limitation in the exploration of its micro-geometrical parameters.

Contrary to the behavior in small topologies, von Mises statistics are more influenced by *Ds* parameter than *Dc*, as shown in the first order surfaces plotted in Figure 3-20. R^2 indicator for this geometry is greater than 0.83, thus showing better fit for von Mises median as in the previous analysis.

Table 3-6: Mean and median stresses on the newly formed tissue domain for large spheric pore array for 1 MPa.

Geometry ID	*Ds* (mm)	*Dc* (mm)	Porosity (%)	VMMean (MPa)	VMMedian (MPa)	REL (%)
A	0.8190	0.250	60.0	0.00366	0.00254	89.11
B	0.8190	0.414	61.8	0.00348	0.00283	89.14
C	0.8190	0.578	72.7	0.00501	0.00447	78.11
D	0.9044	0.460	75.0	0.00531	0.00439	76.22
E	0.9044	0.549	76.2	0.00541	0.00474	73.14
F	0.9044	0.638	81.5	0.00785	0.00705	42.57
G	1.0180	0.660	90.0	0.01646	0.01485	2.70
H	1.0180	0.689	90.2	0.01770	0.01615	2.08
I	1.0180	0.718	91.2	0.02403	0.02194	0.92

Figure 3-20: Response surfaces of pore parameters vs. von Mises mean (Left) and von Mises median (right) of spheric large topology for 1 MPa.

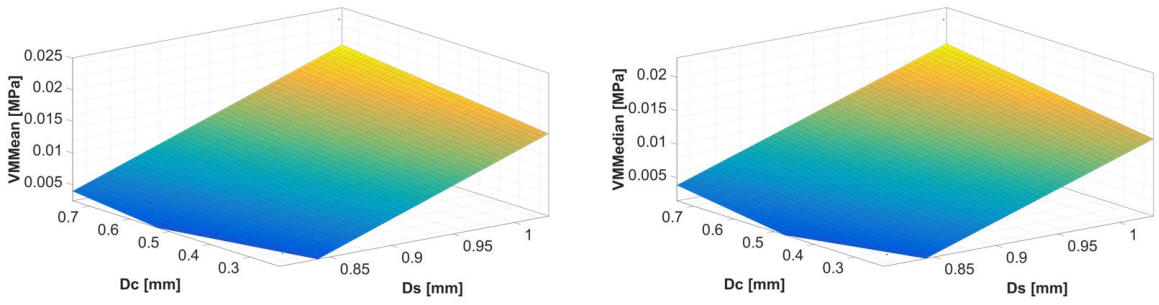

Since the variations of von Mises statistics and performance in the amount of bone predicted were more evident in large topologies than in small ones and the ranges were encompassed widely, it is possible to observe the evolution of the amount of bone when the von Mises statistics increase in the granulation tissue due to the increment in geometrical parameters (Figure 3-21).

Figure 3-21: Curve fitting between the relative amount of bone predicted and VMMean (left) and VMMedian (right) for spheric large topology set under 1 MPa.

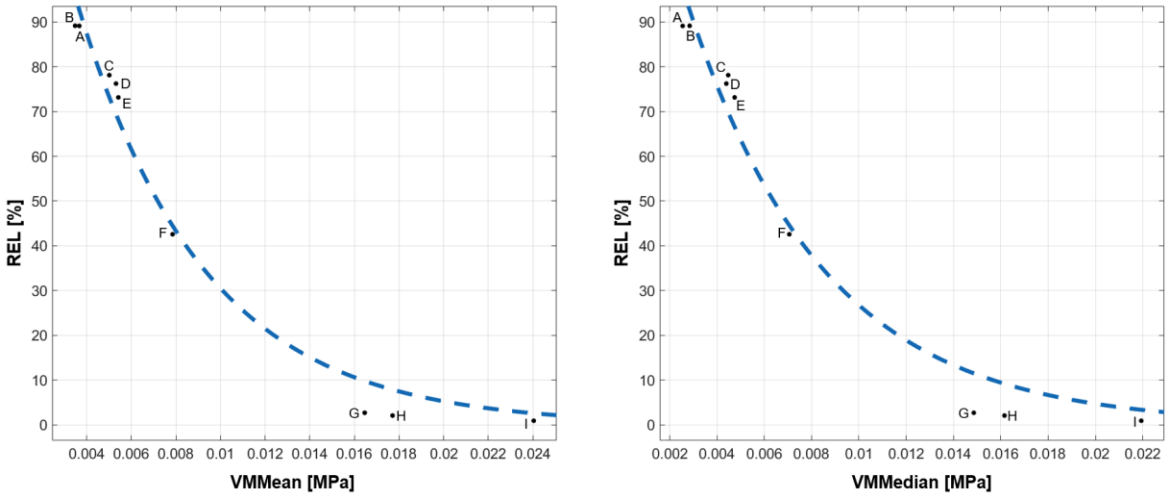

Curve fitting was achieved by the use of the exponential first degree curve with R^2>0.97. It is worth noting that similar porosities in small and large spherical topologies could lead to similar von Mises statistics and performance, as observed when comparing **I** geometry in the small topology set to **B** geometry in the large topology set.

Histograms of von Mises stress for large topologies exhibit unimodal shape as shown in Figure 3-22. Increase in *Ds* produces displacement in von Mises values and widens the distribution body. On the other hand, increase in *Dc* produces a redistribution around the central region of the histogram, thus reducing the modal peak.

In Figure 3-23, interestingly and contrary to small pores geometries, the predominant maximum principal stress of the elements in the domain of granulation tissue is negative. This fact illustrates that small changes in the geometrical parameters of a same pore family can produce significant changes in the general state of stresses in the newly formed tissue.

Figure 3-22: Normalized von Mises distributions of the large spheric pore set under 1 MPa.

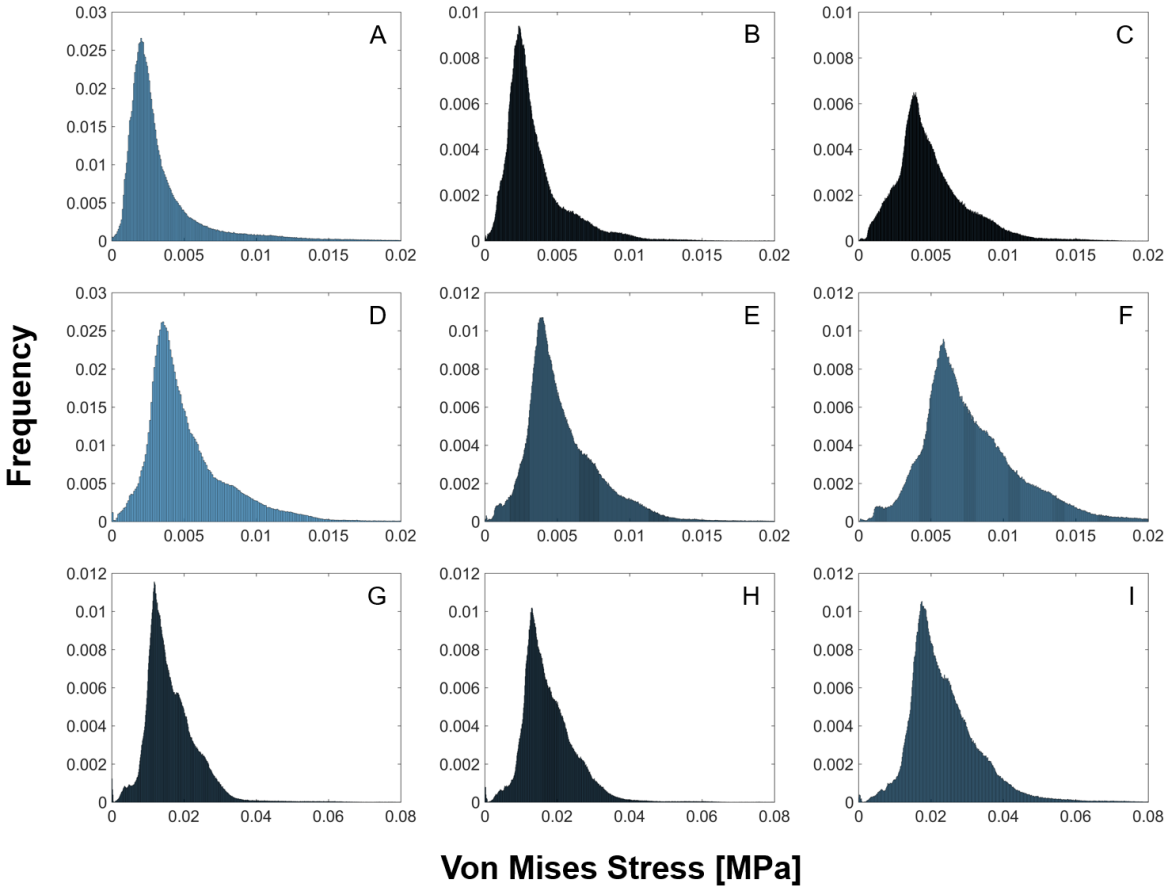

3.6 Conclusions

This chapter examined the stresses in the newly formed tissue inside some regular scaffolds topologies and how they change when the geometrical parameters that define these topologies are altered.

A computational framework to study the mechanobiological behavior of the tissue growing inside the scaffolds was successfully implemented. The methodologies developed here enhance the knowledge about the biophysical phenomena that occur inside a scaffold and become a promising strategy to achieve better designs according to mechanobiological criteria.

Figure 3-23: Normalized histograms of maximum principal stress absolute for large spheric pore set under 1 MPa.

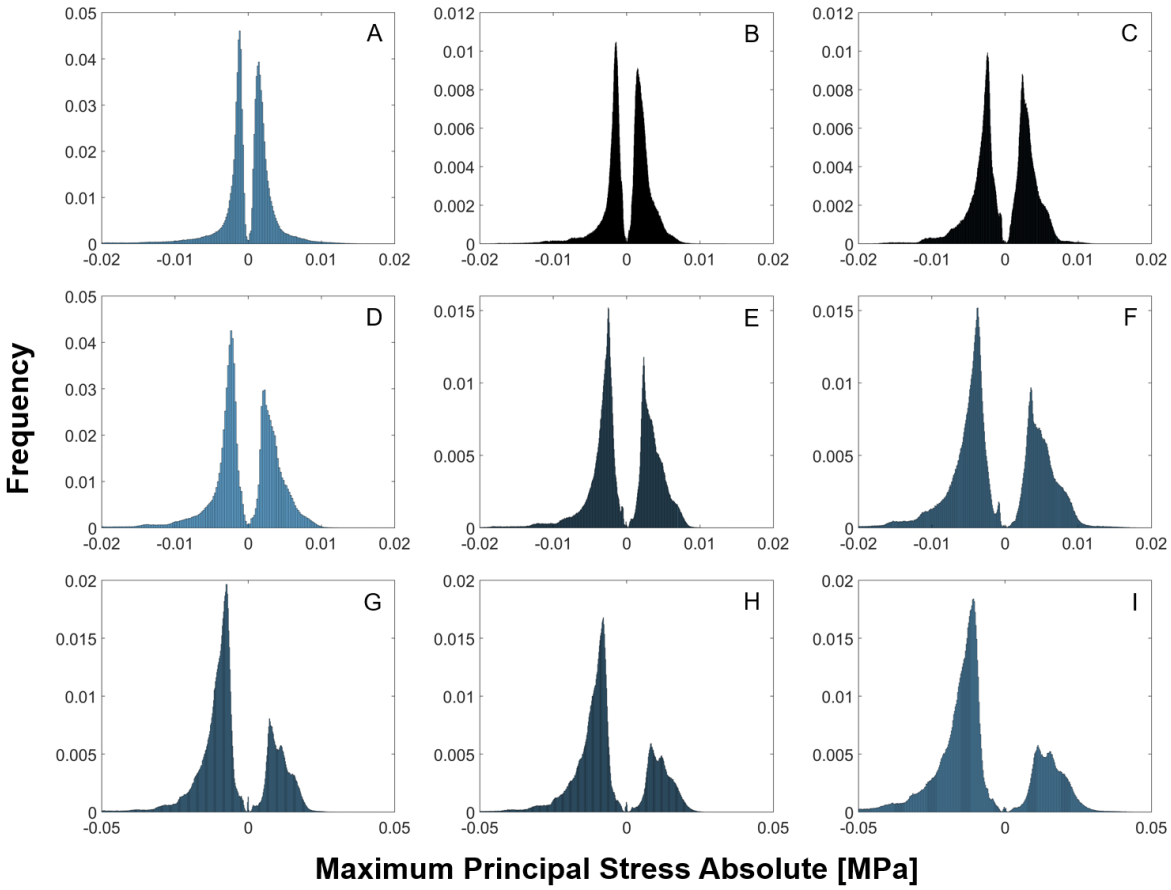

The differences observed between the results of stresses and performance among the studied topologies suggest that each topology has significant parameters, which are different between the distinct topology families.

There is a stability effect in lower porosities in the studied sets that hold the stresses in a favorable range and lead to predict high relative amounts of bone. However, it is possible obtain more absolute amount of bone by the use of high porosity structures and the proper selection of the geometrical parameters of the pores.

We found that small features on the geometries influence the stresses on granulation tissue even in the same families, such as spherical pores in whose stresses behave different in

two topologies from the same family. In general, von Mises statistics and performance exhibit nonlinear negative correlations in all studied topologies.

For both maximum principal stresses of compression and tension groups, it was not possible to find an association between the predominance and the performance, since for some geometries tension predominance was observed in best performance geometries but in others compression predominance coincides with the best performance geometries. Therefore, it was not possible to draw a stress state configuration that, in general, favors the differentiation of bone tissue inside the scaffold.

The parameters were not studied in the full range, especially in low porosities below 25% in which the mechanical stimulation on tissue will be very low. Therefore, the performance will have decreasing values as the stimulus becomes lower until reaching a zero value. In an attempt to describe a complete behavior of the relation between von Mises statistics and performance, probably a complete description along the entire stress axis will be a piecewise function according to the thresholds of the mechanobiological approach used. The function will start at values close to zero, and then increases with a positive sigmoid shaped or S-shaped function from these lower values, in which granulation tissue is not sufficiently stimulated. After to reach the segment studied here, in which in the range of von Mises statistics values is narrow, the performance will be close to a maximum value, then it will finally decrease, thus showing an inverse sigmoid or S-shaped function. It is worth noting that scaffolds with low porosities are not suitable in tissue engineering field since the final purpose is to obtain structures with high porosities to allow the maximum amount of tissue and favor the differentiation to the desired phenotype.

Finally, this chapter allows elucidating the phenomenon and gives insights on the interplay in geometrical design parameters, stresses, and performance of regular bone scaffolds. However, simplifications were made, specially associated with the non-existence of the time evolution behavior of the system. Therefore, further studies are needed to determine how these temporal effects influence the phenomena inside the scaffold-tissue system.

4. Optimization of micro-geometrical features of unit cells

In the previous chapter, it was observed that some scaffold geometries perform better than others if they are compared based on a mechanobiological criterion. The aim of this chapter was to implement a procedure, based on the Prendergast mechanobiological criterion and for different load schemes, to find the optimal geometrical parameters of different scaffolds families of beam-based repeating unit cells, namely, truncated cuboctahedron, truncated cube, rhombic dodecahedron and diamond. **The content of this chapter is based on publication I** (see Associated publications).

The methodology presented in chapter 3 regarding the mechanobiological approach is adequate to suggest a performance criterion to evaluate designs of scaffold microgeometries. For this purpose, a script to automatize the construction of three-dimensional finite element models is included in an iterative procedure that evaluates the mechanobiological performance of each scaffold geometry and perturbs its geometrical parameters towards an optimal value that maximizes the predicted amount of bone for different load regimes. Optimizing the scaffold performance from a mechanobiological perspective, could produce a faster healing process, increase the success rate of the scaffold implantation, and reduce expensive costs of experimental trials.

4.1 Modeling of the beam-based unit cells

The previous chapter described the modelling of unit cells of hexahedrons for rectangular, elliptic and spherical pore geometries. However, the literature provides an extensive number of interesting regular geometries known as cellular solids [80]. Particularly, some of them are microarchitectures of engineered biomaterials suitable for TE applications and with possibilities of translating into scaffold fabrication with advanced manufacturing techniques, as discussed in section 2.4. The analyses of mechanical properties and their analytical relationships have been carried out regarding regular microgeometries such as FCC, BCC, minimal surfaces, and the different families of beam-based and regular structures [64], [140], [152], [180], [181].

From all geometries previously described, a group of unit cells of interest was selected: truncated cuboctahedron, truncated cube, rhombic dodecahedron and diamond structure [140]. Since these geometries have a different nature from those based on hexahedrons, their geometrical definition is formed by regular oriented beams with a square or circular section. The topology was fixed for each geometry family, i.e., the orientation of the beams is not altered in the parametrical analysis.

The micrometrical feature that controls the stiffness of the system and thus, the mechanobiological performance is the parameter ***D*** that defines the cross section of the beams. These beam-based geometries are one-parametric in contrast to those presented in the previous chapter which are two-parametric, that is, all the beams included inside the unit cell were hypothesized to possess the same cross section dimension ***D***. In the case of the circular cross section, ***D*** represents the diameter of the section, while in the case of the square cross section, ***D*** is the side length of the square.

The side of the cubic unit cell in which each different microstructure is delimitated was equal to Q=637 μm, which is based on the dimensions of the volume studied by Byrne et al. [62]. The different topologies of the four unit cells studied have the following general modeling methodology. First, a bi-dimensional trajectory was defined. Second, the sweep of the cross section along the trajectory was performed. Third, by exploiting the symmetry of the unit cells, the solids generated by sweep were replicated using some CAD tools available in ABAQUS®, such as mirror, translate, rotate, etc. Finally, the unit cell generated was cut along the faces of a cube (in which the unit cell is inscribed) to make the unit cell replicable in the three directions. The details of the modeling of each geometry are described below.

4.1.1 Truncated cuboctahedron

The first step to generate the truncated cuboctahedron structure was to make an octagonal trajectory with equal sides L_1 that served afterward to sweep a selected cross-section and generate a solid sub-unit that contains eight beams (Fig. 4-1(a)). Taking advantage of the symmetry of the cell, two axes were defined and the sub-units were replicated around them and displaced to form the unit cell (Fig. 4-1(b)). To link the sub-units, beams from vertex to vertex of longitude L_1 were added (Fig. 4-1(c)).

Figure 4-1: Steps followed to build the truncated cuboctahedron unit cell (a-e)**.** An octagonal trajectory t_1 was first traced. Then, a sweep of the circular or a square cross section was performed along t_1, thus obtaining a solid subunit including eight beams (a). Two axes (a_{1_x} and a_{1_y}) were hence defined and, through rotation operations around them, the original solid sub-unit was replicated five times (b). The resulting disconnected sub-units were finally connected by means of beams (c). The unit cell generated was cut along the planes π_{M1}, π_{M2}, …π_{M6}, thus obtaining the final unit cells: circular (d) and square (e) cross section.

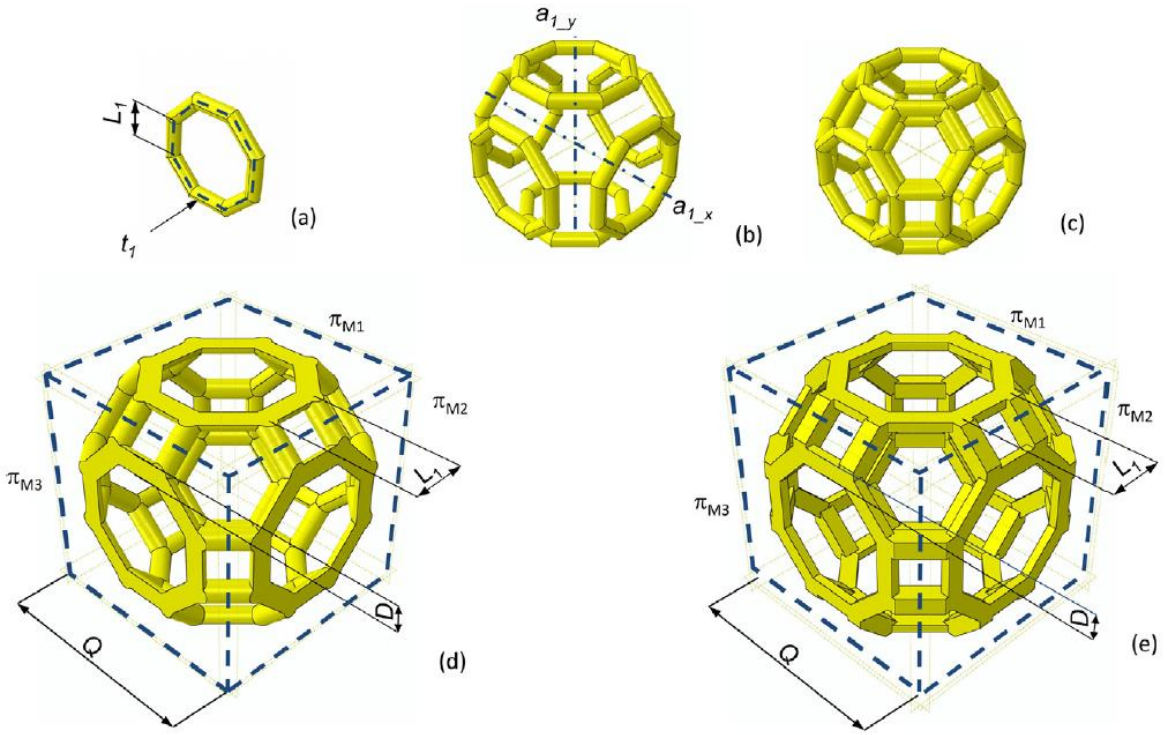

To ensure the capability to replicate the unit cell infinitely, the full unit cell was cut using four planes defined by a cube with dimensions *Q* for both circular cross section (Fig. 4-1(d)) and square cross-section beams (Fig. 4-1(e)). The *Q* dimension was selected according to previous works [165] and the relation between *Q* and L_1 was defined as:

$$Q = L_1 \cdot \left(1 + 4 \cdot \cos\left(\frac{\pi}{4}\right)\right) \tag{4.1}$$

Truncated cuboctahedron topology shows octagonal, hexagonal and square interconnectivity. To determine the upper bounds that limit the interconnectivity of this

topology, relationships between Q, L_1 and D dimensions were developed and can be found in the Annex B.

4.1.2 Truncated cube

A similar previous strategy was employed to model the truncated cube, but only the replication of the octagonal sub-units was required and the rotation about the axes so that the unit cell was linked completely (Figs 4-2(a) to 4-2(b)).

Figure 4-2: Steps followed to build the truncated cube unit cell (a-d). After building the first solid sub-unit (a), two axes were defined (a_{2_x} and a_{2_y}, (b)) and replications of the original sub-unit were performed by rotating it around a_{2_x} and a_{2_y}. The unit cell obtained was cut along the same planes π_{M1}, π_{M2}, …, π_{M6} which delimit the cubic volume $Q \times Q \times Q$ ((c) circular cross section, (d) square cross section).

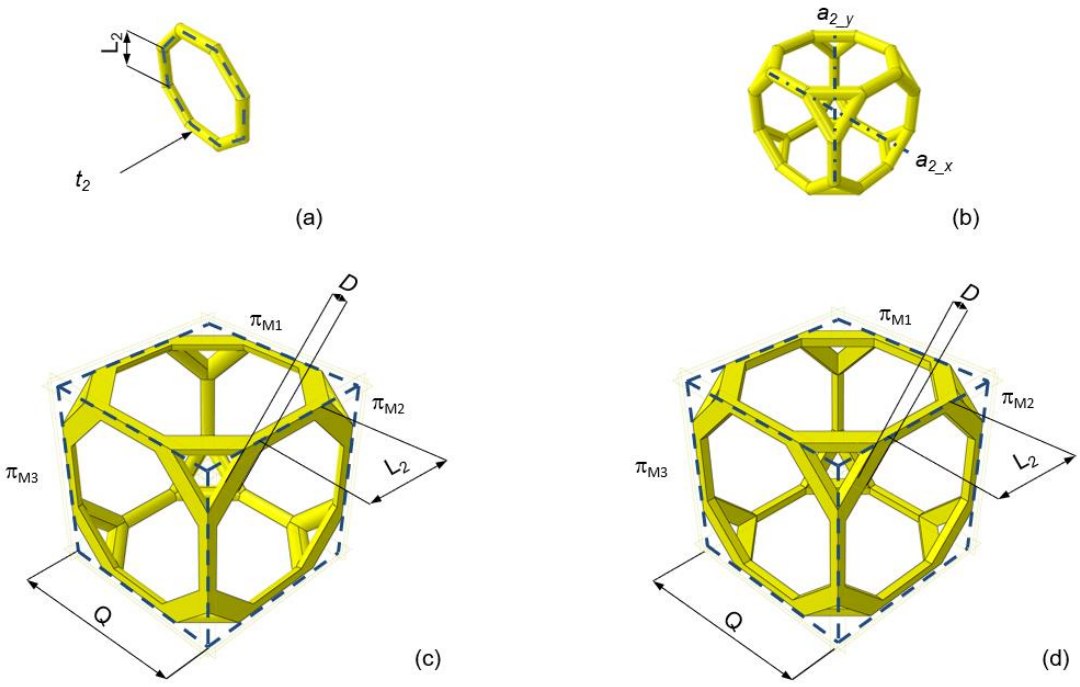

In the same way, the full cell was cut using the cube of dimension Q for both cross-sections (Figs 4-2(c) to 4-2(D)). In this case, Q and L_2 hold the next relation:

$$Q = L_2 \cdot \left(1 + 2 \cdot \cos\left(\frac{\pi}{4}\right)\right) \tag{4.2}$$

4.1.3 Rhombic dodecahedron

The third geometry modelled was the rhombic dodecahedron, a structure composed of 24 beams (Figure 4-3). The initial bidimensional trajectory was a rhombic shape with side dimensions of L_3, determined by the relation:

$$Q = 4 \cdot L_3 \cdot sin(\alpha) \tag{4.3}$$

Figure 4-3: Steps followed to build the rhombic dodecahedron unit cell (a-g). A rhombic trajectory t_3 was first traced and then the sweep of a circular or a square section was performed (a), thus obtaining a first solid sub-unit. After defining the axis a_{3_x} (b), three replications of the initial sub-unit were obtained by rotating it around a_{3_x} by the angles π/2, π and 3π/2. To link completely the cell, half subunits were finally added in the horizontal plane π_H (c) and in the vertical plane π_V(d) of the cell. The resulting unit cell was finally cut along the faces of the planes π_{M1}, π_{M2}, …π_{M6} ((e) circular cross section, (f) square cross section). In order to evaluate the effect of the cell orientation, the same rhombic topology with a rotation of π/2 was modelled (g).

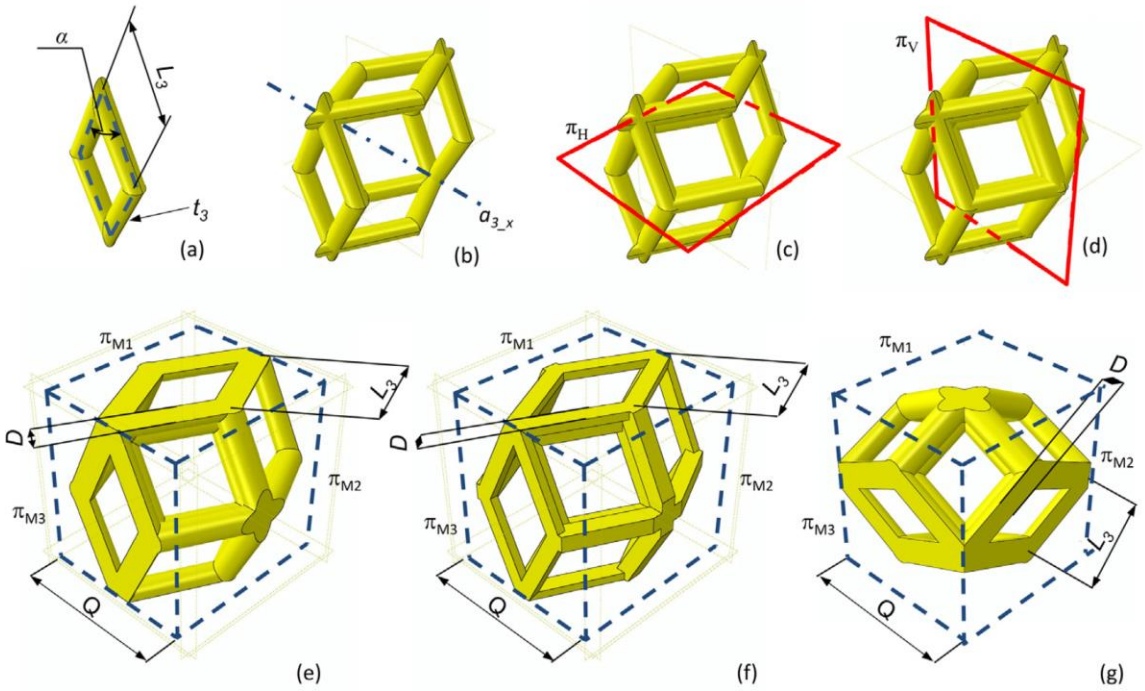

This relationship was made to guarantee the L_3 dimensions for all the beams of the unit cell. To determine the upper bounds D_{max_3} that limit the interconnectivity of the truncated cube topology, relationships between Q, L_3 and D dimensions were developed (Annex B).

The first step was sweeping the cross-section through the path defined by the two-dimensional trajectory (Fig. 4-3(a)). Afterward, the replication of three rhombic sub-units around the x axis was performed (Fig. 4-3(b)). To link completely the cell, half sub-units were added in horizontal and vertical planes (Figs 4-3(c) to 4-3(d)). Once the cell was defined, the cut was made inside the cube (Figs 4-3(e) to 4-3(f)). The resultant cell exhibited rhombic interconnectivity. Additionally, to evaluate the effect of cell orientation, the same rhombic topology with a rotation of ninety degrees was modeled in Figure 4-3(g).

4.1.4 Diamond structure

The last cell is the diamond structure known for its angles of 109.47 degrees between the axis of its beams (b_1, b_2, b_3 and b_4), where the length of these beams is denoted as L_4 (Figure 4-4(a)). Although the diamond unit cell has symmetry properties, there are some geometrical issues in this type of cell. First, the connection in the different beams is not continuous (Fig. 4-4(b)). To solve this issue, spheres with 1.1 times the dimension D of the beams were included in the intersections (Fig. 4-4(c)). Once the unit cell was built, a change of orientation was necessary to align the structure vertices V_1, V_2, V_3, and V_4 with those of the cubic volume. For this purpose, the distance between the free vertexes of the structure should be fit to the transversal distance of the cube face (Fig. 4-4(d)). The final unit cells for circular and square cross-sections are shown in Figures 4-4(e) and 4-4(f), respectively. Geometrical upper bounds for the diamond structure are shown in Annex B. The relationship between Q and L_4 assumes the form:

$$Q = 2\sqrt{2} \cdot L_4 \cdot sin\left(\frac{\beta}{2}\right) \tag{4.4}$$

Additionally to the beam-based unit cells, by following the same procedure previously described, a parametric spherical unit cell was modelled to mirror it in orthogonal directions and obtain scaffolds with spherical topology. As the parameters *Dc* and *Ds* control the

geometry of these scaffold families, those parameters were perturbed in order to get new candidate solutions toward a geometry that maximizes the amount of bone predicted.

Figure 4-4: Steps followed to build the diamond unit cell (a-f). This unit cell was built by performing the protrusion of the cross section along linear paths (a) inclined to each other by the angle β=109.47°. In order to guarantee the continuity (b) between the single beams, connection spheres were included in the model (c). Once the unit cell was built, it was properly oriented so that vertices V_1, V_2, V_3 and V_4 are coincident with those of the cubic volume $Q \times Q \times Q$ (d). Cuts were finally performed along the faces of the planes π_{M1}, π_{M2}, …π_{M6}((e) circular cross section, (f) square cross section).

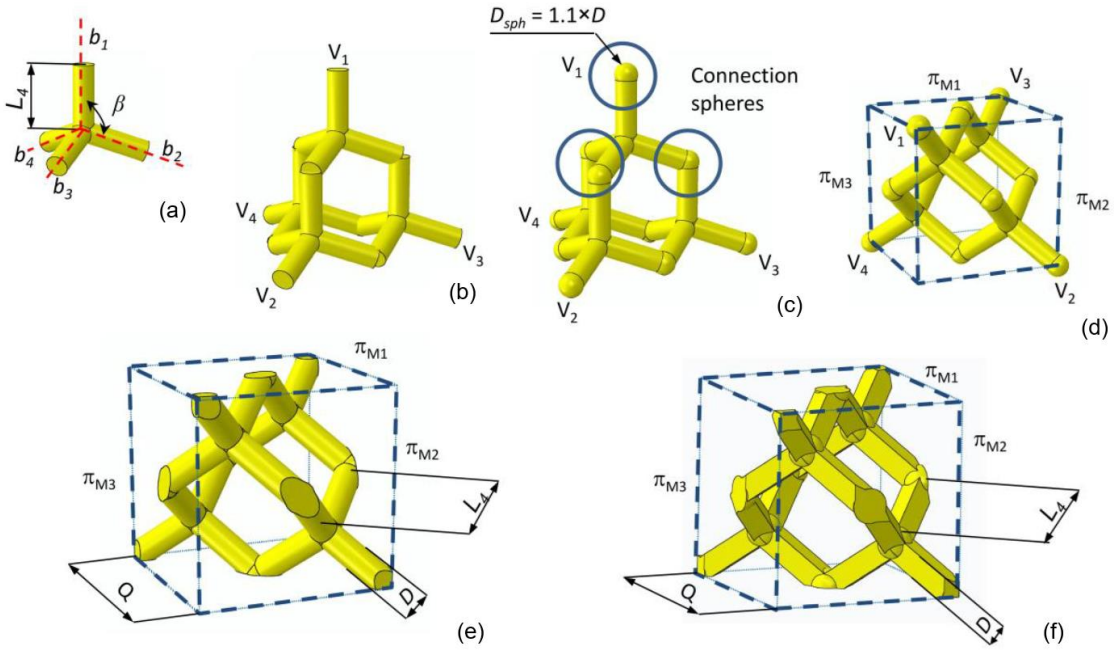

4.2 Geometrical modeling of the scaffold tissue-scaffold system

Once all the cells were defined, the replication of each of them in the three orthogonal axes was performed using a mirror technique. The resultant scaffold has cubic shape according to Byrne et al. [62]. To model the scaffold-tissue system, a negative volume of scaffold was obtained using a Boolean operation. The scaffold and the granulation tissue were assembled together with an upper rigid plate to the load application (Fig. 4-5(a)). The link

between these elements was a tie constraint to guarantee the same displacement in the whole system. A compression load *F* was applied linearly during one second in the center of the plate to produce an apparent compressive load *p*, thus representing a typical *in vivo* mechanical solicitation of the system [182]. Boundary conditions were established, such as clamp over the lower face of the system and pore pressure equal to zero to represent the free exudation of the granulation tissue in the side faces (Fig. 4-5 (a)) [62].

Figure 4-5: Boundary and loading conditions acting on the scaffold model (a). By exploiting the symmetry of the problem, the volume analyzed was reduced to one quarter of the total volume (b). Symmetry constraints were utilized on the faces of the model lying on the symmetry planes π_{1-2} and π_{3-2}, where the absence of any fluid flow was imposed ((b) and (c)).

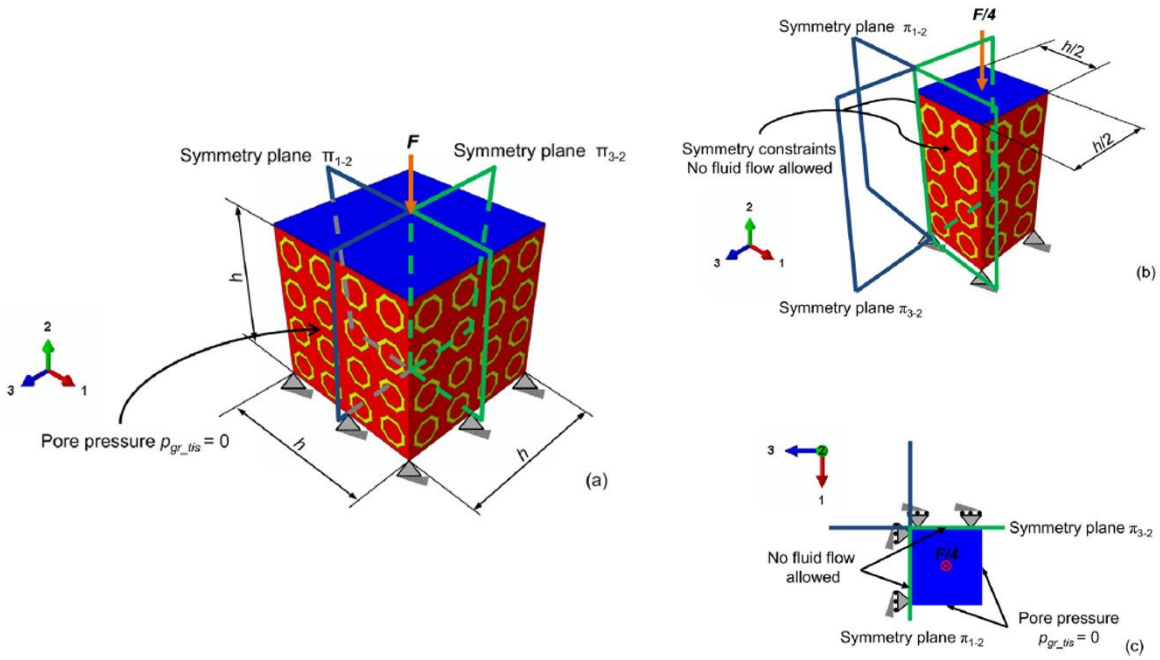

All quarter volumes were discretized into finite elements. The meshing process was performed using Abaqus Mesher with an average size of 30 µm and maximum deviation factor of 0.01. The elements were defined as C3D4P (ABAQUS documentation), which are linear tetrahedral four node displacement-pore pressure elements. All the reduced scaffolds and negatives, that is, the granulation tissue within, together with their respective meshes are shown in the Figure 4-6.

Figure 4-6: Scaffold and granulation tissue models (first two columns) and finite element mesh used (second two columns).

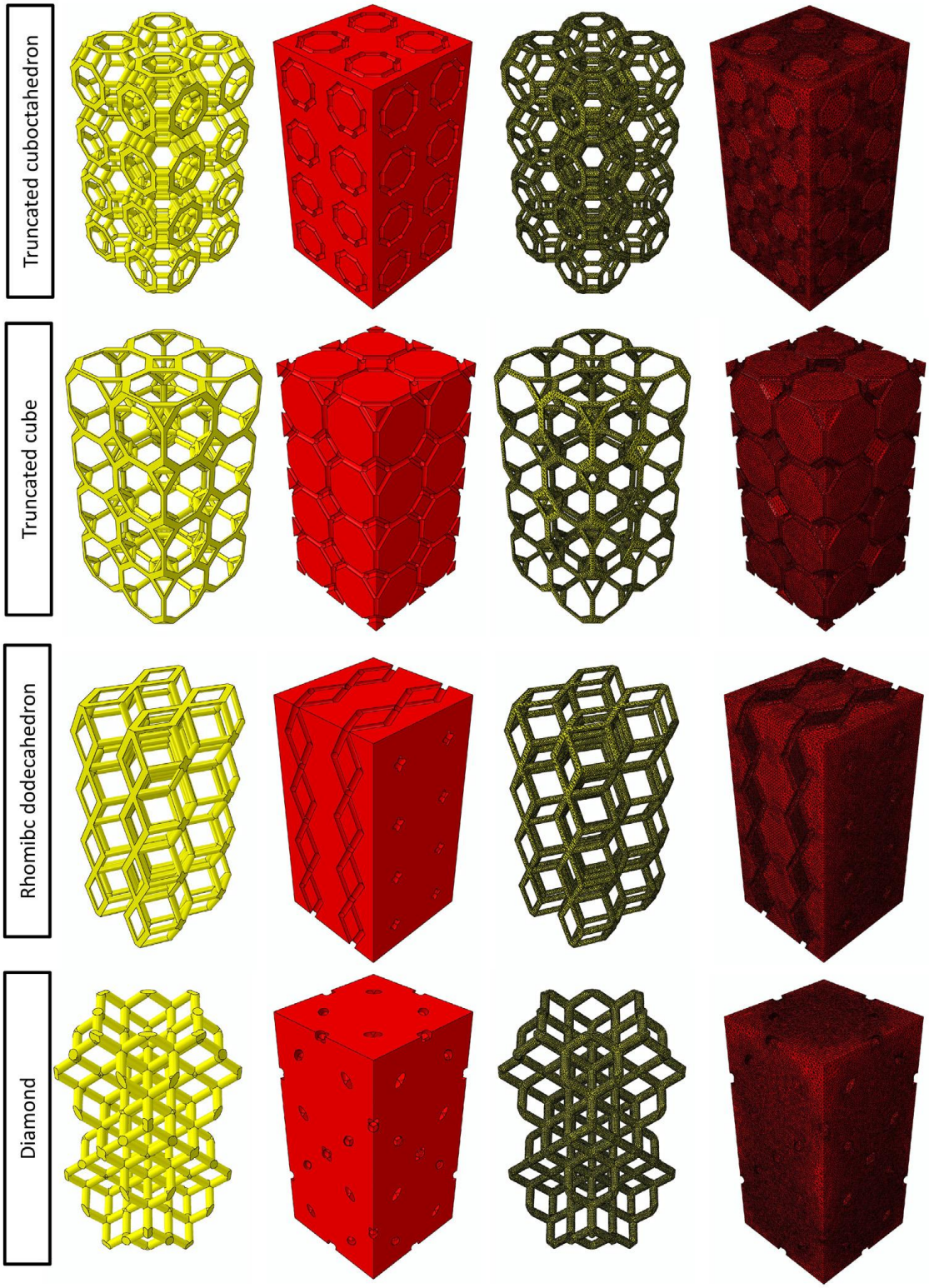

In order to compare the effects of pressure on the mechanobiological response, seven values of load ***F*** were hypothesized and applied in the different scaffolds to produce the following *p* values: 0.05, 0.1, 0.15, 0.25, 0.5, 1 and 1.5 MPa. Additionally, data from previous studies of hexahedral [81] and rhombicuboctahedron [165] were added to the simulated scaffolds. Linear interpolation was used to obtain the unavailable cases of load in the modeled scaffolds as well as in the previous studies. Material properties were the same used in Table 3-1 from chapter 3.

4.3 Optimization Algorithm

To find the optimal dimensions of the cross sections for each beam-based scaffold and each load case, an *ad hoc* algorithm was used and written in Matlab based on [81]. This algorithm allowed selecting the type of cell, shape of cross-section and particular load case (Fig. 4-7 Steps (1) – (3)). The next steps were the initialization of the *D* parameter (4) to create the python script that start the geometrical and FEM modeling of the scaffold (5).

The parameter *D* represents the diameter and side for circular and square cross sections, respectively. The ranges of the *D* values are defined by a lower and upper bound for each type of cell. The lower bound D_{min} is established as 28 µm following the hypothesis that values smaller than this are not of interest for the load cases studied [165]. On the other hand, the upper bounds D_{max} were determined by means of geometrical considerations related to shape of cross sections, *Q* and L_i, where *i* is each unit cell studied (Annex B).

After finishing the FEM analysis (6), the necessary data to compute the mechanical stimulus were saved in a .dat file and later the algorithm did the calculations associated with the obtained bone volume (Steps (7)-(9)). Using the volume of bone obtained for the *D* value used, the algorithm computes an objective function (10) and perturbs the function through the Matlab function *fmincon* to find a new value of *D* that produces a higher volume of bone. This process is repeated until the stopping criterion is satisfied, which means that the largest amount of bone for the specific type of cell was reached (steps (11)-(13)).

Figure 4-7: Schematic of the algorithm written in Matlab environment to determine the optimal dimension D for different unit cell geometries.

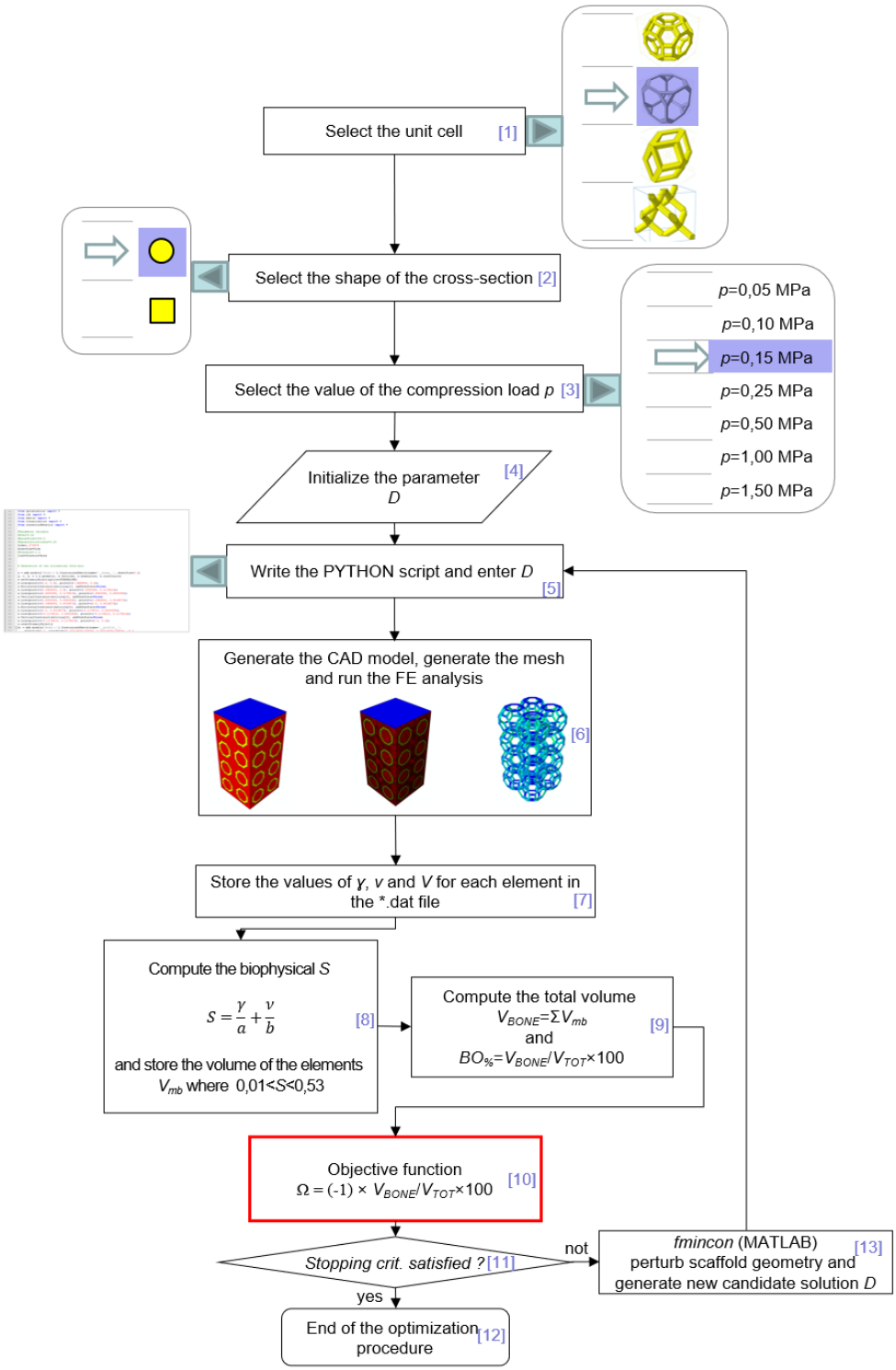

4.4 Results and discussion

Increasing dimensions of the optimal diameter *D* were predicted for increasing levels of load (Fig. 4-8(a)), which is consistent with our expectations. In fact, as the load increases, the resulting scaffold deformation increases too (if *D* remains constant), which leads to the formation of soft tissues, such as fibrous tissue and/or cartilage, according to equation (3.2) and the resultant inequalities of its solution. To contrast the excessive deformation, the algorithm increases the dimension *D*, thus making the scaffold stiffer and promoting the formation of bone. However, the trend of the optimal *D* in function of the load is asymptotic (Fig. 4-8(a)). Due to the constraints imposed to the upper bound D_{max_1}, the unlimited increase of the cross section is not allowed and, consequently, a saturation load exists. Behind this load, the optimal *D* cannot increase anymore but must be $D=D_{max\_1}$.

Figure 4-8: Optimization of the truncated cuboctahedron unit cell. Values of the optimal diameter D (a) and of $BO_{\%MAX}$ (b) predicted for different levels of load.

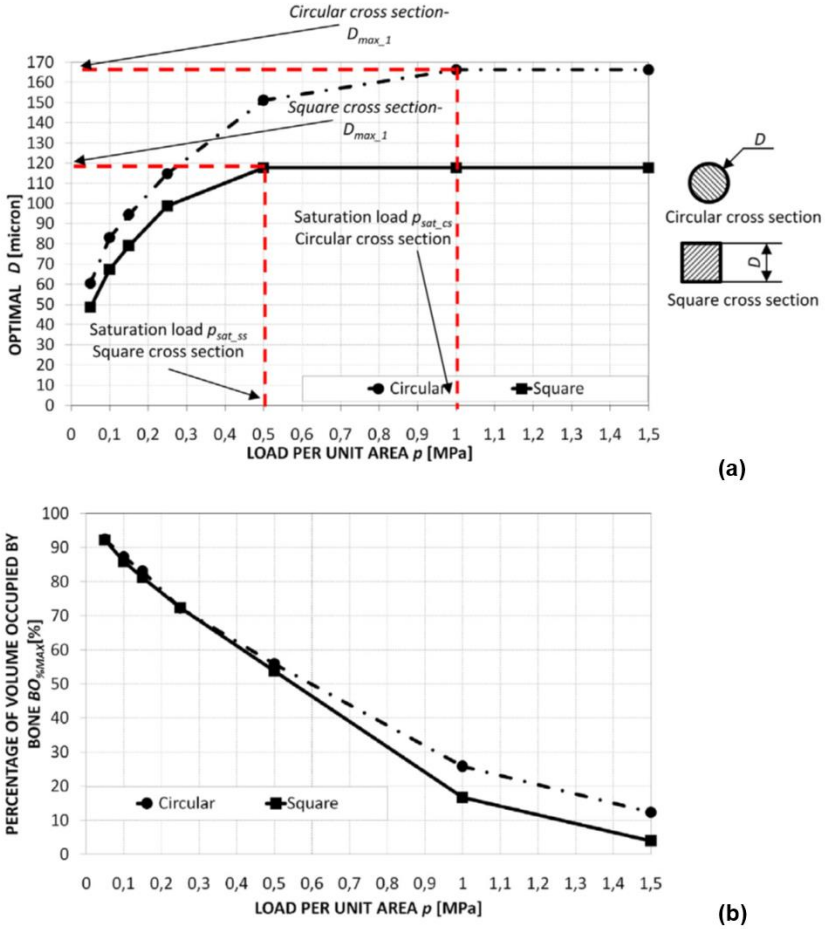

Interestingly, the amounts of bone $BO_{\%MAX}$ predicted for the circular and square cross sections are very close at low load levels but differ significantly with higher values of *p* (Fig. 4-8(b)). This behavior can be explained by the fact that the saturation load (p_{sat_ss} = 0.5 MPa) is smaller for the square cross section than that predicted for the circular cross section (p_{sat_cs} = 1 MPa). In other words, for the square cross section the range of the load values *p*, where the algorithm can properly optimize the cross section dimension *D*, is smaller than in the case of the circular cross section. Consequently, for higher load levels than those of the saturation load, the amounts of bone $BO_{\%MAX}$ predicted for the square cross sections are smaller than those obtained for the circular ones.

In the case of the truncated cube, the optimal diameter *D* was predicted to be greater as levels of the applied compression load *p* increase (Fig. 4-9(a)).

Figure 4-9: Optimization of the truncated cube unit cell. Values of the optimal diameter D (a) and of $BO_{\%MAX}$ (b) predicted for different levels of load.

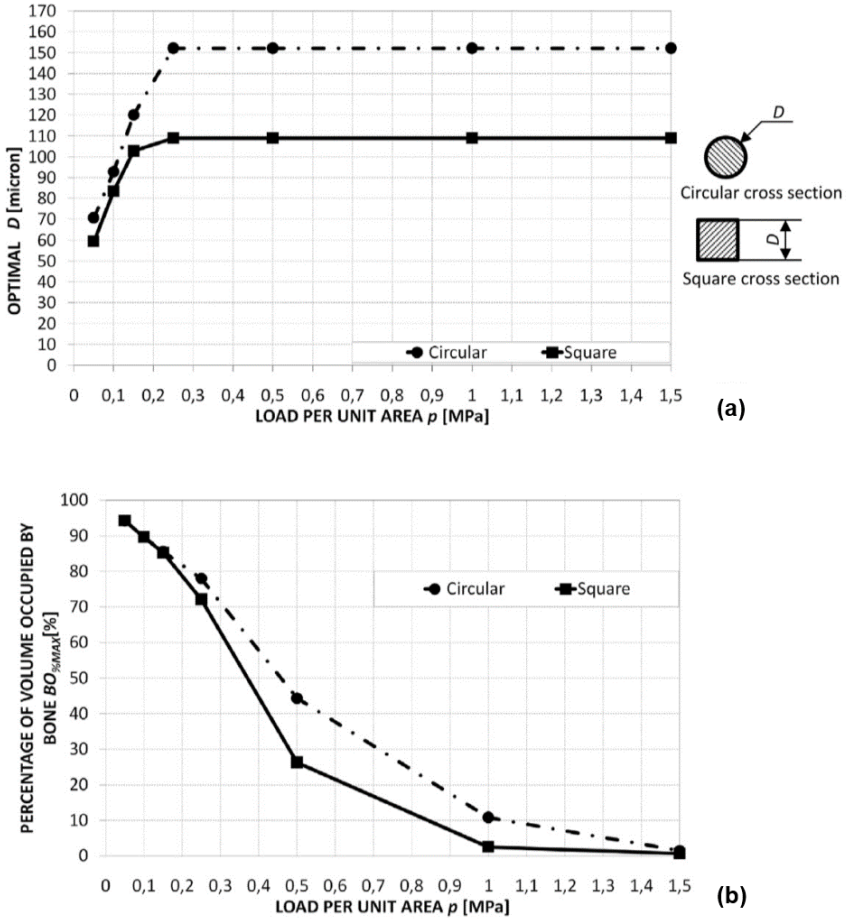

However, for the truncated cube unit cell, the saturation load was smaller than that predicted for the truncated cuboctahedron and for both, square and circular cross sections, it assumed the value of $p_{sat\_ss}=p_{sat\_cs}$ =0.25 MPa (Fig. 4-9(a)). In other words, for higher values of *p* than the saturation load, the optimization algorithm always gives the same scaffold geometry in output. The amounts of bone $BO_{\%MAX}$ predicted for the circular cross section were overlapping to those predicted for the square cross section for load values within the intervals $0.05 < p < 0.15$ MPa and $p > 1.5$ MPa, while differing significantly within the interval $0.15 < p < 1.5$ MPa (Fig. 4-9(b)). In particular, for p=1.5 MPa, very small amounts (≈ 1%) of bone $BO_{\%MAX}$ were predicted to form.

Figure 4-10: Optimization of the rhombic dodecahedron unit cell. Values of the optimal diameter *D* (a) and of $BO_{\%MAX}$ (b) predicted for different levels of load.

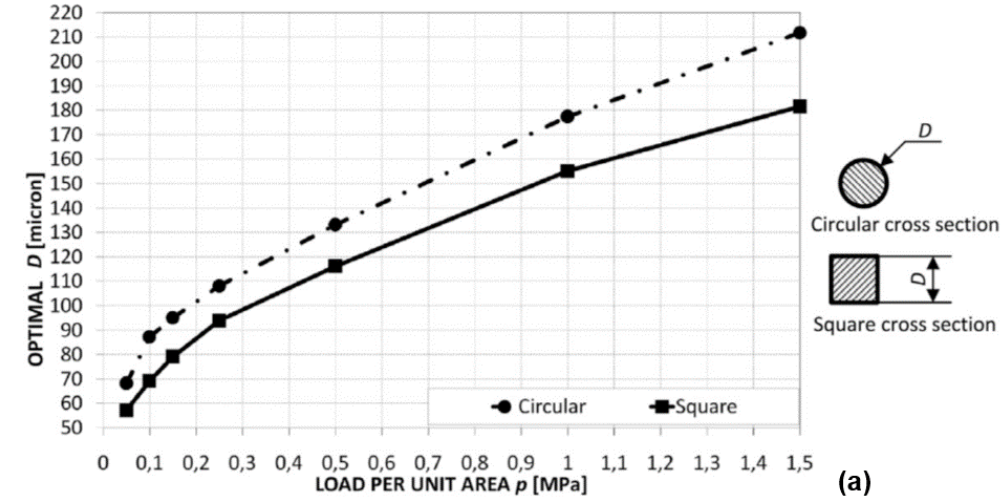

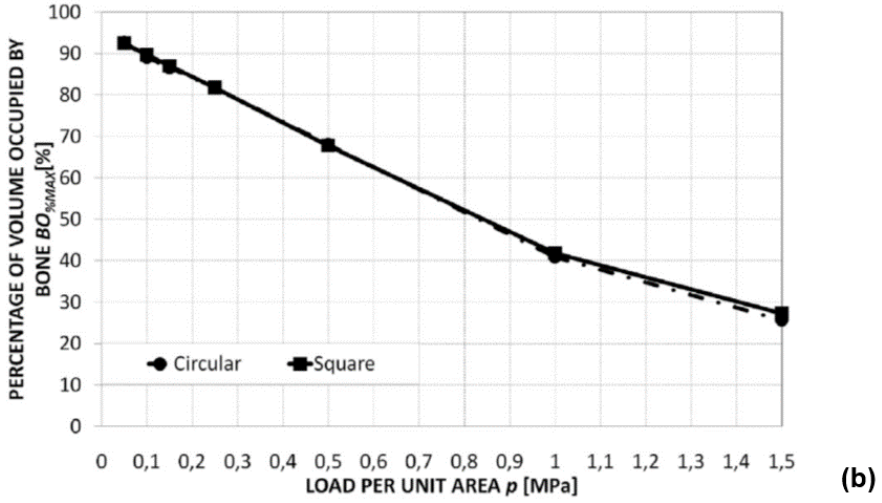

The trend of the optimal value of *D* in function of the load *p* for rhombic dodecahedron, is increasing, but does not present an asymptote, as in the previously analyzed cases. In other words, within the load levels hypothesized in this study, the saturation condition is never met (Fig. 4-10(a)), hence the optimizer can identify the optimal scaffold geometry for all the values of *p*. The amounts of bone predicted for the square cross section were practically overlapped to those computed for the circular one (Fig. 4-10(b)).

An interesting aspect of the rhombic dodecahedron unit cell is that it can be oriented, with respect to the loading direction, in two different ways: orientation A (previously analyzed in Fig. 4-10) and orientation B, where the longer diagonal of the rhombic elements is parallel and perpendicular, respectively, to the loading direction (Fig. 4-11(a)). Interestingly, for orientation B, the optimal dimensions *D* are significantly larger than those computed for orientation A (Fig. 4-11(b)). This result can be explained by the fact that with orientation A the beams can better distribute/transfer the load within the scaffold construct, compared with orientation B, hence the optimization algorithm can predict rather small values of *D*. Conversely, in the case of orientation B the spatial arrangement of beams is less favorable and, therefore, the algorithm tends to balance this disadvantage by increasing dimension *D*. Given that the optimal diameters *D* are larger for orientation B, hence a larger volume of the scaffold system is occupied by beams, it follows that a smaller volume is available for bone, which explains why smaller amounts of bone $BO_{\%MAX}$ were predicted for this orientation (Fig. 4-11(c)). Interestingly, no important differences were observed between $BO_{\%MAX}$ values computed for the circular cross section and those computed for the square one.

In the diamond structure, circular and square cross sections showed a different behavior (Fig. 4-12(a) and (b)). In fact, while the square cross section presented a saturation point at *p*=1 MPa, for the circular one no saturation load was found within the load interval studied. The values of $BO_{\%MAX}$ were very close for low levels of *p* and started to diverge as the square cross section reaches the saturation point (Fig. 4-12(b)). After this point, the difference became larger as the optimizer increased further the value of *D* in the case of the circular section but could not make the same for the square cross section.

Figure 4-11: Comparison between two different unit cell orientations: Orientation A and Orientation B. (a) Values of $BO_{\%MAX}$ (b) and optimal diameter D (c) predicted by the algorithm for different levels of load and for the two different cell orientations.

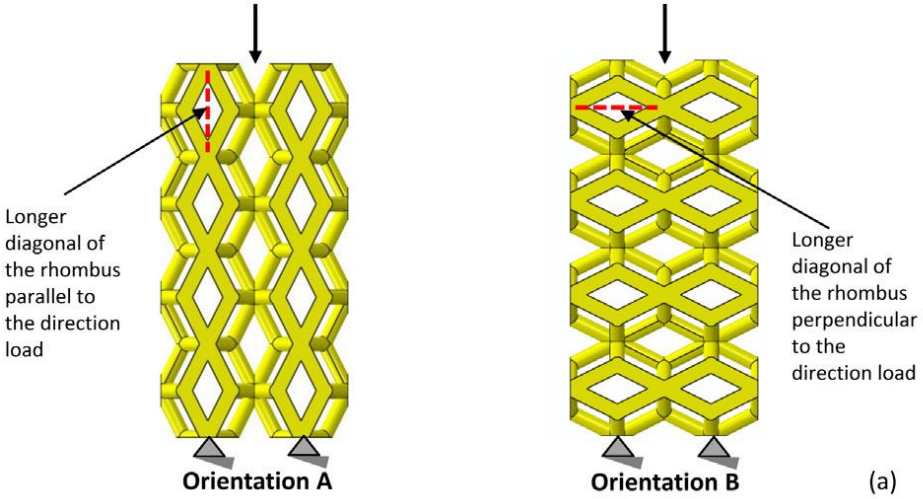

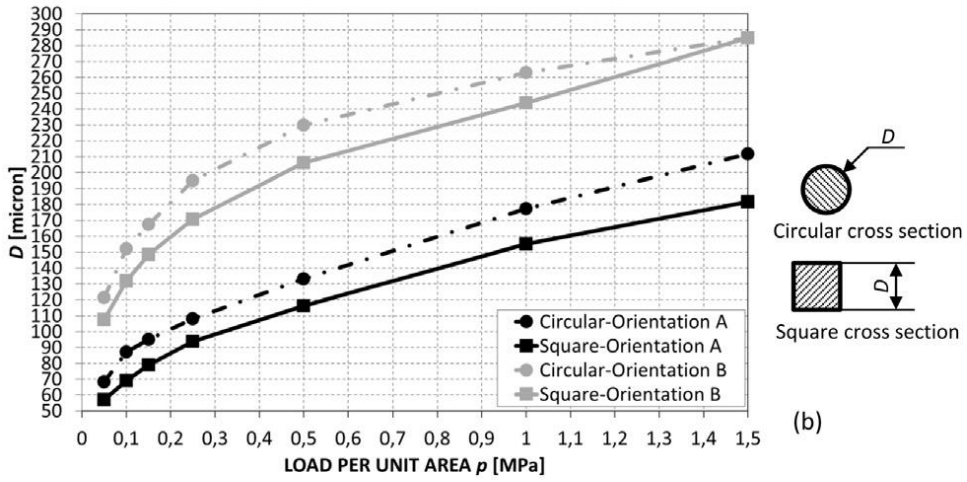

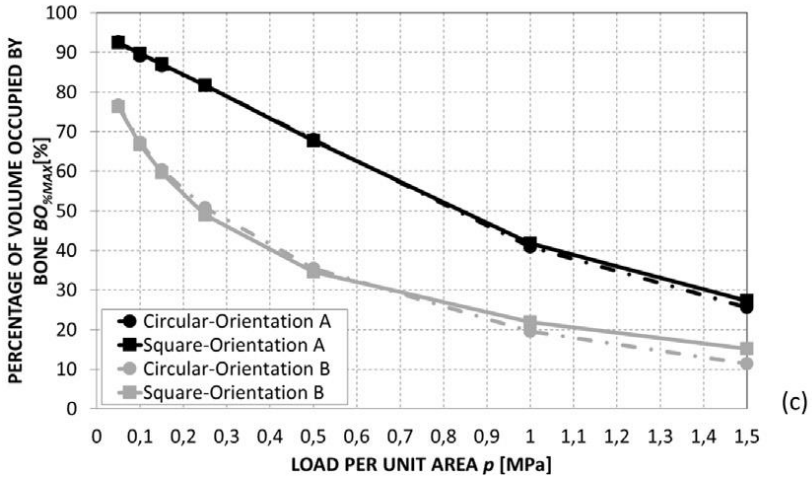

Figure 4-12: Optimization of the diamond unit cell. Values of the optimal diameter *D* (a) and of $BO_{\%MAX}$ (b) predicted for different levels of load.

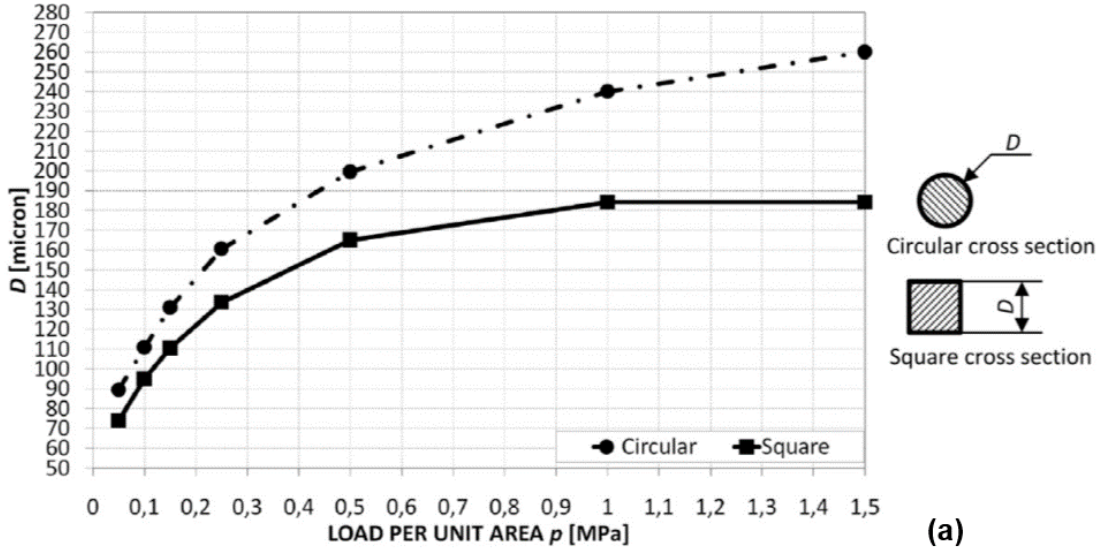

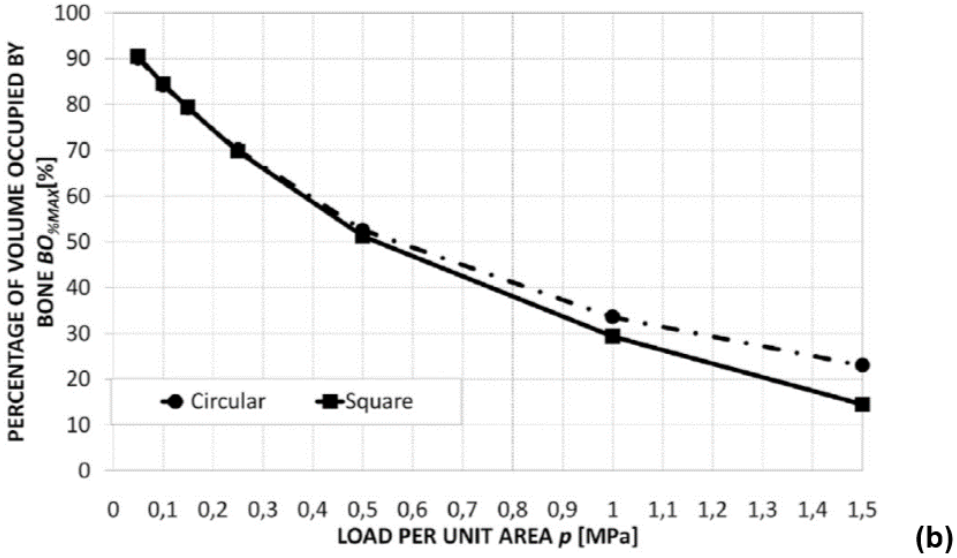

4.4.1 Comparison of different unit cells

The amounts of bone predicted by the proposed optimization algorithm for the different unit cells studied were compared with those obtained in previous studies for other unit cells, namely, a rhombicuboctahedron [165] unit cell including beams with both circular and

square cross section and a hexahedron unit cell with both elliptic and rectangular pores [81] (Fig. 4-13(a)). On the one hand, the $BO_{\%MAX}$ predicted for all the unit cells studied in the case of the circular cross section were compared with those obtained for rhombicuboctahedron with circular cross section and hexahedron with elliptic pores (Fig. 4-13(b)). On the other hand, the $BO_{\%MAX}$ predicted in the case of the square cross section were compared with those computed for rhombicuboctahedron with square cross section and hexahedron unit cell with rectangular pores (Fig. 4-13(c)). In the case of the circular cross section and for very low levels of load, the best unit cell was predicted to be the truncated cube. For medium-low loads, the rhombic dodecahedron produced the largest amounts of bone, while for the highest ones, the hexahedron unit cell with elliptic pores was the best (Fig. 4-13(b)).

A very intriguing behavior was observed for the truncated cube that was predicted to be the best unit cell for low values of *p* and the worst for high levels of load (Fig. 4-13(b)). In the case of the square cross section and for the entire range of load studied, the best unit cell was predicted to be the hexahedron unit cell with rectangular pores (Fig. 4-13(c)). In general, for low values of load, the diamond was predicted to be the worst unit cell, while for high values, the worst unit cell was the truncated cube (Fig. 4-13(c)). This is true in both circular and square cross sections.

For all the optimized scaffolds, the percentage of the volume occupied by the mature bone (i.e. the same quantity so far denoted as $BO_{\%MAX}$), the scaffold itself and other tissues (cartilage, fibrous tissue etc.) were diagrammed in function of the load (Fig. 4-14). For the sake of brevity, the results regarding only the circular cross section were reported. For low values of load, small percentages of volume were predicted to be occupied by other tissues but, for higher values, these percentages became significant especially in the truncated cuboctahedron (Fig. 4-14(a)) and the truncated cube (Fig. 4-14(b)) unit cells. This behavior can be explained by the saturation load that was predicted to be very low just in these unit cells. For all the load cases studied, the smallest volume percentage occupied by a scaffold was predicted for the truncated cube (Fig. 4-14(b)).

Figure 4-13: Comparison of the amounts of bone $BO_{\%MAX}$ predicted to form for different unit cell geometries (a) with both circular (b) and square (c) cross sections. In order to improve the visualization of data, a logarithmic scale was used on the axis of the load.

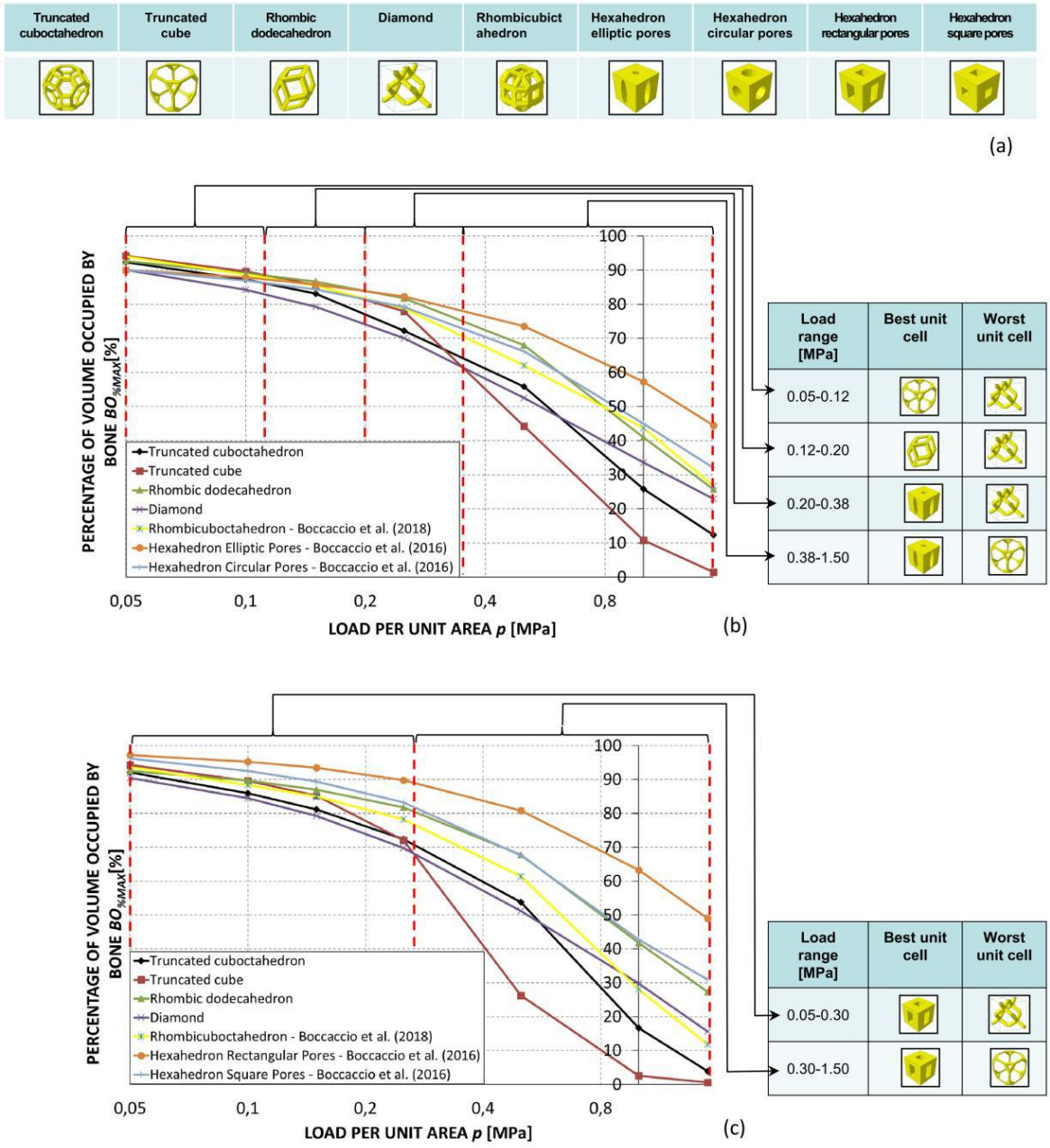

Figure 4-14: Percentage of volume occupied by mature bone, scaffold and other tissues predicted for truncated cuboctahedron (a), truncated cube (b), rhombic dodecahedron (c) and diamond (d) unit cells. For the sake of brevity, only the results regarding the circular cross section are reported. Note. The percentage occupied by mature bone is the same quantity so far denoted as $BO_{\%MAX}$.

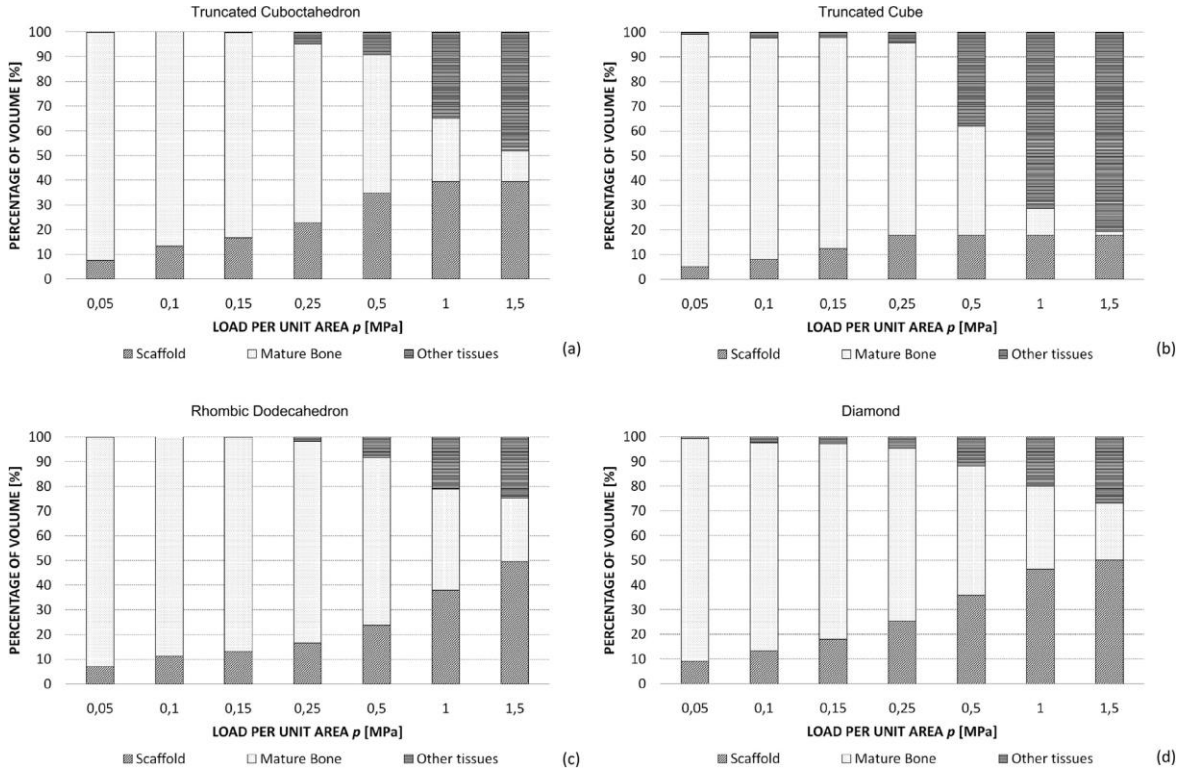

Interesting behaviors have been observed regarding of the mechanobiological performance of the modeled scaffolds and its relationship with the micro-geometrical features that define them. However, *in silico* models based on optimization algorithms present an important limitation. There are as many optimization models in the literature as there are optimized variables. The resulting solution is, therefore, optimal with respect to the variable taken into account, but not optimal in general terms. Mechanical and biological properties measured in terms of physical characteristics, such as surface area, permeability, stiffness, and porosity, are commonly used variables for optimization. However, all these quantities are, in general, not reciprocally independent.

4.5 Conclusions

Beam-based scaffolds made from different unit cells were modelled in this study to evaluate their mechanobiological performance. Results show that such scaffolds allow the formation of large amounts of bone for low levels of load, whereas for high values of load, scaffolds based on hexahedron unit cells are preferable instead. A very intriguing behavior was observed for the truncated cube that was predicted to be the best unit cell for low values of *p* and the worst for high levels of load. For low values of load, the diamond was predicted to be the worst unit cell, while for high values, the worst unit cell was the truncated cube. The study can guide in the choice of the best scaffold to implant in a given anatomic region and provides useful information to the scaffold designers regarding the geometrical constraints and the amount of material needed to build the construct.

From the previous results, it can be theorized that different unit cells could be suitable in different loading ranges of magnitude. Additionally, the general trend is that beams with a circular cross section perform better than those with square cross sections. This fact is consistent with the experimental evidence in which cells prefer curved surfaces for attachment and for developing processes such as proliferation and migration.

As an extension of the scope of this dissertation, we highlight our implementation of a similar procedure to the one used in the present chapter. It was developed to suggest favorable micro-geometrical features from a mechanobiological standpoint for scaffolds with irregular structures. These scaffolds are generated using a bio-inspired design technique to mimic natural structures, such as trabecular bone, which is a highly organized and irregular structure with trabeculae oriented according to the principal stress direction (Annex C).

5. Time evolution scaffold modeling

This chapter describes the implementation of a simplified model to assess the temporal evolution of the newly formed tissue within the scaffold regarding the changes in the biophysical environment. These changes are the result of an increase of the mechanical properties of the differentiated tissue and the physical changes in the scaffold produced by its dissolution. Analyses of stresses in a set of rectangular geometry family, considering and neglecting the scaffold dissolution, were performed to study the structural response within the newly formed tissue.

The third chapter of this dissertation explored the stresses in the newly formed tissue at an early stage of healing, where it can be assumed that there are some “static” conditions, such as no changes in the micro-geometry, in the mechanical properties of scaffold and in the newly formed tissue stiffness. In an effort to address the temporal component of healing inside a scaffold, a simplified mechanobiological model was implemented to represent in a more truthful way the phenomena that occur when the tissue is evolving inside the scaffold. The problem is highly time-dependent since both the scaffold physical properties and the micro geometrical environment are changing constantly due to the material dissolution. However, there are scenarios in which the micro-geometry and properties of an implanted biomaterial remain unaltered or have small changes in large time periods such as permanent implants, metallic scaffolds, etc.

5.1 Representative volume modeling

Following the conditions employed for the RV described in chapter 3, the dimensions were hypothesized to be the same as those defined before, that is, the side of the entire RV is 2.34 mm long and the porosity of the reference geometry is 50%. This porosity is obtained using square pores with a size of 0.39 mm, which are modeled inside a cubic unit cell of 0.78 mm. Since the analysis including the time variable can require computationally much more time than the “static” case [81], a domain reduction was used comparable to the one used in chapter 4. Therefore, taking advantage of the symmetry of RV and following Byrne et al. [62], only one-eighth of this volume has been modelled as a cubic RV of 1.17 mm of side.

Symmetry conditions were established in the three orthogonal internal planes of RV. With respect to the entire RV used in Figure 3-1, the selected one-eighth is enclosed by the dashed line (Figure 5-1). In this way, it is possible to reduce the load ***F*** to one quarter, thus producing the same effect that if the complete load were applied to the complete RV, that in this chapter is, an apparent compression load of 1 MPa produced by a point load of 1.3689 N.

Figure 5-1: Representative volume reduction. Taking advantage of the symmetry, only one-eighth is necessary to represent the entire RV.

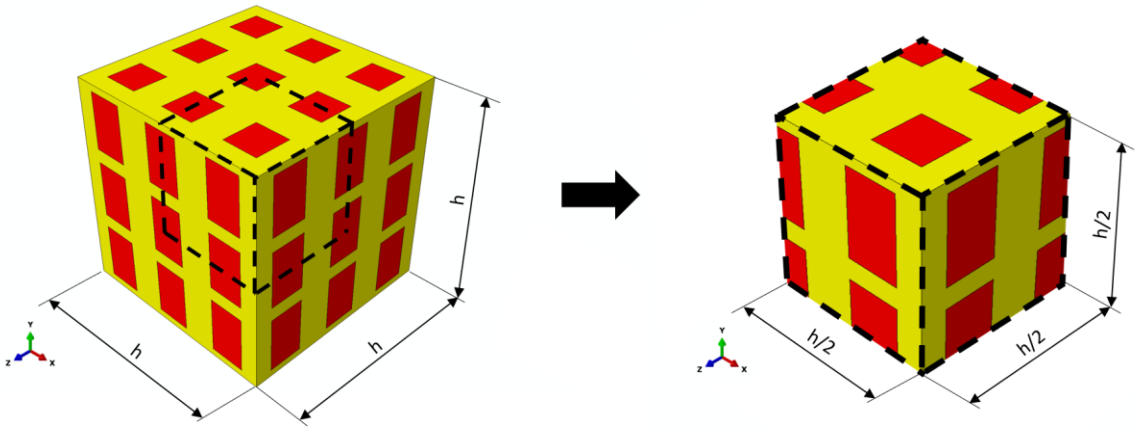

5.2 Geometry setup

Since the reference geometry was selected as a square pore of 50% of porosity, an array of sixteen geometries was proposed. However, as explained in the next sections, the requirements of the model architecture involve the voxelization of the domains that will correspond to the mesh employed in the FEM model. Consequently, the definition of pore dimension will be limited to the resolution provided by the voxels, i.e., the finite elements.

A script was developed to select the finite elements that correspond to each pore geometry defined by the dimensions *X* and *Y* reported in Table 3-3. The selected elements represent the pore geometries used in chapter 3 as closely as possible that the resolution provided

by the voxels allows (Figure 5-2). Despite this drawback, the size of pores was fairly approximated to the pore dimensions of the rectangular set obtained previously.

Figure 5-2: Profile view of voxelized rectangular arrangement geometries.

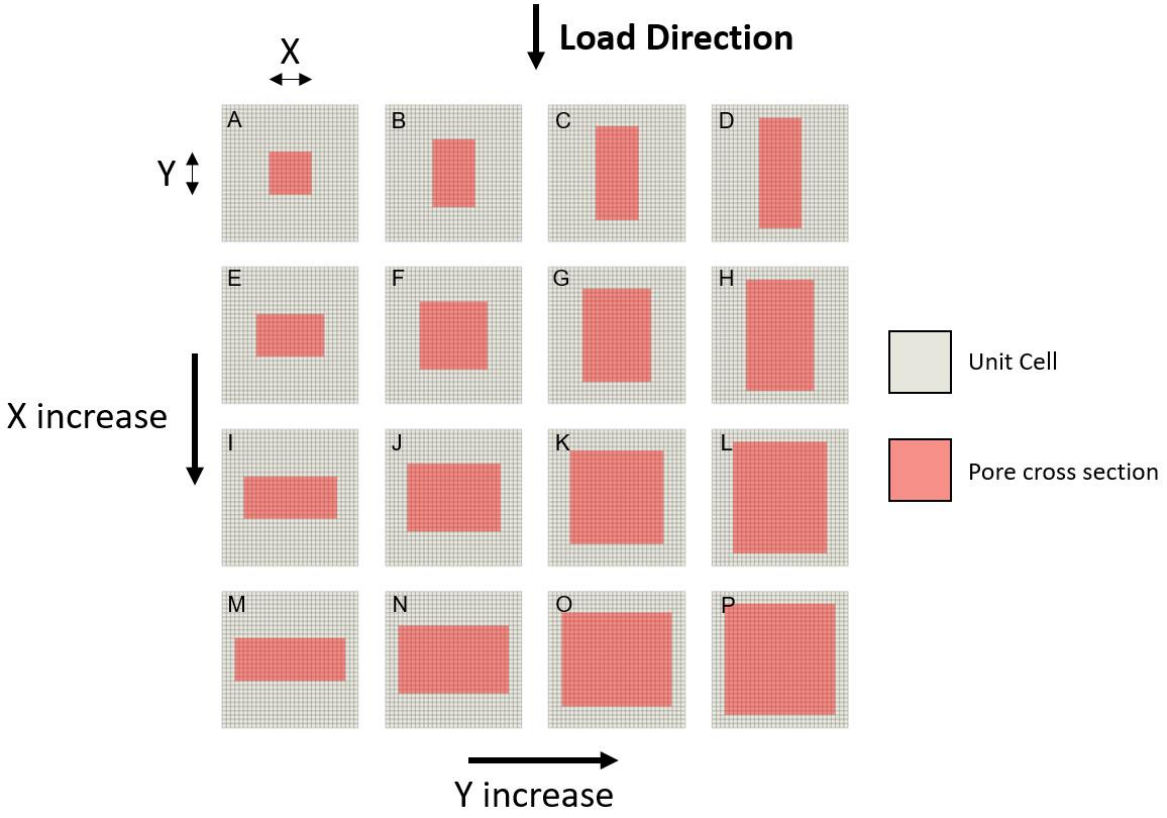

5.3 Mechanobiological approach

The mechanobiological approach proposed by Prendergast et al. was used and described in equation (3.2). However, in order to include an upper bound of the mechanical stimuli ***S*** in the tissue, a new range for fibrous tissue and a condition of necrosis by high stimuli were established according to Sandino and Lacroix [183] together with the boundaries reported in [184]. The new resultant inequalities of the solution of equation (3.2) with the new ranges are:

$$6 < \boldsymbol{S} \qquad \text{Necrosis}$$

$$3 < \boldsymbol{S} \leq 6 \qquad \text{Fibroblasts (Produce Fibrous tissue)}$$

$$1 < \boldsymbol{S} \leq 3 \qquad \text{Chondrocytes (Produce Cartilage tissue)}$$

$$0.267 < \boldsymbol{S} \leq 1 \qquad \text{Osteoblasts (Produce Immature bone tissue)}$$

$$0.01 < \boldsymbol{S} \leq 0.267 \qquad \text{Osteoblasts (Produce Mature bone tissue)}$$

$$0 < \boldsymbol{S} \leq 0.01 \qquad \text{Bone resorption}$$

The stimulus $\boldsymbol{S}$ calculated, and hence the predicted tissue, is for each entire element. One of the most relevant hypotheses in previous chapters is that the tissue phenotype can be predicted for each element, despite the fact that the elements are tetrahedrons with different size and ratios, produced by the mesh process of the complex geometries studied. This approach can arise difficulties when modelling the temporal behavior of the cells, such as the migration of cells and the change of the mechanical properties produced by the synthesis of ECM by the differentiated cells, which often implies an increase in properties, for instance, the Young's modulus.

To address the previous issue and looking for uniformity in the elements to guarantee independence of the mesh process in each geometry, the studied RV is composed of voxels defined by cubic finite elements C3D8RP of a fixed side of 24 μm. This strategy brings possibilities to link the finite element domain with a cell domain composed of a lattice of cells to model cellular processes, such as cell proliferation and movement.

The cell domain was programmed in Matlab and is composed of simple cubic lattice structures. In these structures, each cell is separated from the others by a distance of 24 μm, that is, the side of the cubic finite elements, so that in this way the centroid of each voxel coincides with each cell position [185]. Therefore, each element has a cell inside it and the lattice will have as many cells as elements the RV has (Figure 5-3). Although this is a simplistic way to model it, these facts are consistent with the size of the MSC reported in [186] and it can be assumed that a cell and its ECM are both included in each finite element [62].

Figure 5-3: Neighboring in the lattice and cell domains of the highlighted cell-element position.

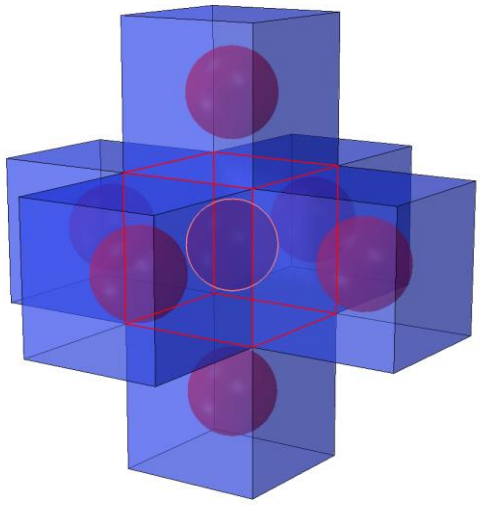

5.4 Cell behavior modeling

Some mechanisms of dispersal of cells have been discussed in the literature. The most used mechanisms by researchers are diffusion models, which have a deterministic nature. An alternative used by some authors is the random walk, which is the probabilistic description of the trajectory of an entity (particle, body, cell, animal etc.) from successive random steps. This approach seems interesting, since it exhibits the stochastic nature of the cell dispersal, often observed experimentally [187].

The parallel existence of both the cells and finite elements domains used is suitable to model the cell behavior in a discrete form. The biological behavior of cells included in the modelling was the cell proliferation and movement, both modelled using a non-biased random walk approach, that is, without a preferent direction. MSC are seeded randomly at the first iteration of the simulation in the lattice in 1% of the total of the initial available space for cells in the granulation tissue [62]. Then, the proliferation and migration process start with a rate of one per iteration until all the available spaces are colonized [187]. Each iteration represents one day of the time course of healing.

MSC have a maturation time of seven days and before this time, it is not possible to differentiate them. After the MSC reach the maturation time, they can be differentiated into the different phenotypes established in the mechanoregulation ranges contemplated in this chapter. The differentiation probability is controlled by a rate of 30% after reaching the maturation time in MSC [62]. Once cells are differentiated, they can also begin proliferation and migration processes. Although the de-differentiation, trans-differentiation and apoptosis processes can occur in fracture healing, they were not considered in this work.

The cell can move or keep the position in the lattice in each iteration if there are available adjacent positions, which are defined by a 6-neighborhood connectivity that allows six new possible states of the cell, as depicted in Figure 5-4. Proliferation by mitosis occurs in a similar way, the mother cell divides and creates a new cell that can adopt, from the possible states, an adjacent position to the original one, which can be occupied or not after the division [49].

Figure 5-4: Cell migration and proliferation scheme.

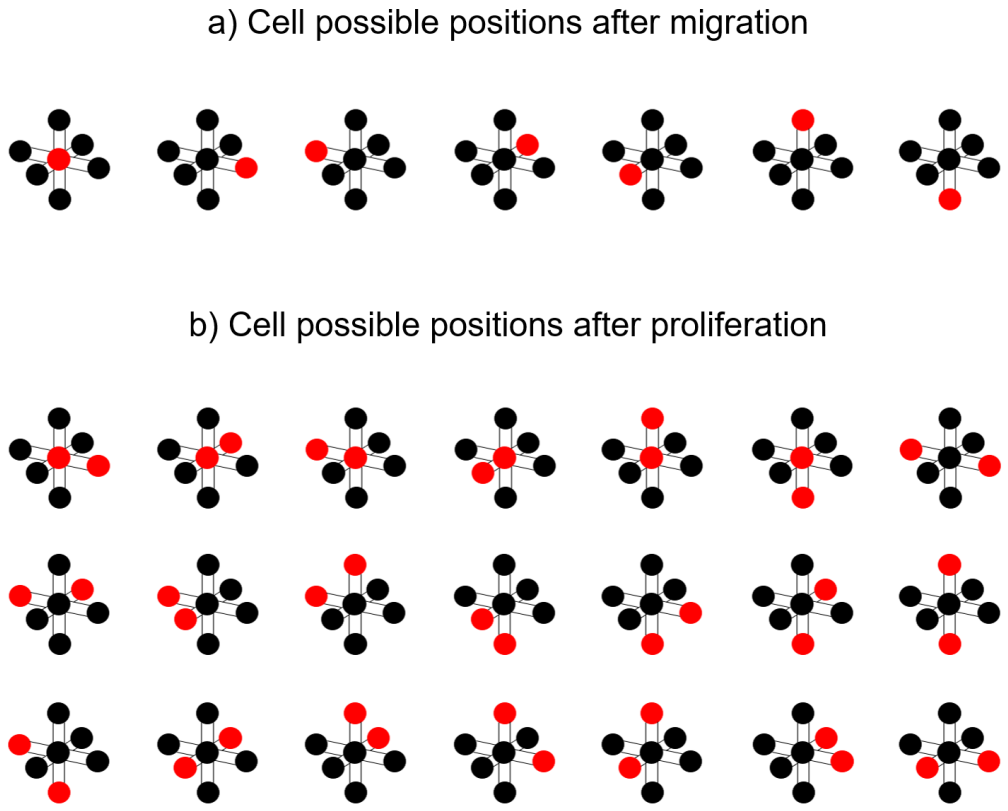

Looking for the consistency of the cell lattice with the biological reality, it is possible to verify that if the entire domain reaches the saturation of cells, i.e., all existent positions are filled, there will be 110592 cells in the RV or 69000 cells/mm^3 approximately. This value is consistent with the density of cells in mature bone tissue according to the ranges established in the literature, which can vary between 32000 and 93000 cells/mm^3 [188]. In the fracture healing process, if MSC reach a density higher than 100000 cells/mm^3, a saturation effect can be produced, where the only way in which the cell can survive and proliferate is by increasing the size of the callus [71].

The time window in which the healing process is simulated in this work was twelve weeks, which is consistent with the time of inflammation and reparative phase in a normal bone healing process in humans and the time used in *in vivo* animal models for assessment of scaffold architectures [138]. The remodeling phase exhibits different biological and biomechanical events, spending most of the time in the full process of healing that can last from months to years. For this reason, this phase is not considered in this work.

5.5 Material properties in the tissue domain

There are two types of materials in the domain: The scaffold material and the tissue material. The variation of mechanical properties of tissue obey to the tissue stiffening that occurs in the normal development over time after cells synthesize ECM and it begins its maturation. This stiffening was simulated using a smoothing procedure to avoid sudden changes in the tissue stiffness that are not physiologically reasonable. The procedure consisted in the computation of the average ten previous values predicted $\bar{E}$ and an exponential law [189], as described in equations 5.1 and 5.2, respectively:

$$\bar{E} = \frac{1}{10} \sum_{it=-9}^{it=n} E_i \tag{5.1}$$

where E_i is the Young's modulus for the each i tissue phenotype and *n* is the present iteration.

$$E_i = K_i e^{\beta_i t} \tag{5.2}$$

where K_i and β_i are the parameters that control the shape of the exponential curve for each i phenotype and t is the iteration [189]. The assumption of the mechanobiological approach in which each cell and its ECM is contained in each element allows avoiding the use of the mixture law often used in previous studies to determine the mechanical properties of the elements with different cells inside and enhance the accuracy in which the phenomenon is observed.

The time in which Equation (5.2) reaches the value of the predicted tissue is sixty days according to [62], [164]. After this time, the maximum value is maintained, that is, the value of the predicted phenotype reported in Table 3-1. Constants K_i and β_i for each phenotype were determined according to these values. Only the Young's modulus was calculated using the exponential law. Other properties were computed using only the average of the ten previous historical values, similarly to equation (5.1).

If degradation of the elements of scaffold occurs, there will be new space available for tissue growing and the degraded element will be filled by granulation tissue, thus acquiring its properties and becoming available space for MSC colonization. The change of the properties of the scaffold material due to dissolution will be discussed in the next section. Both resorbed elements by low stimuli and elements in which necrosis are predicted by excess of mechanical stimuli will adopt the mechanical properties of granulation tissue but these elements will not be available for new cells.

5.6 Degradation modeling

The mechanical properties used throughout this dissertation were those of the type found in biomaterials such as polymers. These materials have interesting possibilities to vary its properties, for instance, by modifying the molecular weight or the monomers and copolymers that compound them.

The dissolution of these polymers produces alterations in different physical properties as discussed in chapter 2. Principally, there are two mechanisms in which the different polymers degrade: surface erosion and bulk erosion. In the first mechanism, the biomaterial is eroded in its surface layer by an agent and in the second one, all the entire volume is attacked by the agent. Both of them are produced by chemical reactions.

As discussed in chapter 2, the model proposed by Adachi et al. [66] is enough for considering the degradation phenomenon. For simplicity purposes, this model was used to represent the scaffold degradation in which it is assumed that the molecular weight loss due to hydrolysis depends on the content of an aqueous solution in the domain, governed simply by a diffusion equation. However, this approach is very simple and disregards the possible loading effects, the stochastic nature of the phenomenon, and the crystallization and autocatalytic effects proper of the polymer degradation. Despite this, the modular architecture of the proposed computational framework will allow including the programming of different degradation mechanisms, as reported in [104], [114], [168], [185], [190], or experimental curves that represent the molecular weight loss, since it is strongly related to the mechanical properties of the polymers.

Adachi's model is characterized by the use of the following set of coupled equations: (5.3), (5.4) and (5.5):

$$\boldsymbol{E_s}\big(\boldsymbol{W(t)}\big) = \boldsymbol{E_{s0}}\,\frac{\boldsymbol{W(t)}}{\boldsymbol{W_0}} \tag{5.3}$$

where E_s is the Young's modulus of scaffold material that depends on molecular weight W in time t, E_{s0} is the initial Young's modulus and W_0 is the initial molecular weight. The decrease rate in molecular weight due to hydrolysis $\dot{\boldsymbol{W}}$ depends on the local water content $\boldsymbol{c}$:

$$\dot{\boldsymbol{W}}(\boldsymbol{c}) = -\boldsymbol{\beta c} \tag{5.4}$$

where $\boldsymbol{\beta}$ is a constant of the material. The rate of water content $\dot{\boldsymbol{c}}$ is governed by the following diffusion equation:

$$\dot{\boldsymbol{c}} = \boldsymbol{\alpha \nabla^2 c} \tag{5.5}$$

where $\boldsymbol{\alpha}$ is the diffusion coefficient in the bulk of the polymers. Solving the previous equations for the scaffold elements, the model computes their molecular weight and compares them with a threshold value. If the molecular weight is lower than the threshold

value, the element is considered completely degraded, loses its mechanical function and becomes a void space.

For the implementation of the previous model in this work, a diffusion analysis for the RV domain was performed in Abaqus® for each iteration of the time window observed to solve equation (5.5) with α =4x10^{-4} mm^2. In this way, it is possible to determine the properties of the scaffold material elements modified by the loss of the molecular weight due to hydrolysis process using equations (5.3) and (5.4) with E_{s0}=1000 MPa, $\beta = 4000$ (dimensionless), and $W_0 = 70000$ g/mol, in the case of elements that are not degraded according to [66]. If the element degrades, that is, the molecular weight reaches the threshold of 10000 g/mol, it becomes a granulation tissue element and an available space for a new MSC that eventually will start the tissue differentiation process. Then, the mechanical properties of the element will be governed by equations (5.1) and (5.2).

In the degradation model presented here, there is an important supposition: The diffusion analysis neglects the change of the boundaries in the domain of aqueous solution, assuming that the solution domain is the initial pore topology. However, the process is much more complex since each released volume could become part of the aqueous solution, hence a new source of water diffusion. This issue is defined mathematically as a moving boundary problem [191]. Nevertheless, it is not expected that the supposition about the domain affects notably the result. Further research in this topic is needed to verify the effects of the moving boundaries. Moreover, it should be emphasized that the degradation modeling presented in this chapter do not attempt to represent the complexity of the chemical reactions involved in the degradation process. The intention of this model is to predict the physical alterations in the scaffold such as changes in geometry and mechanical properties, produced by the interaction with an aqueous solution.

5.7 Algorithm description

Previous sections discussed the different modules that conform the architecture of the model. The model starts with the selection of the scaffold geometry from the studied array and then the initial conditions of the simulation are defined. Subsequently, the lattice domain is created and then seeded with MSC in 1% of the selected randomly positions of

the structure. Afterward, the finite element domain is created and, depending on whether the scaffold is designated as biodegradable or not, a diffusion analysis is performed.

An iterative procedure starts after the scaffold dissolution behavior is determined, that is, if it occurs or not. Cellular processes initialize and occur as detailed in previous sections. Then, in each iteration a biphasic poroelastic FEM analysis was performed with the updated mechanical properties obtained from previous days simulated. Finally, the entire process starts again until the final day is reached (See Figure 5-5).

The same stress measurements from chapter 3 were computed in each iteration to analyze the behavior of the stress within the tissue. However, unlike chapter 3 outcomes, in this model the properties of the tissue are evolving over time, so the Python scripts were modified to obtain data in each iteration. The absolute and relative amount of each tissue phenotype were calculated and stored similarly to equations 3.4 and 3.5 to observe the different effects in the tissue produced by the different scaffold geometries in each iteration.

Since mechanical properties of the voxels are changing in each iteration, the global stiffness of the entire tissue-scaffold system is changing in time. To determine the value of the RV stiffness in the load direction and be able to see its evolution in the course of simulation, the coefficient C_{22} of the effective stiffness tensor C_{ij} is computed using equations 5.6, 5.7 and 5.8 [192]. This coefficient is one of the most vital parameters to reflect the mechanical performance in the scaffold [164].

$$C_{ij} = \frac{\bar{\sigma}_{ij}}{\bar{\varepsilon}_{ij}} \tag{5.6}$$

where $\bar{\sigma}_{ij}$ and $\bar{\varepsilon}_{ij}$ are the average stresses and strains, defined in the entire domain by:

$$\bar{\sigma}_{ij} = \frac{1}{V_{RV}} \int_V \sigma_{ij}(x, y, z) dV \tag{5.7}$$

$$\bar{\varepsilon}_{ij} = \frac{1}{V_{RV}} \int_V \varepsilon_{ij}(x, y, z) dV \tag{5.8}$$

where σ_{ij} and ε_{ij} are the stress and strain in the domain, respectively.

Figure 5-5: Brief algorithm flowchart.

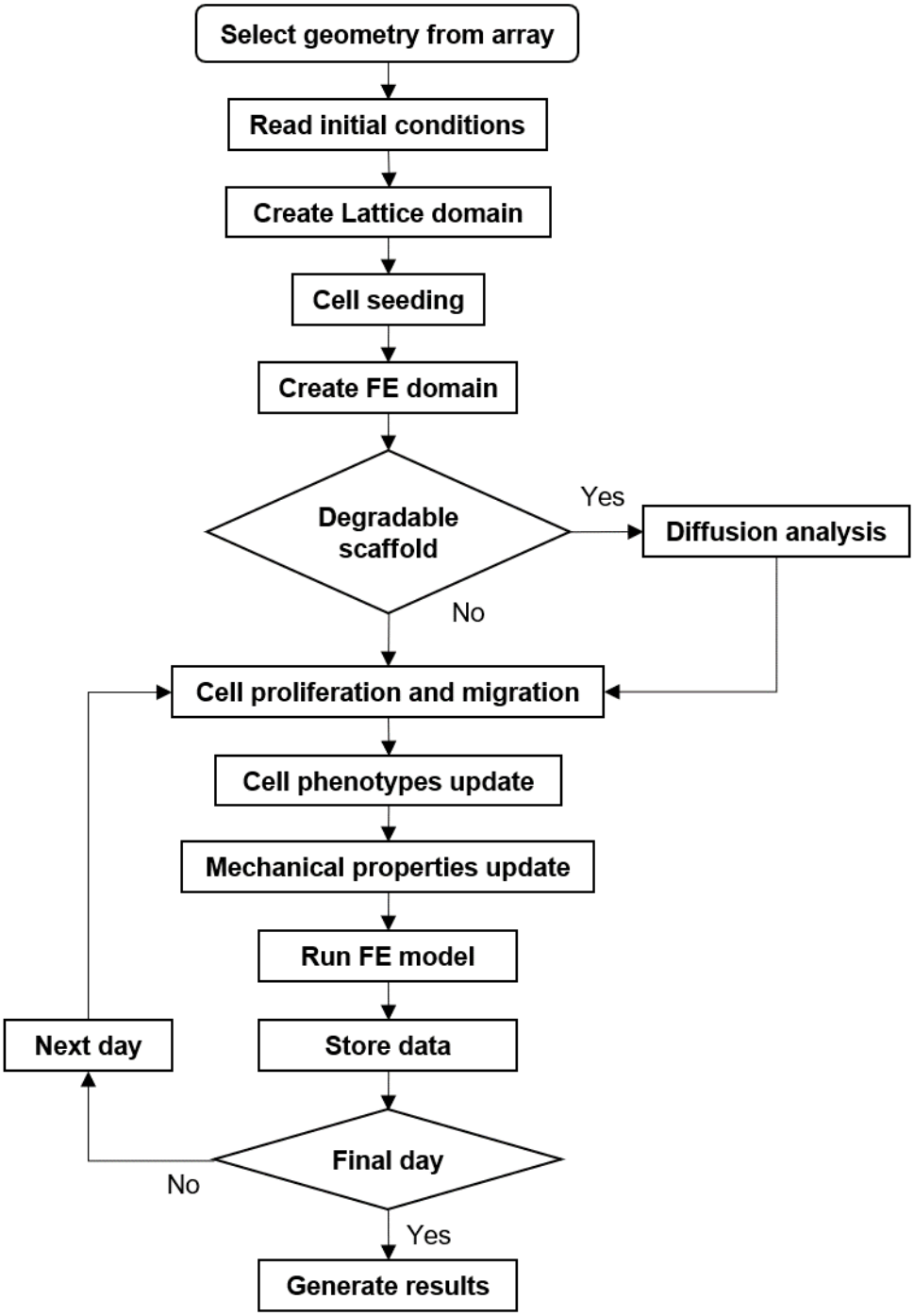

5.8 Verification

To verify the similarity between the results obtained in the early stage of the tissue and the model presented in this chapter, Figure 5-6 shows the overplotted stress distribution histograms of both the reference geometry from chapter 3 and the one obtained in this chapter. It is possible to observe that both geometries induce an equivalent stress distribution in the newly formed tissue although different kinds and sizes of elements were used to discretize these geometries. Statistics from both histograms were similar: VMMean 3.16E-3 MPa for the static model, initial VMMean 3.06E-3 MPa for the time evolution model, and the same VMMedian 2.70E-3 MPa value in both cases. C_{22} parameters also exhibit similar values: 280 for the static model vs. the initial value of 272 from the time evolution model. The differences between the values were around 3% and are reasonable due to both discretization techniques and the particularities of the models [193], [194].

Figure 5-6: Stress distributions histograms overplotted for **F** geometry. Histogram of the reference geometry from chapter 3 is colored in orange and the one obtained in this chapter is colored in blue. The intersection between both appears in brown.

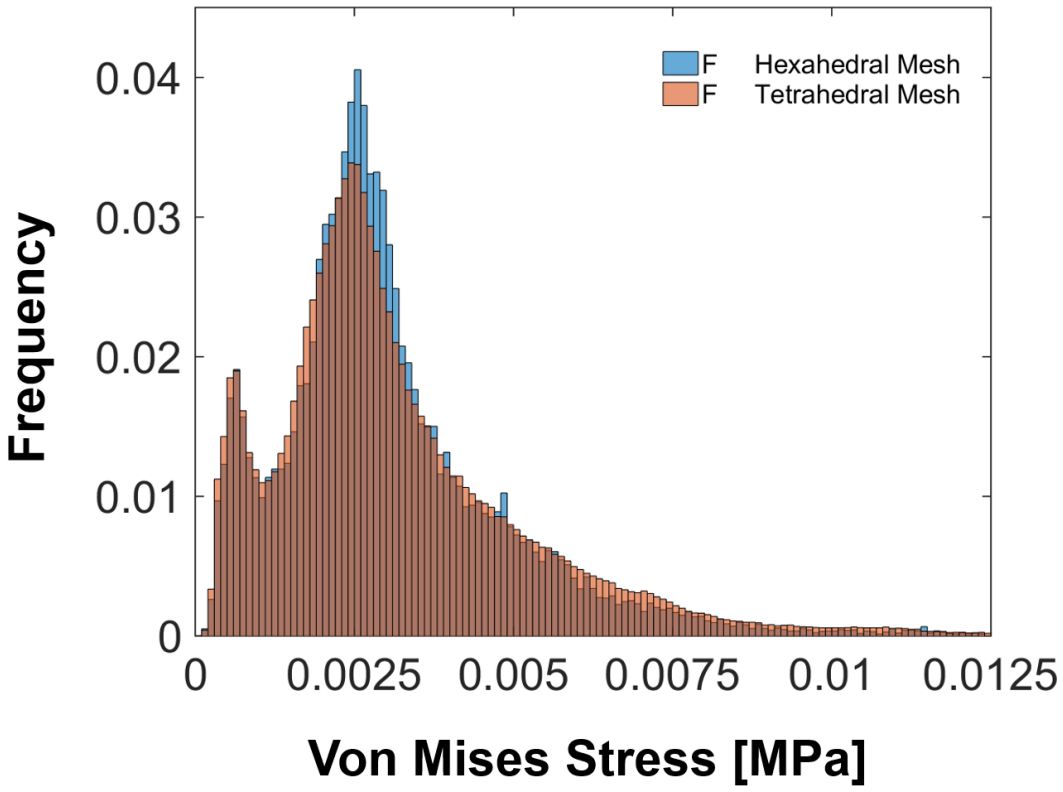

Several simulations were carried out to determine their variability, since there is a stochastic component in each simulation provided by the cell seeding and the individual behavior of cells, which depend on probabilistic activities. The square 50% reference geometry was used for the runs, with load=1 MPa and without degradation for simplicity purposes (Table 5-1).

Table 5-1: Comparison of different runs of the algorithm under the same conditions for the reference geometry.

RUN	Bone (%)	Cartilage (%)	Fibrous (%)	Resorption (%)	Necrosis (%)	Final VMMean (MPa)	Final C_{22}
1	46.76	3.23	0	0	0	1.058	1093
2	46.66	3.33	0	0	0	1.058	1087
3	46.76	3.23	0	0	0	1.057	1090
4	46.76	3.23	0	0	0	1.057	1088
5	46.79	3.20	0	0	0	1.058	1093
6	46.81	3.18	0	0	0	1.060	1095
7	46.69	3.30	0	0	0	1.057	1090

As expected, despite the stochastic components of the simulation, the system has a trend at the end and the variability in each run exhibits differences by less than 0.15% approximately in each final tissue phenotypes, 3E-3 MPa in the final VMMean and 8 in the final C_{22} index. This fact is reasonable because the mechanical environment is not changing abruptly even when there is a high number of cells already differentiated. However, these cells still do not reach the maximum stiffness level of the exponential law, therefore, it is expected that the mechanical environment changes notably due to the influence of the newly formed tissue inside the scaffold only after sixty days of simulation.

The conceptual implementation developed here corresponds largely to the works by Prendergast and Byrne. In order to verify the consistency of the proposed model, feasible scenarios with results reported in the literature were implemented using it with the parameters employed by [49], [62], [184]. Scaffolds of square geometries with porosities of 30%, 50% and 70% were simulated by the model described in this chapter in order to compare the phenotype outcomes with those provided for the same geometries by Byrne et al. for 1 MPa, 2 MPa and 4 MPa compression loading conditions. Variation of cell size was necessary to reach each porosity, and had values in the range described by [186].

The scaffold degradation was turned off in this test since the degradation mechanism implemented here is different to the one presented by Byrne et al., which had a linear form while here it was governed by a diffusion equation emulating some features of the real phenomenon.

Figure 5-7 shows a comparison of the percentages of phenotypes used in this model and those published by Byrne et al. The comparison shows that the results presented here have good agreement with Byrne's results. However, differences are expected, since there are different conditions in the modeling of both studies, such as the possible slight differences in size and structure, constants, details of the mesh and others not clearly stated, and of course the absence of mixture law that was replaced in this model by cells per each finite element.

Figure 5-7: Comparison between the present model and results by Byrne et al. [62].

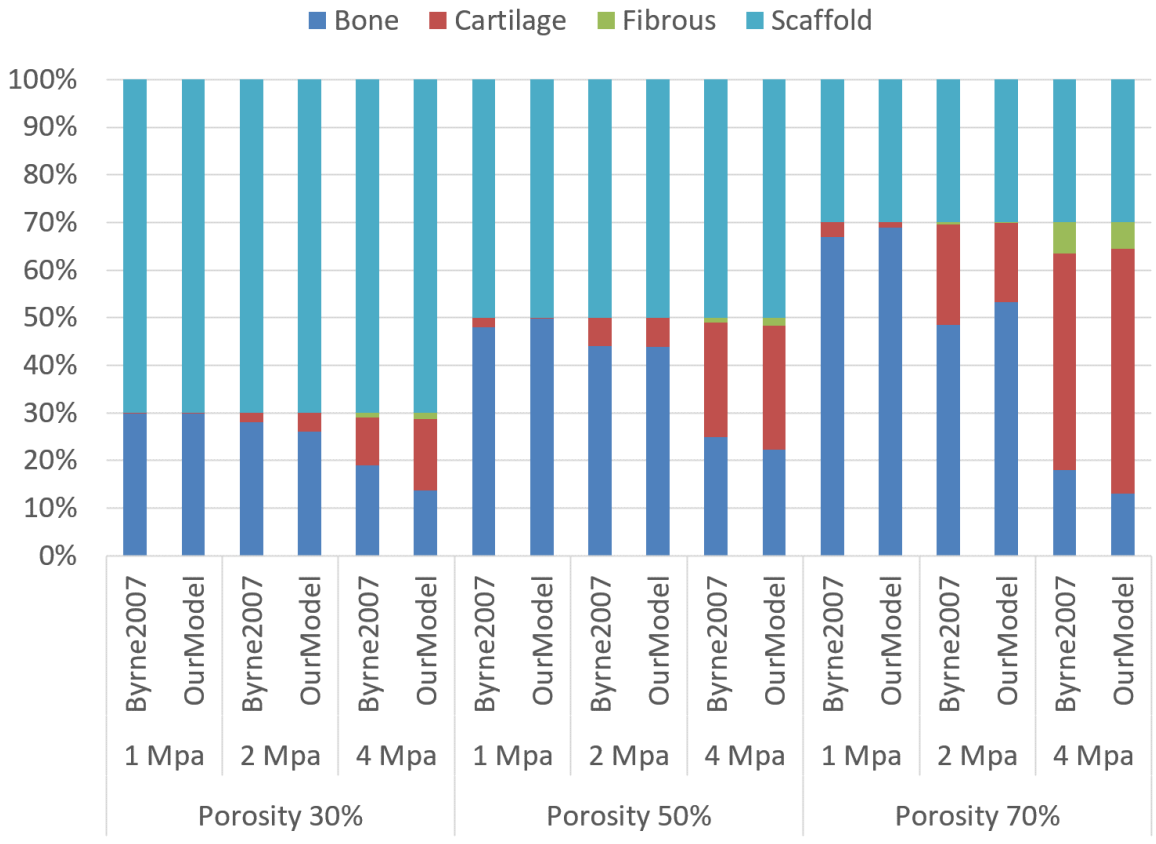

After verifying the consistency of our model with Byrne's results, it was interesting to verify the consistency of the predictions of the model with the experimental results available in the literature. An important limitation for the *in silico* research of scaffolds is the lack of data about the performance in *in vivo* and *in vitro* scenarios with detailed data. Despite this, the experimental results provided by Entezari et al. allow some comparisons with the proposed *in silico* framework. Entezari control architecture was useful to determine the size of the RV studied in this work. Although it is not exactly equivalent to the geometries of the scaffold modelled here (Figure 5-8), it is possible to make some analogies to compare the values produced by our model with the results obtained experimentally.

Figure 5-8: Left: Control geometry used by Entezari. Adapted from [138]. Red square is the region of interest used to idealize the square reference geometry. Right: Square reference geometry.

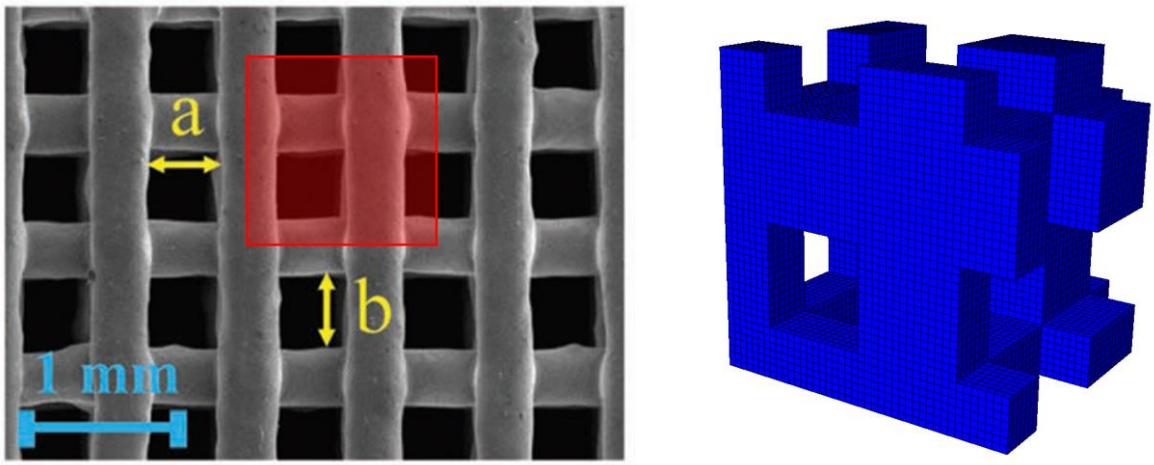

The first comparison regards the stiffness of the scaffold prior to implant. The square 50% geometry used as reference along this dissertation matches conveniently with the control architecture (Architecture A) used by Entezari et al. that has a conventional square mesh-like pattern presented in Figure 5-8 [138]. Material properties of the scaffold were modified to match those reported by Entezari, who used a ceramic material with Young's modulus of 33 GPa and Poisson ratio of 0.3. All the remaining properties were the same used for the modeling of polymers in previous chapters.

The four architectures studied by Entezari prior to implantation remain in a range of stiffness of 12-16 GPa approximately and all have porosities around 50%. The reference geometry implemented in this thesis exhibits a stiffness of 9.84 GPa approximately, that is, underestimation regarding the experimental comparison (Figure 5-9).

Figure 5-9: Comparison of stiffness prior to implant from Entezari's architectures with the stiffness of the reference geometry. Adapted from [138].

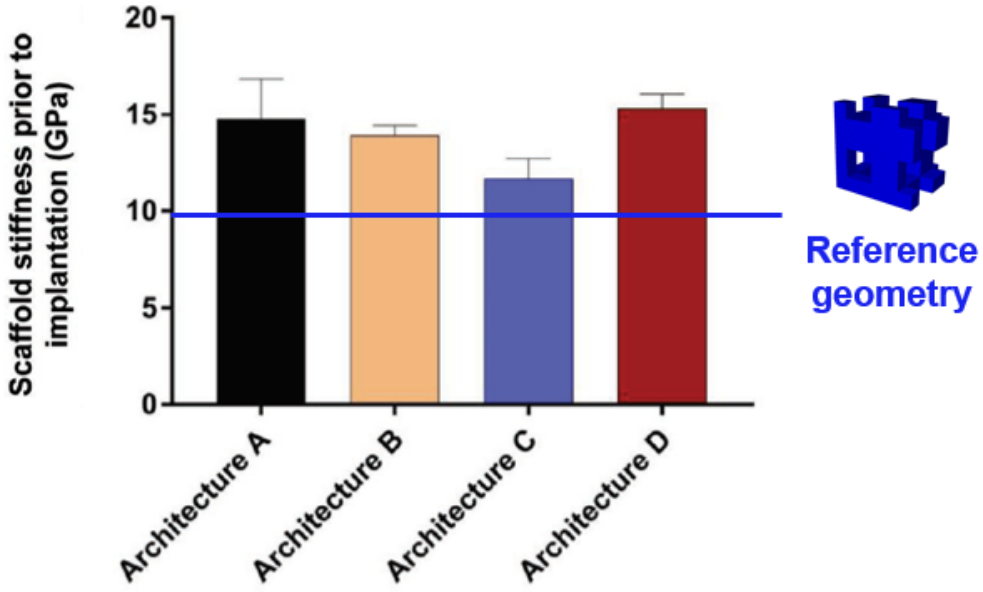

In the study developed here, one of the most helpful results obtained by Entezari et al. is the bone volume/available volume index, which allows comparisons between the experimental architectures with our reference geometry. However, there is an important limitation since there is no specific loading condition in [138]. To solve this issue, it is possible to find in the literature a range of apparent stress results of the superposition in different load cases of daily activities in human calvaria (0 - 0.9 MPa) [195]. On the other hand, external loading schemes have been used in the ranges of 1 MPa - 2.8 MPa.

From the range presented in [195], it was hypothesized a set of 3 values of apparent compressive stress: low (0.25 MPa), medium (0.5 MPa) and high (0.75 MPa). Using these values in the reference geometry model and with the mechanical properties of the scaffold prior to the implantation, the index in Figure 5-10 was obtained and compared with that reported experimentally.

Figure 5-10: Comparison of Bone volume/Available volume index from Entezari's results with the reference geometry in hypothesized low, medium and high loads, considering properties of the scaffold prior implantation and properties hypothesized post implantation.

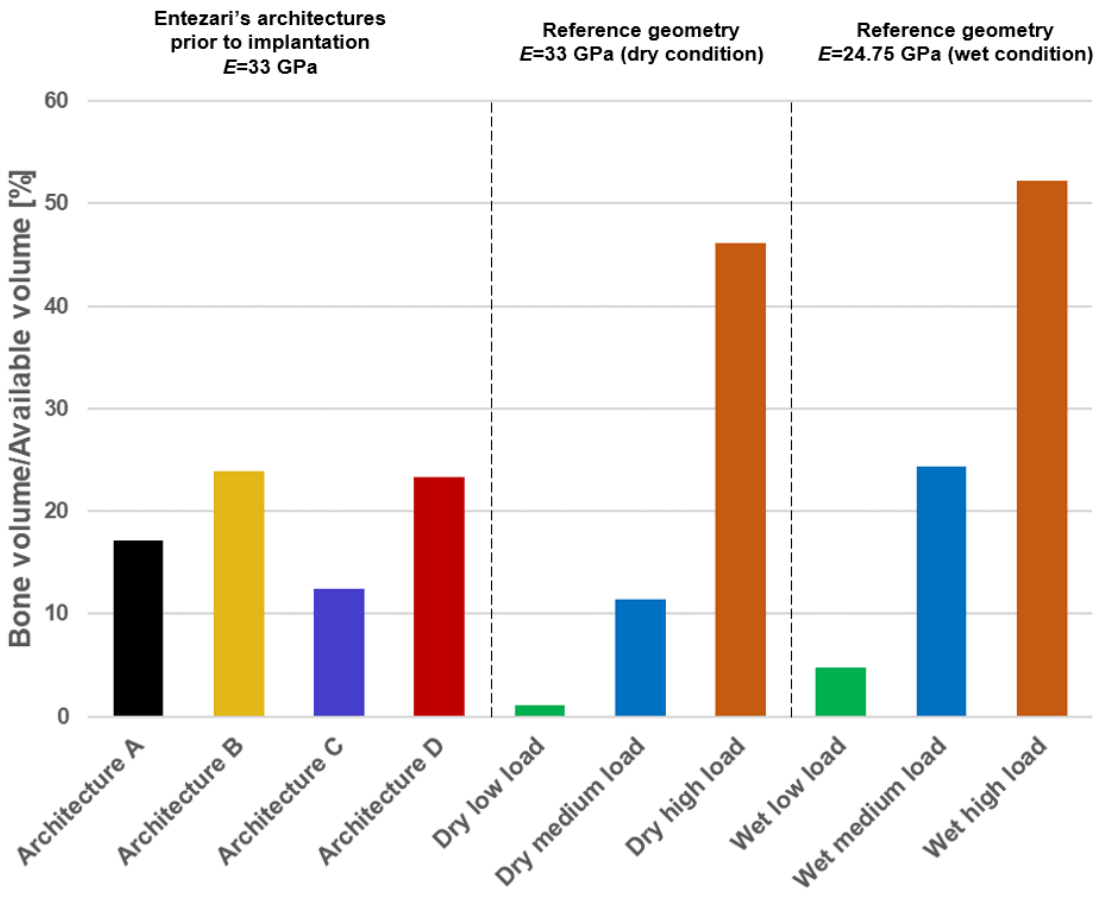

For medium and high loads, Figure 5-10. shows that the index is close to the half of those reported experimentally. Low load exhibits a low amount of bone, which is expected considering that the Young's modulus was 33 times the one used in chapter 3 and the load was also reduced in a percentage of 75%, which led to a substantial reduction of the mechanical stimuli.

It is reported that the mechanical properties of the scaffold decrease when it is implanted. In bioceramics similar to those employed by Entezari et al., the reduction of stiffness reaches up to 60% of its dry value [196]. Using a hypothetical reduction of 75% of the value of Young's modulus prior to implantation, results for a hypothetical wet scaffold were obtained.

The results obtained from the hypothesized scenario showed that the model is in a reasonable range of tissue prediction regarding the experimental scenario. However, there are many uncertain data around the experimental setup that made difficult the definition of the conditions for modeling the phenomenon.

An important supposition was that the bioceramic material is not losing its properties and geometry while the tissue is growing during the time window. However, in practice, the action of a dissolution effect is expected after implantation, although it is not noticeable.

5.9 Results

5.9.1 Rectangular scaffolds without degradation

The dimension of the pores for each geometry in the arrangement and their respective porosities are listed in Table 5-2. Initial (IVMMean, IVMMedian) and final (FVMMean, FVMMedian) von Mises statistics and effective normal stiffness C_{22} were calculated to analyze the evolution in time of the mechanical properties of the tissue-scaffold system.

Table 5-2: Initial and final von Mises mean and median stresses on the newly formed tissue domain of rectangular pore arrangement for 1 MPa and initial and final effective normal stiffness for each scaffold-tissue system in the rectangular arrangement without considering the degradation.

Geometry ID	X (mm)	Y (mm)	Porosity (%)	IVMMean (MPa)	IVMMedian (MPa)	FVMmean (MPa)	FVMMedian (MPa)	Initial C_{22}	Final C_{22}
A	0.243	0.243	23.19	2.77E-03	2.34E-03	1.3022	1.0183	530	1105
B	0.243	0.390	31.24	2.43E-03	2.02E-03	1.3113	9.40E-01	491	1269
C	0.243	0.536	39.3	2.19E-03	1.78E-03	1.3424	9.16E-01	464	1514
D	0.243	0.633	44.67	2.05E-03	1.64E-03	1.3739	1.204	452	1771
E	0.390	0.243	40.62	3.44E-03	3.01E-03	1.0863	1.0378	304	960
F	0.390	0.390	50	3.06E-03	2.70E-03	1.0574	0.9397	272	1090
G	0.390	0.536	59.37	2.74E-03	2.37E-03	1.0439	0.8522	253	1225
H	0.390	0.633	65.62	2.55E-03	2.16E-03	1.0577	0.7680	245	1383
I	0.536	0.243	60.69	5.61E-03	4.61E-03	0.9176	0.6845	135	358
J	0.536	0.390	68.74	5.48E-03	4.99E-03	0.9410	0.8209	115	486
K	0.536	0.536	76.8	5.16E-03	4.67E-03	0.9113	1.0596	104	610
L	0.536	0.633	82.17	4.87E-03	4.39E-03	0.9182	1.1180	99	647
M	0.633	0.243	75.53	1.05E-02	8.09E-03	0.4923	0.1829	57	78
N	0.633	0.390	81.24	1.15E-02	1.02E-02	0.4161	0.1906	46	61
O	0.633	0.536	86.96	1.16E-02	1.07E-02	0.3231	0.2136	39	50
P	0.633	0.633	90.77	1.12E-02	1.01E-02	0.2695	0.2277	36	46

Despite the voxel discretization, the pore parameters and porosities obtained under this approach were fairly close to those obtained in chapter 3. Similarly, initial von Mises statistics and the effective normal stiffness C_{22} indicators obtained were close to those obtained for the geometries modeled through the CAD environment.

For each increment in time window, histograms of von Mises stress were obtained for each geometry in the rectangular arrangement. For simplicity purposes, Figure 5-11 shows the histograms of 3 time points: days 1, 42 and 84 for the reference geometry **F** under a compression load of 1 MPa. As expected, the distribution is comparable to that obtained in chapter 3 since the geometry and loading conditions are similar in both cases.

Figure 5-11: Histograms of von Mises stress in 3 time points for **F** geometry.

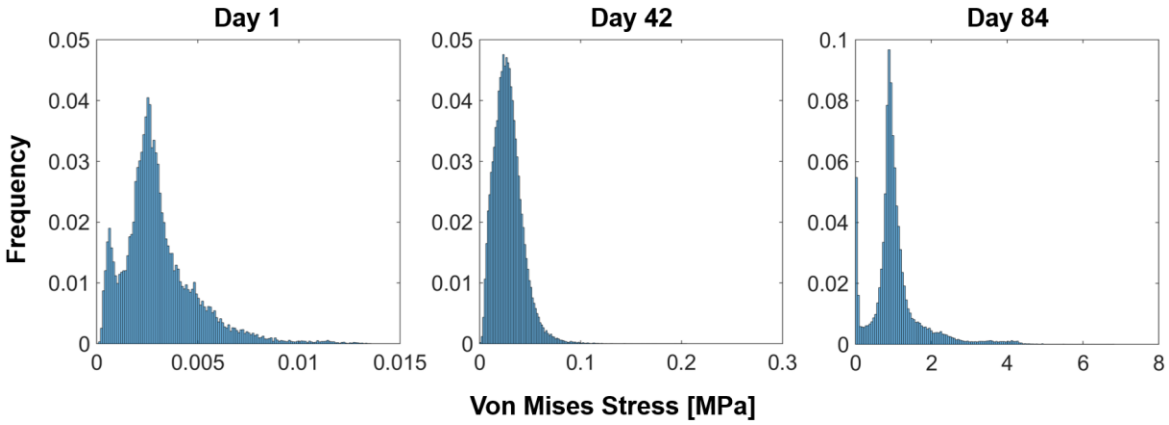

There is a very intriguing behavior in which the distribution become unimodal during the time evolution from the twenty days until the fifty days and then return to a similar pattern such as the start shape, but with mode or highest frequency close to a value of von Mises of 1 MPa.

Figure 5-12 shows the initial von Mises stress distribution for each geometry in the arrangement. Once again, as expected, the distributions are similar to those observed in Figure 3-6 in chapter 3 and the same behaviors occur as dimensions *X* and *Y* increase, that is, spreading of the von Mises values in the elements as dimension *X* increases and the crowding of the values around the central region as *Y* dimension increases.

Figure 5-12: Normalized initial stress distribution for each geometry in the arrangement.

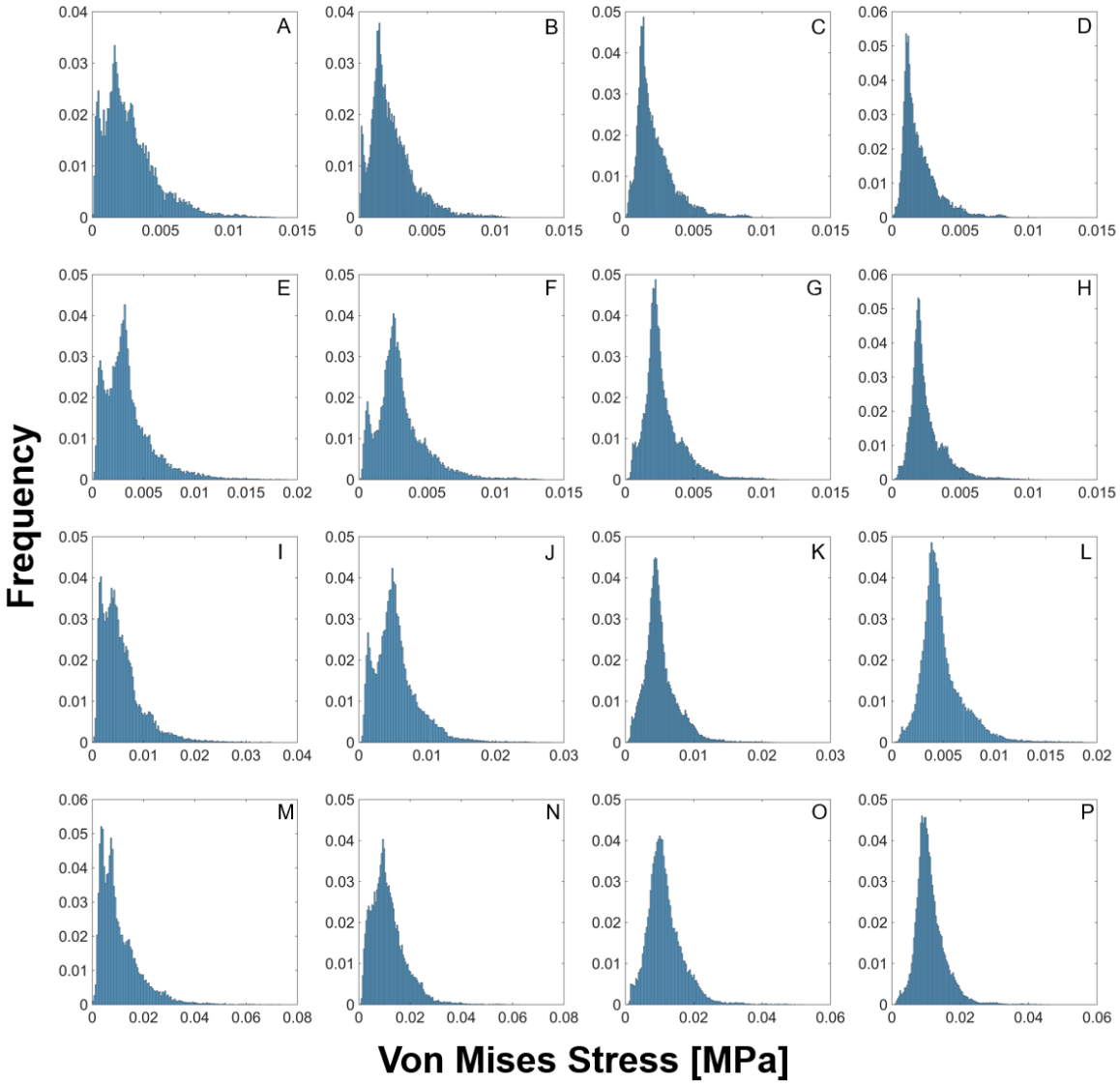

Figure 5-13 shows the final von Mises stress distributions obtained at the end of the twelve weeks period. Each row of the arrangement has different features in their histograms. First row **ABCD** exhibits 3 regions with stress concentrations. A common feature that can be observed in all geometries is a concentration of low stresses, which corresponds to the volume occupied by soft tissues since these tissues are not bearing the load. A second stress concentration of the first row occurs around a von Mises value of 1 MPa, that is, as the macroscopic load exerted in the system, and this value corresponds to the mode in **B**,

C and **D** geometries. In **A** geometry the mode is close to zero values, thus suggesting the presence of more soft tissues than in the other geometries in the row.

Figure 5-13: Normalized final stress distribution for each geometry in the arrangement.

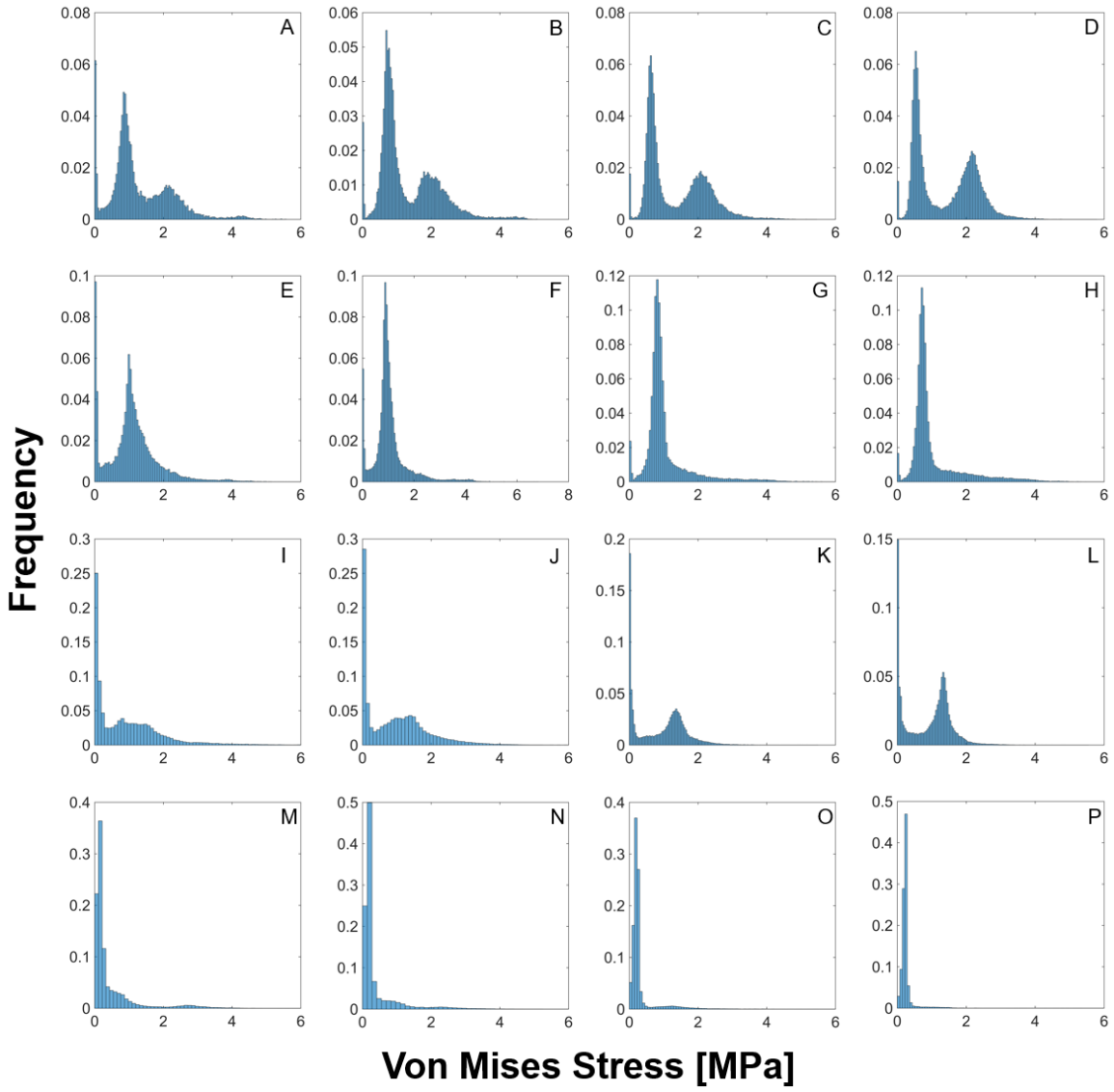

A remarkable feature observed is that, as *Y* dimension increases in rows **ABCD** and **EFGH**, the number of elements with low stress values are reduced, i.e. elements differentiated to soft tissues. Moreover, a major concentration also occurs in the peak around the 1 MPa value and the *Y* dimension increases as well. This suggests that at the end of the tissue stiffening, more elements are bearing the apparent compressive load exerted on the

system. The second row exhibits bimodal shape histograms and keep the features discussed for the first row.

The temporal evolution of the von Mises stress mean for the reference geometry **F** is shown in Figure 5-14. The increase of this von Mises statistic is related to the rate equation behavior, which also influence the stiffness of all models. An exponential behavior such as the pure rate equation would be expected, but reach the maximum values of stiffness for the differentiated phenotypes in different times produces instead an exponential behavior such as the pure rate equation, a behavior with S-shape, corresponding to the logistic growth typical from the dynamics of biological populations [197].

Figure 5-14: Evolution of Von Mises stress mean in time for **F** geometry.

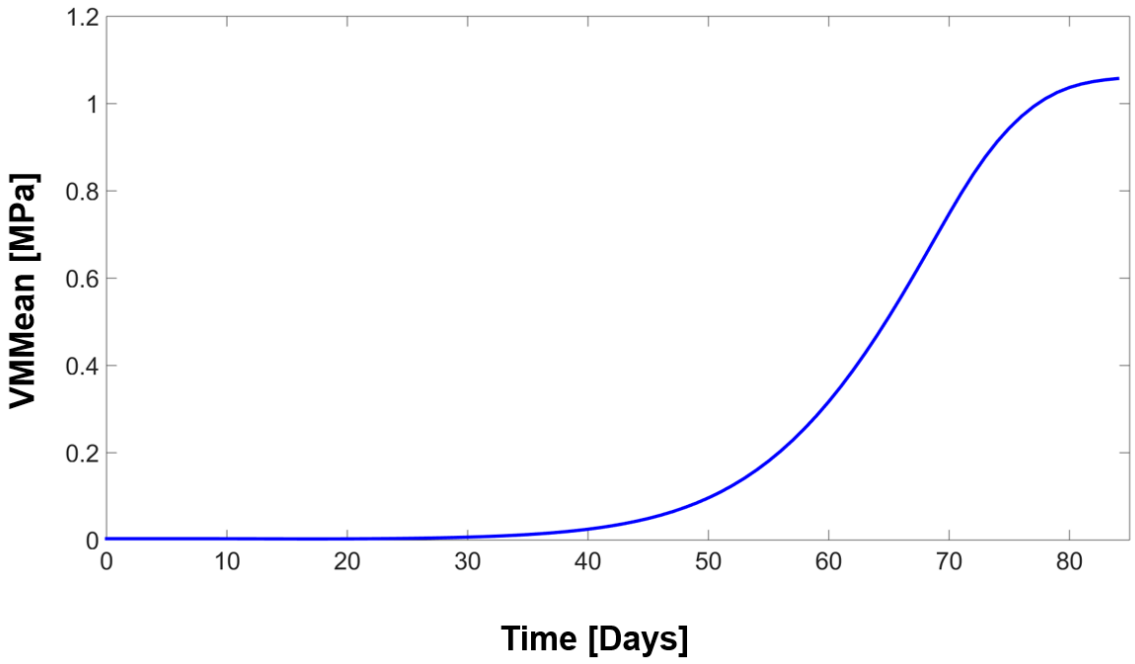

Von Mises stress starts with low values, since the newly formed tissue is not supporting load and the scaffold biomaterial carries out the loading instead, bearing it almost in its totality. When the newly formed tissue becomes stiffer, that is, MSC differentiate into bone cells and take some time so that the synthesized tissue gets stiffer, this tissue starts to carry the load and then, the stresses in the tissue increase. This explains why as the relative amount of bone increases in the row, the final VMMean increases too. A comparison

between the temporal behavior of VMMean for each geometry in the arrangement is shown in Figure 5-15.

Figure 5-15: Evolution of Von Mises stress mean in time for each geometry in the arrangement. The curve corresponding to the current position of the arrangement is plotted in blue, while the rest of geometries are plotted in grey.

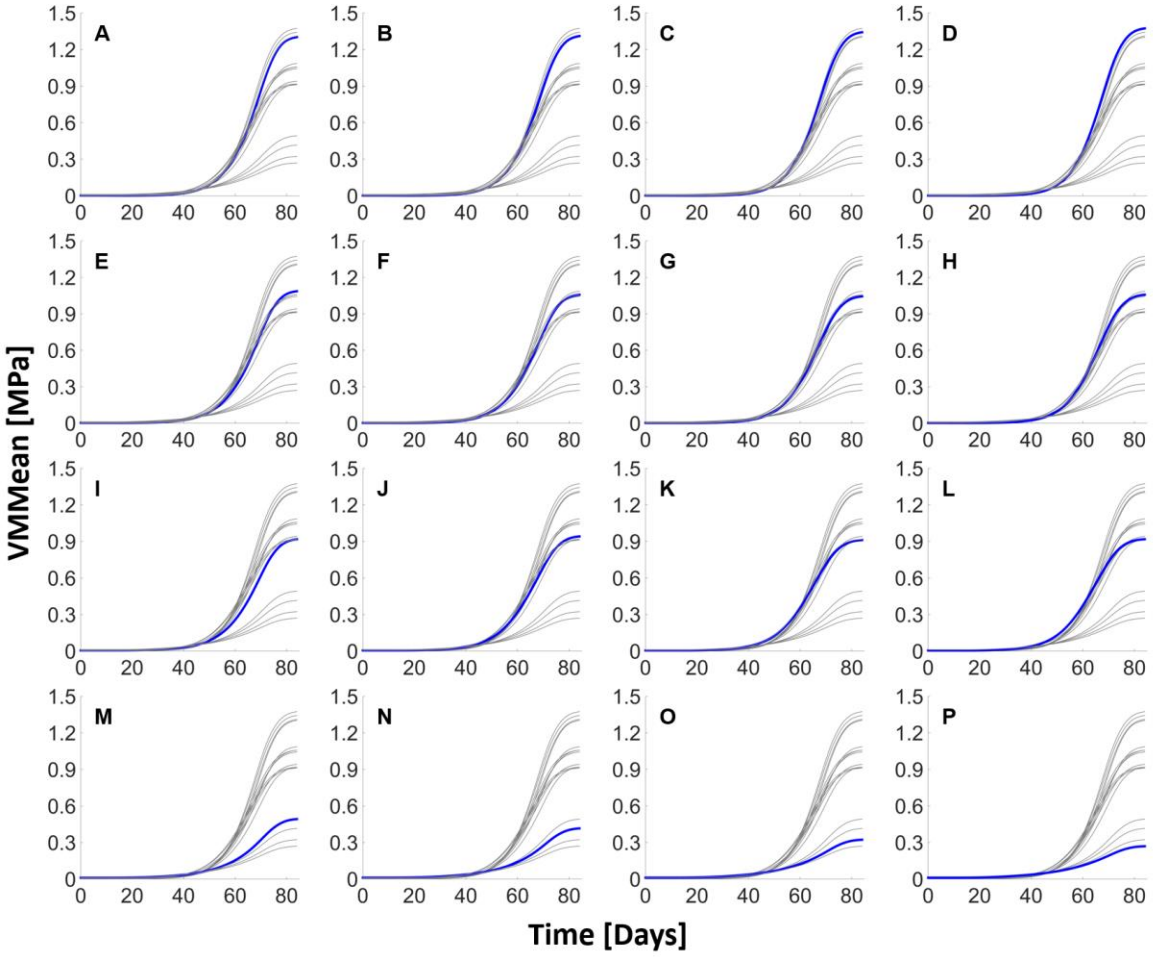

Each geometry develops different amounts of tissues that finally lead to different final stiffness in the tissue-scaffold system. Figure 5-16 describes the effective normal stiffness behavior in time of each geometry, all influenced by the behavior of the rate equation. The stiffer scaffold-tissue system was the **D** geometry, while the lowest was the **P** geometry. The higher stiffness values of the system are consistent with the stiffness values reported for FCC scaffolds by Sanz-Herrera et al. [64].

Figure 5-16: Effective normal stiffness evolution in time of each geometry in the arrangement. Current position is plotted in blue, while the rest is plotted in grey.

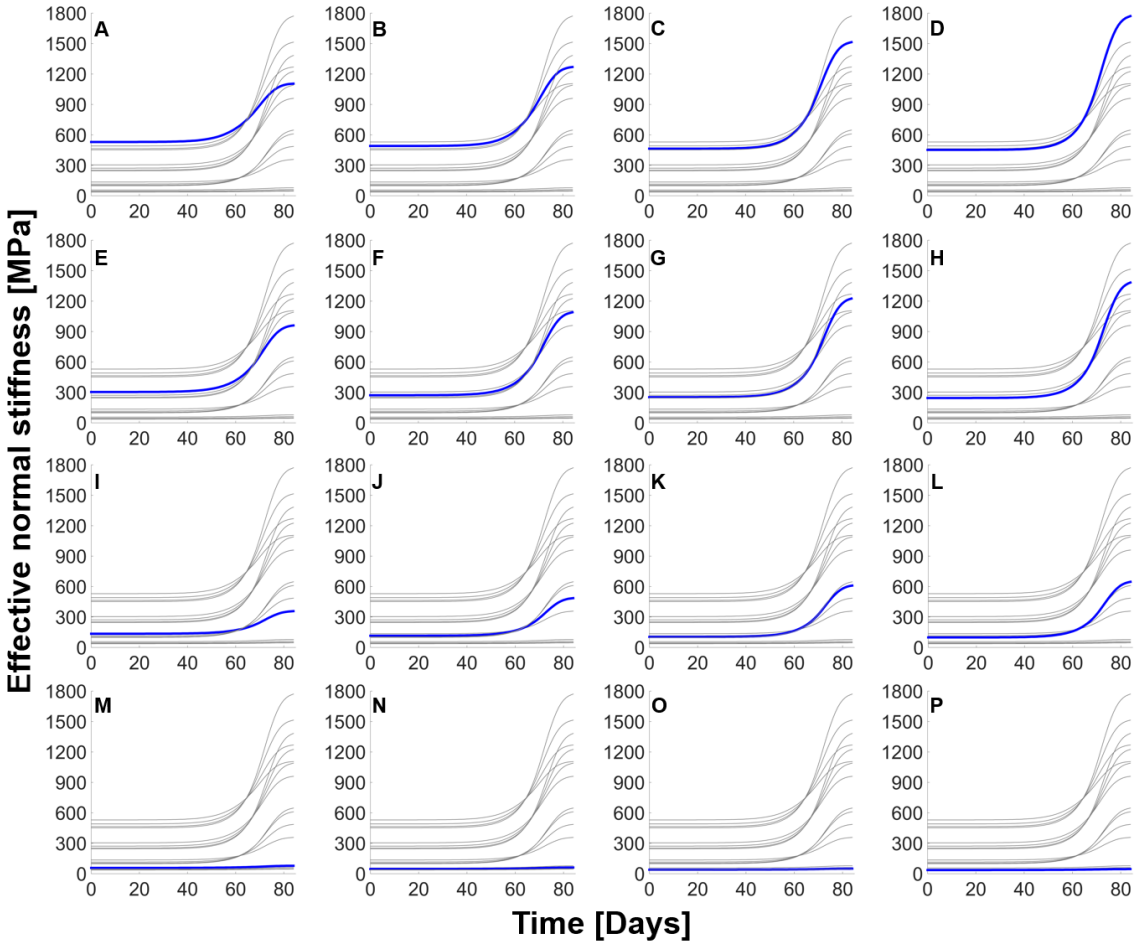

Maximum principal stress absolute histograms in 3 time points show curious behaviors (Figure 5-17). As in the von Mises histograms, there is a tendency of the positive and negative portions of the histogram to become unimodal as time passes. Finally, the negative portion exhibits two peaks, one close to zero values, which is related to the elements that do not differentiate into bone and one close to -1 MPa, corresponding to the nature of apparent compressive loading with 1 MPa value. A very low amount of elements with positive maximum principal stress absolute is observed for this geometry. As usual in the comparisons with the results from the rectangular arrangement of chapter 3, the initial maximum principal stress absolute distributions obtained from the time evolution model for all geometries are consistent with those estimated previously (Figure 5-18).

Figure 5-17: Histograms of the maximum principal stress absolute in 3 time points for **F** geometry.

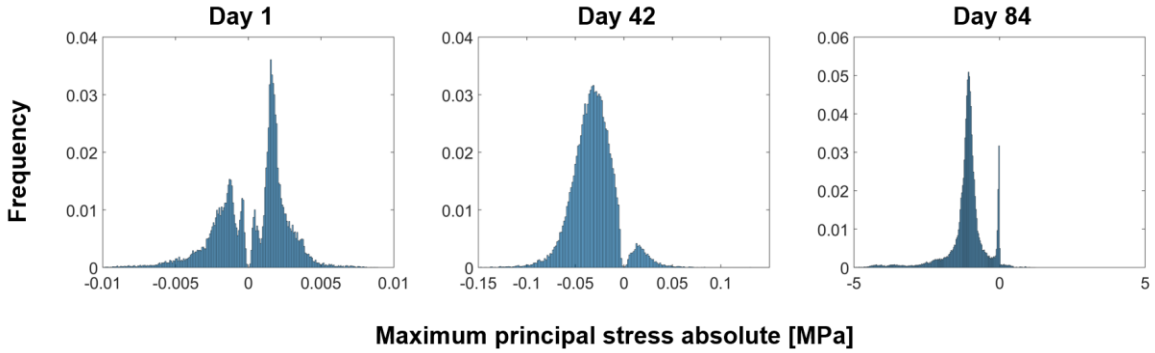

Figure 5-18: Initial maximum principal stress absolute histograms for each geometry in the arrangement.

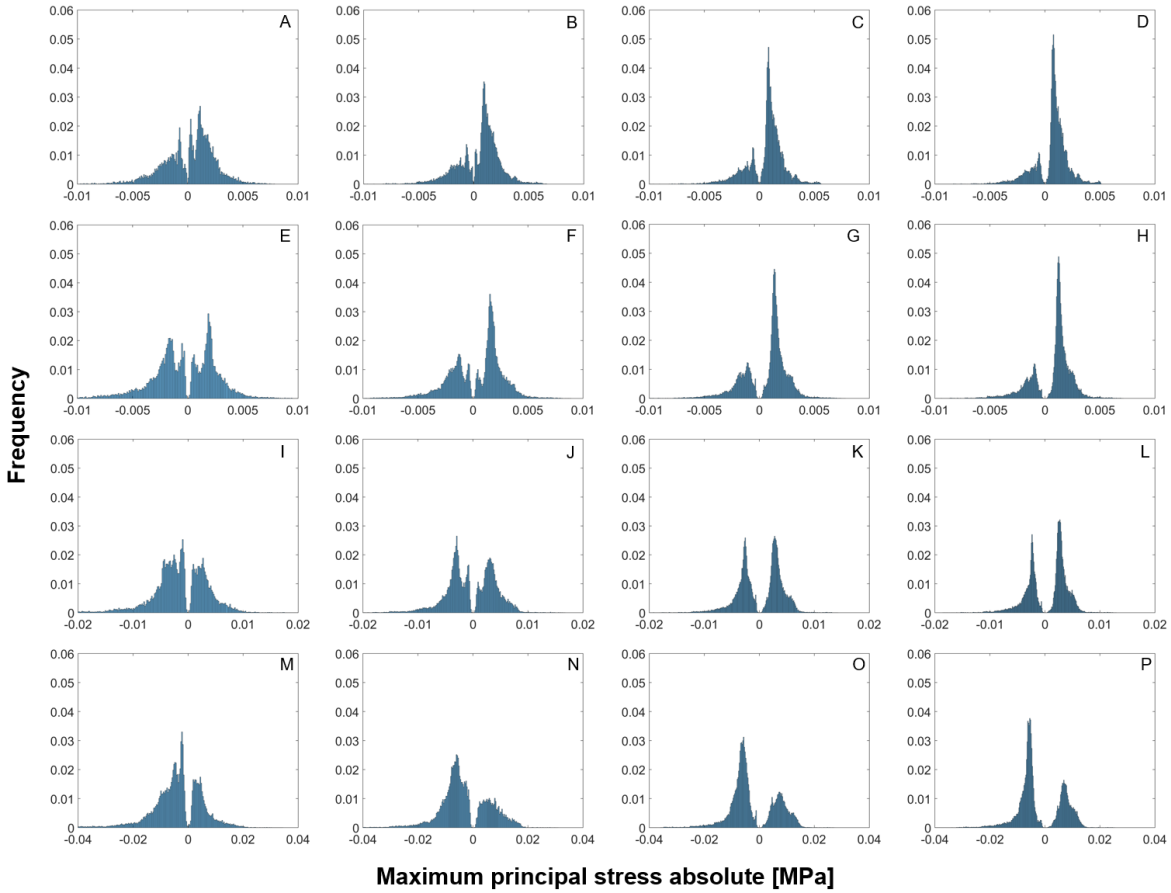

For the final maximum principal stress absolute distributions for the geometries in the rectangular arrangement (Figure 5-19), it was found an interesting characteristic. **ABCD** and **EFGH** rows exhibit a predominance in the stresses in the negative portion of the histogram, which implies that the bone tissue developed in these geometries is successfully assuming the load in the scaffold-tissue system.

Figure 5-19: Final maximum principal stress absolute histograms for each geometry in the arrangement.

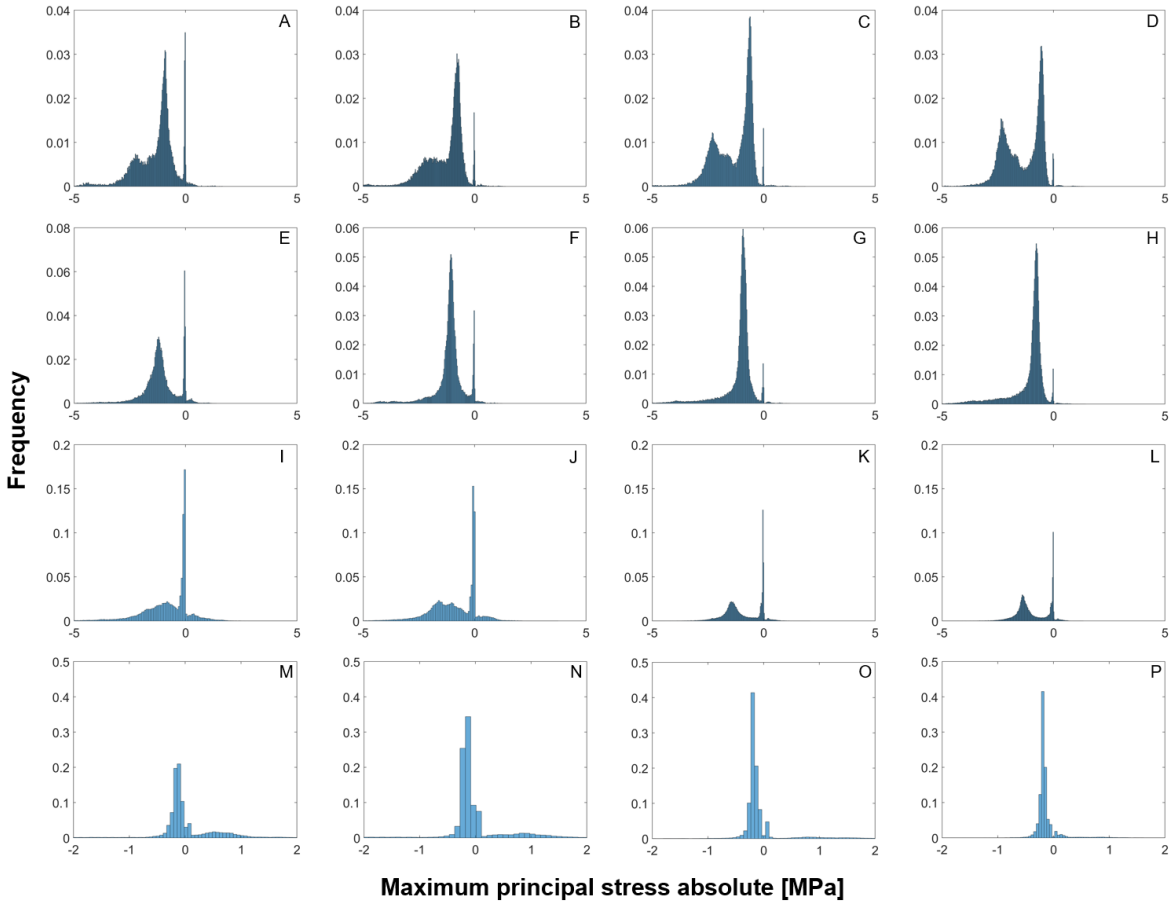

To observe the relations between the pore dimension parameters and stresses in the formed tissue inside the scaffold, final von Mises mean statistics were used to generate the corresponding response surface, since it has better goodness of fit than the mean (Figure 5-20). Similarly, final von Mises stress mean were used to show the relation between the stresses inside the differentiated tissue and the relative amount of bone (Figure 5-21).

Details of goodness of fit for both the response surface and the curve fitting for final von Mises mean can be found in Annex A.

Figure 5-20: Response surfaces of pore parameters vs. final von Mises mean of rectangular arrangement for 1 MPa.

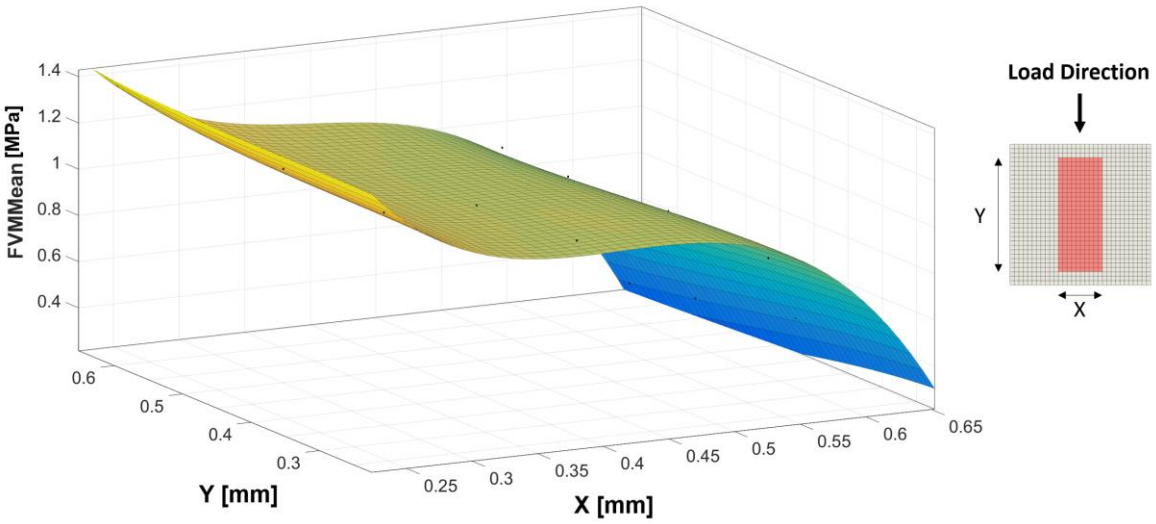

Figure 5-21: Curve fitting between the relative amount of bone predicted (REL) and the final VMMean for 1 MPa.

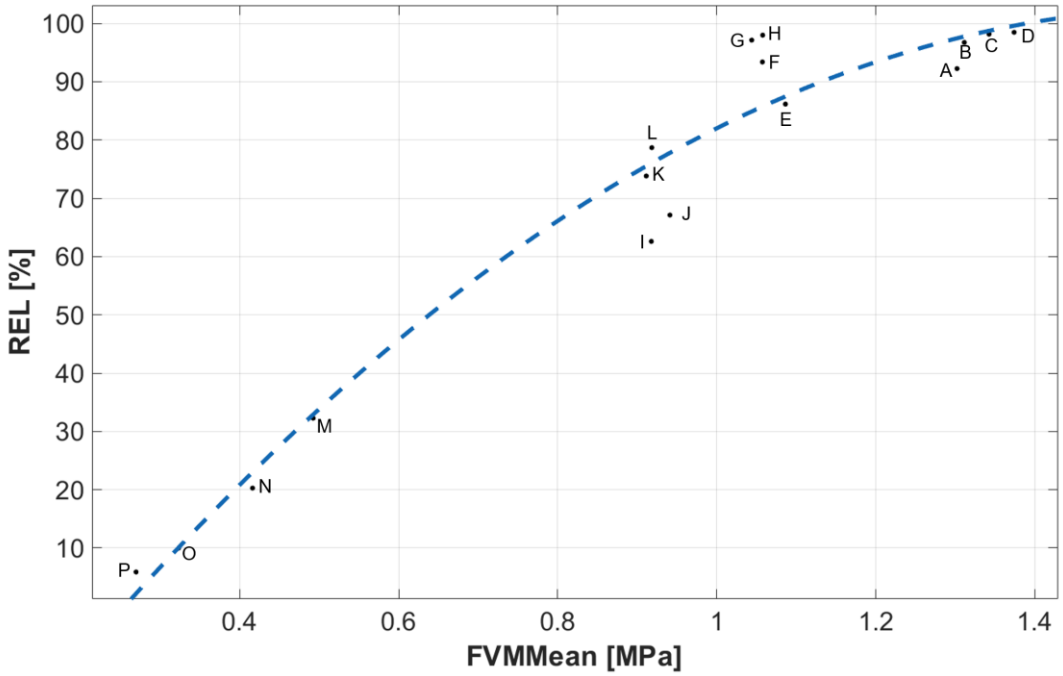

Contrary to the response surfaces obtained in chapter 3 comparing the same parameters, the response surface obtained herein exhibits an inverse nonlinear relation with the *X* dimension and it is not very sensitive to the changes in *Y* parameters. This behavior is natural since the presence of soft tissue implies low stresses on the volume of tissue regenerated, while the differentiation of tissue in bone allows the regenerated tissue to bear load and hence increase the stresses within it. This fact is restated by the correlation between the relative amount of bone and final von Mises mean showed in Figure 5-21, in which less stress implies less bone tissue and vice versa.

Results in Table 5-3 confirm that since the mechanical environment inside the scaffold starts to change notably after 60 days, the results of the different amount of tissue phenotypes will be consistent with the initial biomechanical environment reported in chapter 3. The cell behavior features in the model do not affect significantly the results of the differentiation of tissue despite the presence of the stochastic component of cell behavior. However, the situation will be different if the scaffold degrades due to the new available spaces for the tissue growth will be affected by the changes of the mechanical environment, which is completely different due to the maturation of the initial tissue and the degradation of scaffold, as we will observe in next section.

Table 5-3: Final predicted tissue phenotypes for each geometry in the rectangular arrangement.

Geometry ID	Bone ABS (%)	Cartilage ABS (%)	Fibrous ABS (%)	Resorption ABS (%)	Necrosis ABS (%)
A	21.39	1.79	0	0	0
B	30.22	1.01	0	0	0
C	38.58	0.71	0	0	0
D	43.99	0.67	0	0	0
E	35.00	5.59	0.02	0	0
F	46.69	3.30	0	0	0
G	57.67	1.69	0	0	0
H	64.30	1.32	0	0	0
I	37.99	20.97	1.71	0	0.008
J	46.14	22.00	0.59	0	0
K	56.70	19.88	0.21	0	0
L	64.66	17.46	0.04	0	0
M	24.37	39.10	10.33	0	1.725
N	16.47	51.91	11.98	0	0.862
O	8.68	68.62	9.17	0	0.474
P	5.34	78.49	6.68	0	0.247

The porosities and load scheme used in this chapter do not reduce the mechanical stimulation of the tissue until the point in which the resorption process can be occur. Reaching this point could be possible if the porosity in the system or the load scheme exerted is very low or if the stiffness is high as the one used in verification simulating bioceramic materials. This resorption region will be located before a region where practically all tissue is induced to bone, which is consistent with the results reported in the literature for low load regimes [62], [81].

Regarding cell behavior inside the reference geometry, Figure 5-22 shows the temporal evolution of the cells by means of the normalized available volume inside the pore. At the beginning of the simulation, 1% of the volume available is seeded with MSC and the remaining 99% stays available. As time passes, MSC invade the domain reaching their maximum value around day 9 when the available volume approximates to 0%. Differentiation of mature MSC starts at day 7, which for this reference geometry is predicted just for osteoblast and chondrocytes phenotypes. At day 30, most cells are differentiated. This fact is consistent with some *in silico* data from the literature, which state that low porosities produce high relative amounts of bone [62], [81].

Figure 5-22: Cell behavior inside reference **F** geometry for 1 MPa.

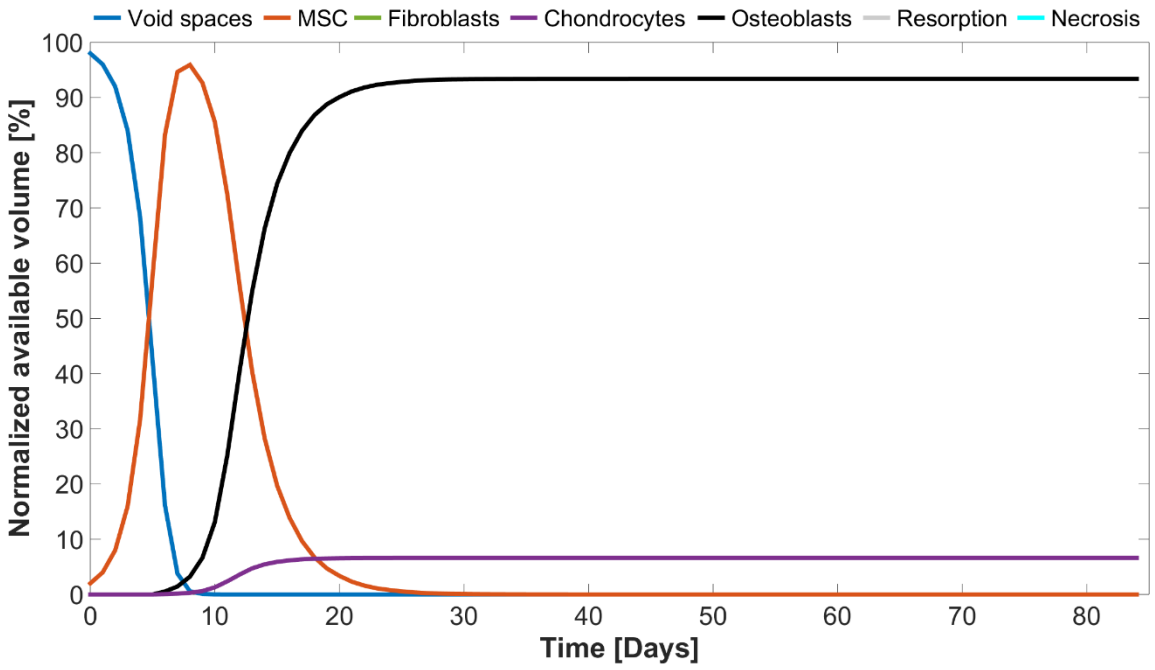

In contrast with the aforementioned results, in practice a scaffold with low porosities presents some drawbacks that make it unviable, such as the reduction of specific surface area for cell attachment as well as the reduction of permeability that leads to a deficient exchange of mass and supply of oxygen and nutrients.

5.9.2 Rectangular scaffolds with degradation

Each scaffold from the sixteen arrangement was simulated including the degradation approach described in section 5.6. Table 5-4 indicates the initial and final results obtained from the simulations:

Table 5-4: Initial and final mean and median stresses on the newly formed tissue domain of rectangular pore arrangement for 1 MPa, and initial and final effective normal stiffness for each scaffold-tissue system in the rectangular arrangement considering the degradation.

Geometry ID	X (mm)	Y (mm)	Porosity (%)	IVMmean (MPa)	IVMMedian (MPa)	FVMmean (MPa)	FVMMedian (MPa)	Initial C_{22}	Final C_{22}	Final day
A	0.243	0.243	23.19	2.77E-03	2.34E-03	1.1769	1.302E-1	530	164	84
B	0.243	0.39	31.24	2.43E-03	2.02E-03	1.1405	3.975E-1	491	279	84
C	0.243	0.536	39.30	2.19E-03	1.78E-03	1.0277	6.603E-1	464	685	84
D	0.243	0.633	44.67	2.05E-03	1.64E-03	9.86E-1	6.096E-1	452	1308	84
E	0.390	0.243	40.62	3.44E-03	3.01E-03	1.1578	3.237E-1	304	91	84
F	0.390	0.390	50.00	3.06E-03	2.70E-03	1.1178	5.911E-1	272	233	84
G	0.390	0.536	59.37	2.74E-03	2.37E-03	1.0496	1.0101	253	460	84
H	0.390	0.633	65.62	2.55E-03	2.16E-03	1.0095	1.1372	245	639	84
I	0.536	0.243	60.69	5.61E-03	4.61E-03	1.33E-1	1.224E-1	135	3	25
J	0.536	0.390	68.74	5.48E-03	4.99E-03	2.07E-1	1.992E-1	115	1	25
K	0.536	0.536	76.80	5.16E-03	4.67E-03	2.61E-1	2.53E-1	104	1	25
L	0.536	0.633	82.17	4.87E-03	4.39E-03	3.23E-1	3.09E-1	99	1	25
M	0.633	0.243	75.53	1.05E-02	8.09E-03	1.16E-1	9.74E-2	57	2	18
N	0.633	0.390	81.24	1.15E-02	1.02E-02	1.69E-1	1.55E-1	46	1	18
O	0.633	0.536	86.96	1.16E-02	1.07E-02	2.11E-1	2.04E-1	39	1	18
P	0.633	0.633	90.77	1.12E-02	1.01E-02	2.32E-1	2.27E-1	36	1	18

The initial conditions are the same as those obtained in the previous section for the scaffolds without degradation obtained from each geometry in the rectangular arrangement. Under the degradation parameters used here, all the scaffold geometries degrade to 100%.

When the scaffold loses its mechanical function, i.e., the global stiffness in the system is lower than 1, the simulation ends and then the immediately previous result is settled as the last day. Geometries **A** to **H** keep their mechanical function and reach day 84, but geometries **I** to **L** lose it at day 25 and geometries **M** to **P** at day 18.

It should be emphasized that in the modeling of the tissue evolution that considers the scaffold degradation, the domain of the newly formed tissue is changing, particularly increasing as the scaffold is losing volume and hence, the newly formed tissue gains it.

The von Mises stress histograms plotted in Figure 5-23, obtained in 3 time points of the course of healing for the reference geometry, were compared with the histograms obtained for the same geometry but without degradation (Figure 5-11). The comparison revealed that the same initial conditions of stress can be observed in day 1 because the degradation process is not affecting the mechanical environment at that point. On the contrary, the histogram in day 42 shows that the newly formed tissue is already assuming much more load than the same case without degradation, because the scaffold has been losing gradually its mechanical function.

Figure 5-23: Histograms of von Mises stress in 3 time points for **F** geometry.

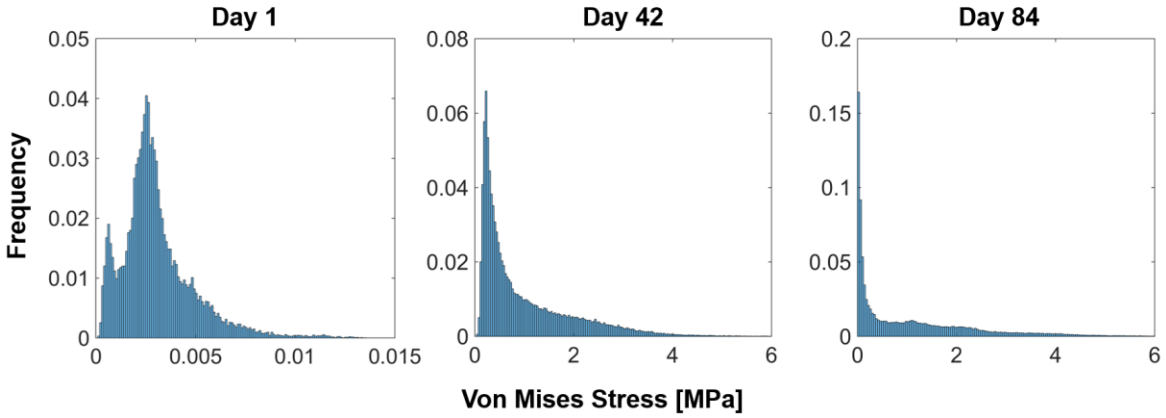

Due to the filling of the newly formed tissue in the volume released by the scaffold when it degrades, a significant volume with low von Mises stress will be present at the end of the twelve weeks window in the distribution. The reason is that this new tissue is not plenty maturated and hence exhibits no stresses such as the one carried by the bone with its final stiffness.

A concentration of the elements around a specific von Mises stress values is observed as *Y* dimension increases at the end of the first two rows in the sixteen geometries arrangement (Figure 5-24). The last two rows show only the final distribution before the

tissue-scaffold system loses its mechanical function, i.e., distributions of tissue inside a failed scaffold. These distributions are consistent with those observed when the tissue is in development and it is not capable of bearing loads.

Figure 5-24: Normalized final stress distributions for each geometry in the arrangement at the end of simulation. Geometries in rows **IJKL** and **MNOP** lose their mechanical function before reaching day 84.

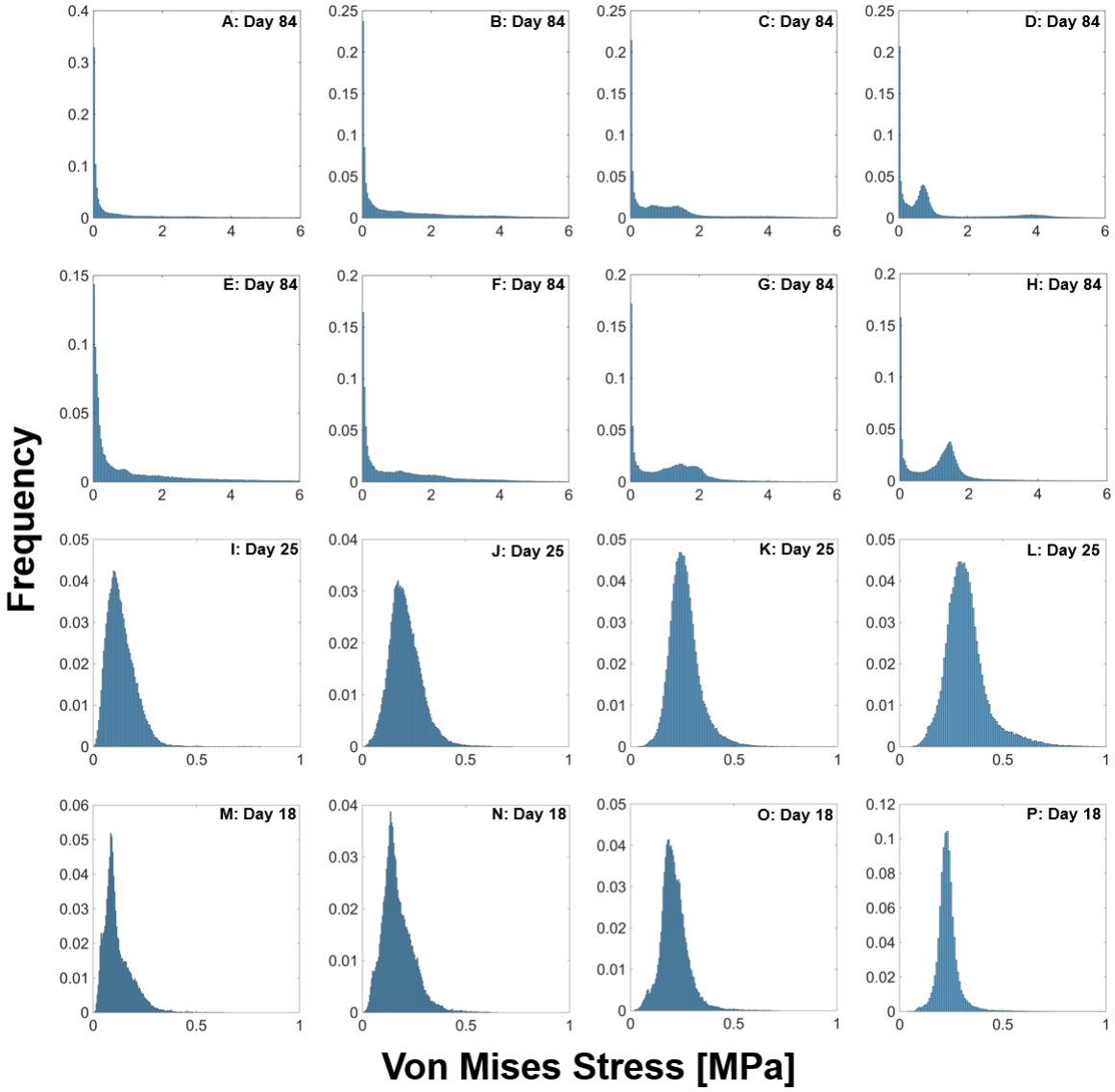

Comparing the von Mises stress statistics with those observed in the simulations without degradation, the degradation produces a reduction of the von Mises mean and notably

reduces the final von Mises median in the first row of the arrangement (See Table 5-4). This fact is attributable to the presence of newly formed tissue in the released spaces produced by the degradation, which could be soft tissues or hard tissues that begin to form but do not reach their maximum stiffness value that requires sixty days after the differentiation. Therefore, the stresses in the last formed tissues were low and they affect the statistics by reducing its values. It is worth noting that if porosity is low in the scaffold, it is expected that its total degradation takes more time than one with higher porosity and, therefore, the low porosity geometry is capable of supporting the load more time than the high porosity geometry.

Geometries **E**, **F** and **G** from the second row exhibit higher values of von Mises mean than the scenario without degradation. The reason is that the values of von Mises stresses are more dispersal when the scaffold degrades and are not crowded in a region, as in the case when the mechanical environment provided by the scaffold is not changing. **H** geometry exhibits a peak of counts of elements with values around a von Mises stress greater than 1 MPa, thus suggesting that the scaffold degradation induces regions with load concentrations greater than the load exerted macroscopically.

Figure 5-25: Evolution of Von Mises stress mean in time for **F** geometry with (orange) and without degradation.

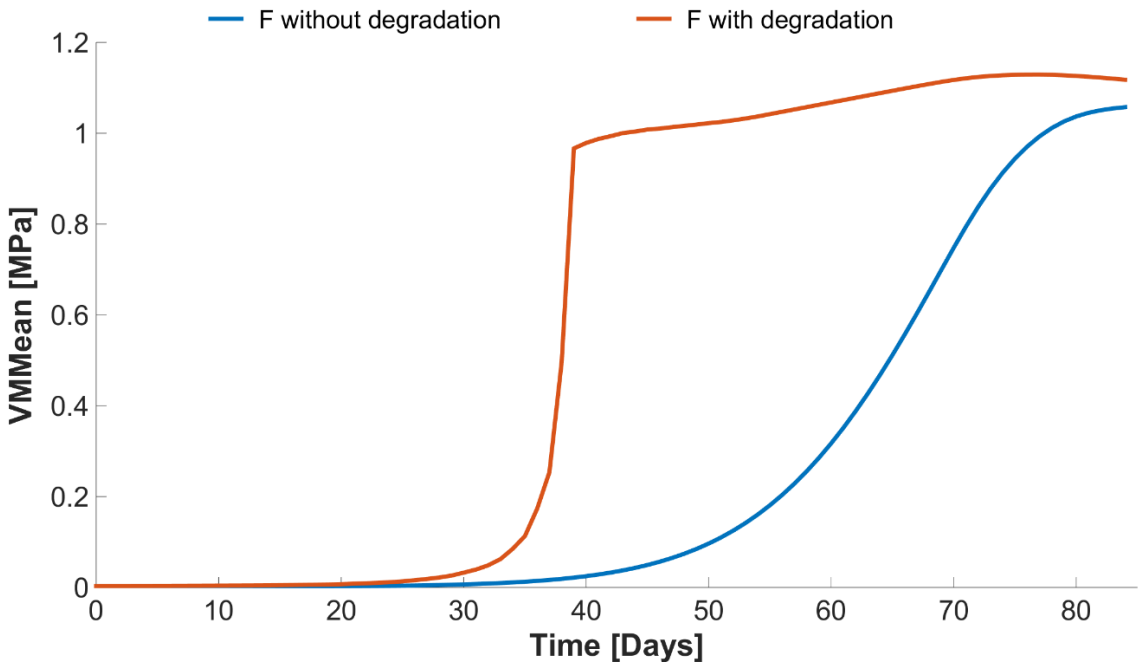

The evolution of the statistics in the newly formed tissue is different if the degradation is considered or not, as observed in the von Mises stress mean for the **F** geometry in both cases (Figure 5-25). The rate in which the mean increases is higher in the model that degrades and has exponential shape due to the loss of stiffness in the system. This high rate is finally interrupted when the scaffold loses its structural connectivity and it becomes slow by the action of the new volume released and by the stiffening of the tissues that were differentiated initially. The temporal behavior of the stiffness for each geometry in the arrangement is shown in Figure 5-26.

Figure 5-26: Evolution of Von Mises stress mean in time for **F** geometry with degradation. Current position is plotted in blue, while the rest is plotted in grey.

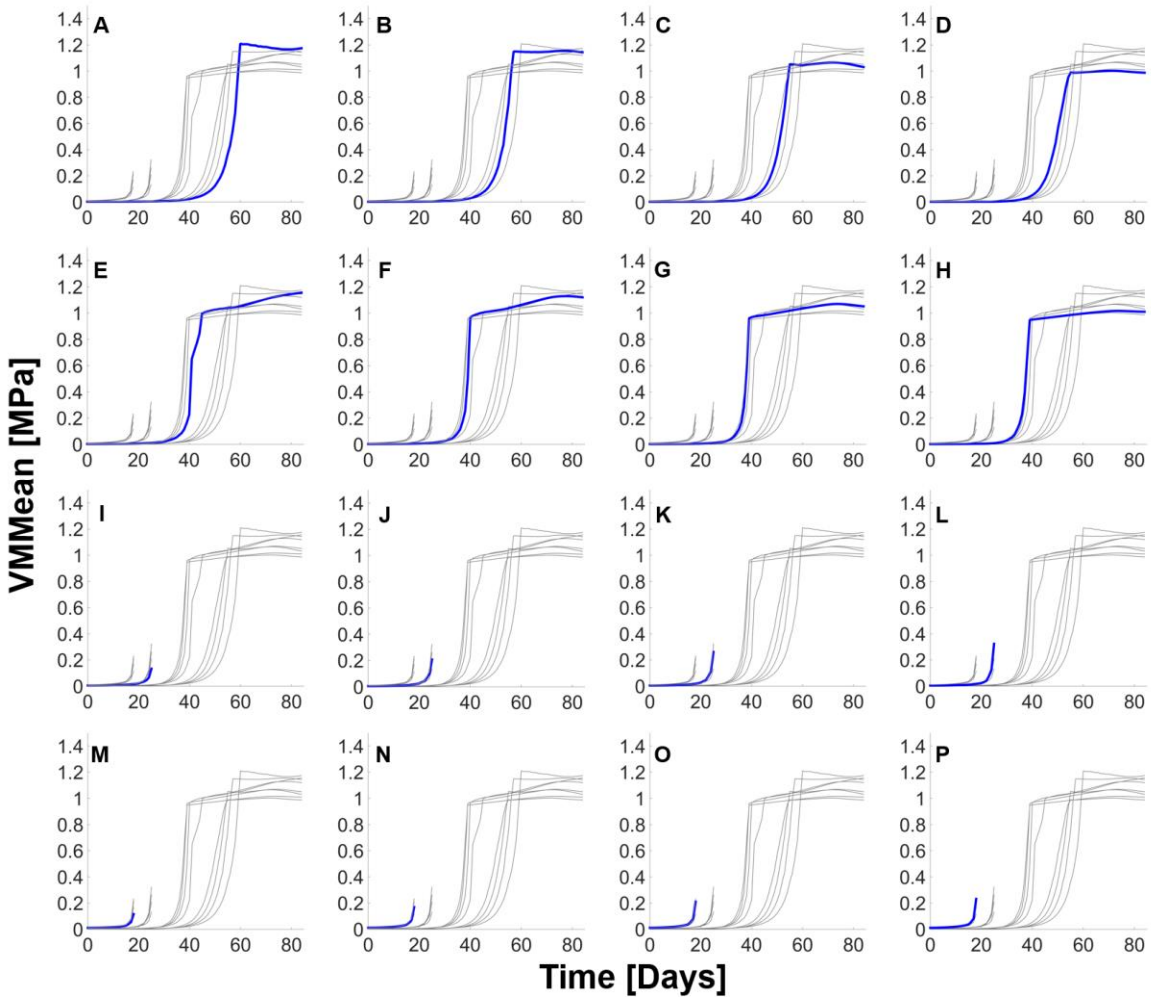

Consistently with the results obtained previously from von Mises stress, the maximum principal stress histogram for reference geometry indicates that the tissue is already assuming load considerably at mid time of simulation (Figure 5-27). The main peak in the distribution indicates that an important volume is not bearing efficiently load at that moment and this effect is held until the end of the simulation.

Figure 5-27: Histograms of the maximum principal stress absolute in 3 time points for **F** geometry.

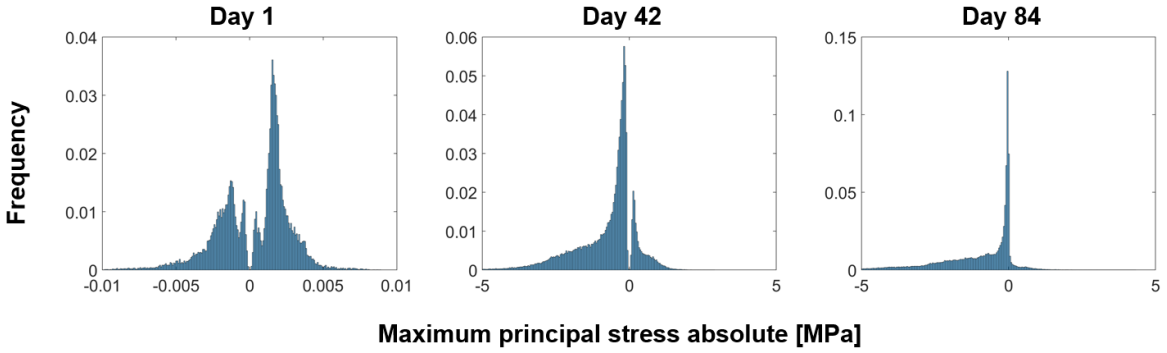

The first rows of the final histograms for maximum principal stress absolute (Figure 5-28) show that as *Y* dimension increases, the amount of elements under compressive stresses start to stack and the tissue elements that are not bearing load reduces. However, the last two rows do not show the final results and the distributions exhibited are undeveloped and reveal mostly that the elements are experiencing a compressive load. The region of crowded elements around a von Mises stress value previously mentioned is observed in the portion of negative maximum principal stress, thus corroborating that these elements are supporting the compressive load applied to the scaffold-tissue system.

Figure 5-28: Final histograms of the final maximum principal stress absolute for each geometry in the arrangement.

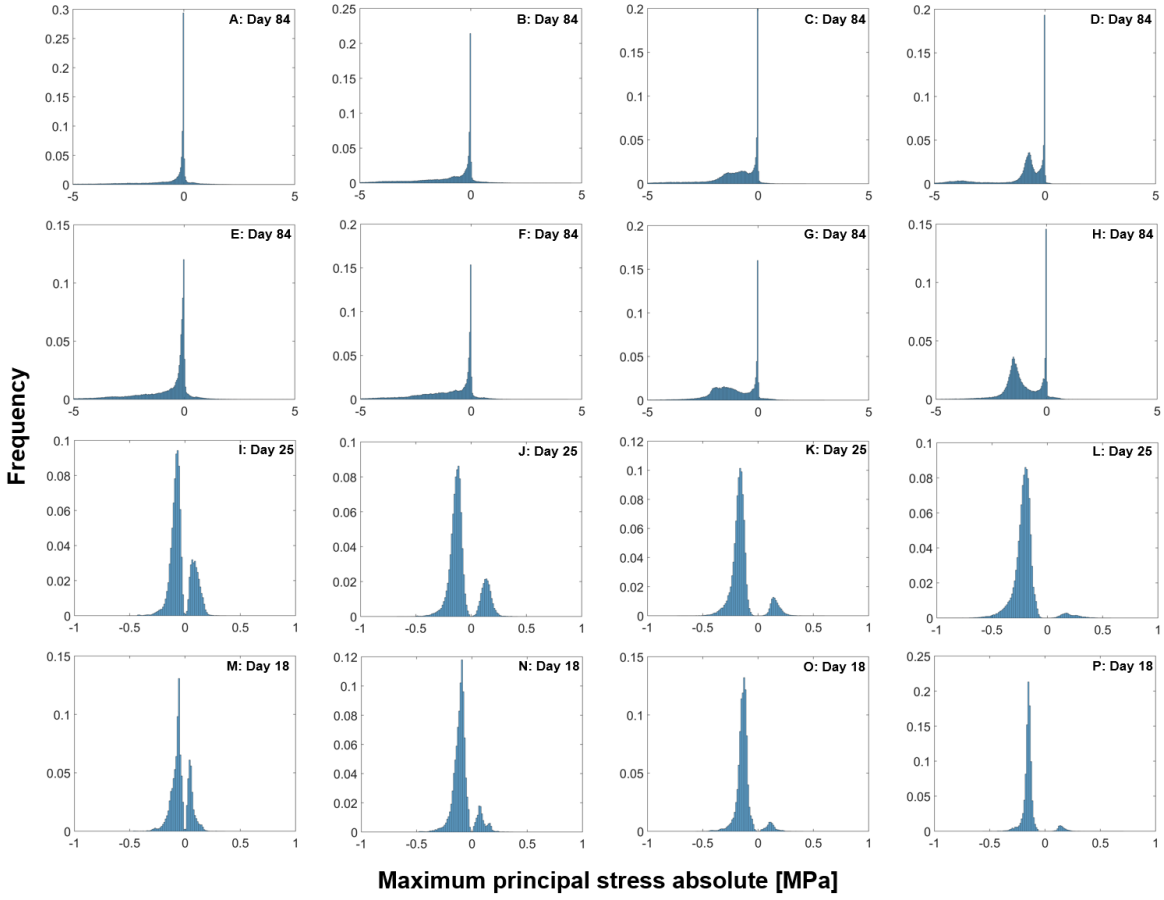

Although the last two rows in the arrangement of maximum principal stress absolute do not reach the end of simulation and fail early, they show that as dimension *Y* increases, the number of elements submitted to a positive stress reduces.

The absolute percentages of each phenotype at the end of simulation are presented in Table 5-5. Despite the last rows in the arrangement lose their mechanical function before reach the twelve weeks period, almost the entire volume was invaded by MSC that subsequently differentiated in various phenotypes.

High levels of necrosis occur in the last row even if the simulation only reaches day 18, which indicates that the scaffold lost early its capability of bearing the load and producing

an excess of mechanical stimulation on the newly formed tissue that leads to a necrosis process.

Table 5-5: Final predicted tissue phenotypes for each geometry in the rectangular arrangement.

Geometry ID	Bone ABS (%)	Cartilage ABS (%)	Fibrous ABS (%)	Resorption ABS (%)	Necrosis ABS (%)
A	76.65	21.62	1.03	0	0.49
B	82.99	15.69	0.83	0	0.47
C	86.85	12.38	0.60	0	0.15
D	90.11	9.74	0.14	0	0.001
E	63.52	31.32	2.19	0	2.96
F	70.56	24.37	1.55	0	3.49
G	76.79	19.91	0.92	0	2.36
H	80.87	16.48	0.88	0	1.74
I	25.58	37.69	11.62	0	2.27
J	20.14	49.25	11.73	0	2.62
K	16.73	60.00	11.19	0	2.74
L	16.18	65.30	10.60	0	2.24
M	7.99	32.47	27.10	0	25.04
N	4.28	23.47	34.51	0	31.93
O	1.29	17.94	40.21	0	35.93
P	0.38	14.37	45.16	0	35.63

An interesting pattern can be observed in the cartilage tissue predicted, which reduces in each row as *Y* dimension increases. However, in the third row, as *Y* dimension increases the amount of cartilage tissue predicted increases too. This suggests that the geometrical parameters in this row are the most favorable for cartilage development. This data could be useful since cartilage tissue is hypoxic, so the vascularization is less critical. It is an avascular nature tissue, which can be attractive to stimulate since it does not heal itself.

Both response surfaces and curve fitting were performed previously for different geometry arrangements. Since two entire rows of the simulations of the studied arrangement in this chapter fail, it is meaningless to compare the results obtained from the different scaffolds geometries of the arrangement.

Regarding the stiffness of each simulation, Figure 5-29 shows the effective normal stiffness evolution, i.e. the C_{22} index of each geometry in the rectangular arrangement studied. The geometry with the greatest final C_{22} was **D** as in the simulations without degradation. This was expected since in this geometry, more bone tissue was predicted and then, it has notably the capability of reaching a high stiffness value. However, all geometries

experimented a reduction in their final C_{22} value in different proportions. The failure of the last two rows of the arrangement in days 18 and 25 is indicated in Figure 5-27.

Figure 5-29: Effective normal stiffness evolution in time of each geometry in the arrangement. Current position is plotted in blue, while the rest is plotted in grey.

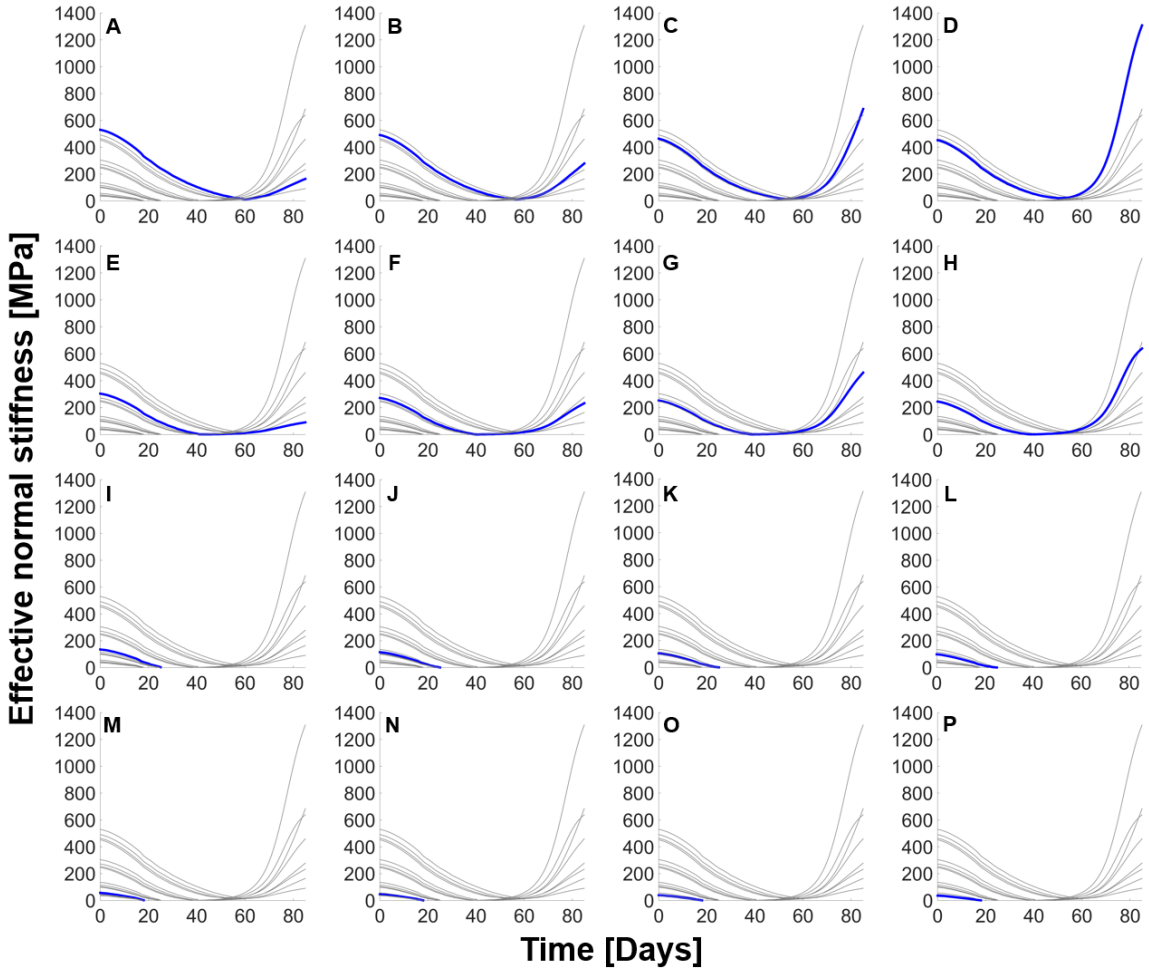

Figure 5-30 shows the normalized volume occupied by different cells and the development of its respective tissues in the time window. The stabilization of the different tissues occurs after fifty days compared to twenty days for the tissues in scaffolds without degradation. Large amounts of cartilage were predicted comparing to those obtained for the same micro-geometry in previous section.

Figure 5-30: Cell behavior inside reference **F** geometry for 1 MPa.

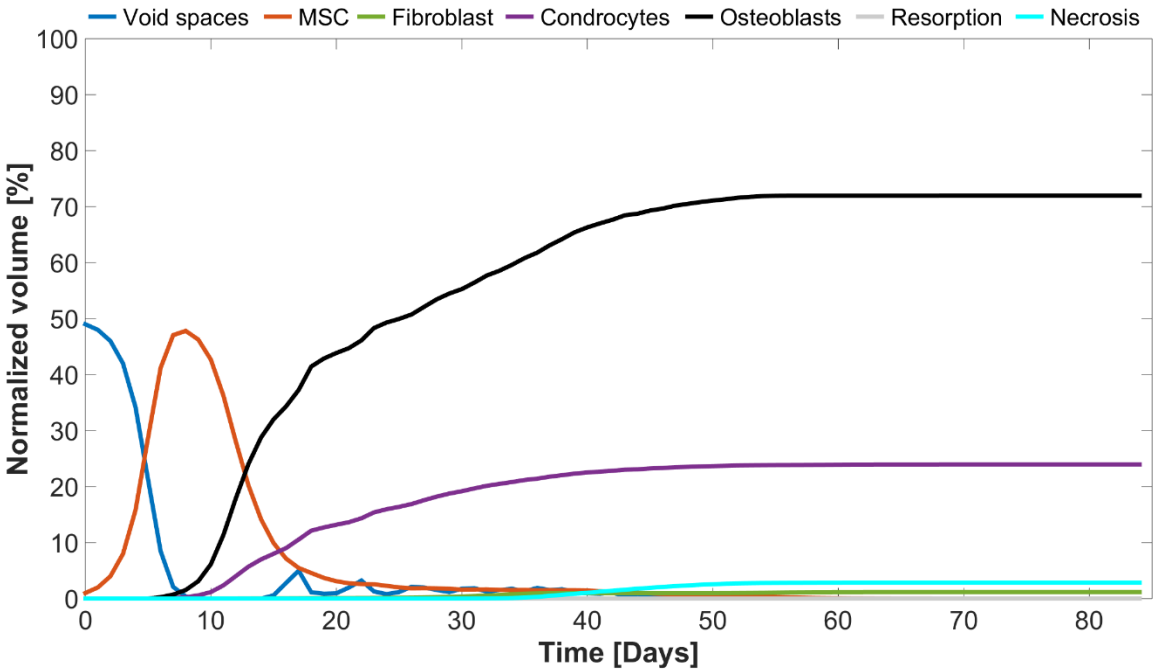

A remarkable result in this chapter is to explore whether a relationship exists among scaffold micro-geometry and its degradation or not. Figure 5-31 show the normalized average molecular weight in time for each geometry in the rectangular arrangement, thus indicating that there are different rates of the physical changes in the scaffold, produced by its micro-geometry.

Mass loss percentage from each geometry is presented in Figure 5-32 in the course of the time window studied. This corroborates the fact that low porosities take more time to degrade.

5.10 Conclusions

The main aim of this chapter was to introduce a methodology for modeling the behavior in time of the newly formed tissue inside different scaffold geometries. First, the evolution of the tissue ignoring the dissolution of the scaffold was conducted and afterward, a scaffold degradation approach was included in the model to compare both scenarios.

Figure 5-31: Normalized average molecular weight in time for each geometry in the rectangular arrangement. Current position is plotted in blue, while the rest is plotted in grey.

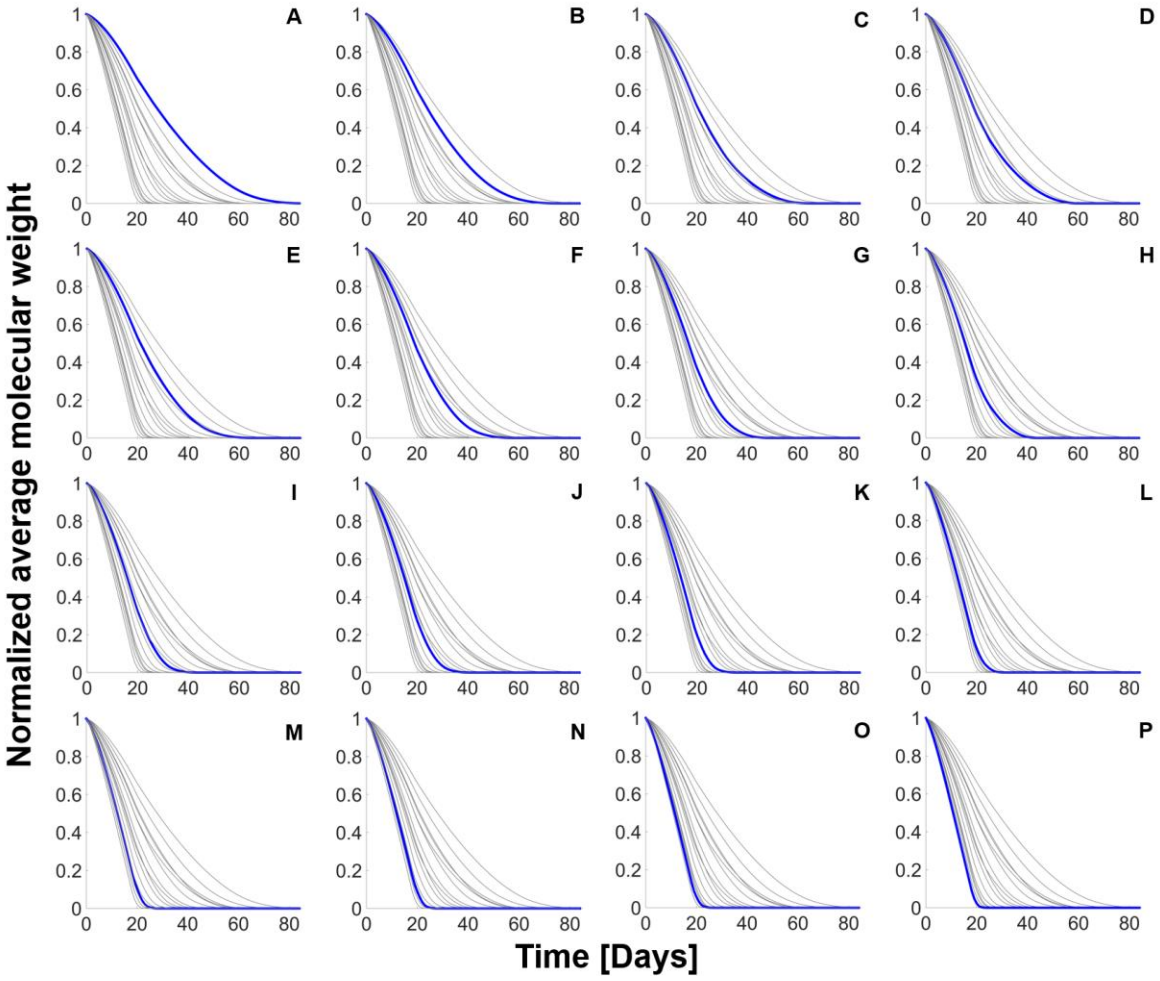

Using the concept of pore geometry arrangements from chapter 3, the stresses in the newly formed tissue inside the different scaffold topologies were obtained and it was observed how they change for each topology, which represents the initial biomechanical environment condition. If degradation is not considered, the changes of the biophysical environment will be governed principally by the rate equation and the logistic growth behavior produced. If degradation occurs, it was observed that the complexity of the mechanical environment increases considerably. The statistics are notably affected because when a scaffold element degrades and the produced void space is filled by newly formed tissue, the stresses in the system could change abruptly. The reason is that a low stress value is added into the group of tissue elements that have possibly already increased its properties, thus

influencing the statistic values. Indeed, the degradation has a paramount influence in the biomechanical behavior of the tissue-scaffold system.

Figure 5-32: Mass Loss in time for each geometry in the rectangular arrangement. Current position is plotted in blue, while the rest is plotted in grey.

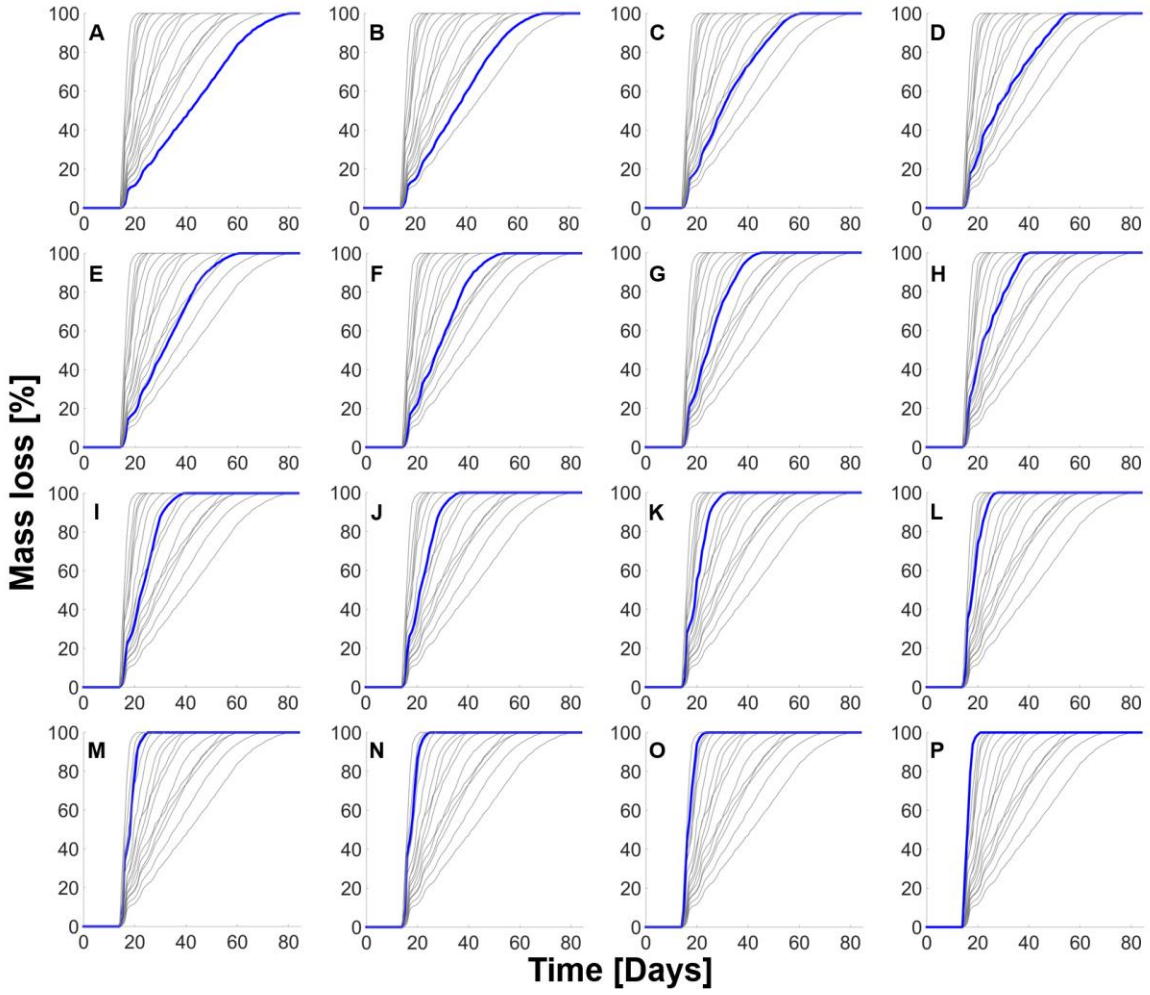

It was demonstrated that the distribution of the stresses is changing in time even if degradation happens or not and that stress statistics can describe some interesting features that occur within the newly formed tissue.

Curiously, the stress correlations determined in this chapter are contrary to those determined in chapter 3. High stresses at the end of time in a geometry that considers the evolution of the tissue in time indicates that the scaffold has developed neo-formed bone

and it reaches its natural stiffness. In contrast, the static model indicates that more stress in the newly formed tissue affects the prediction of bone tissue negatively.

The results presented help to understand how micro-geometry features influence the degradation of the structure and modify the physical environment. The scaffold environment changes easily, even just during the implantation. Nevertheless, the pore orientation seems an influencing factor to achieve highly osteogenic microarchitectures. The failure observed for the scaffolds and the estimated necrosis volume could help to understand why scaffolds failed in some experimental scenarios, hence reiterating the need of keeping the mechanical function enough time until the tissue is capable of bearing the load.

Many assumptions were made since the proposed model is a simplified model. Some of these suppositions are that the tissue is involved in an ideal scenario regarding the vascularization, host tissue competition and supply of nutrients and oxygen or the simplistic way to model the scaffold degradation. However, in real life the phenomenon inside the scaffold is affected by countless conditions of different nature that still are not clearly defined.

The verification process carried out reveals that the results presented here are reasonable for both *in silico* and experimental data available in the literature, which confirmed the correctness of the developed model. A better approximation of the results will be possible as new experiments are made with controlled variables and environments, or they are designed trying to validate an *in silico* study as the one presented here in order to calibrate the parameters and the model used.

Although the model has an important stochastic component, there is a particular tendency for each geometry in the results among different runs. This indicates that the initial mechanical environment has a more important role in the fate of the newly formed tissue than the random cellular process, thus suggesting the applicability of static analysis. However, these analyses are useful only for early stages of tissue development under ideal conditions and mostly for scenarios in which the scaffold does not degrade or takes a considerable time to do it.

An important limitation was that the permeability properties of the scaffold, which is known to be relevant for its performance, was neglected. Further research regarding permeability is still needed.

Each day the models become more complex as well as computational available power allows it. Thanks to this, it was possible to present here a high-resolution model with basic units of cell size and a parallel finite element domain. Of course, this model can easily be adjusted to achieve more complex geometries than the rectangular family studied in this chapter.

6. Conclusions and future perspectives

The motivation of this research stem from some questions about the neo tissue that is forming inside a scaffold after its implantation: How does the micro-geometry of the scaffolds for bone regeneration influence the stresses on the newly formed tissue? How are those stresses? How they change as time passes? From these questions, the following hypothesis rises: the micro-geometrical features of the scaffold, such as pore shape and size, have a significant relation with the stress distributions on the newly formed tissue.

After a comprehensive review of the literature and of the state-of-the-art in this topic, there was no clear information about the stresses in the newly formed tissue. However, the review in chapter 2 reveals the enormous complexity behind the scaffolds for bone tissue engineering, which is an interdisciplinary scientific field that requires the integration of knowledge from life sciences, physics, mathematics and engineering. The bone tissue scaffolds are a promissory solution for bone healing treatments, especially to tackle the limited availability of bone substitutes. Despite the constant advances on this field, solutions translated into clinical and commercial scenarios are still unsuccessful because the outcomes move in a wide range of success and failure, some of them contradictory. This is due to the fact that many processes occurring inside the scaffolds are not yet unveiled and the experimental studies do not control clearly all the key factors supposed to influence the process. In the context of this research, one of these factors is the relation between the scaffold micro-geometry and the final outcomes regarding to regenerated tissue.

In an effort to start responding the raised questions, chapter 3 presents a methodology to develop models of the scaffold-tissue systems at an early stage of the reparative phase of bone healing, in which the scaffolds are filled by granulation tissue that is rich in mesenchymal stem cells. Even if this model does not consider the evolution over time of the tissue, it allows determining how are the stresses that the newly formed tissue experiments after being implanted at *in vivo* hypothetical scenarios under compressive load. Although the newly formed tissue does not load bearing, a slight load is transferred to it through the scaffold structure. This load produces deformations and stresses that are related to the mechanical stimulation that promotes the formation of the different tissue phenotypes involved in the bone healing process.

Several sets of topologies of pores for different families of regular scaffolds, such as rectangular, elliptical and spherical, were proposed in order to observe how the stresses change when there are variations in the micro-geometrical parameters that define the pores. It was found that each parameter has a different influence in the stress distribution produced by the scaffold in the tissue and in the statistical magnitudes obtained from it. The purpose of these statistics was to introduce simplified measures that allow characterizing the general state of the stresses in the tissue, since it contains numerous terms that are represented by the stress tensor and they vary through the studied domain.

It was found that the change of the parameters that define the pores are correlated to the von Mises statistics determined for each geometry in the proposed pore arrangements and to the amount of bone predicted determined with a mechanoregulatory model for tissue differentiation widely used in mechanobiology research. Regarding the micro-geometrical parameters, it was found that in the axial-oriented pore families, such as rectangular and elliptical, the parameters that mostly influence the performance of the scaffold were those perpendicular to the load direction. The results show that the orientation of pores has a great significance for the mechanical signaling that the scaffold transmits to the newly formed tissue. This suggests the importance of the pore orientation in relation to the applied load as key feature, even more than other common measured features of the scaffolds. For instance, porosity is usually a measure employed for the characterization of scaffolds, but from a mechanobiological perspective, similar porosities can lead to very different performance of the structure. In this way, the pore orientation combined with other physical measurements such as porosity could be a better criterion to select a geometry in order to fulfill the design requirements for the device.

This research has demonstrated that the selection of the adequate micro-geometrical features of the scaffolds is critical for their performance. From the selection of these features, it is possible to control design elements such as pore size, effective surface for cell attachment, porosity, stiffness, among others. However, many signals that control the fate of the regeneration depend neither on the micro-geometrical features of the scaffold nor on the physical signaling.

A negative correlation was found between the stress statistics in the newly formed tissue and the amount of bone predicted. It suggests that the stimulation level in medium

porosities for a scaffold with mechanical properties of polymers and medium-high loads is enough to stimulate the bone formation through the stimulation of mesenchymal cells to differentiate in osteogenic phenotypes. However, according to the experimental findings and most mechanoregulation theories, if the stimulation is too low, resorption process could be induced. This condition could be produced when the stiffness properties of the material are too high, as in the case of bioceramics and biometals, or, equivalently, if the load is too low. The results of the different arrangements regarding stresses and the amount of bone produced reiterate that a combination of geometrical parameters can be found to maximize the performance of the scaffold regarding the mechanobiological criterion.

The stress distribution shape does not depend on the size of the unit cell or the load applied to the system, but is more influenced by the morphology of the pores. The shape of the distribution remains when the load is modified, however, the value of stress statistics changes because the values of the bins in the stress axis scale together. If the load is reduced, the histogram scales to left; and if the load increases, the histogram scales to right. This is a consequence of the linearity of the constitutive models used.

To explore how the geometrical parameters influence the mechanobiological performance of other geometry families, several geometries of the beam-based scaffolds category were analyzed in chapter 4. The modeling procedure was integrated with an optimization algorithm that perturbs the geometrical parameters that define the cross section beam of the scaffold. The simulations predict that the beam-based scaffolds studied allow the formation of large amounts of bone for low levels of load. In contrast, for high values of load, scaffolds based on axial-oriented pore families perform better. Also, the differences in the behavior of the circular and square section of the beams were analyzed. Circular sections obtained better performance, which is consistent with experimental observations that state more bone formation in curved surfaces.

The identification of the micro-geometrical features that can affect the bone healing requires the study of different categories of pore shapes in a systematic way. However, none of such studies are available so far in the literature. The *in silico* assessment of different scaffold features, such as beam section, size, orientation and pore features of different geometric families, can provide useful information to scaffold designers regarding the geometrical aspects and, for instance, the amount of material needed to build the construct. The

proposed algorithms could guide designers in the manufacturing of custom scaffolds that better suit the anthropometric and physiological requirements of the patient, thus allowing a successful healing in the shortest possible time.

Another interesting result of this research project was the modeling and analysis of the irregular scaffold geometries, which exhibit a remarkable performance under the mechanobiological assessment. A procedure was developed to model beam-based scaffolds with irregular structure inspired in the trabecular bone arrangement obtained from a combination of load adaptive and mechanobiological algorithms to design and optimize the irregular structures. Different boundary and loading conditions were hypothesized to act on the scaffolds, and in all of them, the irregular scaffolds adapted to the load were predicted to perform better than the others. The developed framework can be used to design and optimize high performance scaffolds to bear complex load distributions.

Thanks to the results obtained to this point, some of the questions initially raised have been responded and our hypothesis begins to be confirmed. However, one of the main challenges regarding the modeling of bone tissue scaffolds is to predict its evolution in time. For this reason, we implemented a simplified model to explore how the stresses are changing from the early state when the scaffold is filled of granulation tissue to an evolved tissue state driven by a mechanoregulatory algorithm. The model developed is based on voxels that represent both the basic geometrical unit and the cells as basic biology unit.

A computational framework was presented consisting in a high-resolution model with basic units of cell size and a parallel finite element domain. It allows modeling the biological and mechanical evolution of the newly formed tissue with the phenomena of the scaffold degradation. The developed model predicted the evolution of the stress distributions as well how the tissue differentiates and its mechanical properties evolve in time. According to some experimental observations, cells differentiate and synthesize ECM to compose tissue that will increase its mechanical properties in time exponentially. It was determined that the mechanical environment is not notably altered by the action of the tissue stiffening in the first days after injury. Without degradation, the scaffold biomechanical environment at first days was comparable to the one determined for the pore rectangular arrangement in chapter 3.

Introducing the degradation modeling into the tissue differentiation model in time reveals the expected changes produced in the environment due to the loss of mechanical properties and the erosion of the geometry shape of the scaffold. The stress distributions show that changes in the biomechanical environment are considerably bigger than those produced only by the tissue maturation. It was evidenced in the rate of change of the von Mises statistics that was faster when the scaffold degrades. This behavior is expected since the scaffold-tissue system will fail if the scaffold does not hold its stiffness enough time until the tissue can support the load. This fact was observed in several geometries of the rectangular arrangement studied.

Observing the data regarding the stiffness of the scaffold-tissue system, molecular weight and mass loss of the scaffold, it is possible to state that different topologies will lead to different rates of variations in the biomechanical environment in which the tissue is developing. Indeed, the degradation has more influence on this environment than the slow modifications introduced by the tissue synthesis and maturation.

Through the data obtained in this chapter, the initial questions that were raised can be responded. The models that do not consider the time show the initial state of the stresses and a transitory prediction of the tissues that could be developed, while the tissue evolution model exposes how the stress distributions are when the tissue is differentiated and gained its final mechanical properties reported. However, the final stress distributions depend on the differentiated tissue. It is expected that the stresses are bigger if the scaffold stimulates the differentiation of bone tissue, since it will be capable to bear the load acting on the regenerated after obtaining its final mechanical properties. On the contrary, if soft tissues such as fibrous, cartilage or even if the granulation tissue remain by the prediction of resorption or necrosis processes, the tissues developed will not be capable of bearing the load and the scaffold-tissue system will fail.

From this work, it can be inferred that the state of stresses on the newly formed tissue is changing depending on the way in which the tissue is synthesized and its mechanical properties are obtained. Indeed, the scaffold micro-geometrical features can notably influence this process.

The verification procedure allows corroborating the consistency of the results regarding *in silico* and experimental literature. However, the work is limited by the many assumptions made, since the proposed models were simplified models of the phenomena that occur into the scaffold and an ideal scenario was supposed regarding the vascularization, host tissue competition and supply of nutrients and oxygen, and removal of wastes.

We suppose that in general the same principles by which the fracture heal occurs in a normal injury will take place within scaffolds. For the sake of simplicity, we overlooked phenomena that are natural in fracture healing such as changes on loading during the differentiation process, and de-differentiation processes. Also, an important drawback of this work is that the frequency in the load application was ignored. However, a theoretical model that describes a clear and direct relationship among the scaffold geometry, loads schemes, their frequency of application and the consequent tissue outcome at the end of the process is still unknown.

More research on bone tissue engineering scaffolds is necessary to tackle the limited clinical success of these devices and the wide range of outcomes. By means of integrative approaches of *in vivo* or *in vitro* scenarios and simulation, it is possible to develop better models to describe the phenomena more closely to its real nature. However, a challenge in those experimental studies is to guarantee factors such as enough vascularization, load schemes and the use of different regular scaffold geometries with controlled environments. Knowledge about the behavior of regular microstructures can lead to enhance the understanding of the behavior of irregular structures.

The time evolution model presented is adaptable to different time curves of tissue behavior and degradation of materials, thus allowing adaptation to specific cases or regions with particular physiological environments. Even without the time evolution capabilities, the biomechanical environment modelled using “static” models is useful to predict the scaffold behavior and could be an interesting tool taking into account the relation low cost vs. the resources spent in a time evolution model.

The differences in the stress distributions rise the question about whether there is a pattern or feature in the stress distributions that characterize an appropriate scaffold. Probably, the identification of distinctive features of the distribution can suggest strategies of design

without incurring in complex mechanobiological analyses. It is necessary to search for better characterizers, since histograms exhibit features in the stress distributions that are distinctive of each geometry but could also be hard to analyze and use in the design scenario.

Even without mechanobiological data, knowing statistical parameters of a stress distribution inside the scaffold, such as median and mean, allow comparing them with favorable values stablished in this research to choose scaffold designs without complex mechanobiological routines. Stress distributions in combination with artificial intelligence techniques could be interesting tools to predict scaffold behavior and performance without complex approaches.

Depending on the clinical scenario, time and nature of the tissue that is intended to recover can lead to different necessities. For instance, for rapid filling and more spontaneous regeneration, inducing cartilage to stablish an endochondral ossification environment can be useful, or stimulating immature bone in order to create a less rigid environment adequate to remodeling. Mature bone regenerated allows a rigid environment, but it can be less propense to allow vascularization, while immature bone has high osteogenic cell density and potential of organization that should be guided naturally by the macroscopic environment of the injury. The proposed *in silico* framework can be adjusted to design scaffolds considering all these specific requirements.

Clearly, this research is far to be finished, instead this is just the beginning of the development of a multiscale integrative approach that takes into account the key aspects that govern the tissue behavior growing inside biodegradable scaffolds. Integrative approaches for scaffold design should be adopted, based on a full understanding of the different key factors of biological chemical and physical nature and including experimental support to validate and feed the computational models employed. In the distant future, implanted scaffolds should have controllable properties in non-invasive ways, for instance, changes in their topology in a controlled manner using an external signal to control the degradation properties. These developments should be directed towards concepts such as precision medicine, in which the medical treatments are oriented to the specific conditions and necessities of the patient.

A. Annex: Goodness of fit details

Different models were used to fit the relations among the micro-geometrical parameters, stress statistics and performance of the studied geometries. The models were named according to the MATLAB definitions (Version R2016b, MathWorks, Natick, MA, USA) and the parameters of each arrangement and load case are defined below.

Table A-1: Function fitting models

Model	Equation form
Third order polynomial surfaces (**Poly33**)	f(x,y) = p00 + p10*x + p01*y + p20*x^2 + p11*x*y + p02*y^2 + p30*x^3 + p21*x^2*y + p12*x*y^2 + p03*y^3
Cubic polynomial curve (**Poly3**)	f(x) = p1*x^3 + p2*x^2 + p3*x + p4
Fourth order polynomial curve (**Poly4**)	f(x) = p1*x^4 + p2*x^3 + p3*x^2 + p4*x + p5
Exponential first order curve (**Exp1**)	f(x) = a*exp(b*x)
First order polynomial surfaces (**Poly11**)	f(x,y) = p00 + p10*x + p01*y
Square polynomial curve (**Poly2**)	f(x) = p1*x^2 + p2*x + p3

Table A-2: Function fitting details for rectangular pore geometry under 0.5 MPa

Function fitting	SSE	R-square	Adjusted R-square	RMSE	Model	Coefficients (with 95% confidence bounds):
VMMean vs. REL	31.86	0.9871	0.9851	1.565	Poly2	p1 = -1.515e+06 (-2.035e+06, -9.954e+05) p2 = 3076 (-503.4, 6655) p3 = 98.58 (93.95, 103.2)
VMMedian vs. REL	99.45	0.9596	0.9534	2.766	Poly2	p1 = -1.405e+06 (-2.472e+06, -3.387e+05) p2 = 428 (-6032, 6888) p3 = 101.5 (94.23, 108.7)
X Y vs. VMMean	1.437e-08	0.9997	0.9992	4.894e-05	Poly33	p00 = -0.006526 (-0.009367, -0.003684) p10 = 0.07078 (0.05676, 0.08481) p01 = -0.002267 (-0.01629, 0.01176) p20 = -0.1886 (-0.2192, -0.1579) p11 = -0.01317 (-0.03089, 0.004552) p02 = 0.00835 (-0.02226, 0.03896) p30 = 0.1681 (0.1455, 0.1907) p21 = 0.02823 (0.01403, 0.04242) p12 = -0.0106 (-0.0248, 0.003598) p03 = -0.003134 (-0.02571, 0.01944)
X Y vs. VMMedian	4.295e-08	0.9988	0.997	8.461e-05	Poly33	p00 = -0.006769 (-0.01168, -0.001857) p10 = 0.06734 (0.04309, 0.09158) p01 = 0.0004646 (-0.02378, 0.02471) p20 = -0.1792 (-0.2322, -0.1263) p11 = -0.01055 (-0.04118, 0.02009) p02 = 0.00115 (-0.05177, 0.05407) p30 = 0.152 (0.113, 0.191) p21 = 0.04392 (0.01937, 0.06846) p12 = -0.02575 (-0.05029, -0.001202) p03 = 0.005657 (-0.03336, 0.04468)

Table A-3: Function fitting details for rectangular pore geometry under 1.0 MPa

Function fitting	SSE	R-square	Adjusted R-square	RMSE	Model	Coefficients (with 95% confidence bounds):
VMMean vs. REL	383.1	0.9745	0.9682	5.65	Poly3	p1 = -1.184e+08 (-6.026e+08, 3.659e+08) p2 = 2.012e+06 (-7.006e+06, 1.103e+07) p3 = -1.802e+04 (-6.557e+04, 2.954e+04) p4 = 130.4 (58.1, 202.7)
VMMedian vs. REL	187	0.9875	0.9844	3.955	Poly3	p1 = -9.401e+07 (-3.353e+08, 1.473e+08) p2 = 1.286e+06 (-2.752e+06, 5.325e+06) p3 = -1.409e+04 (-3.342e+04, 5250) p4 = 120.3 (93.74, 147)
X Y vs. VMMean	5.855e-08	0.9997	0.9992	9.879e-05	Poly33	p00 = -0.01315 (-0.01889, -0.007415) p10 = 0.1415 (0.1132, 0.1698) p01 = -0.003571 (-0.03188, 0.02474) p20 = -0.3768 (-0.4385, -0.315) p11 = -0.02698 (-0.06275, 0.008795) p02 = 0.01456 (-0.04723, 0.07634) p30 = 0.3356 (0.29, 0.3811) p21 = 0.05801 (0.02936, 0.08667) p12 = -0.02206 (-0.05072, 0.006593) p03 = -0.004337 (-0.0499, 0.04122)
X Y vs. VMMedian	1.706e-07	0.9988	0.997	0.0001686	Poly33	p00 = -0.01355 (-0.02333, -0.003757) p10 = 0.1341 (0.08583, 0.1825) p01 = 0.00159 (-0.04673, 0.04991) p20 = -0.3572 (-0.4627, -0.2518) p11 = -0.02126 (-0.08231, 0.03979) p02 = 0.0006836 (-0.1048, 0.1061) p30 = 0.303 (0.2253, 0.3808) p21 = 0.0883 (0.03939, 0.1372) p12 = -0.05176 (-0.1007, -0.002855) p03 = 0.01267 (-0.06508, 0.09043)

Table A-4: Function fitting details for rectangular pore geometry under 1.5 MPa

Function fitting	SSE	R-square	Adjusted R-square	RMSE	Model	Coefficients (with 95% confidence bounds):
VMMean vs. REL	371.4	0.974	0.9675	5.564	Poly3	p1 = -3.543e+07 (-1.771e+08, 1.062e+08) p2 = 1.492e+06 (-2.466e+06, 5.449e+06) p3 = -2.376e+04 (-5.507e+04, 7559) p4 = 154.8 (83.41, 226.2)
VMMedian vs. REL	265.3	0.9815	0.9768	4.702	Poly3	p1 = -7.399e+07 (-1.59e+08, 1.101e+07) p2 = 2.398e+06 (2.641e+05, 4.532e+06) p3 = -2.917e+04 (-4.45e+04, -1.385e+04) p4 = 154.4 (122.8, 186)
X Y vs. VMMean	1.242e-07	0.9997	0.9992	0.0001438	Poly33	p00 = -0.01956 (-0.02791, -0.01121) p10 = 0.2105 (0.1693, 0.2517) p01 = -0.004837 (-0.04606, 0.03638) p20 = -0.5613 (-0.6512, -0.4713) p11 = -0.03989 (-0.09198, 0.01219) p02 = 0.02019 (-0.06978, 0.1102) p30 = 0.5008 (0.4344, 0.5671) p21 = 0.0858 (0.04407, 0.1275) p12 = -0.03243 (-0.07416, 0.009296) p03 = -0.005355 (-0.07169, 0.06098)
X Y vs. VMMedian	3.837e-07	0.9988	0.997	0.0002529	Poly33	p00 = -0.02031 (-0.03499, -0.005626) p10 = 0.2012 (0.1287, 0.2737) p01 = 0.002315 (-0.07016, 0.07479) p20 = -0.5358 (-0.694, -0.3777) p11 = -0.03184 (-0.1234, 0.05973) p02 = 0.001188 (-0.157, 0.1594) p30 = 0.4545 (0.3379, 0.5712) p21 = 0.1323 (0.0589, 0.2056) p12 = -0.0775 (-0.1509, -0.004137) p03 = 0.01884 (-0.09779, 0.1355)

Table A-5: Function fitting details for elliptic pore geometry under 0.5 MPa

Function fitting	SSE	R-square	Adjusted R-square	RMSE	Model	Coefficients (with 95% confidence bounds):
VMMean vs. REL	50.98	0.9975	0.9969	2.061	Poly3	p1 = -7.108e+07 (-1.101e+08, -3.206e+07) p2 = 7.897e+05 (5.563e+04, 1.524e+06) p3 = -5250 (-8845, -1656) p4 = 105.3 (100.8, 109.7)
VMMedian vs. REL	35.96	0.9982	0.9978	1.731	Poly3	p1 = 9.94e+06 (-2.182e+07, 4.17e+07) p2 = -7.21e+05 (-1.299e+06, -1.43e+05) p3 = -607.7 (-3560, 2345) p4 = 101.3 (97.88, 104.7)
X Y vs. VMMean	2.791e-07	0.9993	0.9981	0.0002157	Poly33	p00 = -0.03847 (-0.05012, -0.02682) p10 = 0.2951 (0.2448, 0.3453) p01 = 0.001246 (-0.04902, 0.05151) p20 = -0.67 (-0.7657, -0.5744) p11 = -0.05519 (-0.1107, 0.0003423) p02 = 0.01694 (-0.07873, 0.1126) p30 = 0.4961 (0.4347, 0.5575) p21 = 0.06711 (0.02841, 0.1058) p12 = -0.005002 (-0.0437, 0.03369) p03 = -0.008741 (-0.07015, 0.05267)
X Y vs. VMMedian	4.359e-07	0.9985	0.9962	0.0002695	Poly33	p00 = -0.03481 (-0.04937, -0.02025) p10 = 0.2625 (0.1997, 0.3254) p01 = 0.004753 (-0.05806, 0.06756) p20 = -0.5889 (-0.7085, -0.4694) p11 = -0.06209 (-0.1315, 0.007303) p02 = 0.0128 (-0.1068, 0.1324) p30 = 0.4274 (0.3506, 0.5041) p21 = 0.08343 (0.03507, 0.1318) p12 = -0.01058 (-0.05893, 0.03778) p03 = -0.005001 (-0.08174, 0.07174)

Table A-6: Function fitting details for elliptic pore geometry under 1.0 MPa

Function fitting	SSE	R-square	Adjusted R-square	RMSE	Model	Coefficients (with 95% confidence bounds):
VMMean vs. REL	78.72	0.9965	0.9956	2.561	Poly3	p1 = -9.421e+06 (-1.548e+07, -3.36e+06) p2 = 5.522e+05 (3.241e+05, 7.803e+05) p3 = -1.261e+04 (-1.485e+04, -1.038e+04) p4 = 123.9 (118.4, 129.4)
VMMedian vs. REL	88.45	0.9961	0.9951	2.715	Poly3	p1 = -8.853e+06 (-1.508e+07, -2.629e+06) p2 = 5.439e+05 (3.173e+05, 7.704e+05) p3 = -1.293e+04 (-1.524e+04, -1.061e+04) p4 = 121 (115.6, 126.4)
X Y vs. VMMean	1.114e-06	0.9993	0.9981	0.0004309	Poly33	p00 = -0.07691 (-0.1002, -0.05364) p10 = 0.5902 (0.4897, 0.6906) p01 = 0.00231 (-0.09811, 0.1027) p20 = -1.34 (-1.531, -1.149) p11 = -0.1103 (-0.2212, 0.0006559) p02 = 0.03418 (-0.157, 0.2253) p30 = 0.9923 (0.8696, 1.115) p21 = 0.1341 (0.05681, 0.2114) p12 = -0.009985 (-0.0873, 0.06733) p03 = -0.01767 (-0.1404, 0.105)
X Y vs. VMMedian	1.749e-06	0.9985	0.9962	0.00054	Poly33	p00 = -0.06967 (-0.09884, -0.04051) p10 = 0.5249 (0.3991, 0.6508) p01 = 0.00993 (-0.1159, 0.1358) p20 = -1.177 (-1.417, -0.9378) p11 = -0.1245 (-0.2635, 0.01453) p02 = 0.02485 (-0.2147, 0.2644) p30 = 0.8543 (0.7006, 1.008) p21 = 0.1671 (0.07024, 0.264) p12 = -0.02109 (-0.118, 0.07578) p03 = -0.009545 (-0.1633, 0.1442)

Table A-7: Function fitting details for elliptic pore geometry under 1.5 MPa

Function fitting	SSE	R-square	Adjusted R-square	RMSE	Model	Coefficients (with 95% confidence bounds):
VMMean vs. REL	324.2	0.9847	0.9791	5.429	Poly4	p1 = 1.867e+08 (-5.824e+08, 9.557e+08) p2 = -2.329e+07 (-9.178e+07, 4.52e+07) p3 = 1.049e+06 (-8.458e+05, 2.943e+06) p4 = -2.029e+04 (-3.659e+04, -3999) p5 = 147 (108.9, 185)
VMMedian vs. REL	323	0.9847	0.9837	4.803	Exp1	a = 153.6 (136.9, 170.3) b = -187.5 (-216.4, -158.7)
X Y vs. VMMean	2.511e-06	0.9993	0.9981	0.0006469	Poly33	p00 = -0.1154 (-0.1503, -0.08043) p10 = 0.8851 (0.7343, 1.036) p01 = 0.003598 (-0.1472, 0.1544) p20 = -2.01 (-2.297, -1.723) p11 = -0.1654 (-0.3319, 0.001209) p02 = 0.05098 (-0.236, 0.3379) p30 = 1.488 (1.304, 1.672) p21 = 0.2012 (0.08517, 0.3173) p12 = -0.01512 (-0.1312, 0.101) p03 = -0.0263 (-0.2105, 0.1579)
X Y vs. VMMedian	3.923e-06	0.9985	0.9962	0.0008086	Poly33	p00 = -0.1044 (-0.1481, -0.06077) p10 = 0.7873 (0.5989, 0.9757) p01 = 0.01459 (-0.1738, 0.203) p20 = -1.766 (-2.125, -1.407) p11 = -0.1862 (-0.3944, 0.02195) p02 = 0.03769 (-0.321, 0.3963) p30 = 1.282 (1.051, 1.512) p21 = 0.2503 (0.1052, 0.3954) p12 = -0.03182 (-0.1769, 0.1132) p03 = -0.01454 (-0.2447, 0.2157)

Table A-8: Function fitting details for spheric small topology under 1 MPa

Function fitting	SSE	R-square	Adjusted R-square	RMSE	Model	Coefficients (with 95% confidence bounds):
Ds Dc vs. VMMean	5.855e-08	0.9997	0.9992	9.879e-05	Poly11	p00 = 0.001348 (0.0005825, 0.002113) p10 = 0.0007067 (-0.0009769, 0.00239) p01 = 0.00298 (0.000812, 0.005148)
Ds Dc vs. VMMedian	1.706e-07	0.9988	0.997	0.0001686	Poly11	p00 = 0.0007331 (0.0001422, 0.001324) p10 = -0.0004619 (-0.001762, 0.0008383) p01 = 0.005333 (0.003659, 0.007007)

Table A-9: Function fitting details for spheric large topology under 1 MPa

Function fitting	SSE	R-square	Adjusted R-square	RMSE	Model	Coefficients (with 95% confidence bounds):
VMMean vs. REL	383.1	0.9745	0.9682	5.65	Exp1	a = 176.6 (132.8, 220.3) b = -175.6 (-227.1, -124.1)
VMMedian vs. REL	187	0.9875	0.9844	3.955	Exp1	a = 151.6 (115.3, 187.9) b = -173.5 (-232, -115)
X Y vs. VMMean	5.855e-08	0.9997	0.9992	9.879e-05	Poly11	p00 = -0.05744 (-0.09682, -0.01806) p10 = 0.06935 (0.01299, 0.1257) p01 = 0.007176 (-0.02489, 0.03924)
X Y vs. VMMedian	1.706e-07	0.9988	0.997	0.0001686	Poly11	p00 = -0.05285 (-0.08891, -0.0168) p10 = 0.06223 (0.01063, 0.1138) p01 = 0.008648 (-0.02071, 0.038)

Table A-10: Function fitting details for rectangular geometry under 1 MPa in time

Function fitting	SSE	R-square	Adjusted R-square	RMSE	Model	Coefficients (with 95% confidence bounds):
FVMMean vs. REL	714.7	0.9577	0.9512	7.415	Poly2	p1 = -56.35 (-92.41, -20.29) p2 = 180.8 (120.7, 240.9) p3 = -42.47 (-64.79, -20.15)
X Y vs. FVMMean	0.006053	0.9969	0.9924	0.03176	Poly33	p00 = 5.087 (3.521, 6.654) p10 = -30.08 (-37.95, -22.2) p01 = 0.09739 (-7.778, 7.972) p20 = 72.01 (54.63, 89.39) p11 = 4.376 (-5.662, 14.41) p02 = -1.958 (-19.34, 15.42) p30 = -57.2 (-70.1, -44.3) p21 = -4.661 (-12.76, 3.438) p12 = -2.194 (-10.29, 5.905) p03 = 2.355 (-10.55, 15.26)

B. Annex: Definition of the upper bounds for beam-based scaffolds

The definition of the upper bounds is taken from **Publication I** for each beam-based geometry studied. (Rodríguez-Montaño et al., Comparison of the mechanobiological performance of bone tissue scaffolds based on different unit cell geometries. *Journal of the mechanical behavior of biomedical materials*, 2018, vol. 83, p. 28-45.)

B1. Truncated cuboctahedron

The upper bound D_{max_1} for the truncated cuboctahedron, circular cross section is defined as the beam diameter for which the square interconnection formed by the orange bars showed in Fig. B-1(a) disappears. This occurs when:

$$D_{max\ \_1} = L_1 \qquad \text{(B1)}$$

In the case of the square cross section the square interconnection disappears when (Fig. B-1(b)):

$$D_{max\ \_1} = L_1 \cdot \frac{\sqrt{2}}{2} \qquad \text{(B2)}$$

B2. Truncated Cube

The upper bound D_{max_2} for the truncated cube, circular cross section is defined as the beam diameter for which the triangular interconnection formed by the orange bars showed in the Fig. B-2(a) disappears. If r_c is the radius of the circle inscribed in the triangular interconnection, it follows that this interconnection will disappear when the following relationship is satisfied:

$$D_{max\ \_2} = 2 \cdot r_c \qquad \text{(B3)}$$

The radius r_c of a circle inscribed in a triangle with area A_T and perimeter P_T is given by:

$$r_c = \frac{2 \cdot A_T}{P_T} \qquad \text{(B4)}$$

Figure B-1: Definition of the upper bound D_{max_1} for the truncated cuboctahedron unit cell, circular (a) and square (b) cross section.

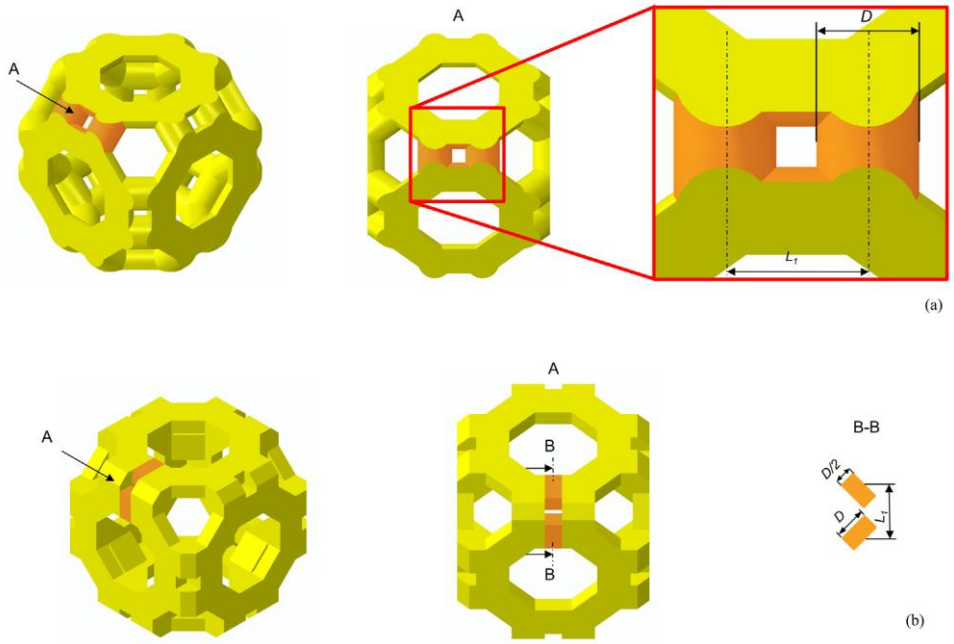

Figure B-2: Definition of the upper bound D_{max_2} for the truncated cube unit cell, circular (a) and square (b) cross section.

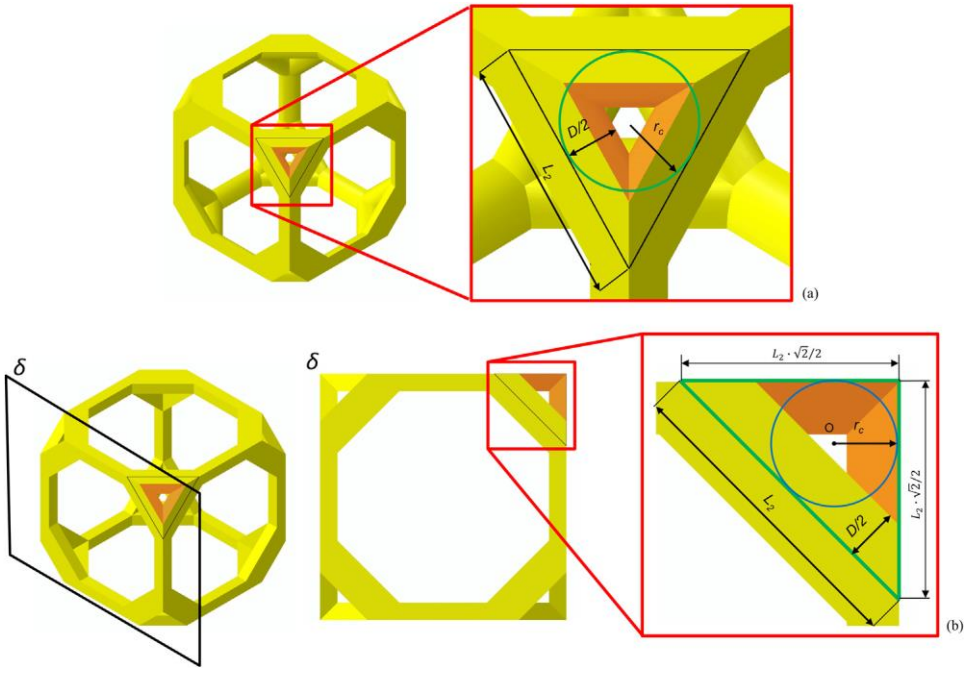

Therefore, the following relationship between the upper bound D_{max_2} and the beam length L_2 can be written:

$$D_{max\ \_2} = 2 \cdot r_c = \frac{L_2 \cdot \sqrt{3}}{3} \qquad \text{(B5)}$$

To compute D_{max_2} in the case of square cross section, the triangular interconnection must be projected onto the lateral plane δ (Fig B-2(b)). This triangular interconnection will disappear when $D_{max\_2}/2 = r_c$ which leads to the following relationship:

$$D_{max\ \_2} = 2 \cdot r_c = \frac{L_2}{1 + \sqrt{2}} \qquad \text{(B6)}$$

B3. Rhombic Dodecahedron

The upper bound D_{max_3} for the rhombic dodecahedron unit cell with both circular and square cross section is defined as the beam diameter for which the rhombic interconnection shown in Fig B-3(a) disappears. If d is the height of the triangle shown in Fig. B-3(a), the following relationships can be written to compute D_{max_3} in function of the beam length L_3 and the angle α = 53.13°:

$$\begin{cases} d = L_3 \cdot \cos\left(\frac{\alpha}{2}\right) \cdot \sin\left(\frac{\alpha}{2}\right) \\ D_{max} = 2 \cdot L_3 \cdot \cos\left(\frac{\alpha}{2}\right) \cdot \sin\left(\frac{\alpha}{2}\right) \end{cases} \qquad \text{(B7)}$$

Figure B-3: Definition of the upper bound D_{max_3} and D_{max_4} for the rhombic dodecahedron (a) and the diamond (b-d) unit cell, respectively, with both circular and square cross section.

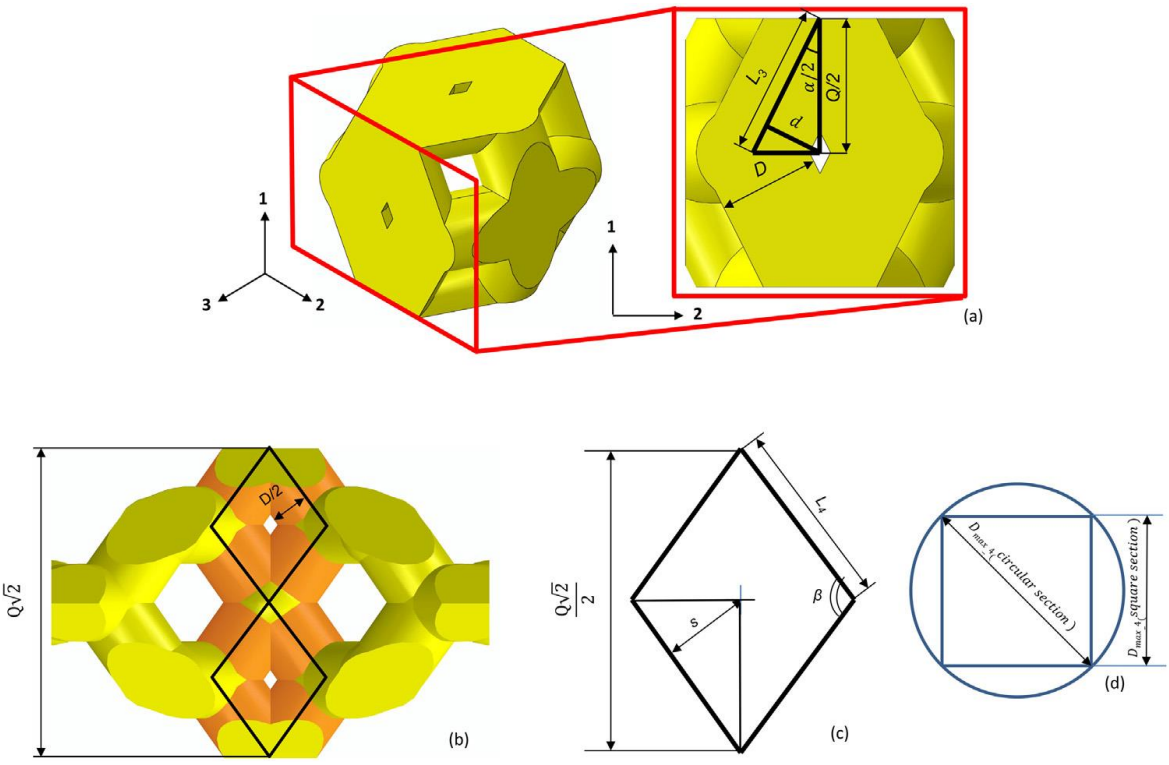

B4. Diamond

The upper bound D_{max_4} of the diamond unit cell with circular cross section is defined as the beam diameter for which the rhombic interconnections (highlighted in orange in Fig. B-3(b)) will disappear. If s is the height of the triangle shown in Fig. B-3(c), the following relationships can be written:

$$\begin{cases} s = L_4 \cdot \cos\left(\frac{\beta}{2}\right) \cdot \sin\left(\frac{\beta}{2}\right) \\ D_{max\_4} = 2 \cdot L_4 \cdot \cos\left(\frac{\beta}{2}\right) \cdot \sin\left(\frac{\beta}{2}\right) \end{cases} \quad \text{(B8)}$$

where β = 109.47°.

D_{max_4} for the square cross section depends on the orientation of the beams included in the unit cell. However, it is possible to state that in the worst case D_{max_4} for square cross section will be equal to D_{max} computed for the circular section (Equation B8) divided by $\sqrt{2}$ (Fig. B-3(d)):

$$D_{max\_4} = \frac{2}{\sqrt{2}} \cdot L_4 \cdot \cos\left(\frac{\beta}{2}\right) \cdot \sin\left(\frac{\beta}{2}\right) \qquad \text{(B9)}$$

C. Annex: Irregular Load Adapted Scaffold Optimization: A computational Framework Based on Mechanobiological Criteria

The original publication can be found here:
https://pubs.acs.org/doi/abs/10.1021/acsbiomaterials.9b01023

Abstract:

By combining load adaptive algorithms with mechanobiological algorithms, a computational framework was developed to design and optimize the microarchitecture of irregular load adapted scaffolds for bone tissue engineering. Skeletonized cancellous bone-inspired lattice structures were built including linear fibers oriented along the internal flux of forces induced by the hypothesized boundary conditions. These structures were then converted into solid finite element models, which were optimized with mechanobiology-based optimization algorithms. The design variable was the diameter of the beams included in the scaffold, while the design objective was the maximization of the fraction of the scaffold volume predicted to be occupied by neo-formed bony tissue. The performance of the designed irregular scaffolds, intended as the capability to favor the formation of bone, was compared with that of the regular ones based on different unit cell geometries. Three different boundary and loading conditions were hypothesized, and for all of them, it was found that the irregular load adapted scaffolds perform better than the regular ones. Interestingly, the numerical predictions of the proposed framework are consistent with the results of experimental studies reported in the literature. The proposed framework appears to be a powerful tool that can be utilized to design high-performance irregular load adapted scaffolds capable of bearing complex load distributions.

References

[1] S. H. Kim, Y. Jung, Y. H. Kim, and S. H. Kim, “Mechano-active scaffolds,” in *Handbook of Intelligent Scaffolds for Tissue Engineering and Regenerative Medicine*, G. Khang, Ed. Pan Stanford Publishing, 2012, pp. 537–559.

[2] D. A. Wahl and J. T. Czernuszka, “Collagen-hydroxyapatite composites for hard tissue repair,” *Eur. Cells Mater.*, vol. 11, pp. 43–56, 2006, doi: vol011a06 [pii].

[3] J. Guo, D. Y. Nguyen, R. T. Tran, Z. Xie, X. Bai, and J. Yang, “Design Strategies and Applications of Citrate-Based Biodegradable Elastomeric Polymers,” in *Natural and Synthetic Biomedical Polymers*, 1st ed., S. Kumbar, C. Laurencin, and M. Deng, Eds. Elsevier, 2014, pp. 259–285.

[4] J. Brown, S. Kumbar, and B. Banik, *Bio-Instructive Scaffolds for Musculoskeletal Tissue Engineering and Regenerative Medicine*. Academic Press, 2016.

[5] L. Geris, J. Vander Sloten, and H. Van Oosterwyck, “In silico biology of bone modelling and remodelling: regeneration,” *Philos. Trans. R. Soc. A Math. Phys. Eng. Sci.*, vol. 367, no. 1895, pp. 2031–2053, 2009, doi: 10.1098/rsta.2008.0293.

[6] Y. Li, S. K. Chen, L. Li, L. Qin, X. L. Wang, and Y. X. Lai, “Bone defect animal models for testing efficacy of bone substitute biomaterials,” *J. Orthop. Transl.*, vol. 3, no. 3, pp. 95–104, 2015, doi: 10.1016/j.jot.2015.05.002.

[7] S. Stewart, S. J. Bryant, J. Ahn, and K. D. Hankenson, “Bone regeneration,” in *Translational Regenerative Medicine*, A. Atala and J. Allickson, Eds. Academic Press, 2015, pp. 313–334.

[8] A. Oryan, A. Kamali, A. Moshirib, and M. B. Eslaminejad, “Role of Mesenchymal Stem Cells in Bone Regenerative Medicine: What Is the Evidence?,” *Cells Tissues Organs*, vol. 204, no. 2, pp. 59–83, 2017, doi: 10.1159/000469704.

[9] C. E. Holy, M. S. Shoichet, and J. E. Davies, “Engineering three-dimensional bone tissue in vitro using biodegradable scaffolds: Investigating initial cell-seeding density and culture period,” *J. Biomed. Mater. Res.*, vol. 51, no. 3, pp. 376–382, 2000, doi: 10.1002/1097-4636(20000905)51:3<376::AID-JBM11>3.0.CO;2-G.

[10] E. Gómez-Barrena, P. Rosset, D. Lozano, J. Stanovici, C. Ermthaller, and F. Gerbhard, “Bone fracture healing: Cell therapy in delayed unions and nonunions,” *Bone*, vol. 70, pp. 93–101, 2015, doi: 10.1016/j.bone.2014.07.033.

[11] K. F. Leong, C. M. Cheah, and C. K. Chua, “Solid freeform fabrication of three-dimensional scaffolds for engineering replacement tissues and organs,” *Biomaterials*, vol. 24, no. 13, pp. 2363–2378, 2003, doi: 10.1016/S0142-9612(03)00030-9.

[12] F. J. O’Brien, “Biomaterials & scaffolds for tissue engineering,” *Mater. Today*, vol. 14, no. 3, pp. 88–95, Mar. 2011, doi: 10.1016/S1369-7021(11)70058-X.

[13] C. M. Murphy, F. J. O’Brien, D. G. Little, and A. Schindeler, “Cell-scaffold

interactions in the bone tissue engineering triad," *Eur. Cells Mater.*, vol. 26, pp. 120–132, 2013.

[14] K. A. Hing, "Bone repair in the twenty-first century: Biology, chemistry or engineering?," *Philos. Trans. R. Soc. A Math. Phys. Eng. Sci.*, vol. 362, no. 1825, pp. 2821–2850, 2004, doi: 10.1098/rsta.2004.1466.

[15] G. Brunetti, P. D'Amelio, M. Wasniewska, G. Mori, and M. F. Faienza, "Editorial: Bone: Endocrine target and organ," *Front. Endocrinol. (Lausanne).*, vol. 8, no. DEC, pp. 249–257, Dec. 2017, doi: 10.3389/fendo.2017.00354.

[16] E. F. Morgan, G. L. Barnes, and T. A. Einhorn, "The Bone Organ System," in *Osteoporosis*, 4th Ed., Elsevier, 2013, pp. 3–20.

[17] B. Clarke, "Normal bone anatomy and physiology.," *Clinical journal of the American Society of Nephrology : CJASN*. 2008, doi: 10.2215/CJN.04151206.

[18] M. Doblaré, J. M. García, and M. J. Gómez, "Modelling bone tissue fracture and healing: A review," *Engineering Fracture Mechanics*, vol. 71, no. 13–14. pp. 1809–1840, 2004, doi: 10.1016/j.engfracmech.2003.08.003.

[19] R. Florencio-Silva, G. R. D. S. Sasso, E. Sasso-Cerri, M. J. Simões, and P. S. Cerri, "Biology of Bone Tissue: Structure, Function, and Factors That Influence Bone Cells," *Biomed Res. Int.*, vol. 2015, 2015, doi: 10.1155/2015/421746.

[20] R. Ozawa, Y. Yamada, T. Nagasaka, and M. Ueda, "A comparison of osteogenesis-related gene expression of mesenchymal stem cells during the osteoblastic differentiation induced by Type-I collagen and/or fibronectin," *Int. J. Oral-Medical Sci.*, vol. 1, no. 2, pp. 139–146, 2003, doi: 10.5466/ijoms.1.139.

[21] L. Qin, W. Liu, H. Cao, and G. Xiao, "Molecular mechanosensors in osteocytes," *Bone Res.*, vol. 8, no. 1, pp. 1–24, 2020, doi: 10.1038/s41413-020-0099-y.

[22] B. Alberts *et al.*, *Molecular Biology of the Cell*. W.W. Norton & Company, 2017.

[23] P. R. Buenzli, P. Pivonka, and D. W. Smith, "Bone refilling in cortical basic multicellular units: Insights into tetracycline double labelling from a computational model," *Biomech. Model. Mechanobiol.*, vol. 13, no. 1, pp. 185–203, 2014, doi: 10.1007/s10237-013-0495-y.

[24] J. R. Perez, D. Kouroupis, D. J. Li, T. M. Best, L. Kaplan, and D. Correa, "Tissue Engineering and Cell-Based Therapies for Fractures and Bone Defects," *Front. Bioeng. Biotechnol.*, vol. 6, no. July, pp. 1–23, 2018, doi: 10.3389/fbioe.2018.00105.

[25] T. A. Franz-Odendaal, B. K. Hall, and P. E. Witten, "Buried alive: How osteoblasts become osteocytes," *Dev. Dyn.*, vol. 235, no. 1, pp. 176–190, 2006, doi: 10.1002/dvdy.20603.

[26] D. C. Betts and R. Müller, "Mechanical regulation of bone regeneration: Theories, models, and experiments," *Front. Endocrinol. (Lausanne).*, vol. 5, no. DEC, pp. 1–14, 2014, doi: 10.3389/fendo.2014.00211.

[27] R. Marsell and T. A. Einhorn, "The biology of fracture healing," *Injury*, vol. 42, no. 6,

pp. 551–555, Jun. 2011, doi: 10.1016/j.injury.2011.03.031.

[28] M. R. Appleford, “Trabecular Calcium Phosphate Scaffolds for Bone Regeneration Trabecular Calcium Phosphate Scaffolds for Bone Regeneration,” 2007, doi: 10.21007/etd.cghs.2007.0017.

[29] P. Su *et al.*, “Mesenchymal stem cell migration during bone formation and bone diseases therapy,” *Int. J. Mol. Sci.*, vol. 19, no. 8, 2018, doi: 10.3390/ijms19082343.

[30] S. J. Shefelbine, P. Augat, L. Claes, and U. Simon, “Trabecular bone fracture healing simulation with finite element analysis and fuzzy logic,” *J. Biomech.*, vol. 38, no. 12, pp. 2440–2450, 2005, doi: 10.1016/j.jbiomech.2004.10.019.

[31] M. A. Fernandez-Yague, S. A. Abbah, L. McNamara, D. I. Zeugolis, A. Pandit, and M. J. Biggs, “Biomimetic Approaches in Bone Tissue Engineering: Integrating Biological and Physicomechanical Strategies,” *Adv. Drug Deliv. Rev.*, vol. 84, pp. 1–29, Sep. 2014, doi: 10.1016/j.addr.2014.09.005.

[32] E. C. Yusko and C. L. Asbury, “Force is a signal that cells cannot ignore,” *Mol. Biol. Cell*, vol. 25, no. 23, pp. 3717–3725, 2014, doi: 10.1091/mbc.E13-12-0707.

[33] A. Gelmi and C. E. Schutt, “Stimuli-Responsive Biomaterials: Scaffolds for Stem Cell Control,” *Adv. Healthc. Mater.*, vol. 10, no. 1, pp. 1–30, 2021, doi: 10.1002/adhm.202001125.

[34] U. Meyer, T. Meyer, J. Handschel, and H. P. Wiesmann, *Fundamentals of Tissue Engineering and Regenerative Medicine*. Berlin, Heidelberg: Springer Berlin Heidelberg, 2009.

[35] L. Polo-Corrales, M. Latorre-Esteves, and J. E. Ramirez-Vick, “Scaffold design for bone regeneration.,” *J. Nanosci. Nanotechnol.*, vol. 14, no. 1, pp. 15–56, 2014, doi: 10.1166/jnn.2014.9127.

[36] K. S. Houschyar *et al.*, “Wnt Pathway in Bone Repair and Regeneration – What Do We Know So Far,” *Front. Cell Dev. Biol.*, vol. 6, no. January, pp. 1–13, 2019, doi: 10.3389/fcell.2018.00170.

[37] M. Levin and C. G. Stevenson, “Regulation of cell behavior and tissue patterning by bioelectrical signals: challenges and opportunities for biomedical engineering.,” *Annu. Rev. Biomed. Eng.*, vol. 14, pp. 295–323, 2012, doi: 10.1146/annurev-bioeng-071811-150114.

[38] C. Chen, X. Bai, Y. Ding, and I. S. Lee, “Electrical stimulation as a novel tool for regulating cell behavior in tissue engineering,” *Biomater. Res.*, vol. 23, no. 1, pp. 1–12, 2019, doi: 10.1186/s40824-019-0176-8.

[39] L. Leppik, K. M. C. Oliveira, M. B. Bhavsar, and J. H. Barker, “Electrical stimulation in bone tissue engineering treatments,” *Eur. J. Trauma Emerg. Surg.*, vol. 46, no. 2, pp. 231–244, 2020, doi: 10.1007/s00068-020-01324-1.

[40] A. S. Çakmak *et al.*, “Synergistic effect of exogeneous and endogeneous electrostimulation on osteogenic differentiation of human mesenchymal stem cells

seeded on silk scaffolds," *J. Orthop. Res.*, 2016, doi: 10.1002/jor.23059.

[41] M. G. Vavva *et al.*, "Effect of ultrasound on bone fracture healing: A computational bioregulatory model," *Comput. Biol. Med.*, vol. 100, pp. 74–85, 2018, doi: 10.1016/j.compbiomed.2018.06.024.

[42] K. N. Grivas *et al.*, "Effect of ultrasound on bone fracture healing: A computational mechanobioregulatory model," *J. Acoust. Soc. Am.*, vol. 145, no. 2, pp. 1048–1059, 2019, doi: 10.1121/1.5089221.

[43] H. Huang, R. D. Kamm, and R. T. Lee, "Cell mechanics and mechanotransduction: pathways, probes, and physiology.," *Am. J. Physiol. Cell Physiol.*, vol. 287, no. 1, pp. C1-11, 2004, doi: 10.1152/ajpcell.00559.2003.

[44] A. J. Steward and D. J. Kelly, "Mechanical regulation of mesenchymal stem cell differentiation," *J. Anat.*, vol. 227, no. 6, pp. 717–731, 2015, doi: 10.1111/joa.12243.

[45] D. Huber, A. Oskooei, X. Casadevall Solvas, Andrew Demello, and G. V. Kaigala, "Hydrodynamics in Cell Studies," *Chem. Rev.*, vol. 118, no. 4, pp. 2042–2079, 2018, doi: 10.1021/acs.chemrev.7b00317.

[46] W. R. Thompson, C. T. Rubin, and J. Rubin, "Mechanical regulation of signaling pathways in bone," *Gene*, vol. 503, no. 2, pp. 179–193, 2012, doi: 10.1016/j.gene.2012.04.076.

[47] E. K. Rodriguez, A. Hoger, and A. D. McCulloch, "Stress-dependent finite growth in soft elastic tissues," *J. Biomech.*, vol. 27, no. 4, pp. 455–467, 1994, doi: 10.1016/0021-9290(94)90021-3.

[48] D. Ambrosi *et al.*, "Growth and remodelling of living tissues: Perspectives, challenges and opportunities," *J. R. Soc. Interface*, vol. 16, no. 157, 2019, doi: 10.1098/rsif.2019.0233.

[49] P. J. Prendergast, S. Checa, and D. Lacroix, "Computational Models of Tissue Differentiation," in *Computational Modeling in Biomechanics*, S. De, F. Guilak, and M. R. K. Mofrad, Eds. Springer Science, 2010, pp. 353–372.

[50] L. E. Delgado, "Modelos matemáticos de reparación ósea," Universidad Complutense de Madrid, 2009.

[51] S. M. Perren and J. Cordey, "The concept of interfragmentary strain pp. 63- 77. Current concepts of internal fixation of fractures.," *Curr. concepts Intern. Fixat. Fract.*, pp. 63–77, 1980.

[52] H. M. Frost, "Bone's Mechanostat: A 2003 Update," *Anat. Rec. - Part A Discov. Mol. Cell. Evol. Biol.*, vol. 275, no. 2, pp. 1081–1101, 2003, doi: 10.1002/ar.a.10119.

[53] S. C. Cowin and D. H. Hegedus, "Bone remodeling I: theory of adaptive elasticity," *J. Elast.*, vol. 6, no. 3, pp. 313–326, 1976, doi: 10.1007/BF00041724.

[54] S. C. Cowin, "Bone poroelasticity," *Bone Mech. Handbook, Second Ed.*, vol. 32, pp. 23-1-23–31, 2001.

[55] R. Huiskes, H. Weinans, H. J. Grootenboer, M. Dalstra, B. Fudala, and T. J. Slooff, “Adaptive bone-remodeling theory applied to prosthetic-design analysis,” *J. Biomech.*, vol. 20, no. 11–12, pp. 1135–1150, 1987, doi: 10.1016/0021-9290(87)90030-3.

[56] H. Weinans, R. Huiskes, and H. J. Grootenboer, “The behavior of adaptive bone-remodeling simulation models,” *J. Biomech.*, vol. 25, no. 12, pp. 1425–1441, 1992, doi: 10.1016/0021-9290(92)90056-7.

[57] D. R. Carter, G. S. Beaupré, N. J. Giori, and J. A. Helms, “Mechanobiology of skeletal regeneration,” *Clin. Orthop. Relat. Res.*, no. 355 Suppl, pp. S41-55, 1998, doi: Non-programmatic.

[58] L. E. Claes and C. A. Heigele, “Magnitudes of local stress and strain along bony surfaces predict the course and type of fracture healing,” *J. Biomech.*, vol. 32, pp. 255–266, 1999.

[59] P. J. Prendergast, R. Huiskes, K. Søballe, and S, “Biophysical stimuli on cells during tissue differentiation at implant interfaces,” *J. Biomech.*, vol. 30, no. 6, pp. 539–548, 1997, doi: 10.1016/S0021-9290(96)00140-6.

[60] D. Lacroix and P. J. Prendergast, “A mechano-regulation model for tissue differentiation during fracture healing: Analysis of gap size and loading,” *J. Biomech.*, vol. 35, no. 9, pp. 1163–1171, 2002, doi: 10.1016/S0021-9290(02)00086-6.

[61] D. R. Suárez, “Theories of mechanically induced tissue differentiation and adaptation in the musculoskeletal system,” *Ing. y Univ.*, vol. 20, no. 1, pp. 21–40, 2015, doi: 10.11144/javeriana.iyu20-1.tmit.

[62] D. P. Byrne, D. Lacroix, J. A. Planell, D. J. Kelly, and P. J. Prendergast, “Simulation of tissue differentiation in a scaffold as a function of porosity, Young’s modulus and dissolution rate: Application of mechanobiological models in tissue engineering,” *Biomaterials*, vol. 28, no. 36, pp. 5544–5554, 2007, doi: 10.1016/j.biomaterials.2007.09.003.

[63] H. Khayyeri, S. Checa, M. Tägil, F. J. O’Brien, and P. J. Prendergast, “Tissue differentiation in an in vivo bioreactor: in silico investigations of scaffold stiffness.,” *J. Mater. Sci. Mater. Med.*, vol. 21, no. 8, pp. 2331–6, 2010, doi: 10.1007/s10856-009-3973-0.

[64] J. A. Sanz-Herrera, J. M. Garcia-Aznar, and M. Doblare, “A mathematical model for bone tissue regeneration inside a specific type of scaffold,” *Biomech. Model. Mechanobiol.*, vol. 7, no. 5, pp. 355–366, 2008, doi: 10.1007/s10237-007-0089-7.

[65] J. A. Sanz-Herrera, J. M. García-Aznar, and M. Doblaré, “Micro-macro numerical modelling of bone regeneration in tissue engineering,” *Comput. Methods Appl. Mech. Eng.*, vol. 197, no. 33–40, pp. 3092–3107, 2008, doi: 10.1016/j.cma.2008.02.010.

[66] T. Adachi, Y. Osako, M. Tanaka, M. Hojo, and S. J. Hollister, “Framework for optimal design of porous scaffold microstructure by computational simulation of bone regeneration,” *Biomaterials*, vol. 27, no. 21, pp. 3964–3972, 2006, doi:

10.1016/j.biomaterials.2006.02.039.

[67] G. S. Beaupre and T. E. Orr, “An approach for time-dependent bone modeling and remodeling—theoretical development - Beaupré - 2005 - Journal of Orthopaedic Research - Wiley Online Library,” *J. Orthop. …*, no. 3, pp. 651–661, 1990, [Online]. Available: http://onlinelibrary.wiley.com/doi/10.1002/jor.1100080506/abstract%5Cnpapers2://publication/uuid/945494C3-62EC-49A9-849A-91728212793D.

[68] A. Bailón-Plaza and M. C. H. Van Der Meulen, “A mathematical framework to study the effects of growth factor influences on fracture healing,” *J. Theor. Biol.*, vol. 212, no. 2, pp. 191–209, 2001, doi: 10.1006/jtbi.2001.2372.

[69] D. Lacroix, P. J. Prendergast, G. Li, and D. Marsh, “Biomechanical model to simulate tissue differentiation and bone regeneration: application to fracture healing,” *Med. Biol. Eng. Comput.*, vol. 40, no. 1, pp. 14–21, 2002, doi: 10.1007/BF02347690.

[70] L. Geris, A. Gerisch, J. Vander Sloten, R. Weiner, and H. Van Oosterwyck, “Angiogenesis in bone fracture healing: A bioregulatory model,” *J. Theor. Biol.*, vol. 251, no. 1, pp. 137–158, 2008, doi: 10.1016/j.jtbi.2007.11.008.

[71] M. J. Gómez-Benito, J. M. García-Aznar, J. H. Kuiper, and M. Doblaré, “Influence of fracture gap size on the pattern of long bone healing: A computational study,” *J. Theor. Biol.*, vol. 235, no. 1, pp. 105–119, 2005, doi: 10.1016/j.jtbi.2004.12.023.

[72] J. M. García-Aznar, J. H. Kuiper, M. J. Gómez-Benito, M. Doblaré, and J. B. Richardson, “Computational simulation of fracture healing: Influence of interfragmentary movement on the callus growth,” *J. Biomech.*, vol. 40, no. 7, pp. 1467–1476, 2007, doi: 10.1016/j.jbiomech.2006.06.013.

[73] S. Kawamura *et al.*, “Simulation of Fracture Healing Using Cellular Automata (Influence of Operation Conditions on Healing Result in External Fixation),” *JSME Int. J. Ser. A Solid Mech. Mater. Eng.*, vol. 2, no. 48, pp. 57–64, 2005.

[74] M. Wang and N. Yang, “Three-dimensional computational model simulating the fracture healing process with both biphasic poroelastic finite element analysis and fuzzy logic control,” *Sci. Rep.*, vol. 8, no. 1, pp. 1–13, 2018, doi: 10.1038/s41598-018-25229-7.

[75] C. M. Bidan, F. M. Wang, and J. W. C. Dunlop, “A three-dimensional model for tissue deposition on complex surfaces,” *Comput. Methods Biomech. Biomed. Engin.*, vol. 16, no. 10, pp. 1056–1070, 2013, doi: 10.1080/10255842.2013.774384.

[76] C. M. Bidan, K. P. Kommareddy, M. Rumpler, P. Kollmannsberger, P. Fratzl, and J. W. C. Dunlop, “Geometry as a Factor for Tissue Growth: Towards Shape Optimization of Tissue Engineering Scaffolds,” *Adv. Healthc. Mater.*, vol. 2, no. 1, pp. 186–194, 2013, doi: 10.1002/adhm.201200159.

[77] P. F. Egan, K. A. Shea, and S. J. Ferguson, “Simulated tissue growth for 3D printed scaffolds,” *Biomech. Model. Mechanobiol.*, vol. 17, no. 5, pp. 1481–1495, 2018, doi: 10.1007/s10237-018-1040-9.

[78] Y. F. Feng *et al.*, “Influence of Architecture of β-Tricalcium Phosphate Scaffolds on Biological Performance in Repairing Segmental Bone Defects,” *PLoS One*, vol. 7, no. 11, 2012, doi: 10.1371/journal.pone.0049955.

[79] J. Chang, X. Zhang, and K. Dai, “Material characteristics, surface/interface, and biological effects on the osteogenesis of bioactive materials,” in *Bioactive Materials for Bone Regeneration*, Elsevier, 2020, pp. 1–103.

[80] L. J. Gibson and M. F. Ashby, *Cellular materials in nature and medicine*, vol. 51. Cambridge University Press, 2010.

[81] A. Boccaccio, A. E. Uva, M. Fiorentino, L. Lamberti, and G. Monno, “A Mechanobiology-based Algorithm to Optimize the Microstructure Geometry of Bone Tissue Scaffolds,” *Int. J. Biol. Sci.*, vol. 12, no. 1, pp. 1–17, 2016, doi: 10.7150/ijbs.13158.

[82] J. A. a. Sanz-Herrera, M. Doblaré, and J. M. M. García-Aznar, “Scaffold microarchitecture determines internal bone directional growth structure: A numerical study,” *J. Biomech.*, vol. 43, no. 13, pp. 2480–2486, 2010, doi: 10.1016/j.jbiomech.2010.05.027.

[83] G. Li *et al.*, “In vitro and in vivo study of additive manufactured porous Ti6Al4V scaffolds for repairing bone defects,” *Sci. Rep.*, vol. 6, pp. 1–11, 2016, doi: 10.1038/srep34072.

[84] M. A. Velasco Peña and D. A. Garzón Alvarado, “Implantes Scaffolds para regeneración ósea. Materiales, técnicas y modelado mediante sistemas de reacción-difusión,” *Rev. Cuba. Investig. Biomédicas*, vol. 29, no. 1, pp. 0–0, 2010.

[85] Q. Fu, E. Saiz, M. N. Rahaman, and A. P. Tomsia, “Bioactive glass scaffolds for bone tissue engineering: State of the art and future perspectives,” *Mater. Sci. Eng. C*, vol. 31, no. 7, pp. 1245–1256, 2011, doi: 10.1016/j.msec.2011.04.022.

[86] T. Wu, S. Yu, D. Chen, and Y. Wang, “Bionic design, materials and performance of bone tissue scaffolds,” *Materials (Basel).*, vol. 10, no. 10, 2017, doi: 10.3390/ma10101187.

[87] T. Albrektsson and C. Johansson, “Osteoinduction, osteoconduction and osseointegration,” *Eur. Spine J.*, vol. 10, pp. S96–S101, 2001, doi: 10.1007/s005860100282.

[88] M. A. Velasco, C. A. Narváez-Tovar, and D. A. Garzón-Alvarado, “Design, Materials, and Mechanobiology of Biodegradable Scaffolds for Bone Tissue Engineering,” *Biomed Res. Int.*, vol. 2015, p. 21, 2015, doi: 10.1155/2015/729076.

[89] B. P. Chan and K. W. Leong, “Scaffolding in tissue engineering: General approaches and tissue-specific considerations,” *Eur. Spine J.*, vol. 17, no. SUPPL. 4, 2008, doi: 10.1007/s00586-008-0745-3.

[90] T. W. Gilbert, T. L. Sellaro, and S. F. Badylak, “Decellularization of tissues and organs,” *Biomaterials*, vol. 27, no. 19, pp. 3675–3683, 2006, doi: 10.1016/j.biomaterials.2006.02.014.

[91] T. S. Karande and C. M. Agrawal, “Functions and requirements of synthetic scaffolds in tissue engineering,” *Nanotechnol. Tissue Eng. Scaffold*, pp. 53–86, 2008, doi: 10.1201/9781420051834.ch3.

[92] F. R. A. J. Rose and R. O. C. Oreffo, “Bone Tissue Engineering: Hope vs Hype,” *Biochem. Biophys. Res. Commun.*, vol. 292, no. 1, pp. 1–7, 2002, doi: 10.1006/bbrc.2002.6519.

[93] B. Dhandayuthapani, Y. Yoshida, T. Maekawa, and D. S. Kumar, “Polymeric scaffolds in tissue engineering application: A review,” *Int. J. Polym. Sci.*, vol. 2011, no. ii, 2011, doi: 10.1155/2011/290602.

[94] C. Gomez, “A Unit Cell Based Multi-scale Modeling and Design Approach for Tissue Engineered Scaffolds,” Drexel University, 2007.

[95] H. N. Chia and B. M. Wu, “Recent advances in 3D printing of biomaterials,” *J. Biol. Eng.*, vol. 9, no. 1, pp. 1–14, 2015, doi: 10.1186/s13036-015-0001-4.

[96] Z. Gu, J. Fu, H. Lin, and Y. He, “Development of 3D bioprinting: From printing methods to biomedical applications,” *Asian J. Pharm. Sci.*, vol. 15, no. 5, pp. 529–557, 2020, doi: 10.1016/j.ajps.2019.11.003.

[97] S. Checa, C. Sandino, D. P. Byrne, D. J. Kelly, D. Lacroix, and P. J. Prendergast, “Computational techniques for selection of biomaterial scaffolds for tissue engineering,” in *Advances on Modeling in Tissue Engineering*, P. R. Fernandes and P. J. Bártolo, Eds. Springer Science & Business Media, 2011, pp. 55–69.

[98] S. R. Caliari and B. A. C. Harley, “2.216 – Collagen–GAG Materials,” in *Comprehensive Biomaterials*, 2011, pp. 279–302.

[99] R. Hedayati, M. Sadighi, M. Mohammadi-Aghdam, and A. A. Zadpoor, “Mechanical behavior of additively manufactured porous biomaterials made from truncated cuboctahedron unit cells,” *Int. J. Mech. Sci.*, vol. 106, no. November, pp. 19–38, 2016, doi: 10.1016/j.ijmecsci.2015.11.033.

[100] A. Boccaccio, A. E. Uva, M. Fiorentino, G. Mori, and G. Monno, “Geometry design optimization of functionally graded scaffolds for bone tissue engineering: A mechanobiological approach,” *PLoS One*, vol. 11, no. 1, 2016, doi: 10.1371/journal.pone.0146935.

[101] F. J. O’Brien, B. A. Harley, I. V. Yannas, and L. J. Gibson, “The effect of pore size on cell adhesion in collagen-GAG scaffolds,” *Biomaterials*, vol. 26, no. 4, pp. 433–441, 2005, doi: 10.1016/j.biomaterials.2004.02.052.

[102] A. J. EL Haj, K. Hampson, and G. Gogniat, “Bioreactors for Connective Tissue Engineering: Design and Monitoring Innovations,” in *Bioreactor Systems for Tissue Engineering*, vol. 1, C. Kasper, M. Van Griensven, and R. Pörtner, Eds. Springer Science & Business Media, 2009, pp. 81–94.

[103] C. H. Ma, H. B. Zhang, S. M. Yang, R. X. Yin, X. J. Yao, and W. J. Zhang, “Comparison of the degradation behavior of PLGA scaffolds in micro-channel, shaking, and static conditions,” *Biomicrofluidics*, vol. 12, no. 3, 2018, doi: 10.1063/1.5021394.

[104] H. Zhang, L. Zhou, and W. Zhang, “Control of scaffold degradation in tissue engineering: A review,” *Tissue Eng. - Part B Rev.*, vol. 20, no. 5, pp. 492–502, 2014, doi: 10.1089/ten.teb.2013.0452.

[105] A. H. M. Yusop, A. Alsakkaf, M. R. A. Kadir, I. Sukmana, and H. Nur, “Corrosion of porous Mg and Fe scaffolds: a review of mechanical and biocompatibility responses,” *Corros. Eng. Sci. Technol.*, vol. 0, no. 0, pp. 1–17, 2021, doi: 10.1080/1478422x.2021.1879427.

[106] R. Detsch and A. R. Boccaccini, “The role of osteoclasts in bone tissue engineering.,” *J. Tissue Eng. Regen. Med.*, vol. 9, no. 10, pp. 1133–49, Oct. 2015, doi: 10.1002/term.1851.

[107] M. Brugmans, “The interplay between biomaterial degradation and tissue properties: Relevance for in situ cardiovascular tissue engineering,” Technische Universiteit Eindhoven, 2015.

[108] G. Erkizia, A. Rainer, E. M. De Juan-Pardo, and J. Aldazabal, “Computer Simulation of Scaffold Degradation,” *J. Phys. Conf. Ser.*, vol. 252, no. 1, p. 012004, 2010, doi: 10.1088/1742-6596/252/1/012004.

[109] G. Chao, S. Xiaobo, C. Chenglin, D. Yinsheng, P. Yuepu, and L. Pinghua, “A cellular automaton simulation of the degradation of porous polylactide scaffold: I. Effect of porosity,” *Mater. Sci. Eng. C*, vol. 29, no. 6, pp. 1950–1958, 2009, doi: 10.1016/j.msec.2009.03.003.

[110] L. Yunfeng, Z. Gen, X. Jianbin, J. Xianfeng, and P. Wei, “Simulation of Bone Regeneration within Stress Environment based on Scaffold Degradation,” *Int. J. Digit. Content Technol. its Appl.*, vol. 7, no. 6, pp. 799–807, 2013, doi: 10.4156/jdcta.vol7.issue6.90.

[111] Y. Chen, S. Zhou, and Q. Li, “Biomaterials Microstructure design of biodegradable scaffold and its effect on tissue regeneration,” *Biomaterials*, vol. 32, no. 22, pp. 5003–5014, 2011, doi: 10.1016/j.biomaterials.2011.03.064.

[112] A. C. Vieir, R. M. Guedes, and V. Tita, “On different approaches to simulate the mechanical behavior of scaffolds during degradation,” *Procedia Eng.*, vol. 110, pp. 21–28, 2015, doi: 10.1016/j.proeng.2015.07.005.

[113] J. Pan, “Modelling Degradation of Bioresorbable Polymeric Medical Devices,” in *Modelling Degradation of Bioresorbable Polymeric Medical Devices*, J. Pan, Ed. Woodhead Publishing, 2015, pp. 1–14.

[114] Q. Shi, Q. Chen, N. Pugno, and Z. Y. Li, “Effect of rehabilitation exercise durations on the dynamic bone repair process by coupling polymer scaffold degradation and bone formation,” *Biomech. Model. Mechanobiol.*, vol. 17, no. 3, pp. 763–775, 2018, doi: 10.1007/s10237-017-0991-6.

[115] L. Wang, Q. Shi, Y. Cai, Q. Chen, X. Guo, and Z. Li, “Mechanical–chemical coupled modeling of bone regeneration within a biodegradable polymer scaffold loaded with VEGF,” *Biomech. Model. Mechanobiol.*, vol. 19, no. 6, pp. 2285–2306, 2020, doi: 10.1007/s10237-020-01339-y.

[116] M. A. Sulong, I. V. Belova, A. R. Boccaccini, G. E. Murch, and T. Fiedler, “A model of the mechanical degradation of foam replicated scaffolds,” *J. Mater. Sci.*, vol. 51, no. 8, pp. 3824–3835, 2016, doi: 10.1007/s10853-015-9701-x.

[117] D. A. Garzón-Alvarado, M. A. Velasco, and C. A. Narváez-Tovar, “Modeling porous scaffold microstructure by a reaction-diffusion system and its degradation by hydrolysis,” *Comput. Biol. Med.*, vol. 42, no. 2, pp. 147–155, 2012, doi: 10.1016/j.compbiomed.2011.11.002.

[118] S. J. Hollister, “Scaffold engineering: A bridge to where?,” *Biofabrication*, vol. 1, no. 1, 2009, doi: 10.1088/1758-5082/1/1/012001.

[119] M. Rumpler, A. Woesz, J. W. . Dunlop, J. T. van Dongen, and P. Fratzl, “The effect of geometry on three-dimensional tissue growth,” *J. R. Soc. Interface*, vol. 5, no. 27, pp. 1173–1180, 2008, doi: 10.1098/rsif.2008.0064.

[120] E. Saito, E. E. Liao, and W.-W. Hu, “Effects of designed PLLA and 50:50 PLGA scaffold architectures on bone formation in vivo,” *J. Tissue Eng. Regen. Med.*, vol. 4, no. 7, pp. 99–111, 2011, doi: 10.1002/term.

[121] W. Bian *et al.*, “Morphological characteristics of cartilage - bone transitional structures in the human knee joint and CAD design of an osteochondral scaffold,” *Biomed. Eng. Online*, pp. 1–14, 2016, doi: 10.1186/s12938-016-0200-3.

[122] L. Wang, M. Xu, L. Zhang, Q. Zhou, and L. Luo, “Automated quantitative assessment of three-dimensional bioprinted hydrogel scaffolds using optical coherence tomography,” *Biomed. Opt. Express*, vol. 7, no. 3, p. 894, 2016, doi: 10.1364/BOE.7.000894.

[123] A. Liu *et al.*, “3D Printing Surgical Implants at the clinic: A Experimental Study on Anterior Cruciate Ligament Reconstruction.,” *Sci. Rep.*, vol. 6, no. October 2015, p. 21704, 2016, doi: 10.1038/srep21704.

[124] V. T. Athanasiou, D. J. Papachristou, A. Panagopoulos, A. Saridis, C. D. Scopa, and P. Megas, “Histological comparison of autograft, allograft-DBM, xenograft, and synthetic grafts in a trabecular bone defect: an experimental study in rabbits.,” *Med. Sci. Monit.*, vol. 16, no. 1, pp. BR24-31, Jan. 2010, [Online]. Available: http://www.ncbi.nlm.nih.gov/pubmed/20037482.

[125] A. M. Pobloth *et al.*, “Mechanobiologically optimized 3D titanium-mesh scaffolds enhance bone regeneration in critical segmental defects in sheep,” *Sci. Transl. Med.*, vol. 10, no. 423, 2018, doi: 10.1126/scitranslmed.aam8828.

[126] X. Zhou *et al.*, “Improved Human Bone Marrow Mesenchymal Stem Cell Osteogenesis in 3D Bioprinted Tissue Scaffolds with Low Intensity Pulsed Ultrasound Stimulation,” *Sci. Rep.*, vol. 6, no. August, pp. 1–12, 2016, doi: 10.1038/srep32876.

[127] M. Aliabouzar, S. J. Lee, X. Zhou, G. L. Zhang, and K. Sarkar, “Effects of scaffold microstructure and low intensity pulsed ultrasound on chondrogenic differentiation of human mesenchymal stem cells,” *Biotechnol. Bioeng.*, vol. 115, no. 2, pp. 495–506, 2018, doi: 10.1002/bit.26480.

[128] X. Chen and Q. Hu, “Bioactive Glasses,” *Front. Nanobiomedical Res.*, vol. 3, no. October, pp. 147–182, 2017, doi: 10.1142/9789813202573_0004.

[129] I. Gendviliene *et al.*, “Assessment of the morphology and dimensional accuracy of 3D printed PLA and PLA/HAp scaffolds,” *J. Mech. Behav. Biomed. Mater.*, vol. 104, no. December 2019, p. 103616, 2020, doi: 10.1016/j.jmbbm.2020.103616.

[130] C. Silva, C. J. Cortés-Rodriguez, J. Hazur, S. Reakasame, and A. R. Boccaccini, “Rational design of a triple-layered coaxial extruder system: In silico and in vitro evaluations directed toward optimizing cell viability,” *Int. J. Bioprinting*, vol. 6, no. 4, pp. 1–10, 2020, doi: 10.18063/IJB.V6I4.282.

[131] J. Zhang, E. Wehrle, J. R. Vetsch, G. R. Paul, M. Rubert, and R. Müller, “Alginate dependent changes of physical properties in 3D bioprinted cell-laden porous scaffolds affect cell viability and cell morphology,” *Biomed. Mater.*, vol. 14, no. 6, p. 065009, Sep. 2019, doi: 10.1088/1748-605X/ab3c74.

[132] W. Li, “45S5 Bioactive Glass-Based Composite Scaffolds with Polymer Coatings for Bone Tissue Engineering Therapeutics,” Friedrich-Alexander-Universität Erlangen-Nürnberg, 2015.

[133] J. Li, M. Chen, X. Wei, Y. Hao, and J. Wang, “Evaluation of 3D-printed polycaprolactone scaffolds coated with freeze-dried platelet-rich plasma for bone regeneration,” *Materials (Basel).*, vol. 10, no. 7, 2017, doi: 10.3390/ma10070831.

[134] C. D. Chaput, “Optimization of scaffolds and surface-based treatments for orthopedic applications,” *Spine (Phila. Pa. 1976).*, vol. 41, no. 7, pp. S14–S15, 2016, doi: 10.1097/BRS.0000000000001426.

[135] D. Lin, K. Yang, W. Tang, Y. Liu, Y. Yuan, and C. Liu, “Colloids and Surfaces B : Biointerfaces A poly (glycerol sebacate) -coated mesoporous bioactive glass scaffold with adjustable mechanical strength , degradation rate , controlled-release and cell behavior for bone tissue engineering,” *Colloids Surfaces B Biointerfaces*, vol. 131, pp. 1–11, 2015, doi: 10.1016/j.colsurfb.2015.04.031.

[136] F. Westhauser *et al.*, “Three-dimensional polymer coated 45S5-type bioactive glass scaffolds seeded with human mesenchymal stem cells show bone formation in vivo,” *J. Mater. Sci. Mater. Med.*, vol. 27, no. 7, 2016, doi: 10.1007/s10856-016-5732-3.

[137] A. Cipitria *et al.*, “BMP delivery complements the guiding effect of scaffold architecture without altering bone microstructure in critical-sized long bone defects: A multiscale analysis,” *Acta Biomater.*, vol. 23, pp. 282–294, 2015, doi: 10.1016/j.actbio.2015.05.015.

[138] A. Entezari *et al.*, “Architectural Design of 3D Printed Scaffolds Controls the Volume and Functionality of Newly Formed Bone,” *Adv. Healthc. Mater.*, vol. 8, no. 1, pp. 1–12, 2019, doi: 10.1002/adhm.201801353.

[139] A. Anindyajati, P. Boughton, and A. J. Ruys, “Mechanical and cytocompatibility evaluation of UHMWPE/PCL/Bioglass® fibrous composite for acetabular labrum implant,” *Materials (Basel).*, vol. 16, no. 6, 2019, doi: 10.3390/ma12060916.

[140] A. A. Zadpoor and R. Hedayati, “Analytical relationships for prediction of the mechanical properties of additively manufactured porous biomaterials,” *J. Biomed. Mater. Res. A*, vol. 104A, no. 12, pp. 3164–3174, 2016, doi: 10.1002/jbm.a.35855.

[141] K. A. Corin and L. J. Gibson, “Cell Contraction Forces in Scaffolds with Varying Pore Size and Cell Density,” *Am. J. Manag. Care*, vol. 15, no. 3, pp. 189–193, 2009, doi: 10.1038/jid.2014.371.

[142] M. Afshar, A. P. Anaraki, H. Montazerian, and J. Kadkhodapour, “Additive manufacturing and mechanical characterization of graded porosity scaffolds designed based on triply periodic minimal surface architectures,” *J. Mech. Behav. Biomed. Mater.*, vol. 62, pp. 481–494, 2016, doi: 10.1016/j.jmbbm.2016.05.027.

[143] A. Carlier *et al.*, “Designing optimal calcium phosphate scaffold-cell combinations using an integrative model-based approach,” *Acta Biomater.*, vol. 7, no. 10, pp. 3573–3585, 2011, doi: 10.1016/j.actbio.2011.06.021.

[144] W. Sun, B. Starly, A. Darling, and C. Gomez, “Computer-aided tissue engineering: application to biomimetic modelling and design of tissue scaffolds.,” *Biotechnol. Appl. Biochem.*, vol. 39, no. Pt 1, pp. 49–58, 2004, doi: 10.1042/BA20030109.

[145] F. A. Sabet, A. R. Najafi, E. Hamed, and I. Jasiuk, “Modelling of bone fracture and strength at different length scales: A review,” *Interface Focus*, vol. 6, no. 1, pp. 20–30, 2016, doi: 10.1098/rsfs.2015.0055.

[146] A. Sharma, S. Molla, K. S. Katti, and D. R. Katti, “Multiscale models of degradation and healing of bone tissue engineering nanocomposite scaffolds,” *J. Nanomechanics Micromechanics*, vol. 7, no. 4, pp. 1–14, 2017, doi: 10.1061/(ASCE)NM.2153-5477.0000133.

[147] S. Checa and P. J. Prendergast, “Effect of cell seeding and mechanical loading on vascularization and tissue formation inside a scaffold : A mechano-biological model using a lattice approach to simulate cell activity,” *J. Biomech.*, vol. 43, no. 5, pp. 961–968, 2010, doi: 10.1016/j.jbiomech.2009.10.044.

[148] M. J. Song, D. Dean, and M. L. Knothe Tate, “Computational Modeling of Tissue Engineering Scaffolds as Delivery Devices for Mechanical and Mechanically Modulated Signals,” no. February 2011, 2012, pp. 127–143.

[149] N. H. Pham, R. S. Voronov, S. B. Vangordon, V. I. Sikavitsas, and D. V. Papavassiliou, “Predicting the stress distribution within scaffolds with ordered architecture,” *Biorheology*, vol. 49, no. 4, pp. 235–247, 2012, doi: 10.3233/BIR-2012-0613.

[150] F. Zhao, T. J. Vaughan, and L. M. Mcnamara, “Multiscale fluid–structure interaction modelling to determine the mechanical stimulation of bone cells in a tissue engineered scaffold,” *Biomech. Model. Mechanobiol.*, vol. 14, no. 2, pp. 231–243, 2015, doi: 10.1007/s10237-014-0599-z.

[151] A. Campos Marin and D. Lacroix, “The inter-sample structural variability of regular tissue-engineered scaffolds significantly affects the micromechanical local cell environment,” *Interface Focus*, vol. 5, no. 2, pp. 20140097–20140097, 2015, doi: 10.1098/rsfs.2014.0097.

[152] H. a. Almeida and P. J. Bártolo, “Design of tissue engineering scaffolds based on hyperbolic surfaces: Structural numerical evaluation,” *Med. Eng. Phys.*, vol. 36, no. 8, pp. 1033–1040, 2014, doi: 10.1016/j.medengphy.2014.05.006.

[153] A. S. Dalaq, D. W. Abueidda, R. K. Abu Al-Rub, and I. M. Jasiuk, “Finite element prediction of effective elastic properties of interpenetrating phase composites with architectured 3D sheet reinforcements,” *Int. J. Solids Struct.*, vol. 83, pp. 169–182, 2016, doi: 10.1016/j.ijsolstr.2016.01.011.

[154] J. Shi, L. Zhu, L. Li, Z. Li, J. Yang, and X. Wang, “A TPMS-based method for modeling porous scaffolds for bionic bone tissue engineering,” *Sci. Rep.*, vol. 8, no. 1, 2018, doi: 10.1038/s41598-018-25750-9.

[155] A. Salehi and A. Daneshmehr, “Using Minimal Surface theory to design bone tissue scaffold and validate it with SLS 3D printer,” 2019.

[156] S. M. Giannitelli, D. Accoto, M. Trombetta, and A. Rainer, “Current trends in the design of scaffolds for computer-aided tissue engineering,” *Acta Biomater.*, vol. 10, no. 2, pp. 580–594, 2014, doi: 10.1016/j.actbio.2013.10.024.

[157] S. Limmahakhun and C. Yan, “Graded Cellular Bone Scaffolds,” *Scaffolds Tissue Eng. - Mater. Technol. Clin. Appl.*, 2017, doi: 10.5772/intechopen.69911.

[158] C. Y. Lin, N. Kikuchi, and S. J. Hollister, “A novel method for biomaterial scaffold internal architecture design to match bone elastic properties with desired porosity,” *J. Biomech.*, vol. 37, no. 5, pp. 623–636, 2004, doi: 10.1016/j.jbiomech.2003.09.029.

[159] J. Wieding, A. Wolf, and R. Bader, “Numerical optimization of open-porous bone scaffold structures to match the elastic properties of human cortical bone,” *J. Mech. Behav. Biomed. Mater.*, vol. 37, pp. 56–68, 2014, doi: 10.1016/j.jmbbm.2014.05.002.

[160] N. Reznikov *et al.*, “Individual response variations in scaffold-guided bone regeneration are determined by independent strain- and injury-induced mechanisms,” *Biomaterials*, vol. 194, no. August 2018, pp. 183–194, 2019, doi: 10.1016/j.biomaterials.2018.11.026.

[161] W. J. Hendrikson, C. A. van Blitterswijk, J. Rouwkema, and L. Moroni, “The use of finite element analyses to design and fabricate three-dimensional scaffolds for skeletal tissue engineering,” *Front. Bioeng. Biotechnol.*, vol. 5, no. MAY, pp. 1–13, 2017, doi: 10.3389/fbioe.2017.00030.

[162] X. Liu, “Application Of Mechano-Regulatory Tissue Differentiation Theory In Tendon Attachment Scaffold Design - A Finite Element Study,” University of Notre Dame, 2006.

[163] C. Liu, Z. Xia, and J. T. Czernuszka, “Design and development of three-dimensional scaffolds for tissue engineering,” *Chem. Eng. Res.*, vol. 85, no. 1, pp. 1051–1064, 2007, doi: 10.1205/cherd06196.

[164] Y. Chen, S. Zhou, and Q. Li, “Microstructure design of biodegradable scaffold and its effect on tissue regeneration,” *Biomaterials*, vol. 32, no. 22, pp. 5003–5014,

2011, doi: 10.1016/j.biomaterials.2011.03.064.

[165] A. Boccaccio *et al.*, “Rhombicuboctahedron Unit Cell Based Scaffolds for Bone Regeneration : Geometry Optimization with a Mechanobiology – driven Algorithm,” *Mater. Sci. Eng. C*, 2017.

[166] Ó. L. Rodríguez-Montaño *et al.*, “Irregular Load Adapted Scaffold Optimization: A Computational Framework Based on Mechanobiological Criteria,” *ACS Biomater. Sci. Eng.*, vol. 5, no. 10, pp. 5392–5411, 2019, doi: 10.1021/acsbiomaterials.9b01023.

[167] G. Percoco, A. E. Uva, M. Fiorentino, M. Gattullo, V. M. Manghisi, and A. Boccaccio, “Mechanobiological approach to design and optimize bone tissue scaffolds 3D printed with fused deposition modeling: A feasibility study,” *Materials (Basel).*, vol. 13, no. 3, 2020, doi: 10.3390/ma13030648.

[168] C. Gorriz, F. Ribeiro, J. M. Guedes, and P. R. Fernandes, “A biomechanical approach for bone regeneration inside scaffolds,” in *Procedia Engineering*, 2015, vol. 110, pp. 82–89, doi: 10.1016/j.proeng.2015.07.013.

[169] M. A. Velasco, Y. Lancheros, and D. A. Garzón-Alvarado, “Geometric and mechanical properties evaluation of scaffolds for bone tissue applications designing by a reaction-diffusion models and manufactured with a material jetting system,” *J. Comput. Des. Eng.*, vol. 3, no. 4, pp. 1–13, 2016, doi: 10.1016/j.jcde.2016.06.006.

[170] S. Wu, X. Liu, K. W. K. Yeung, C. Liu, and X. Yang, “Biomimetic porous scaffolds for bone tissue engineering,” *Mater. Sci. Eng. R Reports*, vol. 80, pp. 1–36, Jun. 2014, doi: 10.1016/j.mser.2014.04.001.

[171] G. Falvo D’Urso Labate *et al.*, “Bone structural similarity score: a multiparametric tool to match properties of biomimetic bone substitutes with their target tissues.,” *J. Appl. Biomater. Funct. Mater.*, vol. 14, no. 3, p. 0, 2016, doi: 10.5301/jabfm.5000283.

[172] D. F. Williams, “Challenges With the Development of Biomaterials for Sustainable Tissue Engineering,” *Front. Bioeng. Biotechnol.*, vol. 7, no. May, pp. 1–10, 2019, doi: 10.3389/fbioe.2019.00127.

[173] A. De Pieri, Y. Rochev, and D. I. Zeugolis, “Scaffold-free cell-based tissue engineering therapies: advances, shortfalls and forecast,” *npj Regen. Med.*, vol. 6, no. 1, 2021, doi: 10.1038/s41536-021-00133-3.

[174] O. de Weck and I. Y. Kim, “Finite element method.” Massachusetts Institute of Technology, pp. 1–26, 2004.

[175] A. D. Chandrupatla, T. R., Belegundu, T. Ramesh, and C. Ray, *Introduction to finite elements in engineering*, Vol. 2. Upper Saddle River: Prentice Hall, 2002.

[176] Dassault Systèmes, “Abaqus 6.11 Documentation.” Abaqus, 2011.

[177] Ó. L. Rodríguez-Montaño *et al.*, “An algorithm to optimize the micro-geometrical dimensions of scaffolds with spherical pores,” *Materials (Basel).*, vol. 13, no. 18,

pp. 1–17, 2020, doi: 10.3390/ma13184062.

[178] C. E. Korenczuk *et al.*, “Isotropic failure criteria are not appropriate for anisotropic fibrous biological tissues,” *J. Biomech. Eng.*, vol. 139, no. 7, pp. 1–10, 2017, doi: 10.1115/1.4036316.

[179] D. J. Kelly and P. J. Prendergast, “Mechano-regulation of stem cell differentiation and tissue regeneration in osteochondral defects,” *J. Biomech.*, vol. 38, no. 7, pp. 1413–1422, 2005, doi: 10.1016/j.jbiomech.2004.06.026.

[180] F. S. L. Bobbert *et al.*, “Additively manufactured metallic porous biomaterials based on minimal surfaces : A unique combination of topological , mechanical , and mass transport properties,” *Acta Biomater.*, vol. 53, pp. 572–584, 2017, doi: 10.1016/j.actbio.2017.02.024.

[181] P. F. Egan, “Integrated Design Approaches for 3D Printed Tissue Scaffolds: Review and Outlook,” *Materials (Basel).*, vol. 12, no. 15, p. 2355, Jul. 2019, doi: 10.3390/ma12152355.

[182] A. Boccaccio, D. J. Kelly, and C. Pappalettere, “A Mechano-Regulation Model of Fracture Repair in Vertebral Bodies,” no. March, pp. 433–443, 2011, doi: 10.1002/jor.21231.

[183] C. Sandino and D. Lacroix, “A dynamical study of the mechanical stimuli and tissue differentiation within a CaP scaffold based on micro-CT finite element models,” *Biomech. Model. Mechanobiol.*, vol. 10, no. 4, pp. 565–576, 2011, doi: 10.1007/s10237-010-0256-0.

[184] H. Isaksson, W. Wilson, C. C. van Donkelaar, R. Huiskes, and K. Ito, “Comparison of biophysical stimuli for mechano-regulation of tissue differentiation during fracture healing,” *J. Biomech.*, vol. 39, no. 8, pp. 1507–1516, 2006, doi: 10.1016/j.jbiomech.2005.01.037.

[185] J. A. Sanz-Herrera and A. R. Boccaccini, “Modelling bioactivity and degradation of bioactive glass based tissue engineering scaffolds,” *Int. J. Solids Struct.*, vol. 48, no. 2, pp. 257–268, 2011, doi: 10.1016/j.ijsolstr.2010.09.025.

[186] T. E. G. Krueger, D. L. J. Thorek, S. R. Denmeade, J. T. Isaacs, and W. N. Brennen, “Concise Review: Mesenchymal Stem Cell-Based Drug Delivery: The Good, the Bad, the Ugly, and the Promise,” *Stem Cells Transl. Med.*, vol. 7, no. 9, pp. 651–663, 2018, doi: 10.1002/sctm.18-0024.

[187] M. A. Pérez and P. J. Prendergast, “Random-walk models of cell dispersal included in mechanobiological simulations of tissue differentiation,” *J. Biomech.*, vol. 40, no. 10, pp. 2244–2253, 2007, doi: 10.1016/j.jbiomech.2006.10.020.

[188] P. Schneider, M. Meier, R. Wepf, and R. Müller, “Towards quantitative 3D imaging of the osteocyte lacuno-canalicular network,” *Bone*, vol. 47, no. 5, pp. 848–858, 2010, doi: 10.1016/j.bone.2010.07.026.

[189] A. Boccaccio, P. J. Prendergast, C. Pappalettere, and D. J. Kelly, “Tissue differentiation and bone regeneration in an osteotomized mandible: A computational analysis of the latency period,” *Med. Biol. Eng. Comput.*, vol. 46, no.

3, pp. 283–298, 2008, doi: 10.1007/s11517-007-0247-1.

[190] A. Göpferich, “Mechanisms of polymer degradation and erosion,” *Biomaterials*, vol. 17, no. 2, pp. 103–114, 1996, doi: 10.1016/B978-008045154-1.50016-2.

[191] C. Mircioiu *et al.*, “Mathematical modeling of release kinetics from supramolecular drug delivery systems,” *Pharmaceutics*, vol. 11, no. 3, 2019, doi: 10.3390/pharmaceutics11030140.

[192] F. Ye and H. Wang, “A simple Python code for computing effective properties of 2D and 3D representative volume element under periodic boundary conditions,” *arXiv*, 2017.

[193] A. Ramos and J. A. Simões, “Tetrahedral versus hexahedral finite elements in numerical modelling of the proximal femur,” *Med. Eng. Phys.*, vol. 28, no. 9, pp. 916–924, 2006, doi: 10.1016/j.medengphy.2005.12.006.

[194] S. C. Tadepalli, A. Erdemir, and P. R. Cavanagh, “Comparison of hexahedral and tetrahedral elements in finite element analysis of the foot and footwear,” *J. Biomech.*, vol. 44, no. 12, pp. 2337–2343, Aug. 2011, doi: 10.1016/j.jbiomech.2011.05.006.

[195] A. Lipphaus and U. Witzel, “Three-dimensional finite element analysis of the dural folds and the human skull under head acceleration,” *Anat. Rec.*, vol. 304, no. 2, pp. 1–9, Feb. 2020, doi: 10.1002/ar.24401.

[196] J. Y. Won *et al.*, “Evaluation of 3D printed PCL/PLGA/β-TCP versus collagen membranes for guided bone regeneration in a beagle implant model,” *Biomed. Mater.*, vol. 11, no. 5, p. 55013, 2016, doi: 10.1088/1748-6041/11/5/055013.

[197] A. Tsoularis and J. Wallace, “Analysis of logistic growth models,” *Math. Biosci.*, vol. 179, no. 1, pp. 21–55, Jul. 2002, doi: 10.1016/S0025-5564(02)00096-2.